



**Michigan
Technological
University**

Michigan Technological University
Digital Commons @ Michigan Tech

Dissertations, Master's Theses and Master's Reports

2022

Oxidative aging and fracture behavior of polymers and composites: theory, modeling and experiments

Shabnam Konica

Michigan Technological University, skonica@mtu.edu

Copyright 2022 Shabnam Konica

Recommended Citation

Konica, Shabnam, "Oxidative aging and fracture behavior of polymers and composites: theory, modeling and experiments", Open Access Dissertation, Michigan Technological University, 2022.
<https://doi.org/10.37099/mtu.dc.etdr/1392>

Follow this and additional works at: <https://digitalcommons.mtu.edu/etdr>



Part of the [Applied Mechanics Commons](#)

OXIDATIVE AGING AND FRACTURE BEHAVIOR OF POLYMERS AND
COMPOSITES: THEORY, MODELING AND EXPERIMENTS

By

Shabnam Konica

A DISSERTATION

Submitted in partial fulfillment of the requirements for the degree of

DOCTOR OF PHILOSOPHY

In Mechanical Engineering-Engineering Mechanics

MICHIGAN TECHNOLOGICAL UNIVERSITY

2022

© 2022 Shabnam Konica

This dissertation has been approved in partial fulfillment of the requirements for the Degree of DOCTOR OF PHILOSOPHY in Mechanical Engineering-Engineering Mechanics.

Department of Mechanical Engineering-Engineering Mechanics

Dissertation Advisor: *Dr. Trisha Sain*

Committee Member: *Dr. Gregory Odegard*

Committee Member: *Dr. Ibrahim Miskioglu*

Committee Member: *Dr. Shawn Chester*

Department Chair: *Dr. William W. Predebon*

Dedication

To the loving memory of my father.

Contents

List of Figures	xvii
List of Tables	xxv
Preface	xxvii
Acknowledgments	xxix
Abstract	xxxi
 1 A thermodynamically consistent chemo-mechanically coupled	
large deformation model for polymer oxidation	1
1.1 Introduction	1
1.2 Chemistry of oxidation	6
1.3 Thermodynamically consistent chemo-mechanically coupled theory for	
polymer oxidation	8
1.3.1 Kinematics	8
1.3.1.1 Extent of reaction	8
1.3.1.2 Kinematics of the deformation	9

1.3.2	Balance laws	14
1.3.2.1	Mass balance for the diffusing and reacting species	14
1.3.2.2	Specific form of mass balance in polymer oxidation	15
1.3.2.3	Balance of oxygen concentration	17
1.3.2.4	Balance of hydroperoxide, POOH and the polymer substrate, PH and oxidation product, POOP . . .	18
1.3.2.5	Balance of forces and moments	20
1.3.2.6	Energy balance	20
1.3.2.7	Stress-power	22
1.3.3	Constitutive theories	24
1.3.3.1	Basic constitutive equation	24
1.4	Specialization of the constitutive equations	28
1.4.1	Free energy	29
1.4.2	Oxidation dependent shear modulus	31
1.4.3	Stress, chemical potential and affinity	32
1.4.4	Evolution of extent of reaction, $\xi_{(n)}$	33
1.4.5	Oxygen flux and diffusivity	34
1.5	Governing differential equations and the boundary conditions	37
1.6	Representative numerical simulations	38
1.6.1	Parameter estimation	42
1.6.2	Case study 1: Diffusion limited oxidation	47

1.6.3	Case study 2: reaction-limited oxidation	53
1.6.4	Case study 3: coupled mechanical stress -oxidation process .	56
1.6.5	Residual stress and shrinkage strain developed in a randomly distributed fiber composite subjected to oxidation	60
1.7	Concluding remark	61
2	A Reaction-driven Evolving Network Theory Coupled with Phase- field Fracture to Model Polymer Oxidative Aging	63
2.1	Introduction	63
2.2	A reaction-dependent network theory coupled with phase-field fracture for polymers oxidation	68
2.2.1	Chemistry of oxidation:- the reaction kinetics	69
2.2.2	A reaction-dependent network theory based on the statistical mechanics of polymer chains	72
2.2.2.1	Chain distribution function	73
2.2.3	Evolution of chain distribution due to the combined effect of oxidation and mechanical deformation	76
2.2.3.1	Evolution of the concentration of active chains . . .	79
2.2.3.2	Active chain ratio and the dissociated chain ratio .	80
2.2.3.3	Macroscopic property degradation due to oxidative embrittlement	81

2.2.4	The chain distribution tensor and the free energy of the oxidation reacted network	83
2.2.5	A phase-field fracture model to predict macroscale damage and fracture in polymers due to oxidation	86
2.2.5.1	Phase-field order parameter or macroscale damage variable	88
2.2.6	The chemo-mechanically coupled theory for polymer oxidation:- the balance laws and thermodynamic consistency	90
2.2.6.1	Mass balance for the diffusing and reacting species	90
2.2.6.2	Balance of forces and moments	91
2.2.6.3	Energy imbalance and thermodynamic consistency	92
2.2.7	Constitutive equations for the mechanical, diffusion, chemical reactions and phase field damage	95
2.2.7.0.1	Free energy:-	95
2.2.7.0.2	Stress and chemical potential	97
2.2.7.0.3	Governing equation for the phase-field variable d:-	98
2.2.7.0.4	Reaction dependent shear modulus, fracture energy and limiting chain extensibility parameters:-	100
2.2.8	Governing differential equations and the boundary conditions	102

2.3	Material Parameter Estimation	103
2.3.0.0.1	Choice of l_c	105
2.4	Representative numerical simulations	107
2.4.1	Case study-1: Oxidative aging of a dogbone specimen followed by tensile loading	107
2.4.1.0.1	Case $k_a > k_d$:-	113
2.4.2	Case study-2: Oxidation followed by Mode-I loading in a single- edge-notched plate	114
2.4.3	Case study-3: Effect of oxidative aging in an asymmetrically notched specimen	118
2.5	Concluding remark	123
3	A homogenized large deformation constitutive model for thermo- oxidation in fiber-reinforced polymers	124
3.1	Introduction	125
3.2	Homogenized constitutive theory of oxidation in a fiber-reinforced poly- mer matrix composite	130
3.2.1	Oxidation reaction kinetics and the associated state variable	131
3.2.2	Kinematics-incorporating the anisotropic effect due to the fibers	132
3.2.3	Mass balance for the diffusing and reacting species	136
3.2.4	Balance of forces and moments	137

3.2.4.1	Thermodynamics and the energy balance	137
3.2.5	Basic constitutive equations	139
3.2.6	Specific constitutive form for the homogenized fiber-reinforced polymer composites	141
3.2.6.0.1	Cauchy stress, chemical potential and affinity:-	143
3.2.6.0.2	Evolution of extent of reaction ξ_n:-	144
3.2.6.0.3	Oxidation dependent shear modulus, diffusivity and stretchability:-	144
3.2.7	Governing differential equations for the coupled diffusion- reaction-mechanical system	146
3.3	Representative numerical simulations	148
3.3.0.0.1	<u>Case study 1-2-D unidirectional fiber- reinforced composite RVE undergoing isothermal oxidation:-</u>	149
3.3.0.0.2	Comparison between axial and trans- verse oxide layer growth in unidirec- tional RVE:-	153
3.3.0.0.3	Extent of oxidation in composites as a function of fiber volume fraction:-	155

3.3.0.0.4	Comparison of shrinkage strain evolution with experiments as a function of fiber volume fraction:-	158
3.3.0.0.5	Case study 2-oxidation in a unidirectional 3-D composite RVE:-	159
3.3.0.0.6	Case study 3-oxidative aging in a composite bracket with two different fiber orientations:-	161
3.4	Concluding remark	164
4	A unified phase-field fracture model for fiber-reinforced polymer composites	166
4.1	Introduction	166
4.2	Theoretical aspects of the model:-	170
4.2.1	Balance laws	177
4.2.1.0.1	Macro and micro-force balance-	178
4.2.1.0.2	Balance of energy- thermodynamic consideration-	178
4.2.1.0.3	Further consequences of thermodynamics: evolution of temperature-	182
4.3	Specialization of the theory for the constitutive forms	183
4.3.0.0.1	Free Energy:-	183

4.3.0.0.2	Energy split:-	186
4.3.0.0.3	Cauchy Stress:-	188
4.3.0.0.4	Effect of temperature on the FRPC material properties:-	189
4.3.0.0.5	Anisotropic phase-field evolution in FRPC:-	191
4.4	Experiments and material parameter calibration	193
4.4.1	Materials and methods	193
4.4.2	Experimental results	196
4.4.2.0.1	Dynamic mechanical analysis	196
4.4.2.0.2	Quasi-static tensile testing of un-notched bars at different fiber orientations	197
4.4.2.0.3	Effect of temperature on single-edge notched tension (SENT) specimens:-	198
4.4.2.0.4	DIC analysis of the single-edge notched tensile specimens at different fiber orientations:-	200
4.4.3	Calibration of GFRC properties	201

4.4.3.0.1	Determination of the thermo-viscoelastic parameters of epoxy matrix and fiber modulus:	201
4.4.3.0.2	Determination of the length-scale parameters and fracture energies for matrix and fiber:	206
4.5	Representative numerical examples showing model prediction	208
4.5.1	Mode-I fracture tests of a single-edge notched specimens at different fiber orientations and crack length	208
4.5.2	Effect of high temperature on the GFRC response	211
4.6	Conclusion	215
5	Future recommendations	216
	References	221
A	Numerical Implementation of the coupled diffusion-deformation multiphysics problem	263
B	Evolution of the chain distribution tensor	269
C	Principle of virtual power	271
C.1	Energy imbalance	273

List of Figures

1.1	Diffusion limited oxidation in a polymer block.	41
1.2	Effect of χ on the extent of reaction (II)	45
1.3	a) Geometry of the polymer specimen subjected to DLO: E_1 is an element on the top surface and E_2 is an element close to the middle core. b) boundary condition for oxygen concentration at the top surface	48
1.4	Evolution of the extent of reactions: a) ξ_{1a} , b) ξ_2 , c) ξ_3 , d) ξ_6 after 100 hours of oxidation	50
1.5	Contour plots of concentrations in mol/L of : a) O_2 , b) $POOH$, c) PH , d) Carbonyl products after 100 hours of oxidation	51
1.6	Effect of ambient temperature and pressure in polymer oxidation . .	52
1.7	Oxide layer thickness as a function of aging time	53
1.8	a) Evolution of the extent of reactions (Ia), (II), (III) and (VI) for a reaction limited oxidation (RLO) after 200 hours of oxidation, b) corresponding normalized concentration of oxygen, PH and POOH	55

1.9	Comparison of the extent of reactions between DLO and RLO a) $\xi_{(1a)}$, b) $\xi_{(2)}$, c) $\xi_{(3)}$, d) $\xi_{(6)}$	56
1.10	The displacement boundary condition for the stress-coupled oxidation	57
1.11	Comparison between the reactive force between a) pure oxidation and b)stress-coupled oxidation c)effect of external stress on the extent of reaction (II)	58
1.12	Contour plots of Von-Mises stress : a) pure oxidation after 65 hours, and b) stress-coupled oxidation after 65 hours	59
1.13	Geometry of a randomly distributed fiber reinforced polymer composite sample.Geometry of a randomly distributed fiber reinforced polymer composite sample.	61
1.14	a) Contour plot for reaction II after 15 h of oxidation in the randomly distributed carbon fiber composite specimen; b) corresponding maxi- mum (in-plane) principal strain generated within the matrix.	62
2.1	(a) Typical virgin polymer chains with Kuhn segment 'b' and end to end distance vector \mathbf{r} , (b) polymer undergoing oxidation developing new cross-links and broken chains, (c) typical distribution of the end- to-end vector ($\phi(\mathbf{r})$), the black line represents virgin polymer and the red line represents oxidized polymer.	71

2.2	Sharp and diffusive crack topology: a sharp crack Γ embedded into the solid \mathcal{B} (left) and the regularized crack surface Γ_{l_c} with a functional of crack phase field d and the crack regularization length l_c	89
2.3	Linear trend of fracture energy and limiting chain stretchability parameter as a function of dissociated chain ratio	101
2.4	Estimation for the k_a and k_d , the rate-like coefficients for polyethylene; the "markers" correspond to the experimental data from [87]. . . .	104
2.5	(a) Geometry of a dogbone specimen (all dimensions are in mm); (b) boundary condition for the oxygen concentration applied at the edges of the dogbone sample (top) and the displacement boundary condition applied at the top surface of specimen in Step-2 (bottom).	109
2.6	Contour plots for (a) extent of reaction ξ_3 after 30 hours (left), 50 hours (middle) and 200 hours (right); (b) extent of reaction ξ_6 after 30 hours (left), 50 hours (middle) and 200 hours (right).	110
2.7	Contour plots of shear modulus (in MPa) after (a) 30 hours, (b) after 50 hours (with $k_a < k_d$), (c) 50 hours (with $k_a > k_d$) and (d) 200 hours.	110
2.8	(a) Contour plots of λ_L after (i) 30 hours, (ii) after 50 hours (with $k_a < k_d$), (iii) 50 hours (with $k_a > k_d$) and (iv) 200 hours; (b) Comparison of (normalized) limiting stretchability with experiment from [86]. . .	111

2.9	(i) Force vs displacement plots for the dogbone sample subjected to tensile loading upon oxidation for various hours; (ii) Contour plots of the phase field damage variable at significant points in the force-displacement plot as marked 'a', 'b' and 'c'.	112
2.10	(a) Geometry of the single-edge-notched tension sample (all dimensions are in mm); Contour plots for the (b) oxygen concentration (mol/L); (c) extent of reaction (III), ξ_3 ; and (d) chain dissociation ratio c_{rd} , after 100 hours of oxidation.	115
2.11	Contour plots of (a) G_c in (N/m); (b) λ_L after 100 hours of oxidation.	116
2.12	(a) Force vs. displacement plot of the single-edge-notch sample ; (b) Contour plots of the phase field variable d at significant points in the force-displacement plot marked as a, b, and c for the oxidized polymer.	117
2.13	Geometry and dimension for the asymmetrically notched specimen.	120
2.14	a) Contour plots of extent of reaction (III) after 50 hours of oxidation: b) corresponding contour plots of Fracture energy, $G_c(N/m)$ and c) contour plots for limiting stretchability, λ_L ; top row- only left side oxidized; bottom row- both sides oxidized.	121
2.15	(a) Force vs. displacement plot for the asymmetric notched specimen under different oxidation conditions; (b) the corresponding damage contours near the final failure point.	122

3.1	Geometry and boundary conditions for 2D unidirectional composite RVE: (a) (left) Heterogeneous RVE showing fibers and polymer matrix; (right) corresponding homogenized 2D version; (b) chemical boundary condition for oxygen concentration.	151
3.2	Contour plots for the -(a) extent of reaction (II); (b) shrinkage strain and (c) Von-mises stress after 80 hours of oxidation; the left figures correspond to the heterogeneous model while the right figures represent the results from the corresponding homogenized model.	154
3.3	Anisotropic growth of the oxide layer in a typical unidirectional fiber-reinforced PMC as a function of time:- t_a corresponds to the normalized oxide layer along the axial direction; t_t denotes the normalized oxide layer in the transverse direction, respectively.	156
3.4	Effect of fiber volume fraction on the FRPMC oxidized at $150^\circ C$ for 100 hrs- contour plots of (a) extent of reaction (II), ξ_2 ; (b) volume shrinkage, J^s ; and (c) Von-Mises stress.	157
3.5	Effect of fiber volume fraction (or the fiber spacing) on the residual shrinkage generated in the FRPMC – normalized oxidative shrinkage plotted as a function of fiber volume fraction.	160
3.6	Geometry for the 3D unidirectional composite RVE:- (left) the 3-D heterogeneous RVE; (right) the corresponding homogenized model.	161

3.7	Contour plot for the (a) extent of reaction (II) (ξ_2); (b) volumetric shrinkage J^s , after 80 hrs of oxidation.	162
3.8	Geometry and the boundary conditions of the composite bracket.	163
3.9	Contour plots for the (a) extent of reaction (II); (b) volumetric shrinkage; and (c) Von-mises stress after 100hrs of oxidation	164
4.1	(i) Schematic representation of the finite viscoelastic model; (ii) schematic representation of the phase-field approximation of a crack in a 2-D domain: (a) Sharp crack topology and (b) regularized crack approximation over the length l	171
4.2	(a) Single-edge notched tensile bars at different fiber orientations: fiber orientations are shown with single black arrows, L and w represent the gauge length and the width of the specimen, respectively; here crack length $a = 0.2w$; (b) A composite bar with the tabs attached as grips for the tension test.	195
4.3	DMA results: (a) Stress relaxation data of GFRC at 0° and 90° fiber orientations; (b) Temperature sweep; (c) Frequency sweep at 35°C ; (d) Frequency sweep at 125°C . The plots (b-d) considers 90° fiber orientation.	198
4.4	Experimental load-displacement plots for un-notched GFRC bars at different fiber orientations.	199

4.5	Experimental comparison of the load-displacement plots at different temperatures: (a) $\gamma = 0^\circ$; (b) $\gamma = 90^\circ$ (ϑ_{Room} denotes the room temperature).	200
4.6	Fracture patterns observed at different fiber angles after tensile testing of GFRC specimens. The affected fracture zone is marked with red box.	201
4.7	DIC images (displacement contour) of single edge-notched tensile specimens at different fiber orientations: (a) Different stages of crack propagation when fibers are embedded at 0° ; (b) Crack propagation path at fracture for 45° fiber orientation; (c) Crack propagation path at fracture for 90° fiber orientation.	202
4.8	Frequency sweep at 35°C fitted against the Prony series model: (a) Storage modulus; (b) $\tan\delta$ fit	204
4.9	Frequency sweep at 125°C fitted against the Prony series model: (a) Storage modulus; (b) $\tan\delta$ fit	204
4.10	Load vs. displacement plot from the quasi-static tensile testing of unnotched composite bars: model vs. experiment for fiber alignment of 90° with respect to the loading axis.	205
4.11	Load vs. displacement plot from the quasi-static tensile testing of unnotched composite bars: model vs. experiments for fiber alignment of 0° with respect to the loading axis.	206

4.12	Zoomed view of the meshing and the boundary conditions of a single-edge notched $1'' \times 1''$ specimen with $a/w = 0.5$: (a) $\gamma = 0^\circ$; (b) $\gamma = 45^\circ$; and (c) $\gamma = 90^\circ$	210
4.13	Load-displacement plot for SENT specimens: comparison of model prediction with the experiments for (a) 0° with $a/w = 0.2$ and $a/w = 0.5$; (b) 45° with $a/w = 0.5$; (c) 90° with $a/w = 0.2$ and $a/w = 0.5$	211
4.14	Contour plots of d at different fiber orientations for single-edge notched specimen with $a/w = 0.5$ corresponding to Fig. 4.12: (a) $\gamma = 0^\circ$; (b) $\gamma = 45^\circ$; (c) $\gamma = 90^\circ$	212
4.15	Comparison of elastic energy between matrix and fiber and the corresponding history functions at the notch tip of the SENT-specimen with fiber orientation, $\gamma = 45^\circ$	212
4.16	Contour plots of temperature, ϑ at different fiber orientations for single-edge notched specimen with $a/w = 0.5$ corresponding to Fig. 4.12: (a) $\gamma = 0^\circ$; (b) $\gamma = 45^\circ$; (c) $\gamma = 90^\circ$	213
4.17	Load-displacement plot of GFRC at 140°C : (a) $\gamma = 0^\circ$; (b) $\gamma = 90^\circ$	214

List of Tables

1.1	Kinetic parameters related to diffusion and reaction for a typical polymer oxidation reaction	46
1.2	Material parameters for a representative elastomer.	46
2.1	List of symbols and their meanings	69
3.1	Material parameters for a representative fiber-reinforced composite undergoing oxidation	150
4.1	Material parameters for epoxy	203
4.2	Material parameters for glass-fiber and fracture properties of GFRC	208

Preface

Chapter 1 has been published in Journal of Mechanics and Physics of Solid (JMPS).

1st author Shabnam Konica has contributed as a whole in writing the manuscript, generating all the results deriving the theory presented in the manuscript. Corresponding author Dr. Trisha Sain has supervised the entire work, edited the manuscript and the responsible person for any future communication. All authors have participated in (a) conception and design, or analysis and interpretation of the data; (b) drafting the article or revising it critically for important intellectual content; and (c) approval of the final version.

Chapter 2 has also been published in JMPS. 1st author Shabnam Konica has contributed in writing the manuscript, generating all the numerical results, Deriving the theory presented in the manuscript. Corresponding author Dr. Trisha Sain has supervised the entire work, edited the manuscript and the responsible person for any future communication.

Chapter 3 has been published in Mechanics of Materials (MOM). Shabnam Konica has worked for theoretic development, numerical implementation, conducting simulations, manuscript writing and revision of the manuscript. Trisha Sain has worked for conceptualization, supervising, writing and revising the manuscript, and responsible

for any future correspondence related to the proposed work.

Chapter 4 is under preparation to be submitted to a journal. Shabnam Konica has developed the theory, numerical implementation, simulations, experiments, model calibration and validation and written the manuscript. Dr. Trisha Sain has supervised the whole project.

Acknowledgments

This thesis becomes a reality with the kind support and help of many individuals, and I thank and acknowledge all of them. First and foremost, I would like to express my sincerest gratitude to my advisor, Dr. Trisha Sain, for her constant support, guidance, and mentoring throughout this work. Her outstanding work ethic and exceptional standards inspired me to become a better researcher and motivated me to produce quality work. She encouraged me to think out of the box and work independently while continuously offering guidance to nudge me in the right direction, a trait I would surely like to adopt in my future career venture. I would also like to thank my thesis committee members, Dr. Gregory Odegard, Dr. Ibrahim Miskioglu, and Dr. Shawn Chester (NJIT), for their insightful suggestions during my P.hD work. I especially thank Dr. Shawn Chester for his invaluable help with the numerical implementation of my work. My sincere thanks also extend to Dr. Bo Chen and Dr. Kyriaki Kalaitzidou (GTech) for help with the experimental work. Thanks to Dr. Susanta Ghosh for his valuable feedback and encouragement and for teaching me Finite Element Methods. Thanks for all the occasional deserts and treats he brought us in the lab, which gave me one more reason to stay there.

I thank my present and past colleagues of the Laboratory of Mechanics and Modeling of Advanced Materials lab: Dr. Muhammed R. Imam, Rishabh Awasthi, Akash Kumar, Joseph Van Linn, Ben Jewell, and Mark Ousudigian for their help and for being

such great friends. Especially, I thank Joseph and Ben for their assistance with my experimental work. Also, many thanks to our remote lab members, Jeff Wiersma (Herman Miller) and Benedict Egoyibi (Corning Inc.), for being such wonderful friends. Particularly, thanks to Jeff for helping me connect with Avient Corporation. And thanks to Benedict for collaborating with me in the chemically-strengthened glass project. Thanks to Avient Corporation for supplying us with the composite material used in this research, precisely thanks to Dave Jones (Avient Corporation) for his excellent customer support. I also thank the doctoral Students from Dr. Ghosh's lab: Upendra Yadav, Ponkrshnan Thiagarajan, Shashank Pathrudkar, and Revanth Mathey, for their interesting brain-storming luncheon conversations. A big thanks to Sagar Patil from the molecular modeling research group for the emotional support in dire times. Thanks to Cindy Wadaga and Karen Bess for being the friendliest and fastest administrative staff I have ever seen. They made all my complex organizational problems disappear magically. Thanks to Rachel Store, Bob page, Martin Toth, Jonathan Lund, Kevin Johnson, and Paul Fraley for assisting me with the experiments. Last but not least, I am thankful to my mother, sisters and my friend Alam for their faith in me and for encouraging me to pursue my dreams. This long dedication to Ph.D. work would have been impossible without their moral support. Finally, I gratefully acknowledge the support of Michigan Technological University (MTU) and the Air Force Office of Scientific Research (AFOSR) for funding my research.

Abstract

Polymers and their composites (PMC) have emerged as effective alternative materials in structural, aerospace, and automotive industries due to their lightweight and tunable properties compared to metals. However, these materials tend to degrade during their operations in extreme environments. In this work, two extreme conditions are considered: - i) high-temperature oxidative degradation of polymers and polymer-based composites ii) Fracture and damage of polymer-based composites under thermo-mechanical loading. Polymer oxidation starts when oxygen from the ambient diffuses into the bulk material and initiates chemical reactions to develop a coarse, brittle oxide layer on the exposed surface. The oxidative degradation process is inherently complex in nature, as it involves a coupling between diffusion, reaction, and mechanics. As oxygen diffuses into the polymer, a series of chain reactions occur, resulting in residual shrinkage strain on the oxidized layer of the material due to escaping of the volatiles. Consequently, residual stress develops within the material, causing spontaneous cracking even without the application of external loading. Thus, the oxidative aging can cause premature cracking in the material and requires a better understanding of the interaction between the chemistry and mechanics at different length scales and timescales to comprehend the effect of thermo-oxidative aging of polymeric materials. In this work, a fully coupled thermodynamically consistent chemo-mechanical phase-field fracture model is developed that attempts to

bridge the gap between the experimental observations and a constitutive theory for thermo-oxidative aging in polymeric materials. To accomplish this, a novel approach has been adopted considering the chemical reactions at the polymer macromolecular level, a reaction-driven transient network evolution theory at the microscale, and a constitutive model at the macroscale. Finally, a phase-field fracture theory is added to the chemo-mechanical model to predict the oxidation-induced fracture in the polymer under mechanical loading. The model has been further extended to a homogenized continuum theory to capture the anisotropic oxidation characteristic of the fiber-reinforced polymer matrix composites. Specialized forms of the constitutive equations and the governing partial differential equations have also been developed for the polymers and the composite systems and numerically implemented in finite elements.

Lastly, a unified phase-field fracture model is developed to create an experimentally validated, physically motivated, and computationally tractable model to predict the fracture response of the unidirectional fiber reinforced polymer matrix composites. A homogenized, coupled thermo-mechanical model is developed considering a thermo-viscoelastic polymer matrix. The model is numerically implemented by writing a ABAQUS user-element subroutine (UEL). The model can predict the constitutive response and direction-dependent damage propagation and final fracture in commercially acquired unidirectional glass-fiber-reinforced epoxy composite and in substantial agreement with the experiments.

Chapter 1

A thermodynamically consistent chemo-mechanically coupled large deformation model for polymer oxidation

1.1 Introduction

Polymers and polymer matrix composites (PMCs) are candidates for the replacement of metals and alloys in many aeronautic and defense applications due to their

well known specific properties, such as excellent strength to weight ratio, specific toughness, damping, thermal stability, corrosion resistance etc. One of the concerns linked to the long-term use of these materials is the modification of constitutive behavior, degraded mechanical properties and failure due to thermo-oxidation [102, 173, 193, 197, 269]. In general, the performance of polymers degrades significantly due to their long term exposure in extreme environments, such as chemical corrosion, radiation, hygrothermal effect etc. High temperature oxidation or thermo-oxidative aging in the polymer is one such example, where polymer undergoes a set of irreversible chemical reactions, preferably at a temperature near or higher than its glass transition (T_g) temperature, driven by oxygen (O_2) diffusion. As a result of this process, oxide layers form at the exposed surface, (often identified with a distinct color change), which may lead to spontaneous microcracking [63]. These microcracks further act as a favorable path for O_2 diffusion and promotes oxidation inside the material, eventually causing the materials to fail [48, 49, 59, 63, 202, 240, 241]. Therefore, oxidative aging in polymers could be a major concern in the aerospace and automotive industries, as it impacts both the safety and cost-effectiveness of these materials for their long-term applications.

Thermo-oxidative aging in polymers is a highly nonlinear, irreversible phenomena

driven by a coupled diffusion-reaction process, resulting in changes in the materials' molecular configuration as well as at the macro-scale. Numerous studies have been reported in recent literature focusing on the changes in macroscopic properties and molecular structure of polymers due to thermo-oxidation as in [59, 62, 63, 72, 193, 197, 200, 202, 240, 241]. According to these works, at the macro-molecular level, chain scission and oxidative cross-linking affect the polymer network and eventually alters the material property during oxidation. At the macroscale, as oxygen infuses into the polymer, it reacts with the material to create oxides and volatile compounds; latter leaving the material to form voids. Due to the void formation, the material progressively loses weight. At the same time, due to oxidative crosslinking, it becomes denser and end up with lower molecular weight. Ultimately these combined factors result in irreversible volume shrinkage within the polymer. A more detailed explanation of these can be found in [63]. Several quantifiable consequences of oxidation in the polymer such as an increase in modulus and glass transition temperature, and decrease in failure strain, etc. are also being reported in recent literature [40, 82, 87, 88, 172, 173, 193, 197]. Also, other effects of thermal oxidation include debonding on the fiber-matrix interface in PMC's and matrix micro-cracking, which might lead to premature failure of the composites [104, 200, 202, 241].

Modeling of polymer oxidation is a great challenging task as it involves various highly coupled physical and chemical phenomena. Early studies of thermal aging in polymers and PMC's were focused on determining the property deterioration and lifetime

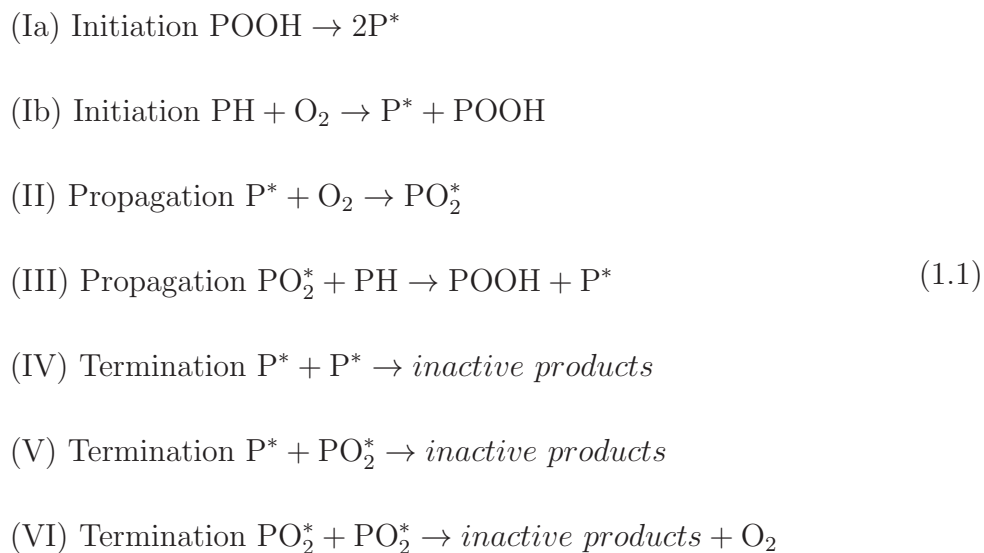
predictions by conducting accelerated aging experiments. These experimental data were further extrapolated using Arrhenius laws to predict the materials' behavior for later periods [25, 32, 33, 168, 184, 243]. However, as mentioned in [64], Arrhenius law can be applied only to an elementary reactive process, whereas polymer oxidation, in general, involves at least six elementary reactions. Therefore, it might not be accurate to use a generalized Arrhenius law for such complex cases. The deviation from Arrhenius law has been shown experimentally in [47, 106, 107, 108, 109, 261]. The multiple closed-loop chain reaction for polymer oxidation was also extensively studied and a kinetic model was formed based on the reaction chemistry to track down oxide layer thickness [19, 20, 21, 57, 59, 60, 61, 62, 63, 64, 193, 213, 262]. An extension of this kinetic model can be found in the literature, which is known as the three-zone oxidation model that emphasized on the heterogeneity of diffusion of oxygen [200, 240, 241]. This heterogeneity in the degree of oxidation results in non-uniform mechanical properties and inhomogeneous stress/strain distribution within an oxidized polymer. For a thick polymer specimen, diffusion-limited oxidation (DLO) model seemed more appropriate, which showed that the oxidation reaction got blunt on the surface of a thick sample instead of spreading toward the core [206]. These aforementioned models used a semi-empirical approach to determine the mechanical properties of oxidized polymers, such as correlating mechanical stiffness to the thickness of the oxidized layer [104, 172, 173, 193, 197]. Till date, prediction of constitutive response of oxidized

polymer is still trifling. The only acceptable thermodynamically consistent continuum model to predict the constitutive response based on high-temperature oxidation behavior was found in the work of [103, 104].

The coupling of multiple physics in the constitutive modeling of materials had been explored in the mechanics' community. For instance, a coupled theory for high-temperature oxidation in metallic alloys had been developed by [153]. The coupled stress-diffusion response in polymer gels had been extensively studied by [52, 53, 54, 77, 113]. Recent work by [267] on the reaction-diffusion coupling in photoresponsive gels is also noteworthy. Several research groups had also published recent works on coupled photochemical reaction-large deformation theory as, [73, 220, 263]. In the present work, a thermodynamically consistent continuum-level theory is developed that incorporates the coupling between diffusion and the kinetics of oxidation reaction along with the large deformation behavior of polymers. The model is further implemented in a FE setting by writing a user element subroutine (UEL), to describe the coupled thermo-chemo-mechanical behavior that arises due to high-temperature oxidation in polymers. The paper is organized as follows- firstly, the coupled theory of oxidation has been explained, followed by the specific constitutive model description. Various numerical simulations have been done, and the results are analyzed in detail to explain the capability of the model. In the end, the concluding remarks have been presented.

1.2 Chemistry of oxidation

The mechanistic reaction schemes proposed to describe the thermal oxidation of polymers had a consensus in the literature except for some minor variation at the initiation stage[19, 20, 21, 57, 59, 60, 61, 62, 63, 64, 213, 262]. According to this standard mechanistic scheme, during oxidation, the polymer undergoes six sets of closed-loop chain reactions involving three major steps identified as initiation, propagation, and termination, respectively, as explained below:



where PH represents the polymer substrate; P^* is the alkyl radicals; POOH is the hydroperoxide, PO_2^* is the peroxy radical and O_2 represents oxygen. These set of

reactions was originally proposed by Verdu and coworkers [64]. For a specific ambient condition, which particular subset of reactions would be dominating the oxidation process is usually determined by comparing the activation energy and the reaction rates for each reaction [57].

Among the two initiation reactions, activation energy associated with the hydroperoxide decomposition (Ia) is noticeably lower than the substrate decomposition or substrate oxidation reaction (Ib). Hence reaction (Ia) is called the initiator of the oxidation reaction as it tends to dominate the initiation rate [64]. On the other hand, at high temperature and low POOH concentration, initiation is predominantly due to the substrate consumption (Ib). In such case the rate of initiation becomes almost constant or slowly decreases. This causes significant structural change in the polymer as a result of the substrate consumption [64].

In the case of propagation reaction, the rate constant k_2 for reaction (II) is much faster than the rate constant k_3 for reaction (III). Therefore, in the case of excess availability of oxygen, reaction(III) becomes the dominant rate-controlling process, as the propagation depends on the availability of polymer [64]. Further, due to the presence of excess oxygen, alkyl radicals (P^*) quickly transforms into peroxy radical (PO_2^*); thus, the termination reaction occurs mostly by reaction (VI). It was reported in the literature that under the steady-state assumption, the overall rate of oxidation in the case of excess oxygen is linked to the constant value of $\frac{k_3^2}{k_6[PH]^2}$ [19]. On the other hand, in the case of limited oxygen availability, the overall rate can be linked

to the constant $\frac{k_2 k_6}{2k_5 k_3 [PH]}$ and $\frac{k_3^2}{k_6 [PH]^2}$ [61, 62]. Finally, it is noteworthy to mention that, there exists a critical oxygen concentration C_c , above which oxygen consumption reaches the saturation limit, and is defined by a relation, $C_c \approx 6 \frac{k_5}{k_2} \frac{[PH]}{k_6}$ [60, 64]. Therefore, the kinetics of the oxidation reaction is influenced by several factors and requires a thorough understanding at the macromolecular level to couple its effect with the deformation kinematics.

1.3 Thermodynamically consistent chemo-mechanically coupled theory for polymer oxidation

1.3.1 Kinematics

1.3.1.1 Extent of reaction

Based on the work of high-temperature oxidation in metallic alloys [153] and a more recent work in curing of glassy polymers [220], we define the extent of reaction for each reaction (n) in a local dimensionless form as,

$$0 \leq \xi_{(n)}(\mathbf{X}, t) \leq 1 \quad (1.2)$$

where (n) is the number of reaction and can vary between 1 to 6 depending on the oxidation kinetics for a specific polymer. Since polymer oxidation is a multi-component system involving multiple reactions (as described earlier), the chemical concentration for each component β would changed depending on the extent of all the reactions in which it is participating,

$$r^{(\beta)} = \sum_{(n)} \left[\mathcal{R}_{(n)} \dot{\xi}_{(n)} \right]^{(\beta)} \quad (1.3)$$

where $r^{(\beta)}$ is the rate of production or consumption of chemical species β and $\mathcal{R}_{(n)}$ is the stoichiometric coefficient in reaction n (measured in moles per volume), denotes the consumption or production rate for any species β .

1.3.1.2 Kinematics of the deformation

The notation used in this work is the standard of continuum mechanics [118]. The function χ defines a map which converts every material point in the reference configuration $\mathbf{X} \in \mathcal{B}_{\mathbf{R}}$ to a spatial or current one as, $\mathbf{x} \in \mathcal{B}_{\mathbf{t}}$. A smooth deformation is a

one to one mapping, $\mathbf{x} = \chi(\mathbf{X}, t)$ with deformation gradient defined as,

$$\mathbf{F} = \frac{\partial \chi}{\partial \mathbf{X}} \text{ with } J = \det \mathbf{F} > 0 \quad (1.4)$$

Oxygen embrittlement causes chain scission and weight loss in the polymer. The combined effect of those induces shrinkage strain in the oxide layer. Treating the shrinkage strain as irreversible, we consider a multiplicative decomposition of the total deformation gradient based on the large deformation theory of polymers [12],

$$\mathbf{F} = \mathbf{F}^e \mathbf{F}^p \quad (1.5)$$

where \mathbf{F}^e is the elastic component of the deformation gradient, \mathbf{F}^p is the irreversible plastic component, which incorporates the deformation due to permanent chemical shrinkage and viscoplastic deformation that can occur in the glassy polymer. Referring to Eq.3.2 the determinant J can be decomposed into,

$$J = J^e J^p, \quad \text{where } J^e = \det \mathbf{F}^e > 0 \quad \text{and} \quad J^p = \det \mathbf{F}^p > 0 \quad (1.6)$$

so that \mathbf{F}^e and \mathbf{F}^p are both invertible. The right polar decomposition of \mathbf{F}^e is given

by,

$$\mathbf{F}^e = \mathbf{R}^e \mathbf{U}^e = \mathbf{V}^e \mathbf{R}^e \quad (1.7)$$

where \mathbf{R}^e is the rotation and \mathbf{U}^e and \mathbf{V}^e are symmetric, positive-definite stretch tensors with,

$$\mathbf{U}^e = \sqrt{\mathbf{F}^{eT} \mathbf{F}^e} \quad \text{and} \quad \mathbf{V}^e = \sqrt{\mathbf{F}^e \mathbf{F}^{eT}} \quad (1.8)$$

The left and right Green-cauchy tensors are then defined as,

$$\mathbf{B}^e = \mathbf{V}^{e2} = \mathbf{F}^e \mathbf{F}^{eT} \quad \text{and} \quad \mathbf{C}^e = \mathbf{U}^{e2} = \mathbf{F}^{eT} \mathbf{F}^e \quad (1.9)$$

Further, the velocity gradient is defined as,

$$\mathbf{L} = \dot{\mathbf{F}} \mathbf{F}^{-1} \quad (1.10)$$

Substituting Eq. 3.2 into Eq. 1.10, we get

$$\begin{aligned} \mathbf{L} &= \dot{\mathbf{F}} \mathbf{F}^{-1} : \\ &= \dot{\mathbf{F}}^e \mathbf{F}^{e-1} + \mathbf{F}^e \mathbf{L}^p \mathbf{F}^{e-1} \end{aligned} \quad (1.11)$$

with,

$$\mathbf{L}^e = \dot{\mathbf{F}}^e \mathbf{F}^{-e} \quad and \quad \mathbf{L}^p = \dot{\mathbf{F}}^p \mathbf{F}^{-p} \quad (1.12)$$

The elastic and plastic deformation tensor can be further defined from the standard continuum mechanics as,

$$\mathbf{D}^e = \text{sym} \mathbf{L}^e, \quad \mathbf{W}^e = \text{skw} \mathbf{L}^e; \quad \mathbf{D}^p = \text{sym} \mathbf{L}^p, \quad \mathbf{W}^p = \text{skw} \mathbf{L}^p \quad (1.13)$$

So that, $\mathbf{L}^e = \mathbf{D}^e + \mathbf{W}^e$ and $\mathbf{L}^p = \mathbf{D}^p + \mathbf{W}^p$. Assuming plastic flow is irrotational, (as, $\mathbf{W}^p = 0$), the plastic velocity gradient becomes,

$$\mathbf{L}^p \equiv \mathbf{D}^p, \quad \text{with} \quad \dot{\mathbf{F}}^p = \mathbf{D}^p \mathbf{F}^p \quad (1.14)$$

We also make another kinematic assumption that the plastic stretch \mathbf{D}^p can be additively decomposed as,

$$\mathbf{D}^p = \mathbf{D}^s + \mathbf{D}^{vp} \quad (1.15)$$

where \mathbf{D}^s represents the inelastic strain rate due to oxidation induced shrinkage and \mathbf{D}^{vp} represents the inelastic strain rate due to bulk viscoplastic deformation in the polymer with $\text{tr} \mathbf{D}^{vp} = 0$. Among the 6 closed-loop chain reactions mentioned in Eq. 1.1, propagation reaction (II) is the one where oxygen reacts with polymer radicals to create peroxy radicals, whose molecular weight is less than the polymer [58]. Thus

we can consider that, the extent of propagation reaction (II), $\xi_{(2)}$, plays a major role in oxidative shrinkage. Assuming chemical shrinkage to be volumetric as well as isotropic and depends on the rate of extent of reaction, we have considered the following simple form for \mathbf{D}^s as,

$$\mathbf{D}^s = \gamma \dot{\xi}_{(2)} \mathbf{I} \text{ with } \text{tr} \mathbf{D}^s = 3\gamma \dot{\xi}_{(2)} \quad (1.16)$$

where $\gamma \leq 0$ is a material parameter that determines the amount of volume shrinkage.

By definition, $\dot{J}^p = J^p \text{tr} \mathbf{D}^p$. Hence, by integrating we can write,

$$J^p = \exp(3\gamma \xi_{(2)}) \text{ and } \frac{\partial J^p}{\partial \xi_{(2)}} = 3\gamma J^p \quad (1.17)$$

Finally, it can be shown that, \mathbf{F}^p , \mathbf{L}^p and \mathbf{C}^e are invariant under any change in frame.

The readers are suggested to refer earlier literature, such as, [9, 11, 12, 52, 53, 54, 153],

for the detailed proof of frame-indifference.

1.3.2 Balance laws

1.3.2.1 Mass balance for the diffusing and reacting species

Let P denotes any arbitrary part of the body \mathcal{B}_R surrounded by the boundary ∂P . Let $c_R^{(\beta)}(\mathbf{X}, t)$ denotes the concentration of species β in moles per unit reference volume which takes part into the oxidation reactions. The changes in the concentration of $c_R^{(\beta)}$ for any species β are caused by diffusion of that species across the boundary ∂P , which is characterized by a flux $\mathbf{j}_R^{(\beta)}(\mathbf{X}, t)$, defined by the number of diffusing species measured per unit area per unit time. Similarly $r_R^{(\beta)}(\mathbf{X}, t)$ denotes the number of moles for species β that is either consumed or produced per unit time due to the chemical reaction. The general mass balance law for any participating species β therefore takes the form,

$$\int_P \overline{\dot{c}_R^{(\beta)}} dv_R = - \int_{\partial P} \mathbf{j}_R^{(\beta)} \cdot \mathbf{n}_R da_R + \int_P r_R^{(\beta)} dv_R \quad (1.18)$$

for every part P , \mathbf{n}_R represents a unit vector in the reference configuration. Bringing the time derivative in Eq. 1.18 inside the integral and using the divergence theorem on the integral over ∂P , we find that

$$\int_P (\dot{c}_R^{(\beta)} + \text{Div} \mathbf{j}_R^{(\beta)} - r_R^{(\beta)}) dv_R = 0 \quad (1.19)$$

Since P is arbitrary, this leads to the local mass balance as,

$$\dot{c}_R^{(\beta)} = -\text{Div} \mathbf{j}_R^{(\beta)} + r_R^{(\beta)} \quad (1.20)$$

Finally, using Eq. 1.3 into 1.20, we can write,

$$\dot{c}_R^{(\beta)} = -\text{Div} \mathbf{j}_R^{(\beta)} + \sum_n [\mathcal{R}_n \dot{\xi}_{(n)}]^{(\beta)} \quad (1.21)$$

1.3.2.2 Specific form of mass balance in polymer oxidation

Based on the kinetics of oxidation reaction provided in the literature and discussed in section 1.2, we make some reasonable assumptions for mass balance of the reacting and diffusing species as given below,

† **Oxygen is the only diffusing species-** during oxidation, oxygen diffuses into the polymer and reacts with polymer macromolecules. As a consequence of the oxidation reactions some volatile compounds are also being produced which eventually leaves the polymer. Therefore, during oxidation both inward and

outward diffusion occurs. However, in this work, we consider oxygen is the only diffusing species and neglect the outward diffusion of the volatile compounds.

† **POOH initiates the oxidation chain-reactions**-As per our discussion in Section 1.2, we consider that initially some peroxide (POOH) is present as unstable hydrocarbon in the system to initiate the oxidation. And since the activation energy for POOH breaking into P^* is much low compared to the activation energy required for a direct reaction between PH and O_2 , the former one is always favored when peroxide is present. Therefore we assume that, only reaction (Ia) from Eq. 1.1 initiates the reaction.

† **Steady-state condition**- In a chain reaction consisting of multiple reactions, steady-state condition means that the reaction reached at a point where the amount of radicals produced at any time step gets consumed instantaneously in the subsequent steps to generate some other product. Thus the radical is considered as extremely reactive and is converted to some other product almost instantaneously. Therefore, the rate of change of concentration of the radical can be considered as zero. For more information on the steady-state chain reaction, please see [18]

† **Extent of reaction**- for each elementary reaction, we have introduced a state variable as, extent of reaction, $\xi_{(n)}$, where n indicates the number of elementary reaction. We consider that, these extent of reactions are directly related to the local reaction rate for each elementary reaction via a stoichiometric coefficient,

\mathcal{R}_n , so that the local reaction rate can be expressed as $\mathcal{R}_n \dot{\xi}_{(n)}$.

† **Global reaction rate for species-** we employ a similar approach as proposed in the kinetic model [64] to calculate the global reaction rate for each species. Following this, the change in rate for any given species concentration is the algebraic sum of elementary rates. Thus for any species β , the rate can be expressed as,

$$r_R^{(\beta)} = \sum_n [\mathcal{R}_n \dot{\xi}_{(n)}]^\beta \quad (1.22)$$

With the assumptions mentioned above and using the closed loop reactions given in Eq. 1.1, we can perform mass balance for oxygen, POOH and PH and POOP as described in the next section.

1.3.2.3 Balance of oxygen concentration

Applying mass balance, to track the oxygen concentration during the oxidation reaction at any time, t , we can write,

$$\dot{c}_R^{(O_2)} = -\text{Div} \mathbf{j}_R^{(O_2)} + r_R^{(O_2)} \quad (1.23)$$

As discussed in section 1.2, oxygen is consumed in reaction (II) and produced in reaction (VI). Thus, we can write,

$$r_R^{(O_2)} = \mathcal{R}_2 \dot{\xi}_{(2)} + \mathcal{R}_6 \dot{\xi}_{(6)} \quad (1.24)$$

where $r_R^{(O_2)}$ is the rate of consumption or production of oxygen. Substituting this into Eq. 1.23 we have,

$$\dot{c}_R^{(O_2)} = -\text{Div} \mathbf{j}_R^{(O_2)} + \mathcal{R}_2 \dot{\xi}_{(2)} + \mathcal{R}_6 \dot{\xi}_{(6)} \quad (1.25)$$

where \mathcal{R}_2 and \mathcal{R}_6 are the stoichiometric coefficients of oxygen in reaction (II) and (VI), respectively. Note that, the stoichiometric coefficients for the consumed and produced O_2 are considered as negative and positive, respectively.

1.3.2.4 Balance of hydroperoxide, POOH and the polymer substrate, PH and oxidation product, POOP

As discussed in section 1.2, POOH is the main initiator of the oxidation reactions. The reaction becomes auto-accelerated due to the formation of this initiator further in the propagation step. Therefore, the balance of POOH concentration comes from the initiation reaction (Ia) and propagation reaction (III); following which we can

write,

$$\dot{c}_R^{(POOH)} = \mathcal{R}_1 \dot{\xi}_{(1)} + \mathcal{R}_3 \dot{\xi}_{(3)} \quad (1.26)$$

where \mathcal{R}_1 and \mathcal{R}_3 are the stoichiometric coefficients of hydroperoxide in reaction (Ia) and (III), respectively.

Since we do not consider initiation reaction (Ib), the rate of change of PH-concentration can be tracked from only reaction (III) as,

$$\dot{c}_R^{(PH)} = \mathcal{R}_3 \dot{\xi}_{(3)} \quad (1.27)$$

where \mathcal{R}_3 is the stoichiometric coefficient of substrate, PH in reaction (III).

The termination products due to oxidation are carboxyls (POOP). They are formed in the termination reaction (V) and (VI). We can write the mass balance for POOP as,

$$\dot{c}_R^{(POOP)} = \mathcal{R}_5 \dot{\xi}_{(5)} + \mathcal{R}_6 \dot{\xi}_{(6)} \quad (1.28)$$

1.3.2.5 Balance of forces and moments

For the reference body, there exists a stress tensor, \mathbf{T}_R , called the Piola stress, such that the surface traction on the surface $\partial\mathcal{B}_R$ of reference body \mathcal{B}_R , is given by,

$$\mathbf{t}_R(\mathbf{n}_R) = \mathbf{T}_R \mathbf{n}_R \quad (1.29)$$

where, $\mathbf{t}_R(\mathbf{n}_R)$ is the surface traction and \mathbf{n}_R is a surface unit vector and \mathbf{T}_R satisfies the local force and moment balance as,

$$\text{Div} \mathbf{T}_R + \mathbf{b}_R = \mathbf{0} \quad \text{and} \quad \mathbf{T}_R \mathbf{F}^T = \mathbf{F} \mathbf{T}_R^T \quad (1.30)$$

where \mathbf{b}_R is non-inertial body force per unit volume of the reference body. Piola stress is related to Cauchy stress in the deformed body by,

$$\mathbf{T} = J^{-1} \mathbf{T}_R \mathbf{F}^T \quad (1.31)$$

1.3.2.6 Energy balance

Let us consider an *isothermal polymer oxidation* process in any arbitrary part P of a reference body B_R . Neglecting the inertia effect, the internal energy in P can be

written as less than or equal to the power expended on the part plus the energy increase in the system due to change in concentration in the species due to the diffusion. Thus, denoting ψ_R as the internal energy density per unit volume of the reference body, we can write the energy imbalance as,

$$\overline{\int_P \dot{\psi}_R dv_R} \leq \int_{\partial P} \mathbf{T}_R \mathbf{n}_R \cdot \dot{\chi} da_R + \int_P \mathbf{b}_R \cdot \dot{\chi} dv_R - \sum_{\beta} \int_{\partial P} \mu^{(\beta)} \mathbf{j}_R^{(\beta)} \cdot \mathbf{n}_R da_R \quad (1.32)$$

where $\mu^{(\beta)}$ is the chemical potential for any species β and $\mu^{(\beta)} \mathbf{j}_R^{(\beta)}$ is the energy carried by species β into part P by the flux $\mathbf{j}_R^{(\beta)}$. Applying divergence theorem to the terms on the integrals over ∂P and bringing the time derivative inside the integral, Eq. 1.32 can be re-written as,

$$\int_P \dot{\psi}_R dv_R \leq \int_P \left(\mathbf{T}_R : \dot{\mathbf{F}} - \sum_{\beta} (\mu^{(\beta)} \text{Div} \mathbf{j}_R^{(\beta)} - \sum_{\beta} (\mathbf{j}_R^{(\beta)} \cdot \nabla \mu^{(\beta)})) \right) dv_R + \int_P (\text{Div} \mathbf{T}_R + \mathbf{b}_R) \cdot \dot{\chi} dv_R \quad (1.33)$$

Using mass balance Eq. 2.24, 1.22 and C.5 in Eq. 1.33 and considering P as arbitrary, we get the local form of energy balance as,

$$\dot{\psi}_R - \mathbf{T}_R : \dot{\mathbf{F}} + \sum_{\beta} \mathbf{j}_R^{(\beta)} \cdot \nabla \mu^{(\beta)} + \sum_{\beta} \mu^{(\beta)} \sum_n [\mathcal{R}_n \dot{\xi}_{(n)}]^{(\beta)} - \sum_{\beta} \mu^{(\beta)} \dot{c}_R^{(\beta)} \leq 0 \quad (1.34)$$

1.3.2.7 Stress-power

Assuming the constitutive behavior of a generic glassy thermoset as elasto-plastic, we can write the stress-power as,

$$\begin{aligned}\mathbf{T}_R : \dot{\mathbf{F}} &= \mathbf{T}_R : (\dot{\mathbf{F}}^e \mathbf{F}^p + \mathbf{F}^e \dot{\mathbf{F}}^p) \\ &= (J \mathbf{F}^{e-1} \mathbf{T} \mathbf{F}^{e-T}) : (\mathbf{F}^{eT} \dot{\mathbf{F}}^e) + (\mathbf{C}^e J \mathbf{F}^{e-1} \mathbf{T} \mathbf{F}^{e-T}) : \mathbf{L}^p\end{aligned}\tag{1.35}$$

From Eq. 3.12 the following stresses have been defined:

- The elastic second Piola stress,

$$\mathbf{S}^e = J \mathbf{F}^{e-1} \mathbf{T} \mathbf{F}^{e-T}\tag{1.36}$$

which is symmetric, as Cauchy stress \mathbf{T} is symmetric.

- The mandel stress,

$$\mathbf{M}^e = J \mathbf{F}^{eT} \mathbf{T} \mathbf{F}^{e-T} = \mathbf{C}^e \mathbf{S}^e\tag{1.37}$$

which drives the inelasticity into the system, and in general, not symmetric. Also, both \mathbf{S}^e and \mathbf{M}^e are invariant under the change of frame, as \mathbf{T} is invariant.

Thus, using Eq. 1.36 and 1.37, the stress power Eq. 3.12 can be re-written as,

$$\mathbf{T}_R : \dot{\mathbf{F}} = \underbrace{\frac{1}{2} \mathbf{S}^e : \dot{\mathbf{C}}^e}_{\text{elastic power}} + \underbrace{\mathbf{M}^e : \mathbf{L}^p}_{\text{inelastic power}} \quad (1.38)$$

Using kinematic relations from Eq. 1.14 and 3.3 we can further simplify the inelastic power as,

$$\begin{aligned} \mathbf{M}^e : \mathbf{D}^p &= \mathbf{M}^e : \mathbf{D}^s \\ &= \mathbf{M}^e : \gamma \dot{\xi}_{(2)} \mathbf{I} \\ &= \gamma \text{tr}(\mathbf{M}^e) \dot{\xi}_{(2)} \end{aligned} \quad (1.39)$$

So that the energy imbalance Eq. 1.34 can be rewritten as,

$$\dot{\psi}_R - \frac{1}{2} \mathbf{S}^e : \dot{\mathbf{C}}^e - \gamma \text{tr} \mathbf{M}^e \dot{\xi}_{(2)} + \sum_{\beta} \mathbf{j}_R^{(\beta)} \cdot \nabla \mu^{(\beta)} + \sum_{\beta} \mu^{(\beta)} \sum_n [\mathcal{R}_n \dot{\xi}_{(n)}]^{(\beta)} - \sum_{\beta} \mu^{(\beta)} \dot{c}_R^{(\beta)} \leq 0 \quad (1.40)$$

1.3.3 Constitutive theories

1.3.3.1 Basic constitutive equation

Guided by the free energy imbalance Eq. 3.11, a functional form is assumed for the free energy ψ_R ; the second Piola stress \mathbf{S}^e and the chemical potential of species $\mu^{(\beta)}$ are then determined by the constitutive equations of the form,

$$\begin{aligned}\psi_R &= \hat{\psi}_R(\mathbf{C}^e, c_R^{(\beta)}, \xi_{(n)}) \\ \mathbf{S}^e &= \hat{\mathbf{T}}^e(\mathbf{C}^e, c_R^{(\beta)}, \xi_{(n)}) \\ \mu^{(\beta)} &= \hat{\mu}^{(\beta)}(\mathbf{C}^e, c_R^{(\beta)}, \xi_{(n)})\end{aligned}\tag{1.41}$$

Further, the species flux $\mathbf{j}_R^{(\beta)}$ can be assumed to have the following constitutive form:

$$\mathbf{j}_R^{(\beta)} = \hat{\mathbf{j}}_R^{(\beta)}(\mathbf{C}^e, c_R^{(\beta)}, \xi_{(n)}, \nabla \mu^{(\beta)})\tag{1.42}$$

Then, by invoking the thermodynamic restrictions it is possible to generate the specific forms for the constitutive equations.

Thermodynamic restrictions: Following Eq. 3.15, we get

$$\dot{\psi}_R = \frac{\partial \hat{\psi}_R}{\partial \mathbf{C}^e} : \dot{\mathbf{C}}^e + \sum_{\beta} \frac{\partial \hat{\psi}_R}{\partial c_R^{(\beta)}} : \dot{c}_R^{(\beta)} + \sum_{\beta} \frac{\partial \hat{\psi}_R}{\partial \xi_{(n)}} : \dot{\xi}_{(n)} \quad (1.43)$$

In view of Eq. C.8, the free energy imbalance Eq. 3.11 is equivalent to the requirement that the following inequality must be satisfied for all the constitutive processes:

$$\begin{aligned} & \left(\frac{\partial \hat{\psi}_R}{\partial \mathbf{C}^e} - \frac{1}{2} \hat{\mathbf{S}}^e \right) : \dot{\mathbf{C}}^e + \sum_{(\beta)} \left(\frac{\partial \hat{\psi}_R}{\partial c_R^{(\beta)}} - \hat{\mu}^{(\beta)} \right) : \dot{c}_R^{(\beta)} - \left(\gamma \text{tr}(\mathbf{M}^e) - \sum_{\beta} \mu^{(\beta)} \mathcal{R}_2 - \frac{\partial \hat{\psi}_R}{\partial \xi_{(2)}} \right) : \dot{\xi}_{(2)} \\ & - \left[\left(- \sum_{\beta} \mu^{(\beta)} \sum_n \mathcal{R}_n - \sum_n \frac{\partial \hat{\psi}_R}{\partial \xi_{(n)}} \right) : \dot{\xi}_{(n)} \right]_{n \neq 2} + \sum_{\beta} \hat{\mathbf{j}}_R^{(\beta)} \cdot \nabla \mu^{(\beta)} \leq 0 \quad (1.44) \end{aligned}$$

To hold the above equation true for any arbitrary $\dot{\mathbf{C}}^e$ and $\dot{c}_R^{(\beta)}$, their coefficients must vanish. Therefore, satisfying the thermodynamic restrictions the following 'state relations' can be obtained:

1. The free energy determines the second Piola stress as,

$$\begin{aligned} \mathbf{S}^e &= \hat{\mathbf{S}}^e(\mathbf{C}^e, c_R^{(\beta)}, \xi_{(n)}) \\ &= 2 \frac{\partial \psi_R(\mathbf{C}^e, c_R^{(\beta)}, \xi_{(n)})}{\partial \mathbf{C}^e} \end{aligned} \quad (1.45)$$

and the chemical potential as,

$$\begin{aligned}\mu^{(\beta)} &= \hat{\mu}(\mathbf{C}^e, c_R^{(\beta)}, \xi_{(n)}) \\ &= \frac{\partial \psi_R(\mathbf{C}^e, c_R^{(\beta)}, \xi_{(n)})}{\partial c_R^{(\beta)}}\end{aligned}\tag{1.46}$$

2. The species flux satisfies the species-transport inequality as,

$$\mathbf{j}_R^{(\beta)}(\mathbf{C}^e, c_R^{(\beta)}, \xi_{(n)}) \cdot \nabla \mu^{(\beta)} \leq 0\tag{1.47}$$

3. The following dissipation inequality must be satisfied by the chemical reactions:

$$\begin{cases} \left(-\sum_{\beta} \mu^{(\beta)} \mathcal{R}_2 + \gamma \text{tr}(\mathbf{M}^e) - \frac{\partial \hat{\psi}_R}{\partial \xi_{(2)}} \right) \dot{\xi}_{(2)} \geq 0, \quad n = 2 \\ \left(-\sum_{\beta} \mu^{(\beta)} \sum_n \mathcal{R}_n - \sum_n \frac{\partial \hat{\psi}_R}{\partial \xi_{(n)}} \right) \dot{\xi}_{(n)} \geq 0, \quad n \neq 2 \end{cases}\tag{1.48}$$

Thus from Eq. 1.48, it is possible to define a force of dissipative nature $\mathcal{F}_{(n)}$

which is a conjugate to $\dot{\xi}_{(n)}$ for each reaction n . Thus,

$$\mathcal{F}_{(n)} = \begin{cases} \mathcal{A}_{(2)} + \gamma \text{tr}(\mathbf{M}^e) - \sum_{\beta} \mu^{(\beta)} \mathcal{R}_2, & n = 2 \\ \mathcal{A}_{(n)} - \sum_{\beta} \mu^{(\beta)} \mathcal{R}_n, & n \neq 2 \end{cases}\tag{1.49}$$

where $\mathcal{A}_{(n)}$ is defined as *affinity* in the chemistry literature and defined by,

$$\mathcal{A}_{(n)} = -\frac{\partial\psi_R}{\partial\xi_{(n)}} \quad (1.50)$$

This reflects the fact that every chemical reaction relates to a dissipative mechanism. The extent of reaction for any reaction n , $\xi_{(n)}$ is assumed to evolve according to a state relation

$$\dot{\xi}_{(n)} = \hat{\xi}_{(n)}(\mathcal{F}_{(n)}, \vartheta, \xi_{(n)}, c_R^{(\beta)}) \geq 0 \quad (1.51)$$

with $\mathcal{F}_{\xi_{(n)}} > 0$, whenever $\dot{\xi}_{(n)} > 0$.

Fluid flux and Fick's law In this work we assume that the fluid flux obeys Fick's law, i.e. flux depends linearly on the gradient of the chemical potential and thus can be expressed by,

$$\mathbf{j}^{(\beta)} = -\mathbf{M}^{(\beta)}(\mathbf{C}_e, c_R^{(\beta)}, \xi_{(n)}) \nabla \mu^{(\beta)} \quad (1.52)$$

with $\mathbf{M}^{(\beta)}(\mathbf{C}_e, c_R^{(\beta)}, \xi_{(n)})$ is the mobility tensor. The consequence of species transportation inequality Eqn.C.12 is that, the mobility tensor is positive-definite for any non-zero concentration $c_R^{(\beta)}$. Considering isotropy of the polymer, the mobility tensor

can be re-written as,

$$\mathbf{M}^{(\beta)}(\mathbf{C}_e, c_R^{(\beta)}, \xi_{(n)}) = -m(\mathbf{C}_e, c_R^{(\beta)}, \xi_{(n)})\mathbf{I} \quad (1.53)$$

with $m > 0$ is a scalar mobility.

1.4 Specialization of the constitutive equations

For deriving the specific constitutive forms, we consider the materials as initially and continually isotropic. Under such assumption, it can be shown that the response of the polymer is invariant under any arbitrary rotation in the reference configuration or intermediate configuration and the constitutive responses do not change [9, 11, 12, 52, 53, 54, 153].

To simplify the numerical implementation, we consider a NeoHookean hyperelastic free energy function for the mechanical part. The viscoplastic deformation of the polymer has been neglected at this stage. For the reactive part of the free energy, a simple quadratic function of the extent of reaction ($\xi_{(n)}$) is considered, (based on the literature [250]). Finally, the free energy for the diffusion is considered as the energy of mixing between the species (β) and the polymer. Polymer has long-chain macromolecules and the oxygen particle size is significantly small compared to the

long polymer chain. Therefore, Flory-Huggin's lattice theory of mixing seem to suit better to model mixing of oxygen into the polymer [149, 225, 234]. In this work, we use a similar expression for energy for diffusion of mixing reported in th earlier works of [52, 53, 54, 91]).

1.4.1 Free energy

Motivated by the free energy representation in [153], a separable form of the free energy has been considered as

$$\hat{\psi}_R(\mathbf{C}^e, c_R^{(\beta)}, \xi_{(n)}) = \psi_I^{mech}(\mathbf{C}^e, c_R^{(\beta)}, \xi_{(n)}) + \psi_I^{chem}(\xi_{(n)}) + \psi_I^{diff}(c_R^{(\beta)}) \quad (1.54)$$

(i) The free energy for a NeoHookean elastomer has the form,

$$\psi_R^{mech}(\mathbf{C}^e, c_R^{(\beta)}, \xi_{(n)}) = \frac{G(\xi_{(n)})}{2}(tr\mathbf{C}_{dis}^e - 3) + \frac{K}{2}(\ln J)^2 \quad (1.55)$$

where $\mathbf{C}^{dis} = J^{-2/3}\mathbf{C}^e$, $G(\xi_{(n)})$ is the oxidation dependent shear modulus and K is the bulk modulus of the polymer.

(ii) ψ_R^{chem} is the reactive part of the free energy influencing the oxidation reaction

and is given by,

$$\psi_R^{chem} = \sum_n \frac{H_{(n)}}{2} (1 - \xi_{(n)})^2 \quad (1.56)$$

where the parameter $H_{(n)}$ is the chemistry modulus of reaction n . This term in the free energy favors the local state ($\xi_{(n)} = 1$) [250].

(iii) ψ_R^{diff} is the part of free energy involved in the diffusion of species (β) into the polymer. As mentioned in section 3.2.3, oxygen is considered as the only diffusing species. Here we have used Flory-Huggins theory of mixing to define the free energy for diffusion [52, 53, 54, 91] as given by,

$$\psi_R^{diff} = \mu_0^{(O_2)} c_R^{(O_2)} + R\vartheta c_R^{(O_2)} \left(\ln \left(\frac{\Omega c_R^{(O_2)}}{1 + \Omega c_R^{(O_2)}} \right) + \chi \left(\frac{1}{1 + \Omega c_R^{(O_2)}} \right) \right) + p_a c_R^{(O_2)} \Omega \quad (1.57)$$

where $\mu^{0(O_2)}$ is the reference chemical potential for oxygen, R is the universal gas constant, ϑ is the temperature, χ is the dimensionless Flory-Huggins interaction parameter, Ω is the volume of a mole of oxygen and p_a is the hydrostatic stress in the materials. In this case, the hydrostatic stress generates due to the oxidative shrinkage as given by $p_a = 1/3 J^e \text{tr} \mathbf{T}$.

Thus the complete free energy expression can now be written as,

$$\begin{aligned} \hat{\psi}_R(\mathbf{C}^e, c_R^{(\beta)}, \xi_{(n)}) = & \frac{G(\xi_{(n)})}{2} (tr \mathbf{C}_{dis}^e - 3) + \frac{K}{2} (\ln J)^2 + \sum_{(n)} \frac{H_{(n)}}{2} (1 - \xi_{(n)})^2 \\ & + \mu_0^{(O_2)} c_R^{(O_2)} + R \vartheta c_R^{(O_2)} \left(\ln \left(\frac{\Omega c_R^{(O_2)}}{1 + \Omega c_R^{(O_2)}} \right) + \chi \left(\frac{1}{1 + \Omega c_R^{(O_2)}} \right) \right) + p_a c_R^{(O_2)} \Omega \quad (1.58) \end{aligned}$$

Note that, here we ignore any contribution to the free energy contributed by the swelling induced volumetric deformation caused by oxygen diffusion. This is due to the fact that, the timescale for diffusion is much slower compared to that of the reaction. Thus any oxygen entering the free volume of the polymer reacts instantaneously with the free radicals. Moreover, the size of an oxygen particle is quite small compared to the size of polymer chain, thus oxygen diffusion inside the polymer should not generate any noticeable deformation in the material. Hence the swelling effect can be considered as negligible. Thus, the volumetric deformation is assumed as primarily contributed by the shrinkage due to chemical reaction.

1.4.2 Oxidation dependent shear modulus

Following the work of [104], we consider that the bulk modulus of the material does not depend on oxidation. However, shear modulus becomes higher due to the oxide formation [104]. As polymer radicals (P^*) reacts with O_2 to create PO_2^* in the propagation reaction (II) (also termed as oxidative crosslinking), we assume that the

change in shear modulus happens mainly due to the propagation reaction (II). Thus, we can write,

$$G(\xi_{(n)}) = (1 - \xi_{(2)})G_{un} + \xi_{(2)}G_{ox} \quad (1.59)$$

where G_{un} and G_{ox} corresponds to the shear modulus of unoxidized and completely oxidized polymer.

1.4.3 Stress, chemical potential and affinity

From the free energy Eq. 3.23 and using the guidelines for thermodynamic restriction, it is possible to get the specific constitutive equations for Cauchy stress \mathbf{T} , chemical potential of oxygen, $\mu^{(O_2)}$ and affinity of each reaction, $\mathcal{A}_{(n)}$.

Using Eq. 3.29 , 1.45 and 1.36, the Cauchy stress can be expressed in the following form:

$$\mathbf{T} = J^{-1}[G(\xi_{(n)})[(\mathbf{B}_{dis})_0] + K(\ln J)\mathbf{1}] \quad (1.60)$$

where \mathbf{B}_{dis} is the deviatoric part of elastic Left Cauchy-Green tensor \mathbf{B}^e .

Chemical potential due to mixing of oxygen and polymer, $\mu^{(O_2)}$, can be obtained by taking derivative of diffusive energy with respect to oxygen concentration as,

$$\mu^{(O_2)} = \mu_0^{(O_2)} + R\vartheta \left(\ln \left(\frac{\Omega c_R^{(O_2)}}{1 + \Omega c_R^{(O_2)}} \right) + \frac{1}{1 + \Omega c_R^{(O_2)}} + \chi \left(\frac{1}{1 + \Omega c_R^{(O_2)}} \right)^2 \right) + p_a \Omega \quad (1.61)$$

Finally, the affinity of any reaction n can be calculated from Eq. 3.20, 3.29 and 3.23 as,

$$\mathcal{A}_{(n)} = -\frac{\partial \psi_R^{mech}}{\partial \xi_{(n)}} + H_{(n)}(1 - \xi_{(n)}) \quad (1.62)$$

.

1.4.4 Evolution of extent of reaction, $\xi_{(n)}$

Based on the kinetics of chemical reaction for polymer oxidation and our discussion in section 1.2, we choose a thermally activated relation for the evolution of extent of reaction $\dot{\xi}_{(n)}$ as,

$$\dot{\xi}_{(n)} = k_n \exp \left(\frac{-Q_{act}^{(n)}}{R\vartheta} \right) \mathcal{F}_{(n)} \quad (1.63)$$

where, k_n is the pre-exponential rate constant for reaction n and has unit of $\frac{1}{MPa-s}$, $Q_{act}^{(n)}$ is the activation energy for reaction n .

As explained earlier, reaction will occur only when $\mathcal{F}_{(n)} > 0$. Further, the reaction will be considered as completed when the extent of reaction reaches unity. Following this, we can rewrite Eq. 1.63 as,

$$\dot{\xi}_{(n)} = \begin{cases} \dot{\xi}_{(n)} = k_n \exp\left(\frac{-Q_{act}^{(n)}}{R\vartheta}\right) \mathcal{F}_{(n)}, & \text{when } \mathcal{F}_{(n)} > 0 \text{ and } \xi_{(n)} < 1 \\ 0, & \text{otherwise} \end{cases} \quad (1.64)$$

1.4.5 Oxygen flux and diffusivity

From Eq. C.13, oxygen flux is given by,

$$\mathbf{j}_R^{(O_2)} = -m^{(O_2)} \nabla \mu^{(O_2)} \quad (1.65)$$

with $m^{(O_2)}$ being the mobility of oxygen. Ignoring the effect of temperature gradient we can write from Eq. 3.25,

$$\nabla \mu^{(O_2)} = \frac{R\vartheta}{c_R^{(O_2)}} \left(\frac{1}{1 + \Omega c_R^{(O_2)}} - \frac{\Omega c_R^{(O_2)}}{(1 + \Omega c_R^{(O_2)})^2} - 2\chi \frac{\Omega c_R^{(O_2)}}{(1 + \Omega c_R^{(O_2)})^3} \right) \nabla c_R^{(O_2)} \quad (1.66)$$

Further, diffusivity of oxygen can be defined as,

$$D = m^{(O_2)} \times \frac{R\vartheta}{c_R^{(O_2)}} \quad (1.67)$$

and using Eq. 1.67 in 1.65 the constitutive relation for species flux can be obtained as,

$$\mathbf{j}_R^{(O_2)} = -D \left(\frac{1}{1 + \Omega c_R^{(O_2)}} - \frac{\Omega c_R^{(O_2)}}{(1 + \Omega c_R^{(O_2)})^2} - 2\chi \frac{\Omega c_R^{(O_2)}}{(1 + \Omega c_R^{(O_2)})^3} \right) \nabla c_R^{(O_2)} \quad (1.68)$$

The diffusivity of oxygen in virgin or unoxidized polymer is different than the diffusivity in the active oxidation zone or completely oxidized zone [240, 241]. Also, diffusivity of the oxide layer is one of the reaction controlling parameter as it determines the availability of oxygen in the core to take part into further oxidation [240]. Thus to comply with the literature, a simple form of diffusivity is assumed in this

work that varies linearly with the extent of propagation reaction (II) as,

$$D = (1 - \xi_{(2)})D_{un} + \xi_{(2)}D_{ox} \quad (1.69)$$

where the parameters D_{un} and D_{ox} indicate the diffusivity of oxygen in the unoxidized polymer and in the oxide layer, respectively. Further, diffusivity follows simple Arrhenius rule to incorporate the temperature dependencies as,

$$\begin{aligned} D_{un} &= D_{0,un} \exp \left(\frac{-Q_{d,un}}{R\vartheta} \right) \\ D_{ox} &= D_{0,ox} \exp \left(\frac{-Q_{d,ox}}{R\vartheta} \right) \end{aligned} \quad (1.70)$$

where $D_{0,un}$ and $D_{0,ox}$ are the reference diffusivity values and $Q_{d,un}$ and $Q_{d,ox}$ are the activation energy of diffusion for the unoxidized and the oxidized material, respectively.

1.5 Governing differential equations and the boundary conditions

There are two governing differential equations required to be solved in this case:

$$\begin{cases} \text{Div} \mathbf{T}_R + \mathbf{b}_R = \mathbf{0} \\ \dot{c}_R^{(O_2)} = -\text{Div} \mathbf{j}_R^{O_2} + \mathcal{R}_2 \dot{\xi}_{(2)} + \mathcal{R}_6 \dot{\xi}_{(6)} \end{cases} \quad (1.71)$$

We require the initial and boundary conditions to complete the solutions of these differential equations. Let, S_1 and S_2 are complementary subsurfaces of the boundary ∂B_R of a reference body B_R such that $S_1 \cup S_2 = \partial B_R$ and $S_1 \cap S_2 = \emptyset$. Similarly, let S_{c_R} and S_{j_R} are complementary subsurfaces of the boundary $\partial B_R = S_{c_R} \cup S_{j_R}$ with $S_{c_R} \cap S_{j_R} = \emptyset$. For a time interval $t \in [0, T]$, two boundary conditions can be described such that displacement is known on S_1 and traction on S_2 . Thus, we can write,

$$\begin{aligned} \chi &= \check{\chi} \text{ on } S_1 \quad \forall t \in [0, T] \\ \mathbf{T}_R \mathbf{n}_R &= \check{\mathbf{t}}_R \text{ on } S_2 \quad \forall t \in [0, T] \end{aligned} \quad (1.72)$$

Similarly, another pair of boundary condition can be considered for a time interval $t \in [0, T]$ such that oxygen concentration is known on S_{c_R} and oxygen flux on S_{j_R} and thus,

$$\begin{aligned} c_R^{(O_2)} &= \check{c}_R \text{ on } S_{c_R} \quad \forall t \in [0, T] \\ -D(\nabla c_R^{(O_2)}) \cdot \mathbf{n}_R &= \check{j}_R \text{ on } S_{j_R} \quad \forall t \in [0, T] \end{aligned} \quad (1.73)$$

The initial conditions are,

$$\chi(\mathbf{X}, 0) = \chi_0(\mathbf{X}), \text{ and } c_R^{(O_2)}(\mathbf{X}, 0) = c_{R_0}(\mathbf{X}) \text{ in } B_R. \quad (1.74)$$

Thus the coupled set of equations, Eq. 3.29, together with 3.30, 3.31 and 3.32 pose an initial boundary value problem to be solved for the displacement $\chi(\mathbf{X}, t)$ and concentration $c_R(\mathbf{X}, t)$ simultaneously. For more details on the solution method, please see [54]. In this work, the system of equations are solved numerically for each element by writing a user element subroutine in ABAQUS/Standard (2017) [1].

1.6 Representative numerical simulations

As mentioned in section 1.2, the activation energy for initiation reaction (Ia) is much lower compared to that of reaction (Ib). Taking this into consideration, we assume

that only reaction (Ia) is responsible for the initiation. Next, using Eq. 3.19 and 3.23, we can express the reactive forces for individual reaction as,

$$\mathcal{F}_n = \begin{cases} \frac{1}{2}(G_{un} - G_{ox})(\text{tr}\mathbf{C}_{dis}^e - 3) + H_2(1 - \xi_{(2)}) + \gamma\text{tr}(\mathbf{M}^e) + \mathcal{R}_2\mu^{(O_2)} , & n = 2 \\ H_n(1 - \xi_{(n)}) + \mathcal{R}_n\mu^{(O_2)} , & n \neq 2 \end{cases} \quad (1.75)$$

As mentioned before, by considering the stoichiometric coefficients as negative for consumption of the reacting species and positive for the formation, we have the following set of mass balance equations (based on Eq. 1.25, 1.26, 1.27 and 1.28):

$$\begin{cases} \dot{c}_R^{(O_2)} = -\text{Div}\mathbf{j}_R^{O_2} - \dot{\xi}_{(2)} + \dot{\xi}_{(6)} & \text{for oxygen} \\ \dot{c}_R^{(POOH)} = -\dot{\xi}_{(1a)} + \dot{\xi}_{(3)} & \text{for POOH} \\ \dot{c}_R^{(PH)} = -\dot{\xi}_{(3)} & \text{for PH} \\ \dot{c}_R^{(POOP)} = \dot{\xi}_{(5)} + \dot{\xi}_{(6)} & \text{for POOP} \end{cases} \quad (1.76)$$

At the steady state, the rate of change of concentration for P^* and PO_2^* radicals is zero. Applying this condition we get two additional set of relations as,

$$\begin{aligned} \dot{\xi}_{(2)} + 2\dot{\xi}_{(6)} &= \dot{\xi}_{(3)} + \dot{\xi}_{(5)} \\ \dot{\xi}_{(1a)} + \dot{\xi}_{(3)} &= 2\dot{\xi}_{(4)} + \dot{\xi}_{(5)} \end{aligned} \quad (1.77)$$

Hence, following Eq. 3.27, we need to define only 4 sets of evolution equations to control the reaction kinetics as,

$$\left\{ \begin{array}{l} \dot{\xi}_{(1a)} = k_{1a} \exp\left(-\frac{Q_1}{RT}\right) \mathcal{F}_1 \\ \dot{\xi}_{(2)} = k_2 \exp\left(-\frac{Q_2}{RT}\right) \mathcal{F}_2 \\ \dot{\xi}_{(3)} = k_3 \exp\left(-\frac{Q_3}{RT}\right) \mathcal{F}_3 \\ \dot{\xi}_{(6)} = k_6 \exp\left(-\frac{Q_6}{RT}\right) \mathcal{F}_6 \end{array} \right. \quad (1.78)$$

Based on the above discussion, we organize our numerical result section as follows: We first discuss how one can obtain kinetic and material parameters for this model. After that, we describe some numerical simulations to describe different physical phenomena involved in the oxidation process.

It is important to note that the timescale for diffusion is much longer and it depends on the diffusivity parameters (D_{un}, D_{ox}) as well as the dimension of the sample in the direction of oxygen diffusion. On the other hand, the reaction time-scale is much faster, and depends on the rate constants as, $\tau_r \approx \sum_n 1/k_n$. When the oxidation reaction depends on the availability of oxygen into the polymer, it is called a diffusion limited case (DLO). In such case the heterogeneity of the concentration of oxygen in the material will lead to a heterogeneous oxide formation as shown in Fig. 1.1. Oppositely, oxide formation depends on the reaction speed, we call it a reaction

limited oxidation (RLO). In such case, oxygen is always available inside the polymer, so how fast the reaction will happen will depend on the reaction kinetics.

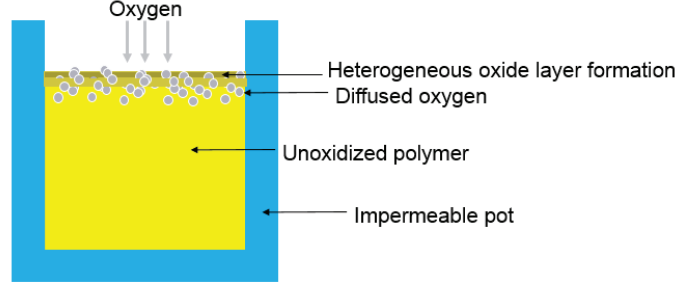


Figure 1.1: Diffusion limited oxidation in a polymer block.

In the following sections, we present numerical simulations considering a diffusion limited case (DLO) and a reaction limited case (RLO). The effect of ambient factors, such as, pressure and temperature is also simulated. Further, simulation is also done considering the coupled mechanical stress-oxidation scenario. The results for all the cases are analyzed in detail to compare the various conditions for the high temperature oxidation in polymer. Finally, we simulate a randomly distributed fiber-reinforced composite to demonstrate how oxidation effects composite behavior.

1.6.1 Parameter estimation

There are numerous material parameters involved in the present theory due to the complex coupling between the mechanics, diffusion and reaction phenomena. Following a detailed review of the literature, we chose typical values for some of these material constants which are realistic to most of the polymers, (based on the work of [57, 60, 63, 212, 213]).

For this coupled chemo-mechanical model, we are tracking four individual reactions. Considering they evolve in an Arrhenius form, we need at least 3 parameters to define each of the individual reaction, H_n , Q_{act}^n and k_n . From Eq. 1.56, the chemical energy is defined as $\frac{H_n}{2}(1 - \xi_{(n)})^2$. This quantity can be related to the Gibbs free energy. Assume, for a particular reaction, r number of species react to produce p number of products. The change in the energy $\Delta\phi$ for this reaction then can be calculated as,

$$\Delta\phi = \sum G_p c_R^p - \sum G_r c_R^r \quad (1.79)$$

where G_p is the Gibbs' energy of formation and c_R^p is the concentration for the product p and G_r is the Gibbs energy of formation and c_R^r is the concentration for the reactant r . The Gibbs energy (Joules per mole) can be found for polymers, radicals, polymer oxides and polymer oxide radicals in the chemistry literature [45]. Now, from Eq. 1.56,

we see that with a variation of $\xi_{(n)}$ from 0 to 1 leads to a chemical energy change of $-\frac{H}{2}$. So we can write,

$$H = -2\Delta\phi \quad (1.80)$$

So this way, we can estimate the chemistry modulus for each reaction. The values of chemistry moduli for a typical polymer chain reaction is given in Table 1.1.

The activation energies for reaction (II), (IV), (V) and (VI) are very low, considering the radicals react instantaneously. Among the all six reactions, decomposition is POOH (reaction Ia) is the slowest and therefore needs a much higher activation energy compared to the other reactions. Finally, hydrogen abstraction reaction of polymer (propagation reaction III) is strictly polymer material specific and can be experimentally evaluated. In this work we chose the activation energy values from [213].

The rate constants, k_n (unit $\frac{1}{s-Pa}$) can be calculated from the known concentration of the products (POOH and POOP). Experimentally, these values can be calculated using FTIR spectrophotometry [212, 213]. For example, a study on the effect of partial pressure of oxygen was performed in the work of [212] and the effect was characterized by tracking the production of carbonyl (POOP). For instance, a 0.2mol/m³ carbonyl was measured at 80°C under 0.2Mpa pressure after 200 hours. This data can be fitted to get values for k_5 and k_6 . Specifically, in this work, we considered that there is enough oxygen available for all P^* radicals to become PO_2^* . Thus, all carbonyls are

mostly formed from the termination reaction (VI) in such case. However, this could be different from a real life oxidation problem, as we can expect both reaction (V) and (VI) should take part in the carbonyl production. Numerically, to calculate the upper bounds of these constants, we can first consider that, all the carbonyl is coming from reaction (V), ignoring (VI) and calculate k_5 . Later, we can assume that all carbonyls are forming from reaction (VI), ignoring (V) and calculate k_6 . This way, it is possible to find the upper bound of both k_5 and k_6 , respectively. Then, we can choose k_6 as less than the value we calculated as the upper bound. For more accuracy, Eq. 1.28 can be fitted into the experimental carbonyl formation data to calculate a more precise value of k_6 . The concentration of peroxide due to oxidation of polypropylene was reported in another work of the same author [213]. From this data, we calibrate k_1 and k_3 using the mass balance Eq. 1.26. Finally, enforcing our steady state assumption (radicals are super reactive and gets consumed instantaneously), we assumed that, for propagation reaction (II), the available P^* that forms PO_2^* comes solely from the peroxide (POOH) decomposition. From the literature [213], we used the peroxide formation data to fit k_2 as well. It is noteworthy to mention that, one can also calibrate k_2 from the knowledge of the size of the oxide layer thickness.

Lastly, we choose Young's modulus of typical polymer as 1.5MPa with a poisson's ratio of 0.45 [147]. For the oxidized material, we assumed a oxidized shear modulus value higher than the virgin polymer. Experimentally, the oxidation modulus can be easily determined by a nano-indentation or a bending test. The diffusivity and

the solubility data is taken from [212, 213]. For the Flory-Huggin's interaction parameter, we assumed a simple value of 0.1 based on [52]. To understand the effect of Flory-Huggin's interaction parameter χ , we run the simulation for two different values of χ , as shown in Fig. 1.2. As shown in the figure, χ does not influence the oxidation reaction. The shrinkage parameter γ is related to the volume change during oxidation reaction, which is experimentally determinable by tracking the volume reduction during oxidation [63]. In this work, we choose a average value of γ based on the weight loss and density variation data provided in literature [63, 241]. The parameters are listed in Table 1.1 and 3.1, respectively.

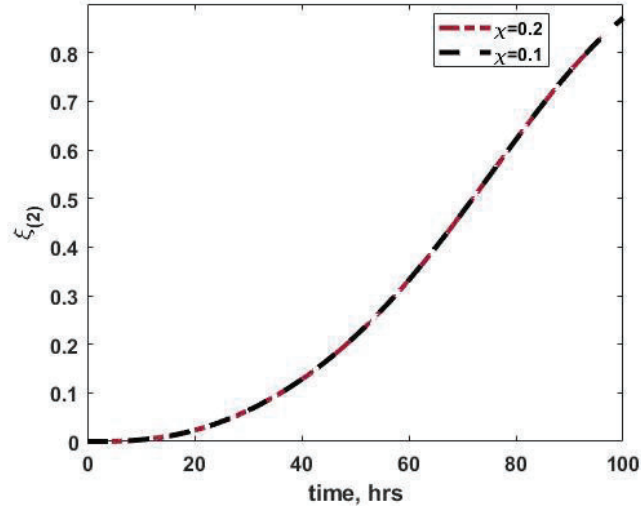


Figure 1.2: Effect of χ on the extent of reaction (II)

Table 1.1
Kinetic parameters related to diffusion and reaction for a typical polymer oxidation reaction

Parameter	Unit	Value	Reference
Solubility coefficient, S	$mol - L^{-1}Pa^{-1}$	1.4×10^{-8}	[213]
Diffusivity (Neat), $D_{0,un}$	m^2s^{-1}	8.8×10^{-5}	[212]
Diffusivity (oxidized), $D_{0,ox}$	m^2s^{-1}	9.06×10^{-4}	calibrated
Diffusive activation energy, E_d	kJ/mol	36.5	[213]
Reaction rate constants			
k_1	$1/Mpa - s$	3.67	calibrated
k_2	$1/Mpa - s$	2.84×10^{-9}	calibrated
k_3	$1/Mpa - s$	2.9×10^{-9}	calibrated
k_6	$1/Mpa - s$	2.76×10^{-9}	calibrated
Q_1	kJ/mol	100	[213]
Q_2	kJ/mol	30	[213]
Q_3	kJ/mol	45	[213]
Q_6	kJ/mol	10	[213]
H_1	J/mol	765.8×10^6	[45]
H_2	J/mol	128×10^6	[45]
H_3	J/mol	40.52×10^6	[45]
H_6	J/mol	267.26×10^6	[45]
Gas constant, R	$J/(mol-K)$	8.31446	
χ		0.1	[54]
μ_0 at STP	J/mol	3.88×10^5	[101]
$C_0^{(PH)}$	mol/L	20	[212]
$C_0^{(POOH)}$	mol/L	1×10^{-4}	[212]

1

Table 1.2
Material parameters for a representative elastomer.

Parameter	Unit	Value	
Bulk Modulus, K	GPa	5	[147]
Poisson ratio, ν		0.45	[147]
Shear Modulus (neat), G_{un}	GPa	0.58	[147]
Shear Modulus (oxidized), G_{ox}	GPa	0.7	Calibrated
Shrinkage parameter, γ		-0.01	Calibrated

1.6.2 Case study 1: Diffusion limited oxidation

In the case of a large polymer specimen, diffusion limited oxidation (DLO) becomes the governing mechanism for oxidation. For the reactions to happen, oxygen must diffuse from the exposed surface into the core of the material. The rate of diffusion depends on the permeability of the material (a combination of diffusivity and solubility). In such case, the rate of oxidation at a material point depends on the time required for enough O_2 to diffuse. Besides, the diffusivity of virgin material is different than that of the oxidized material, which leads to further heterogeneity of diffusion. To demonstrate this, we simulate a case of uni-directional diffusion of oxygen into a 2D block of polymer as shown in Fig. 1.3. The specimen is a 3x3 mm block with the top surface being exposed to oxygen and all the other surfaces are considered impermeable as shown in Fig. 1.3(a). Oxygen flows into the specimen along the negative y-direction. For the mechanical boundary condition, we consider x-symmetry for the left and right side, and y-symmetry at the bottom while keeping the top surface as free. For the chemical boundary condition, we maintain a constant oxygen pressure of 1 atm, which is equivalent to a concentration of $C_s = 2.8\text{mol}/mL$ along the top surface. It is to be noted that, we chose to use oxygen pressure as the boundary condition instead of chemical potential. Chemical potential boundary conditions are more suitable for the case of liquid diffusion in a gel, while in oxidation literature we always see the ambient pressure is defined (pressure guides the flow of oxygen into the

polymer). If the oxygen pressure and solubility of oxygen into the polymer is known, it is possible to define a concentration-type boundary using Henry's law, $C_s = SP$, where C_s is the oxygen concentration, S is the solubility of oxygen into the polymer and P is the partial pressure of oxygen. In order to avoid numerical complicity, we ramp up the oxygen concentration to the maximum value on the top surface over a small time period of 2 hours, as shown in Fig. 1.3(b). The initial concentration of resin (PH) and peroxide (POOH) are listed in table 1.1. We use the material parameters as listed in table 1.1 and 3.1 for the polymer material.

In the simulation, we let the sample oxidize for 100 hours at 80°C and study the

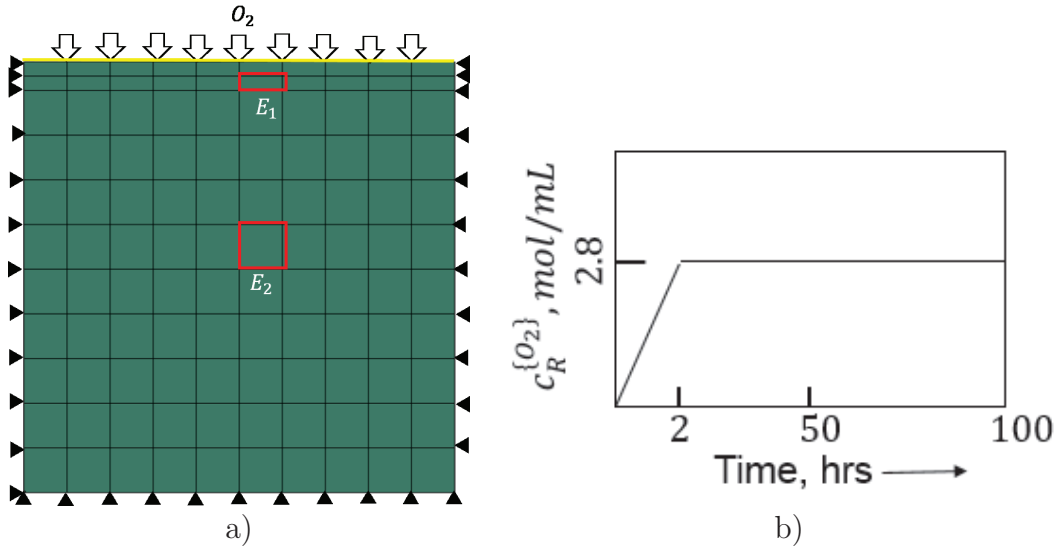


Figure 1.3: a) Geometry of the polymer specimen subjected to DLO: E_1 is an element on the top surface and E_2 is an element close to the middle core. b) boundary condition for oxygen concentration at the top surface

evolution of the extent of reactions. Here, all the 6 set of reactions are active in the reaction process. However, we only track evolution of reaction (Ia), (II), (III) and

(VI), as reaction (IV) and (V) are dependent on the other 4 by the steady-state assumption. The extent of reaction (I) gives a measure of alkyl radical (P^*) formation. The extent of reaction (II) aggregates the oxide volume fraction and the extent of reaction (III) gives information regarding resin depletion while the extent of reaction (VI) gives the termination rate. The contours for the extent of reactions are plotted in Fig. 1.4 at the end of 100hrs. The contours for the oxygen, PH, POOH and carbonyl concentrations are also plotted in Fig. 1.5 at the end of 100 hours. From Fig. 1.4, it can be seen that, the extent of reaction (Ia) evolves at a slower rate compared to the other reactions. This is because of the fact that, the activation energy for reaction (Ia) is much higher than the other reactions. Alternatively, we can also mention that, the radicals will react at a much faster rate than the stable polymer molecules. In reaction (II) and (VI), (P^*) and (PO_2^*) take part in the reaction, leading to a higher rate of the evolution of the extent of those reactions. Conversely, the decomposition of (POOH in reaction (1a) is a much slower process. However, hydrogen abstraction of (PH in reaction (III) is dependent on what polymer is taking part in the oxidation reaction. For example, the hydrogen abstraction of polypropylene needs much less activation energy than BMI ([63, 64, 213]). In this simulation, we chose the activation energy of reaction (III) quite close to the reaction (II), based on the data provided at [213], hence we observe quite a higher value for the extent of reaction (III). The extent of termination reaction (VI) reaches to unity within half of the sample length, as can be seen from Fig. 1.4(d). This is an indicative of the carbonyl (POOP) production.

The contour plots of the concentrations of Fig. 1.5 show a continuous increase in the concentration of (POOH and carbonyl product. The increase of peroxide ((POOH) indicates an auto-acceleration of the oxidation reaction, while the increase of carbonyl products indicate the build of inactive products on the polymer surface.

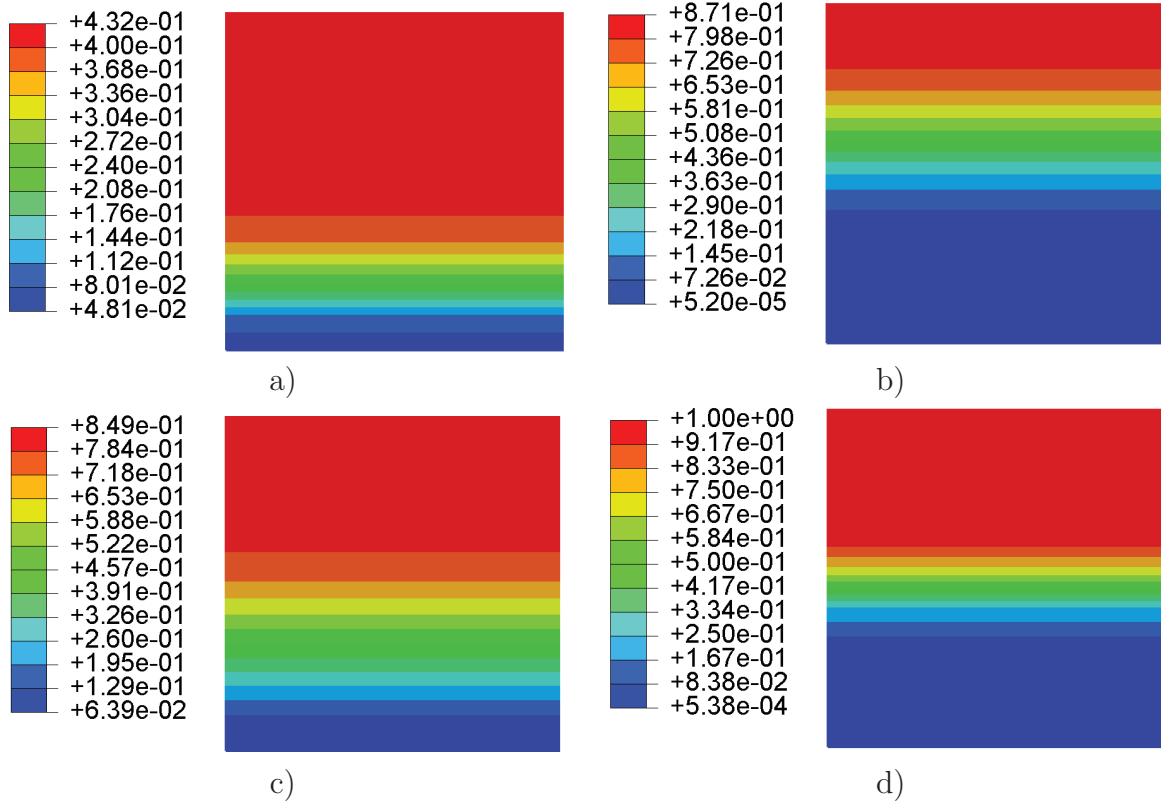


Figure 1.4: Evolution of the extent of reactions: a) ξ_{1a} , b) ξ_2 , c) ξ_3 , d) ξ_6 after 100 hours of oxidation

Effect of ambient pressure and temperature in DLO

Both diffusion and extent of reaction are thermally activated process, indicating that polymer oxidation rate will become faster with increased temperature. Similarly,

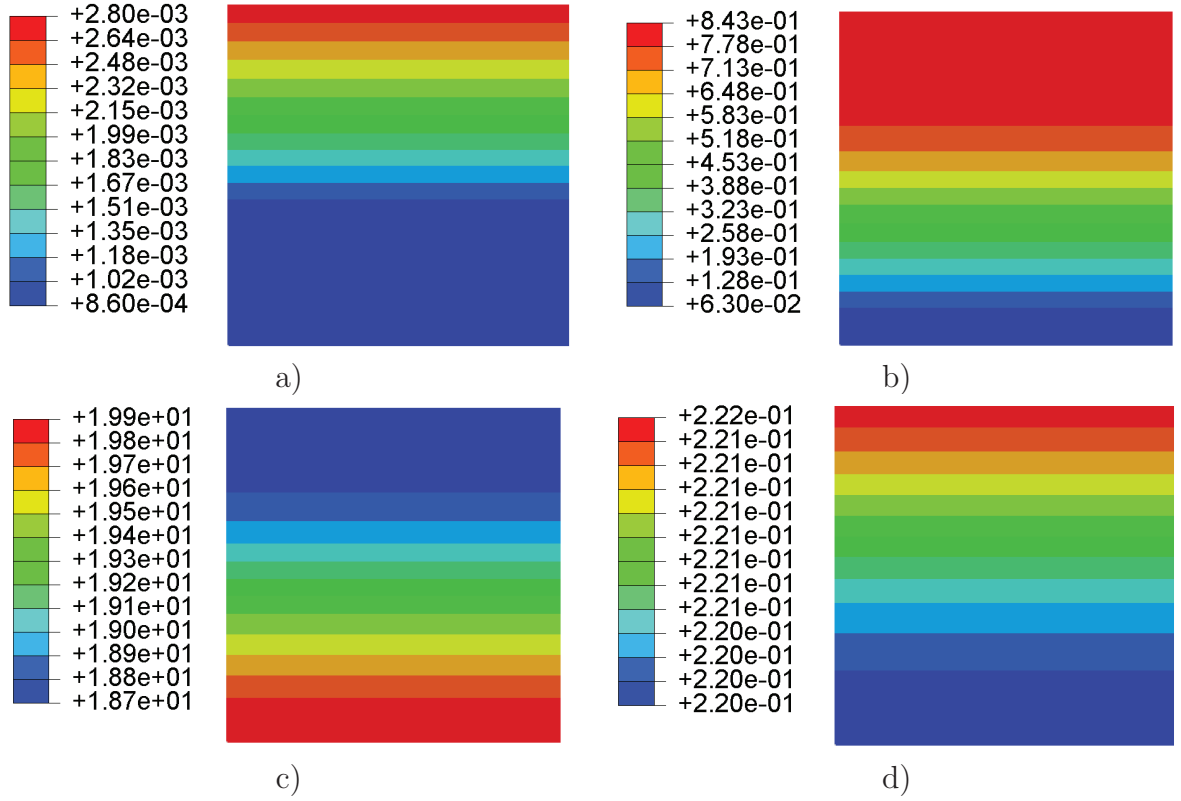


Figure 1.5: Contour plots of concentrations in mol/L of : a) O_2 , b) $POOH$, c) PH , d) Carbonyl products after 100 hours of oxidation

there should be an increase in the evolution of extent of reaction (II) with increased pressure. This is because of the fact that, reactive force is dependent on external pressure. Higher ambient pressure will create higher chemical potential, which in turn, will increase the reactive force. Consequently this will lead to a higher evolution rate of the extent of reaction. To demonstrate the effect of these ambient factors, we perform the following simulations using the same geometry shown in Fig. 1.3: i) We use the same boundary conditions discussed for the diffusion limited oxidation case, and oxidize the sample for 100 hours at $150^\circ C$ at atmospheric pressure (0.2 MPa of O_2), ii) we keep same mechanical boundary condition as before, but apply 2 MPa

pressure of O_2 , indicating a constant oxygen concentration of $C_s = 2.8\text{mol}/mL$ along the top surface and let the sample oxidize at $80^\circ C$ for 100 hours.

Fig. 1.6 shows the effect of increasing temperature and pressure on the extent of reaction (II) on the element E_1 at the surface of the sample. In both cases, we can see a significant increase in the extent of reaction (II) with increased temperature and pressure. While at $80^\circ C$ of temperature and 0.2MPa of oxygen pressure, $\xi_{(2)}$ reaches to a maximum value of 0.8494 , at $150^\circ C$ of temperature and with the same pressure, we observe that $\xi_{(2)}$ reaches to 1 in ~ 30 hours. Similar effect is observed when pressure is increased. We observe complete oxidation on the element E_2 at the surface in ~ 22 hours when oxidized at 2MPa , indicating higher oxygen pressure will increase the oxidation rate.

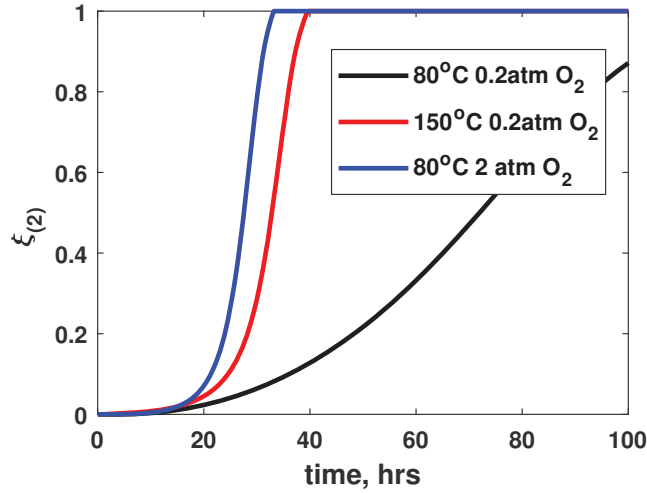


Figure 1.6: Effect of ambient temperature and pressure in polymer oxidation

Oxide Layer thickness

To see how oxide layer evolves with time, we continue the simulation described in the DLO case for 200 hours. The value to $xi_{(2)}$ reaching to unity is an indication complete oxidation at a material point. Fig. 3.3 plots the thickness of oxide layer normalized against the sample thickness formed at the end of 200 hours of oxidative aging. The visible identification of oxidation appears after 120 hours of exposure with a thin oxide layer formation on the top surface which continue to increase monotonically. The whole sample gets completely oxidized after 160 hours.

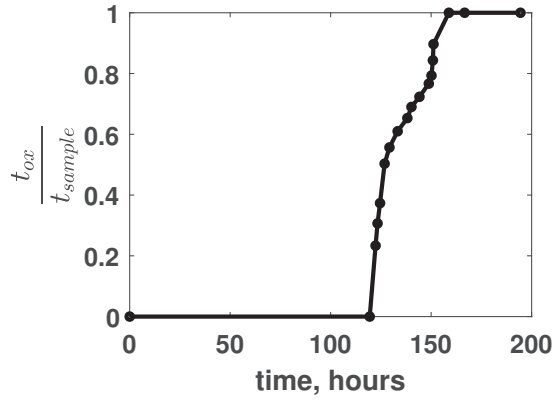


Figure 1.7: Oxide layer thickness as a function of aging time

1.6.3 Case study 2: reaction-limited oxidation

If enough oxygen is available at a material point to react with the polymer molecules, then the rate of oxidation is dependent on how fast the polymer is reacting with

oxygen to create oxides. This can happen in the case of a thin film sample (thickness in the order of microns), where oxygen sorption takes place into the surface instantaneously by Henry's law as. As the thickness of the sample is quite small, the diffusion can be ignored and the entire material can be assumed as saturated with enough oxygen with no further flow. Thereafter the oxidation rate simply depends on the rate of reactions. In such case, the reactions would continue until either ξ_3 or ξ_6 reaches unity at all material points. If ξ_3 reaches to 1 at the material points first, then it indicates all the available PH has been consumed. On the other hand, ξ_6 reaching to unity at all material points first is an indicative of auto-retardation of the oxidation process at that material point.

To simulate the reaction limited scenario, we consider a thin film of polymer sample with initial PH concentration of 20 mol/L. The film is being oxidized under atmospheric pressure. For a thin film, we consider an continuous oxygen sorption into the entire film, allowing oxygen concentration being same as (2.8 mol/mL) everywhere. Since O_2 concentration does not vary within the domain, it suffices to simulate a single element case. The properties of the material is given in table 1.1 and 3.1, as earlier. We let the sample oxidize at $80^\circ C$ for 100 hours. The evolution of the extent of reactions is shown in Fig. 1.8(a). We see that, the rate of evolution of $\xi_{(6)}$ is quite faster compared to $\xi_{(3)}$, indicating auto-retardation of oxidation reaction would occur before the resin gets completely consumed. The variation of O_2 , PH and POOH concentration, normalized against their initial values are shown in Fig. 1.8(b).

The assumption of continuous sorption of atmospheric oxygen within the entire film results in a constant availability of O_2 , as shown in Fig. 1.8(b). The resin gets very

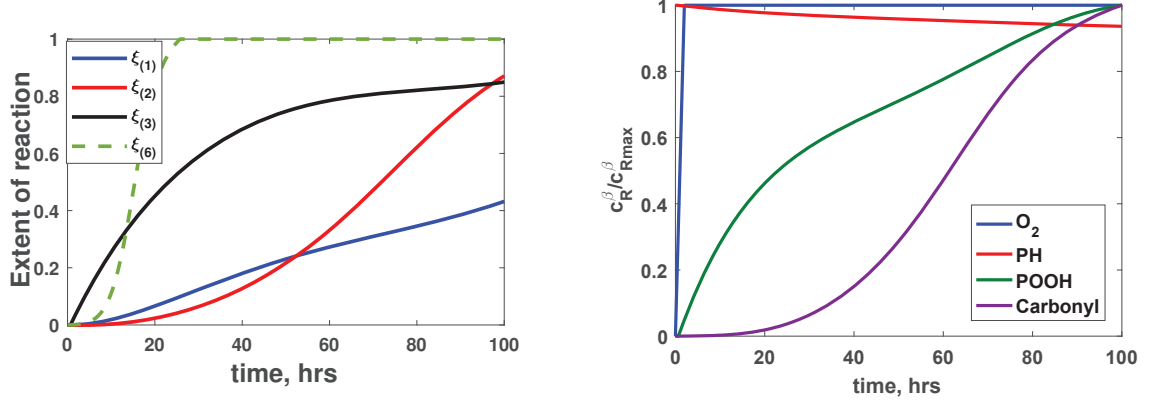


Figure 1.8: a) Evolution of the extent of reactions (Ia), (II), (III) and (VI) for a reaction limited oxidation (RLO) after 200 hours of oxidation, b) corresponding normalized concentration of oxygen, PH and POOH

slowly consumed by the reaction. We observe an increase in the POOH-concentration indicating the auto-acceleration of the oxidation reaction would be followed.

Fig. 1.9 demonstrates a comparison between the extent of reactions considering a DLO and a RLO conditions. We chose two elements as one located at the surface and another at the core of the sample (as shown Fig. 1.3(a)) from the DLO-case study to compare the results with the RLO-case. The extent of reactions are higher in the RLO-element and the surface-DLO element compared to the DLO-core, presumably due to oxygen sorption occurring in the RLO element and DLO-surface element instantaneously. On the other hand, in the DLO-core element, the extent of reactions is totally governed by the diffusion rate and noticeably lower than the surface.

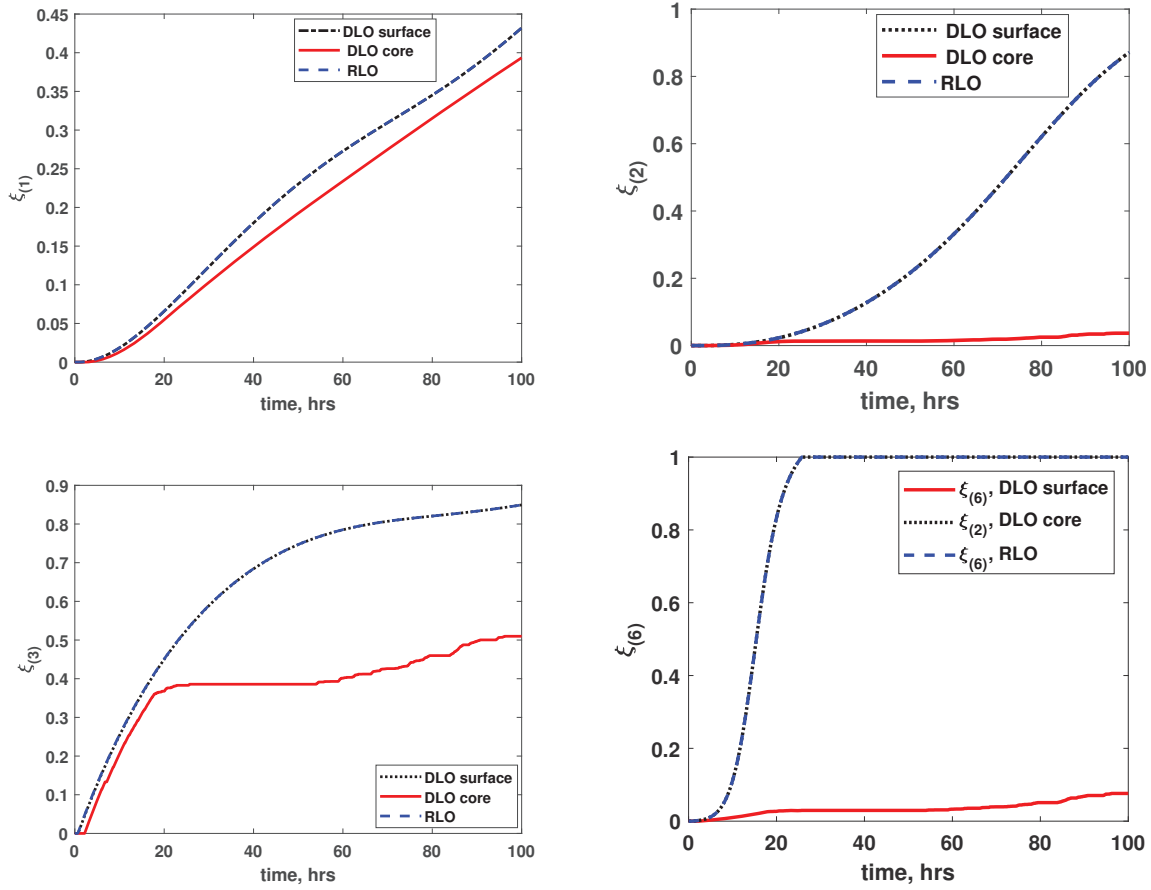


Figure 1.9: Comparison of the extent of reactions between DLO and RLO
a) $\xi_{(1)}$, b) $\xi_{(2)}$, c) $\xi_{(3)}$, d) $\xi_{(6)}$

1.6.4 Case study 3: coupled mechanical stress -oxidation process

To simulate the mechanical stress coupled oxidation scenario, we consider the same geometry as shown in Fig. 1.3a). We use the material parameters are listed in table 1.1. Then we perform two sets of simulations considering a.) pure DLO oxidation and b.) a stress-coupled diffusion limited oxidation process. For the pure DLO case,

we have used the same boundary conditions as mentioned in 1.6.2. For the stress-coupled situation, the chemical boundary condition has remained the same. For the mechanical boundary condition, we set x-symmetry along the left and the right edges and y-symmetry along the bottom surface. The non-zero displacement of 0.03 mm has been applied at the top surface linearly over a time period of 2 hours along upward direction and then held it for the rest of the simulation as shown in Fig. 1.10.

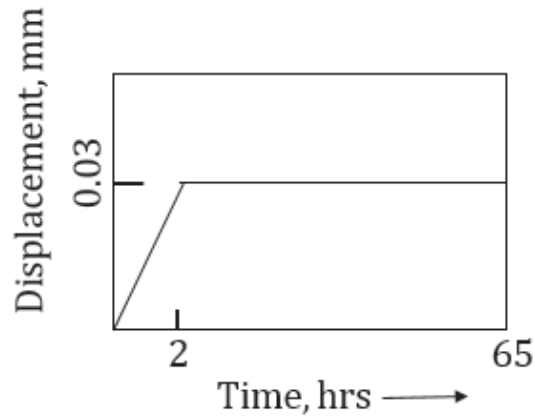


Figure 1.10: The displacement boundary condition for the stress-coupled oxidation

For both cases, we let the sample oxidize at 80°C for 65 hours. Fig.1.11(a) and (b) shows the comparison of the reactive force (II) between the two cases. The comparison between oxide formation is plotted in Fig. 1.11(c). We can see approximately a 5 times increase in the reactive force in case of the stress-coupled condition after 65 hours. Since the rate of extent of oxidation is directly proportional to the reactive force, the

rate of reaction (II) also becomes 5 times faster, which eventually increases the overall extent of reaction (II). In case of pure DLO, while extent of reaction (II) reaches only to 0.45, in case of stress-coupled oxidation, it reaches to 1 in about 20 hours, as we can see in Fig. 1.11(c).

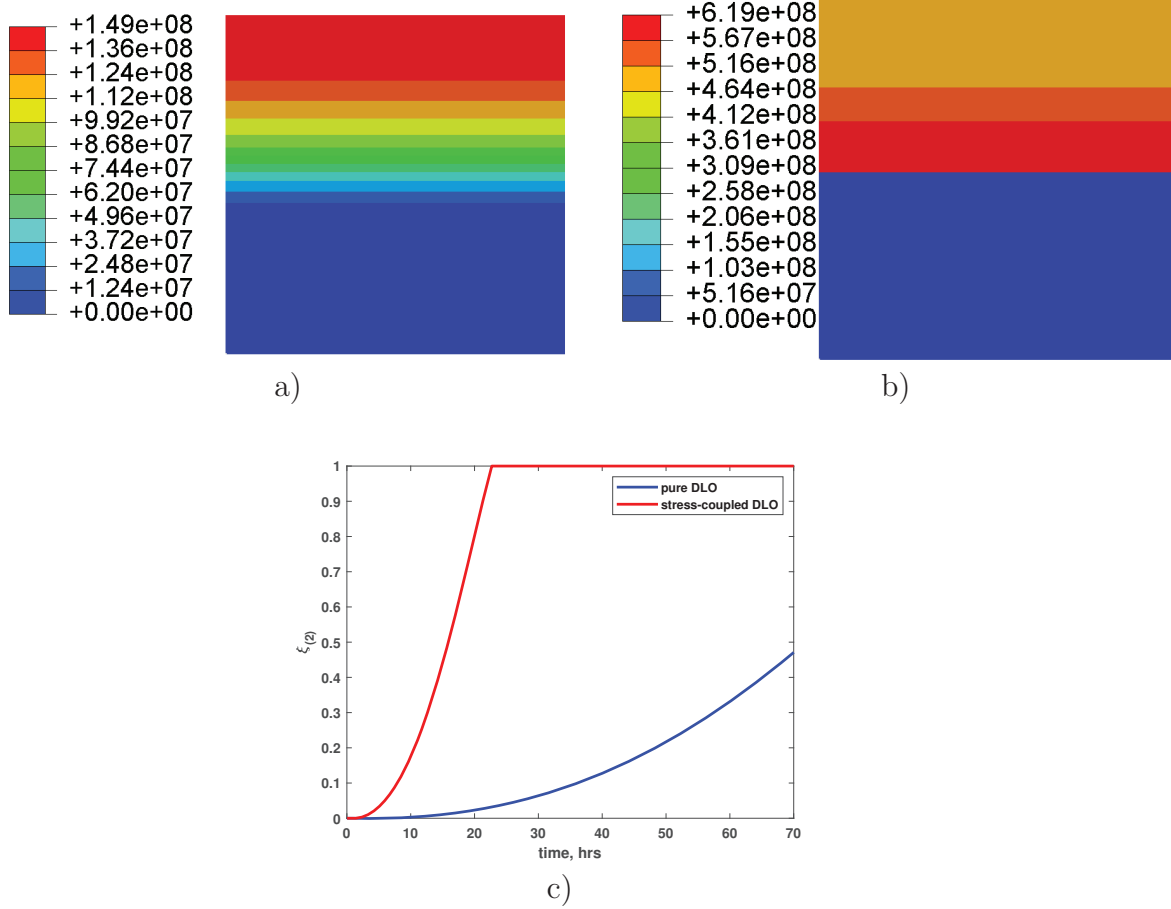


Figure 1.11: Comparison between the reactive force between a) pure oxidation and b) stress-coupled oxidation c) effect of external stress on the extent of reaction (II)

The comparison of Von-Mises stress contour between the two cases are also demonstrated in Fig. 1.12. As expected, the magnitude of the Mises stress is much higher

in the stress coupled case compared to the pure DLO case. The stress distribution is entirely different due to the boundary condition as applied in the simulation- for pure DLO case the top surface is left as free, whereas the non-zero Y-displacement is applied in the stress coupled situation. We have applied the displacement on the top surface of the stress-coupled oxidation sample for 2 hours and then held in in that position for the rest of the simulation time (as can be seen from Fig. 1.10). This indicates that the mechanical stress that is generated because of the displacement should reach to maximum after 2 hours. For the rest of the simulation time, any stress that has been generated can be attributed to the oxidation reaction. Contour plot Fig. 1.12(b) shows the stress generated after 65 hours.

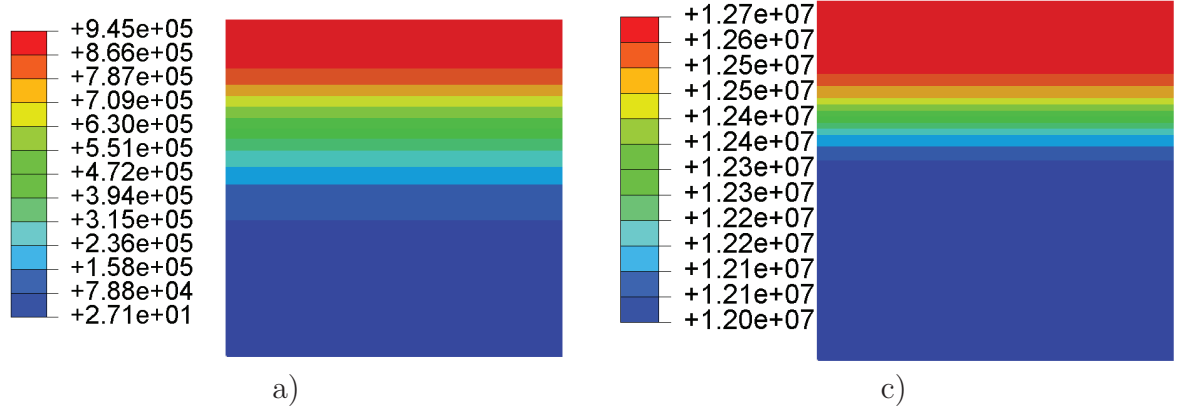


Figure 1.12: Contour plots of Von-Mises stress : a) pure oxidation after 65 hours, and b) stress-coupled oxidation after 65 hours

1.6.5 Residual stress and shrinkage strain developed in a randomly distributed fiber composite subjected to oxidation

In this section, we model a randomly distributed carbon fiber reinforced composite specimen to predict the shrinkage strain developed due to accelerated oxidation and corresponding residual stress following a similar work reported in [102]. The geometry of the model is shown in Fig. 1.13. The dimension of the composite sample is 1 by 1 mm with the fiber radius of $3\mu m$. We model the fibers as linear elastic and has the properties as $E = 230\text{ GPa}$, $\nu = 0.3$. We model the polymer matrix as the user defined material properties given in Table 3.1. We assume the fibers as impermeable and do not take part in the oxidation process. For the mechanical boundary condition, we consider x-symmetry along the top and bottom surface and y-symmetry along the right boundary of the sample. Perfect bonding between the fibers and matrix has also been assumed for the interface. For the diffusion boundary condition, oxygen is allowed to flow from the left side of the specimen geometry along the positive X-direction.

Fig. 1.14a) shows the contour plot of the reaction II in the composite specimen after 15 h of exposure. Since fibers are randomly placed into the specimen, the density of the fiber varies all over the sample. Fig. 1.14b) shows the maximum principal

strain generated within the sample due to oxidation. As seen from Fig. 1.14a), rate of reaction II is predominantly governed by the oxygen diffusion. The rate of reaction is the highest near the left boundary where O_2 concentration would be higher and nearly zero at the right side of the specimen. We can also see (in Fig. 1.14b)) that higher compressive strain getting generated in the less-dense fiber region (matrix-rich). These zones are mostly affected by the oxidation and inhomogeneous shrinkage strain appears.

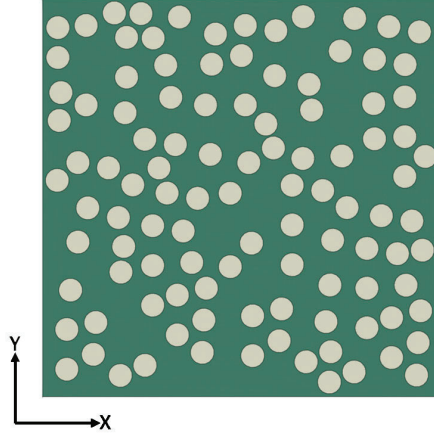


Figure 1.13: Geometry of a randomly distributed fiber reinforced polymer composite sample. Geometry of a randomly distributed fiber reinforced polymer composite sample.

1.7 Concluding remark

In this paper we have presented a thermodynamically consistent, chemo-mechanically coupled large deformation theory for high temperature oxidation in polymers. The

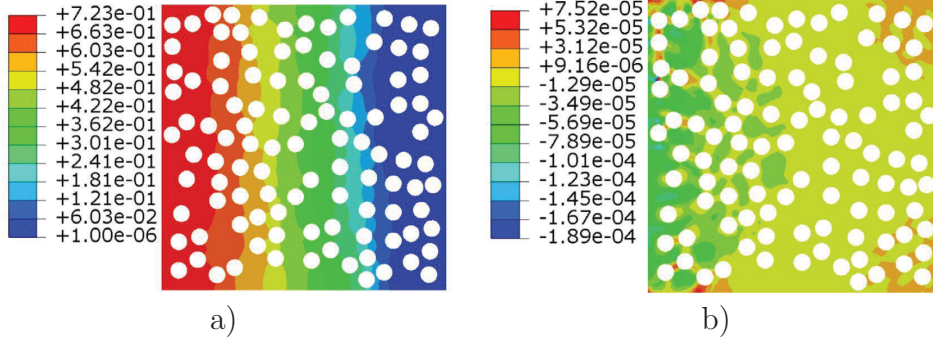


Figure 1.14: a) Contour plot for reaction II after 15 h of oxidation in the randomly distributed carbon fiber composite specimen; b) corresponding maximum (in-plane) principal strain generated within the matrix.

formulation takes into account the coupled effect of diffusion-driven chemical reactions occurring at the molecular level and connects with the continuum level constitutive response. Further, we have tested the capability of the model by implementing it in a commercial FE package. The model shows the capability of predicting the progressive oxidation front in the material for given ambient conditions. The numerical simulations show the usefulness of the model to simulate oxidation process in a randomly distributed fiber composites. In future work, we plan to validate our model with real experimental data for specific polymers. Once fully validated, the present model would be capable of reducing the empiricism in long-term life prediction for polymers due to oxidative aging.

Chapter 2

A Reaction-driven Evolving Network Theory Coupled with Phase-field Fracture to Model Polymer Oxidative Aging

2.1 Introduction

High-temperature oxidative aging in polymers and polymer matrix composites (PMCs) involves a multi-scale phenomena that starts at molecular level with multiple

chain reactions, leading to the microscale chain-scission and oxidative crosslinking. These microscale events eventually degrade the material properties at the macroscale and adversely affect the mechanical response of the polymers [102, 173, 193, 197, 269]. In particular, the inhomogeneous evolution of mechanical properties due to progressive oxidation further promotes stress concentration in the material under loading, initiating localized damage and, ultimately fracturing the material. Oxidation in polymers at high temperature is characterized as a coupled diffusion-reaction phenomenon driven by the diffusion of atmospheric oxygen. The damage induced by oxidation significantly alters the constitutive response of the polymer and notably reduces the lifetime expectancy. Polymeric materials are greatly desirable in many applications for excellent exhibition of competing properties, (such as lightweight, toughness, viscous dissipation, etc.). However, the current literature is still limited in terms of the accurate response predictions of these materials at high temperature oxidative environment, such as in the components of supersonic jets, pipelines and chemical storage etc. [63].

The experimental studies as reported on the high temperature oxidation in polymers, clearly demonstrate degradation of properties and constitutive response, such as an increase in the modulus, decrease in the glass transition temperature and failure strain, shrinkage strain development, etc. [63, 72, 82, 87, 88, 104, 112, 172, 193, 197, 269]. Significant contributions had been made to identify the underlying cause for such embrittlement and degradation over the past few decades [50, 80, 81, 82, 86, 87, 88],

both experimentally and computationally. While experiments are inevitable to characterize the property changes in the course of oxidation, it may sometimes render inadequate to gather all the information regarding material behavior for all the possible scenarios. In reality, the effect of high temperature oxidation in polymer is a slow process requiring days or months to demonstrate measurable changes in polymer response. However, the experiments are commonly being conducted at accelerated aging conditions [49]. Therefore, modeling the oxidation in polymers has always been a strong focus of the polymer-oxidation literature. The most popular model is the mechanistic model, which was developed by a thorough investigation of the oxidation reaction kinetics [21]. An extension of this model can also be found in the literature, known as the three-zone oxidation model, that emphasized the heterogeneity of oxygen diffusion [200, 240, 241]. This heterogeneity in the degree of oxidation results in non-uniform mechanical properties and inhomogeneous stress/strain distribution when the material is subjected to loading [103, 104, 240]. The property degradation can be linked to the reduction of the molecular weight of the material due to an irreversible alteration in the polymer network [87, 88]. Recently, a micro-mechanical model based on the competition between chain-scission and crosslinking events occurring at the polymer network during oxidation was reported to predict the changes in the constitutive behavior of polymers [175]. On the other hand, a thermodynamically consistent continuum model to predict the constitutive response based on high-temperature oxidation behavior was found in the work of [103, 104]. However, these

models do not consider the connection between the micro-scale polymer network evolution with the macroscopic property degradation and damage initiation/propagation for the oxidized polymer under mechanical loading.

In this paper, we develop an oxidation reaction-informed evolving network theory coupled with phase-field fracture to connect the microscale network evolution with macroscopic damage occurring in polymers during oxidative aging. We use the dynamic or transient network theory based on the statistical mechanics framework of the polymer chains, (as used in [219, 239, 246, 253, 255]), to model the microscale network evolution yielded by the chemical reactions. According to this theory, we consider the evolution of the amorphous network in the polymer due to oxidation. The degree of crystallinity in a semicrystalline polymer also gets affected by the influence of high temperature but will not be considered in the present micromechanics. We have also assumed that this amorphous network stays in the rubbery state throughout the oxidation process. It is important to note that for prolonged oxidation the polymer may not remain in the rubbery state for the entire duration and the network's viscoelasticity might get altered which has not been considered here. The configuration of a polymer network changes as chain scission and new crosslinked bonds are formed. We assume that the statistical distribution of the polymer chain configuration can evolve both as a function of mechanical deformation and oxidation reactions. We link this microscale chain distribution to the continuum kinematics description through the definition of a chain distribution tensor, as introduced in [255].

To connect this microscale mechanics with the macroscale damage under mechanical deformation, we further use the phase-field fracture to model the macroscopic damage initiation, propagation, and ultimate fracture. The macroscale property degradation in the aged polymer has been assumed as linear function of the chain-scission and crosslinking events. It is important to note that the concept of network evolution and the mechanical property degradation used in the present work is not thermodynamically consistent, rather guided by the statistical mechanics approach. Finally, we develop a macroscale continuum-level theory to model the coupling between diffusion, chemical reactions and phase-field fracture, in a thermodynamically consistent way.

The novelty of the present work lies in the successful blending and numerical implementation of the two well known theories-namely, the transient network theory and phase-field fracture to model the network evolution, local embrittlement of polymer at the microscale ultimately interacting with the general state of stress to initiate damage at macroscale. The present work provides an efficient theoretical and computational framework to predict oxidative degradation in polymers incorporating all the complex physical/chemical processes involved in the high temperature aging. The paper is organized as follows- firstly, we explain the chemistry of oxidation reactions in polymers followed by the statistics fundamental of the polymer chain network used in the standard network theory and how it has been modified in the present setting to incorporate the reaction-driven evolution. Subsequently, we present a continuum-level chemo-mechanically coupled theory incorporating phase field fracture to model

the macroscale damage initiation and propagation within the oxidized polymer. We implement the proposed theory in a finite element setting by writing a user element subroutine (UEL) in ABAQUS [1] and present several numerical simulations to demonstrate the capability of the model. At the end, the concluding remarks are presented.

2.2 A reaction-dependent network theory coupled with phase-field fracture for polymers oxidation

As mentioned earlier, during oxidation, polymer undergoes a series of chemical reactions that lead to random chain scission and oxidative cross-linking at the microscale. In the present section, we describe a micromechanically informed, chemo-mechanically coupled theory to connect these microscale modifications in the polymer network due to oxidation with the macroscopic damage initiation/propagation under mechanical loading. We have included the description of the important mathematical symbols used throughout this paper in Table 2.1, to add clarity. It is important to note that, all the time derivatives used in the present formulation are considered as local (spatial) for the respective quantities.

Table 2.1
List of symbols and their meanings

symbol	meaning	symbol	meaning
ξ_n	Extent of reaction 'n'	β	Chemical species
$\mathcal{R}_{n\beta}$	Stoichiometric coefficient	$c(t)$	Active chain concentration
C_T	Total chain concentration	c_{rd}	Dissociated chain ratio
c_{rc}	Active chain ratio	G_c	Fracture energy
λ_L	limiting stretchability of the chain network	ϑ	Isothermal temperature
k_B	Boltzmann constant	K_{bulk}	Bulk modulus
G_{shear}	Shear Modulus	b	Length of Kuhn segment
\mathbf{r}	chain end-to-end distance vector	ϕ	Chain distribution function
N	Number of Kuhn segments in a polymer chain	k_a, k_d	Rate like association or dissociation coefficients
f_a, f_d	Reaction dependent functions	J	$\det \mathbf{F}$
\mathbf{F}	Deformation gradient	$\bar{\lambda}$	Average chain stretch of the network
\mathbf{L}	Velocity gradient with $\mathbf{L} = \dot{\mathbf{F}}\mathbf{F}^{-1}$	∇d	Gradient of d
$\boldsymbol{\mu}$	Chain distribution tensor	\mathbf{j}_R^β	Flux of the diffusing species β
d	Phase-field order parameter	$\nabla \mu^\beta$	Gradient of μ^β
l_c	length-scale parameter associated with phase-field	\mathbf{T}	Cauchy stress
c_R^β	concentration of species β	$\boldsymbol{\zeta}$	Vector microscopic stress
μ^{beta}	Chemical potential of species β		
\mathbf{T}_R	Piola stress		
\mathbf{S}	2nd Piola stress		
ϖ	Scalar microscopic stress		
$\mathbf{U} = \sum_i^3 \lambda_i \mathbf{N}_i \otimes \mathbf{N}_i$	Tensor containing principal stretches in the principal direction \mathbf{N}_i		
\mathbf{R}	Orthogonal rotational tensor		

2.2.1 Chemistry of oxidation:- the reaction kinetics

In the recent literature, the kinetics of the closed-loop multiple chain reactions occurring during polymer oxidation have been extensively studied [63, 64]. According to [63, 64], the oxidation process involves a chain scission type event by breaking few unstable hydroperoxides (POOH) to create polymer free radicals (P*) in the initiation stage (as shown in Fig 2.1b). As mentioned in [64], an initiation reaction involving resin depletion (denoted by reaction (Ib)) requires significantly higher amount of activation energy compared to reaction (Ia), and happens only at very high temperature.

Hence in the present work, we assume reaction (Ia) is the only active initiation reaction. The free polymer radicals thus produced by reaction (Ia) eventually react with the diffused oxygen to create (PO_2^*) radicals and the latter can further attack the resin (PH) system to create a large number of chain scissions in the propagation stage. These chain scission events seem to be playing an important role attributing to the property degradation of the polymer [81, 86, 87, 88]. Eventually the reaction gets terminated, as the free radicals react among themselves to create inactive products, as $\text{P} = \text{P}$, POOP, etc. It is important to note that these inactive products do not necessarily promote a healing process, rather the original network gets substituted by these newly formed shorter chained products (also known as "oxidative crosslinking"), as shown in Fig 2.1b). It is also to be noted that the unsaturated double bonds formed in the termination stage might further participate in the polyaddition reaction when it is energetically favorable at comparatively very high temperature; however such events are rarely reported in the oxidation literature.

In our earlier work, we discussed the reaction kinetics of the oxidation process and proposed how the reaction kinetics can be connected to the continuum kinematics with the help of internal state variables, namely *extent of reaction*. These state variables measure and quantify the amount of reactants or products being consumed/generated in one particular reaction [143]. Without reiterating the detail, we define the extent of reaction for each reaction n at every continuum point \mathbf{X} in a local dimensionless form as, $0 \leq \xi_n(\mathbf{X}, t) \leq 1$, with ' n ' varies between 1 to 6. Subsequently, one can

track the rate of change in concentration for species, β (reactants or products) during oxidation via, $r^\beta = \sum_n \mathcal{R}_{n\beta} \dot{\xi}_n$, where r^β is the rate of production or consumption of chemical species β and $\mathcal{R}_{n\beta}$ is the stoichiometric coefficient in reaction n .

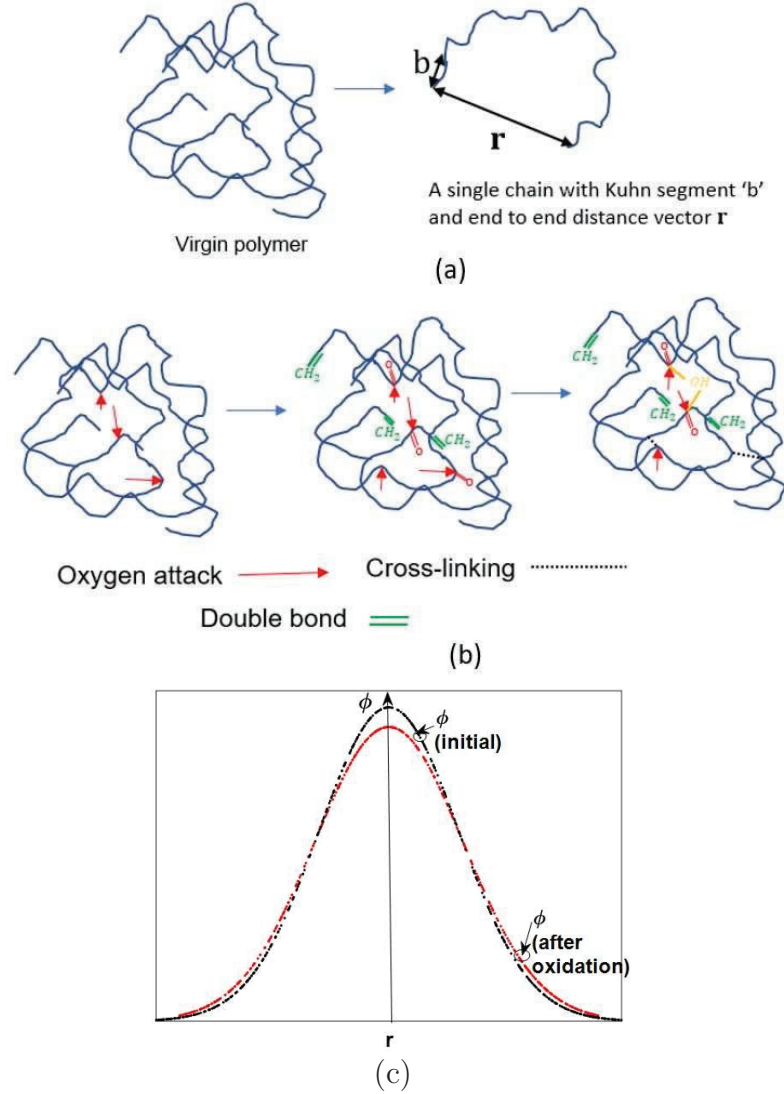


Figure 2.1: (a) Typical virgin polymer chains with Kuhn segment 'b' and end to end distance vector \mathbf{r} , (b) polymer undergoing oxidation developing new cross-links and broken chains, (c) typical distribution of the end-to-end vector ($\phi(\mathbf{r})$), the black line represents virgin polymer and the red line represents oxidized polymer.

2.2.2 A reaction-dependent network theory based on the statistical mechanics of polymer chains

At the outset, we consider most of the polymer chains are attached to each other in an amorphous network via crosslinks, representing a 3D solid polymer at its virgin state. We also assume that, the actively crosslinked chains in the network essentially provides the structural integrity for the polymer. In addition, the network also contains some dangling chains, which could act as the initiator for the oxidation reaction. Hence, the total number of chains in a polymer network (C_T) is the sum of the active ($c(t)$) and inactive chains ($c_d(t)$), expressed in terms of chain concentration per unit volume (mol/m^3). Following [124], under the assumption that individual chains do not diffuse within the polymer, the total concentration follows the standard conservation equation as,

$$\dot{C}_T + C_T \text{tr}(\mathbf{L}) = 0 \quad (2.1)$$

where \mathbf{L} is the macroscopic velocity gradient, defined as, $\mathbf{L} = \dot{\mathbf{F}}\mathbf{F}^{-1}$, with \mathbf{F} being the deformation gradient. During oxidation, some polymer chains get broken (via reactions (I) and (III)). Since polymer radicals are highly reactive, these broken chains can get re-attached via the termination reactions (IV, V, and VI). These new attachments or bonds are formed with a much lower energy compared to the original bonds in the virgin networks as reported in [28, 175]. Thus, one can consider that,

the final oxidative product has more crosslinked network of smaller chains compared to the virgin polymer with longer crosslinked network. It is important to mention that, oxidation reaction gives rise to a different type of network in the oxide zone of the polymer, a "POOP" type network or, a "P=P" type network compared to the original P-P network. We attempt to describe the polymer oxidation phenomena as a collective response of the chain detachments and attachments at the microscale governed by the chain reactions. With the help of a chain distribution function based on the chain end-to-end vector \mathbf{r} , (motivated by the transient network theory as introduced in [239, 253, 254, 255]), we use a statistical framework to describe the physical state of an oxidized polymer network. It is important to note that one of the key limitations of this theory while deriving the free energy is the assumption of Gaussian statistics of the polymer chains, which had been circumvented by [254], with the use of so-called mean field approximation. In the present study, we also assume that this approximation is valid, and the rate of attachment/detachment events due to oxidation reactions are independent of mechanical deformation.

2.2.2.1 Chain distribution function

A standard polymer network constitutes of a large number of long chains spreading in all possible directions and orientations in a 3-D coordinate system. Each chain

can be represented by a vectorial distance between their ends named as chain end-to-end vector (\mathbf{r}). Since the number of chains can be quite large in the network, it is convenient to represent this end-to-end vector for the collection of chains in the network through a statistical distribution. In this work, we describe this distribution of the chain end-to-end vectors via a chain distribution function ($\phi(\mathbf{r}, t)$), indicating the number of chains whose end-to-end vectors lie within \mathbf{r} and $\mathbf{r} + d\mathbf{r}$ inside a representative volume element dV . As the polymer undergoes physical/chemical processes such as deformation or oxidation, this distribution changes. Fig. 2.1(c) represents a typical Gaussian distribution for $\phi(\mathbf{r}, t)$ corresponding to the virgin and oxidative state of the polymer network, respectively. Thus, with the knowledge of why and how this distribution evolves, it is further possible to predict the network's elastic response based on the entropic elasticity theory. In the following section, we define the mathematical form of this distribution function in detail and successively provide an evolution equation for the distribution due to the mechanical deformation and chemical reactions.

To begin with, we consider the end-to-end vector (\mathbf{r}) of a single chain as a primary kinematical quantity to describe the polymer chain configuration. Let us consider that every single chain is comprised of N number of freely joined Kuhn segments of length b as demonstrated in Fig. 2.1a. As postulated in the classical random walk model, we assume that all the actively crosslinked chains are of equal length. Hence, the physical state of the polymer can be represented by the statistical distribution of

the end-to-end vectors ($\phi(\mathbf{r})$) for the entire chain population. Let us consider that, the distribution function $\phi(\mathbf{r})$ can be expressed by a simple relationship between the probability density function $P(\mathbf{r})$ and active chain concentration $c(t)$ as,

$$\phi(\mathbf{r}, t) = c(t)P(\mathbf{r}, t) \quad (2.2)$$

where $c(t)$ has the unit of number of chains per unit of current volume. The active chain concentration is the integral of all the possible chain distributions, $\phi(\mathbf{r}, t)$ and can be written as,

$$c(t) = \langle \phi \rangle \quad (2.3)$$

where the operator $\langle \blacksquare \rangle$ indicates the integral over all the possible chain configuration as,

$$\langle \blacksquare \rangle = \int_0^{2\pi} \int_0^\pi \left(\int_0^\infty \blacksquare r^2 dr \right) \sin\theta \, d\theta \, d\omega \quad (2.4)$$

where θ and ω are the direction of the end-to-end vector \mathbf{r} in the spherical coordinates. Further assuming that, at a length-scale much larger than the individual chains, the network is random and isotropic, the stress-free chain distribution can be expressed as a normal distribution $P_0(\mathbf{r})$ with a zero mean and a standard deviation $\sqrt{N/3}b$ in each of the three spatial directions. We use the expression for $P_0(\mathbf{r})$ as [246],

$$P_0(\mathbf{r}) = \left(\frac{3}{2\pi Nb^2} \right)^{3/2} \exp\left(-\frac{3|\mathbf{r}|^2}{2} \right) \quad (2.5)$$

which leads to the chain distribution at stress-free configuration as,

$$\phi_0(\mathbf{r}, t_0) = c(t_0)P_0(\mathbf{r}) \quad (2.6)$$

where $c(t_0)$ is the active chain concentration at the stress-free configuration at time $t = t_0$.

2.2.3 Evolution of chain distribution due to the combined effect of oxidation and mechanical deformation

The hypothesis is that in a network of polymer chains, the statistical distribution of \mathbf{r} changes as a function of mechanical deformation and chemical reactions. In addition, we assume that the chain-scission and crosslinking events due to oxidation are independent of mechanical deformation (stretching of the network). On the other hand, the network evolution due to mechanical deformation originates in the form of distortion or stretching of the chains without any attachment or detachment events. Hence these two events occur independently of each other and the total change in the network configuration can be expressed as a sum of these two independent evolving phenomena, as,

$$\dot{\phi}(\mathbf{r}, t) = \dot{\phi}(\mathbf{r}, t)\Big|_{ox} + \dot{\phi}(\mathbf{r}, t)\Big|_{\mathbf{F}} \quad (2.7)$$

The subscripts 'ox' and 'F' denote the change in ϕ while oxidation and deformation gradient are held fixed, respectively. Assuming an affine deformation such that the end-to-end vectors of all chains evolve proportionally with respect to the macroscopic deformation gradient [255], we can write the 1st term of Eq. 2.7 as,

$$\dot{\phi}(\mathbf{r}, t) \Big|_{ox} = -\mathbf{L} : (\nabla \phi \otimes \mathbf{r}) \quad (2.8)$$

where \mathbf{L} is the macroscopic velocity gradient. Following the definition of spatial time derivative and the use of transport theorem over the chain distribution space, the derivation of the final form of Eq. 2.8 is not new and can be found in literature [255]. In this work, we investigate the 2nd term in further detail, which incorporates the change in the chain distribution arising from the oxidation reactions.

We can see from Eq. 1.1, chain dissociation or scissions occur during reaction (I) and (III) and chain reattachment happens in reaction (IV), (V) and (VI). We assume that, the chain scission is proportional to the current distribution function $\phi(\mathbf{r}, t)$ and depends on the scission reactions. We further assume that, chain attachment happens in a stress-free configuration depending on the termination reactions. Also, only a fraction of chains that has been scissioned before gets reattached in the termination process. Hence, one can write a kinetic form to accommodate the change in the

distribution due to the reactions as,

$$\dot{\phi}(\mathbf{r}, t)|_{\mathbf{F}} = f_a(\xi_n)c_d(t)P_0(\mathbf{r}) - f_d(\xi_m)\phi(\mathbf{r}, t), \text{ with } m = 1a, 3 \text{ and } n = 4, 5, 6 \quad (2.9)$$

where $c_d(t) = C_T - c(t)$ equals the total number of detached or scissioned chains; f_a and f_d are the reaction dependent functions. Further m, n denotes the reaction number. In addition, we assume that the reaction dependent functions can be expressed as follows:

$$\begin{aligned} f_d(\xi_m) &= k_d(\xi_{1a} + \xi_3) \\ f_a(\xi_n) &= k_a(\xi_4 + \xi_5 + \xi_6) \end{aligned} \quad (2.10)$$

where k_d and k_a are rate-like coefficients, denoting the chain detachment and attachment rates, respectively. Substituting Eq. 2.10 into Eq. 2.9, we can get the evolution of the chain distribution due to the reaction as,

$$\dot{\phi}(\mathbf{r}, t)|_{\mathbf{F}} = k_a(\xi_4 + \xi_5 + \xi_6)(C_T - c(t))P_0(\mathbf{r}) - k_d(\xi_{1a} + \xi_3)\phi(\mathbf{r}, t) \quad (2.11)$$

Substituting Eq. 2.8 and 2.11 into Eq. 2.7 yields the complete evolution equation for

the chain distribution as,

$$\dot{\phi}(\mathbf{r}, t) = -\mathbf{L} : (\nabla\phi \otimes \mathbf{r}) + k_a(\xi_4 + \xi_5 + \xi_6)(C_T - c(t))P_0(\mathbf{r}) - k_d(\xi_{1a} + \xi_3)\phi(\mathbf{r}, t) \quad (2.12)$$

2.2.3.1 Evolution of the concentration of active chains

Following Eq. 2.3, one can see that, the active chain concentration is the integral of all the possible chain distribution function, $\phi(\mathbf{r}, t)$. As the chain distribution evolves, the concentration of the active chains would also change with time. Using the fact, $\dot{c} = \langle \dot{\phi} \rangle$ and by integrating Eq. 2.12 over the chain space, we can write the evolution of the chain concentration as,

$$\dot{c} = k_a(\xi_4 + \xi_5 + \xi_6)(C_T - c(t)) - k_d(\xi_{1a} + \xi_3)c(t)\langle P(\mathbf{r}) \rangle - c(t) \text{tr}(\mathbf{L}) \quad (2.13)$$

where $\langle P(\mathbf{r}) \rangle$ represents the integration of the chain distribution over all the configuration and value of $\langle P_0(\mathbf{r}) \rangle = 1$ is used in the 1st term. As per this expression, the active chain concentration would increase while the reaction kinetics are dominated by the termination reactions and would decrease when the kinetics are dominated by the scission reactions. Also, the term, $\text{tr}(\mathbf{L})$ vanishes for an incompressible polymer. As the active chain concentrations provide rigidity in the polymer network, any change in the active chain concentration would directly influence the mechanical

properties and stored energy of the polymer.

2.2.3.2 Active chain ratio and the dissociated chain ratio

The chain scission and crosslinking events due to the oxidation reactions influence the mechanical properties of the polymer network. We define a non-dimensional parameter as a ratio between the current chain concentration $c(t)$ to the total chain concentration C_{T0} at the virgin state expressed as,

$$c_{rc} = \frac{c(t)}{C_{T0}} \text{ with } c_{rc} \leq 1 \quad (2.14)$$

This nondimensional quantity termed as "active chain ratio", attains a value of 1 for a fully crosslinked network. A value of $c_{rc} = 0$ represents a network without any crosslink (dilute chains). In an oxidative aging situation $c_{rc}|_{t=0} = c_{r0}$ represents the initial crosslinking density of the network, prior to any oxidation event. Further, we also define another ratio termed as, dissociated chain ratio c_{rd} , which measures the concentrations of chains per mole that has been dissociated from the network ($c_d(t)$), normalized with respect to C_{T0} as,

$$c_{rd} = \frac{c_d(t)}{C_{T0}} \text{ with } c_{rd} \leq 1 \quad (2.15)$$

where $c_{rd} = 1$ represents a network completely dissociated and $c_{rd} = 0$ represents a fully crosslinked network.

2.2.3.3 Macroscopic property degradation due to oxidative embrittlement

The continuous occurrence of chain detachment/attachment events during oxidation alters the mechanical properties of the polymer network such as, the shear modulus (G_{shear}), the limiting chain stretchability (λ_L) and the fracture energy (G_c), etc. To correlate these macroscale properties with the evolving network, it is important to mention the recent oxidation experiments highlighting the relation between the polymer molecular weights and the change in mechanical properties [65, 86, 87, 88]. According to these studies, polymer undergoes a ductile to brittle transition during the oxidation induction period, when the chain-scission reactions occur. During this period a direct correlation between the drop in ultimate strain and reduction in molecular weight is observed, as reported in [86, 87]. More than 90% drop in failure strain was observed for oxidized polymer accompanying with a similar percentage reduction in molecular weight. In addition, the chain-scission leads to the breakage of the network entanglement resulting in significant drop in fracture toughness [86]. Based on these studies, we assume that the drop in ductility and fracture toughness can be linked to the chain dissociation events. To quantify the drop in ductility,

we use the limiting stretchability of the network and express that as a function of scissioned chain concentration (c_{rd}). Similarly, the fracture energy of the network also reduces as a function of this scissioned chain concentration. Hence, we assume the functional relations for λ_L and G_c , as,

$$\Gamma = \Xi_i(c_{rd}) \text{ , where } \Gamma \supset [\lambda_L, G_c] \quad (2.16)$$

We assume that the mechanical stiffness or the shear modulus of the network is directly proportional to the active crosslinking density, following the standard definition of modulus in rubber elasticity. The actively crosslinked network imparts the structural integrity of the polymer and the dangling chains do not contribute in this regard. Thus for an amorphous polymer the shear modulus can be assumed as proportional to the actively crosslinked chain density. However, in the case of semi-crystalline polymers, the oxidative chemicrystallization also plays a role in the evolution of the active network and the shear modulus, which has not been considered here. Hence, we express the shear modulus evolution as, $G_{shear} \approx \Upsilon(c_{rc})$. The actual forms for the function Υ and Ξ_i ; $i = 1, 2$; will be discussed later in the specific constitutive forms.

2.2.4 The chain distribution tensor and the free energy of the oxidation reacted network

In order to connect the chain distribution function $\phi(\mathbf{r}, t)$ with the macroscopic description of the state of the polymer chain network at any stage of the deformation process, the chain distribution tensor ($\boldsymbol{\mu}$) is introduced as the second moment of the distribution, following [254, 255]. As mentioned earlier, assuming a Gaussian distribution for $P_0(r)$ at the stress-free configuration, $\boldsymbol{\mu}_0$ can be written as,

$$\boldsymbol{\mu}_0 = \langle P_0 \tilde{\mathbf{r}} \otimes \tilde{\mathbf{r}} \rangle \quad (2.17)$$

where $\tilde{\mathbf{r}}$ is the normalized end to end vector with $\tilde{\mathbf{r}} = \frac{\mathbf{r}}{\sqrt{Nb}}$. Here N represents the number of Kuhn segments in a single chain and b is the length of each segment.

Evaluating the above expression using Eq. 2.4, results into identity tensor, \mathbf{I} . Other than the stress-free configuration, $\boldsymbol{\mu}$ is written as, $\boldsymbol{\mu} = \langle P \tilde{\mathbf{r}} \otimes \tilde{\mathbf{r}} \rangle$. Further assuming the distribution $P(\mathbf{r})$ still remains as Gaussian as the oxidation progresses, with different distribution parameters, $\boldsymbol{\mu}$ can be written as a symmetric (3×3) tensor. As it is well known, the symmetric tensor $\boldsymbol{\mu}$ can be better represented by three of its eigenvalues μ_i , $i = 1, 2, 3$; associated with its principal planes. These eigenvalues are related to the square of the standard deviation of the current end-to-end distance \bar{r}_i^2

as, $\mu_i = 3\bar{r}_i^2/Nb^2$; where $Nb^2/3$ is the mean-square end-to-end distance of the chains at stress-free configuration. Hence, $\boldsymbol{\mu}$ can be related further to the macroscopic principal stretches and their directions as: $\boldsymbol{\mu} = 3 \langle \boldsymbol{\lambda} \otimes \boldsymbol{\lambda} \rangle$; where $\boldsymbol{\lambda}$ is the vector containing the principal stretches [253]. Based on this, the average chain stretch can be represented as,

$$\bar{\lambda} = \frac{\bar{r}}{\bar{r}_0} = \sqrt{\frac{\text{tr} \boldsymbol{\mu}}{3}} \quad (2.18)$$

where, \bar{r}_0 is the root-mean-square (average) distance of the chain end-to-end vector at the stress-free configuration and \bar{r} is the current root-mean-square value of the chain end-to-end distance. In elastomeric materials, the stored energy arises mainly due to entropic contribution. Hence the free energy of the material can be expressed as a function of $\bar{\lambda}$ based on the statistical theory of entropic elasticity as,

$$\psi_R = \bar{\psi}_R \left(G_{shear}, \frac{\bar{\lambda}}{\lambda_L} \right) \quad (2.19)$$

The specific form of the function ψ_R can be chosen as reported in [15, 99, 146] to incorporate the limiting chain extensibility of the network.

To obtain the evolution equation for $\boldsymbol{\mu}$, one needs to integrate the evolution equation for ϕ (Eq. 2.12) over the entire chain space. Finally it turns out as,

$$\dot{\boldsymbol{\mu}} = k_a(\xi_4 + \xi_5 + \xi_6) \left(\frac{C_T - c(t)}{c(t)} \right) \boldsymbol{\mu}_0 - (\langle k_d P \tilde{\mathbf{r}} \otimes \tilde{\mathbf{r}} \rangle)(\xi_{1a} + \xi_3) - \frac{\dot{c}(t)}{c(t)} \boldsymbol{\mu} + \mathbf{L} \boldsymbol{\mu} + \boldsymbol{\mu} \mathbf{L}^T \quad (2.20)$$

The term $\langle k_d P \tilde{\mathbf{r}} \otimes \tilde{\mathbf{r}} \rangle$ can be simplified by assuming that the dissociation rate k_d is independent of \mathbf{r} and hence constant. Hence, we get, $\langle k_d P \tilde{\mathbf{r}} \otimes \tilde{\mathbf{r}} \rangle = k_d \boldsymbol{\mu}$. Replacing it in Eq. 2.20, we can re-write,

$$\dot{\boldsymbol{\mu}} = k_a(\xi_4 + \xi_5 + \xi_6) \left(\frac{C_T - c(t)}{c(t)} \right) \boldsymbol{\mu}_0 - k_d(\xi_{1a} + \xi_3) \boldsymbol{\mu} - \frac{\dot{c}(t)}{c(t)} \boldsymbol{\mu} + \mathbf{L} \boldsymbol{\mu} + \boldsymbol{\mu} \mathbf{L}^T \quad (2.21)$$

The two specific cases for $\boldsymbol{\mu}$ evolution have been presented in the B. It is important to note that the chain distribution may not remain as Gaussian for the entire deformation history (especially in the regime, when the chain end-to-end distance attends full contour length as $|\mathbf{r}| \rightarrow \sqrt{N}b$). For non-Gaussian distribution, simplification of $\boldsymbol{\mu}$ via a symmetric tensor is not possible. In the present study we assume that the chain distribution remains close to Gaussian for the entire oxidation and deformation history and the kinetics of the chain association/dissociation events are independent of the mechanical force.

Another important point is to note that the quantities such as $\phi(\mathbf{r}, t)$, $(c(t))$ and $(\boldsymbol{\mu})$ are not standard kinematic quantities used in the continuum mechanics. However these are very useful for the statistical description of an evolving polymer network and can be correlated with certain macroscopic quantities on an average sense.

2.2.5 A phase-field fracture model to predict macroscale damage and fracture in polymers due to oxidation

In the previous section, we have proposed a method for predicting the microscale evolution of the network morphology depending on the oxidative reaction kinetics. We have also modeled the degradation of the mechanical properties yielded by the network evolution in the oxidized polymers. In this section, our aim is to model macroscale damage initiation and propagation in the oxidized material due to the application of external loading. Hence, we propose a phase-field fracture theory to model macro stress-induced damage initiation and propagation until complete fracture. The final goal is to connect the reaction modified polymer network response with the macroscopic damage behavior originating due to stress inhomogeneity during an oxidative aging process. It is important to note that the microscale chain scission events may cause damage in the three dimensional network. However, as the set of reactions occurs in a closed-loop, the scission events are always accompanied by successive crosslinking. Hence, the usual irreversibility condition of a damage variable might not hold at the microscale for the entire reaction history. As mentioned earlier, these combined effects of chain scissions/crosslinking have been considered as a newly formed network of shorter chains rather than a damaged network. Hence, in

the present work, we have considered that the network modification affects the network elasticity in the form of degraded mechanical properties but no damage at the microscale. It is assumed that the modified network with heterogeneous properties is prone to macroscale damage initiation due to localized stress concentration from mechanical loading.

The use of a phase-field fracture model would help in predicting the macroscale damage initiation and propagation in complex conditions such as mixed-mode, interacting cracks, complex distribution of initiation sites etc., under a coupled physics driven scenario such as oxidative aging. In order to overcome the difficulties in classical Griffith-type theory of brittle fracture, phase-field fracture models have emerged as an alternative way of modeling crack propagation using a smeared representation of the crack topology [38, 39, 93, 169, 171]. The models originally devised as a mathematical regularization of the variational approach to brittle fracture, based on the energetic competition between elastic potential energy and the dissipated fracture energy needed to create fracture surfaces, through a minimization principle [38, 44, 69, 93]. They share a conceptual resemblance with the damage gradient models in which the dissipated energy density contains a regularizing damage gradient term associated with a regularizing internal length scale l'_c [199, 227]. The main advantage of such models is that no ad hoc crack propagation criterion is needed, as the damage evolution is based solely on energetic requirements. In the present work, the model builds

upon a coupled mechanical and oxygen diffusion response, driven by the displacement boundary conditions and the chemical potential gradients. It further considers a reaction dependent amorphous polymer network with constantly evolving network morphology and mechanical properties.

2.2.5.1 Phase-field order parameter or macroscale damage variable

In the phase-field fracture theory, we define a phase-field order parameter or damage variable d such that,

$$0 \leq d(\mathbf{X}, t) \leq 1 \quad (2.22)$$

where $d = 0$ represents the material being intact, and $d = 1$ corresponds to a fully broken material. Thus, the phase-field order parameter or damage variable interpolates between the broken state of the material and its unbroken state [6, 169, 171]. We assume that d monotonically increases, such that $\dot{d} \geq 0$, implying that the damage is irreversible. In order to define a diffusive crack topology to approximate the non-smooth crack field, the phase-field theory introduces an exponential function for $d(\mathbf{X})$, as [169, 170, 171],

$$d(\mathbf{X}, t) = e^{-\frac{\mathbf{x}}{l_c}} \quad (2.23)$$

The length scale parameter l_c is introduced to govern the regularization or the width of the diffusive zone and yields the sharp crack topology for the limiting case as, $l_c \rightarrow 0$ (Fig. 2.2). The theory further considers dependence on d and the gradient ∇d to incorporate the spatial inhomogeneity due to localized damage formation and to avoid the so-called ill-posed nature of the local damage models.

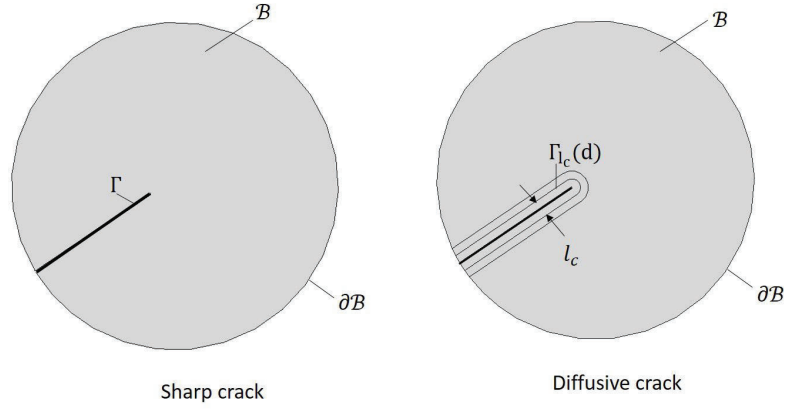


Figure 2.2: Sharp and diffusive crack topology: a sharp crack Γ embedded into the solid B (left) and the regularized crack surface Γ_{l_c} with a functional of crack phase field d and the crack regularization length l_c .

2.2.6 The chemo-mechanically coupled theory for polymer oxidation:-the balance laws and thermodynamic consistency

2.2.6.1 Mass balance for the diffusing and reacting species

In order to avoid redundancy, we rewrite only the specific local form of mass balance for any species, β , as (following [143]):

$$\dot{c}_R^\beta = -\text{Div} \mathbf{j}_R^\beta + \sum_n [\mathcal{R}_{n\beta} \dot{\xi}_n] \quad (2.24)$$

Assuming oxygen is the only diffusing species and for the other constituents, mass balance would involve only the reaction dependant changes, we summarize the mass

balance equation for each individual species as,

$$\left\{ \begin{array}{l} \dot{c}_R^{O_2} = -\text{Div} \mathbf{j}_R^{O_2} - \dot{\xi}_2 + \dot{\xi}_6 \text{ for } O_2 \\ \dot{c}_R^{POOH} = -\dot{\xi}_{1a} + \dot{\xi}_3 \text{ for POOH} \\ \dot{c}_R^{PH} = -\dot{\xi}_3 \text{ for PH} \\ \dot{c}_R^{P=P} = \dot{\xi}_4 \text{ for P=P} \\ \dot{c}_R^{POOP} = \dot{\xi}_5 + \dot{\xi}_6 \text{ for POOP} \end{array} \right. \quad (2.25)$$

For more elaboration on the balance laws, the readers are referred to [143].

2.2.6.2 Balance of forces and moments

Using the principle of virtual power, we can derive the macroscopic and microscopic force balance conditions. Following similar notation as mentioned in [118], we consider the rate-like kinematical descriptors as $\dot{\chi}$, $\dot{\mathbf{F}}$, $\dot{\xi}_n$, \dot{d} and $\nabla \dot{d}$.

For the macroscopic force balance, we consider that, on the arbitrary part P of the reference body \mathcal{B}_R , there exists a traction force $\mathbf{t}_R(\mathbf{n}_R)$ that expends power over the velocity $\dot{\chi}$. There also exists a stress tensor, \mathbf{T}_R that expends power over the rate $\dot{\mathbf{F}}$ of the deformation gradient. Similarly, we consider a scalar microscopic stress ϖ , expending power over the rate of the damage variable, \dot{d} . Additionally, a vector

microscopic stress $\boldsymbol{\zeta}$ is introduced that expends power over the gradient $\nabla \dot{d}$. Finally, there also exists a scalar microscopic traction $\zeta(\mathbf{n}_R)$ that expends power over \dot{d} on the boundary of the part. Subsequently, using the principle of virtual power, we can derive the macro and micro-force balances together with the momentum balance as,

$$\text{Div} \mathbf{T}_R + \mathbf{b}_R = \mathbf{0} \quad \text{and} \quad \mathbf{T}_R \mathbf{F}^T = \mathbf{F} \mathbf{T}_R^T \quad (2.26)$$

$$\text{Div} \boldsymbol{\zeta} - \varpi = 0 \quad \text{and} \quad \zeta(\mathbf{n}_R) = \boldsymbol{\zeta} \cdot \mathbf{n}_R \quad (2.27)$$

In the spatial configuration, the corresponding macro force balance equation can be written as,

$$\text{div} \mathbf{T} + \mathbf{b} = \mathbf{0} \quad \text{and} \quad \mathbf{T} = \mathbf{T}^T \quad (2.28)$$

where \mathbf{T} is the symmetric Cauchy stress tensor and \mathbf{b} is the body force in spatial configuration. The derivation of the force balance conditions are summarized in C.

2.2.6.3 Energy imbalance and thermodynamic consistency

Following the detailed derivation in our previous work ([143]), for an isothermal polymer system undergoing oxidation, combining the 1st and 2nd law of thermodynamics,

we re-write the local form of energy imbalance as:

$$\dot{\psi}_R - \mathbf{T}_R : \dot{\mathbf{F}} - \varpi \dot{d} - \boldsymbol{\zeta} \cdot \nabla \dot{d} + \sum_{\beta} \mathbf{j}_R^{\beta} \cdot \nabla \mu^{\beta} + \sum_{\beta} \mu^{\beta} \sum_n [\mathcal{R}_{n\beta} \dot{\xi}_n] - \sum_{\beta} \mu^{\beta} \dot{c}_R^{\beta} \leq 0 \quad (2.29)$$

It is important to note that, with the specific choice of the free energy as,

$$\psi_R = \psi_R(\lambda_1, \lambda_2, \lambda_3, c_R^{\beta}, \xi_n, d, \nabla d) \quad (2.30)$$

we can determine the thermodynamic constraints for the mechanical, diffusion, extent of reactions and phase field constitutive equations from the dissipation inequality (Eq. 2.29). In Eq. 2.30, λ_1 , λ_2 and λ_3 , are the principal stretches and the corresponding principal directions are given by $(\mathbf{N}_i \otimes \mathbf{N}_i)$ - which can be readily correlated to the eigenvalues and eigenvectors of the chain distribution tensor, $\boldsymbol{\mu}$, as mentioned before.

Further, it is convenient to introduce a new stress measure called the 2nd Piola stress, which is defined as,

$$\mathbf{S} = \sum_{i=1}^3 \frac{1}{\lambda_i} \frac{\partial \psi_R}{\partial \lambda_i} \mathbf{N}_i \otimes \mathbf{N}_i \quad (2.31)$$

Then the Cauchy stress can be written as,

$$\mathbf{T} = J^{-1} \mathbf{R} \left(\sum_{i=1}^3 \mathbf{U}_i \mathbf{S} \mathbf{U}_i \right) \mathbf{R}^T = J^{-1} \mathbf{R} \left(\sum_{i=1}^3 \lambda_i \frac{\partial \psi_R}{\partial \lambda_i} \mathbf{N}_i \otimes \mathbf{N}_i \right) \mathbf{R}^T \quad (2.32)$$

Using the fact that the spectral decomposition of $\boldsymbol{\mu}$ in terms of principal stretches and directions, is given by, $\boldsymbol{\mu}^D = 3 \sum_{i=1}^3 \lambda_i^2 \mathbf{N}_i \otimes \mathbf{N}_i$, and further $\boldsymbol{\mu}^D = \mathbf{R}\boldsymbol{\mu}\mathbf{R}^T$, and $\frac{\partial \psi_R}{\partial \boldsymbol{\lambda}} = \frac{1}{\lambda} \frac{\partial \psi_R}{\partial \lambda} \boldsymbol{\lambda}$, we can re-write Cauchy stress expression from Eq. 2.32 as,

$$\mathbf{T} = \frac{1}{3\bar{\lambda}} J^{-1} \mathbf{R} \sum_{i=1}^3 \left(\frac{\partial \psi_R}{\partial \bar{\lambda}} \mu_i \mathbf{N}_i \otimes \mathbf{N}_i \right) \mathbf{R}^T = \frac{1}{3\bar{\lambda}} J^{-1} \frac{\partial \psi_R}{\partial \bar{\lambda}} \boldsymbol{\mu} \quad (2.33)$$

To construct the specific constitutive forms for the phase field micro-stresses ϖ and $\boldsymbol{\zeta}$, we consider a theory which allows for an energetic and dissipative effects associated with the temporal changes in d , and also an energetic effect due to the gradient ∇d [13, 185]. We also assume that the scalar microstress, ϖ , can be broken down into an energetic and dissipative part respectively, (based on the similar approach proposed in [13, 185]) as,

$$\varpi = \varpi_{en} + \varpi_{dis} \quad (2.34)$$

This along with the thermodynamic constraints, provide us the constitutive relation for energetic microstress as:

$$\varpi_{en} = \frac{\partial \psi_R}{\partial d}, \quad \boldsymbol{\zeta} = \frac{\partial \psi_R}{\partial \nabla d} \quad (2.35)$$

Hence we are finally left with the following dissipation inequality:-

$$\varpi_{dis} \dot{d} + \left[\left(- \sum_{\beta} \mu^{\beta} \sum_n \mathcal{R}_{n\beta} - \sum_n \frac{\partial \hat{\psi}_R}{\partial \xi_n} \right) \dot{\xi}_n \right] \geq 0 \quad (2.36)$$

We assume that each individual term of Eq. 2.36 satisfies the dissipation inequalities as:

$$\begin{cases} \varpi_{dis} \dot{d} \geq 0 \\ \left(- \sum_{\beta} \mu^{\beta} \sum_n \mathcal{R}_{n\beta} - \sum_n \frac{\partial \hat{\psi}_R}{\partial \xi_n} \right) \dot{\xi}_n \geq 0 , \end{cases} \quad (2.37)$$

From Eq. 2.37, we consider that ϖ_{dis} is the driving force for the phase-field damage d . Similarly, we define the bracketed part as conjugate to the extent of reaction (ξ_n) as the driving force for each individual reaction as discussed in our earlier work [143].

2.2.7 Constitutive equations for the mechanical, diffusion, chemical reactions and phase field damage

2.2.7.0.1 Free energy:- To be consistent with our transient network theory, we use a Arruda-Boyce hyperelastic free energy function for the mechanical energy expression [15]. Based on our earlier work [143], we write the free energy as the sum of separable energies arising from mechanical deformation, oxygen diffusion, chemical reaction combined with a quadratic fracture energy to account for the phase field fracture. The chemical energy is considered as a simple reaction dependent quadratic form, as proposed by [250] and later used by [153]. The diffusion energy is considered as following the Flory-Huggins form [91]. As the size of oxygen molecules are quite small compared to the long polymer chains, the diffusion can be best represented by

the Flory-Huggins lattice theory [52, 91]. It is important to note that as the phase field damage progresses, the stored or mechanical energy of the material continues to degrade. In order to model that, we incorporate a widely used degradation function $g(d)$ as reported in the phase-field literature [13, 165, 169, 171, 185]. The function $g(d)$ is a monotonically decreasing function in d and it satisfies:- $g(0) = 1$, $g(1) = 0$, $g'(d) \leq 0$ and $g'(1) = 0$. We use the most common form for degradation function used in the literature [13, 169, 171, 185], as,

$$g(d) = (1 - d)^2 + \kappa \quad (2.38)$$

where κ is a small positive-valued constant which is introduced to prevent ill-conditioning of the model when $d = 1$. Thus the complete free energy expression can now be written as,

$$\begin{aligned} \hat{\psi}_R = g(d) & \left[\underbrace{c(t)k_B\vartheta \lambda_L \left(\frac{\bar{\lambda}\gamma - \gamma_0}{\lambda_L} + \ln \frac{\gamma \sinh(\gamma_0)}{\gamma_0 \sinh(\gamma)} \right) + \frac{K_{bulk}}{2} (\ln J)^2}_{\text{Mechanical}} \right] + \underbrace{\sum_n \frac{H_n}{2} (1 - \xi_n)^2}_{\text{Chemical}} + \\ & \underbrace{\mu_0^{O_2} c_R^{O_2} + R\vartheta c_R^{O_2} \left[\ln \left(\frac{\Omega c_R^{O_2}}{1 + \Omega c_R^{O_2}} \right) + \chi \left(\frac{1}{1 + \Omega c_R^{O_2}} \right) \right]}_{\text{Diffusion}} + \underbrace{\frac{G_c l_c}{2} |\nabla d|^2}_{\text{Fracture}} \quad (2.39) \end{aligned}$$

where, k_B is the Boltzmann constant, ϑ is the oxidation temperature, as standard in rubber elasticity, we consider $G = c(t)k_B\vartheta$ is the shear modulus, λ_L is the limiting chain extensibility parameter, K_{bulk} is the bulk modulus. The terms $\gamma = \mathcal{L}^{-1}\left(\frac{\bar{\lambda}}{\lambda_L}\right)$ and $\gamma_0 = \mathcal{L}^{-1}\left(\frac{1}{\lambda_L}\right)$ are the inverse Langevin function as, $\mathcal{L} = \coth x - x^{-1}$, which

is used to capture strain stiffening response of the polymers at large stretch. H_n is the chemistry modulus for each reaction, ' n ', defined as twice the negative change in Gibbs energy required for reaction ' n ' to take place; μ^{O_2} and $c_R^{O_2}$ are the chemical potential and concentration of oxygen, respectively, Ω is the molar volume of the polymer in L/mol, χ is the dimensionless Flory-Huggins parameter that defines the interaction between oxygen and the polymer. Finally, G_c is the Griffith-type fracture energy of the polymer.

2.2.7.0.2 Stress and chemical potential Following the free energy expression, Cauchy stress can be expressed as,

$$\mathbf{T} = J^{-1} g(d) \left[\frac{ck_B \vartheta \lambda_L}{3} \left[\frac{1}{\bar{\lambda}} \mathcal{L}^{-1} \left(\frac{\bar{\lambda}}{\lambda_L} \right) \boldsymbol{\mu} - \mathcal{L}^{-1} \left(\frac{\bar{\lambda}}{\lambda_L} \right) \mathbf{I} \right] + K_{bulk}(\ln J) \mathbf{I} \right] \quad (2.40)$$

Based on the Flory-Huggins form as given in Eq. 3.23, the chemical potential driving the diffusion of O_2 , μ^{O_2} , can be obtained by taking the partial derivative of the diffusive energy with respect to oxygen concentration as,

$$\mu^{O_2} = \mu_0^{O_2} + R\vartheta \left(\ln \left(\frac{\Omega c_R^{O_2}}{1 + \Omega c_R^{O_2}} \right) + \frac{1}{1 + \Omega c_R^{O_2}} + \chi \left(\frac{1}{1 + \Omega c_R^{O_2}} \right)^2 \right) \quad (2.41)$$

In addition, the reactive force expression (\mathcal{F}_n), conjugate to the extent of reaction for each individual reaction (ξ_n) can also be determined from the dissipation inequality as shown in C.1.

2.2.7.0.3 Governing equation for the phase-field variable d :- We can write

the energetic microstress as,

$$\varpi_{en} = \frac{\partial \psi_R}{\partial d} = -2(1-d)\psi_R^{mech} \quad (2.42)$$

where, ψ_R^{mech} is the mechanical free energy of the reaction modified polymer network, but without any macroscopic damage (the 1st term in Eq. 3.23).

To determine the expression for ϖ_{dis} , let us consider the recent phase field literature [169, 171], where the energy required to create a new fracture surface was given by the crack surface density functional involving both d and ∇d as,

$$\psi_s = \int_P G_c \left(\frac{1}{2l_c} d^2 + \frac{1}{2} l_c |\nabla d|^2 \right) dV \quad (2.43)$$

In order to be consistent with the energy dissipated per unit volume to create new surface (as the first term in Eq. 2.43) the associated microstress is defined as,

$$\varpi_{dis} = \frac{G_c(c_{rd})}{l_c} \quad (2.44)$$

This could be obtained by dividing the 1st term in the fracture energy density with the corresponding 1st term in the crack surface density functional, given as $\left(\frac{d^2}{2} + \frac{l_c^2 |\nabla d|^2}{2} \right)$, with $l_c \rightarrow 0$, as used in the phase-field literature [169, 171]. It is important to recall

that the modification of the fracture energy (G_c) would occur due to the chain scissions occurring in the polymer network during oxidation, as mentioned in Sec.2.2.3.2.

Therefore, Eq. 2.34 can be re-written as,

$$\varpi = \varpi_{en} + \varpi_{dis} = -2(1-d)\psi_R^{mech} + \frac{G_c}{l_c} \quad (2.45)$$

Further, we can derive the vector microstress ζ using Eq. 3.15-b together with the free energy as,

$$\zeta = G_c l_c \nabla d \quad (2.46)$$

Substituting Eq. 4.23 and 2.46 into the microstress balance, $\text{Div}\zeta - \varpi = 0$, yields the evolution equation for d as,

$$2(1-d)\psi_R^{mech} - \frac{G_c}{l_c} + G_c l_c \Delta d = 0 \quad (2.47)$$

where Δd represents the Laplacian of d . It is important to note that the difference in phase-field fracture with the damage mechanics approach lies in the variational approach of solving the fracture problem based on the minimization of the global energy. Hence, the solution of phase field damage variable appears as the solution of the differential equation as given by Eq. 2.47, instead of a time-dependent evolution of a state variable [169, 171].

It is also important to note that the evolution of d in Eq. 2.47 does not ensure the irreversibility constraint of the damage ($\dot{d} \geq 0$). In order to ensure the irreversibility condition, we can rewrite Eq. 2.47 while neglecting the gradient effect (∇d) on the damage variable as,

$$2(1 - d) \left[\psi_R^{mech} - \frac{G_c}{2l_c} \right] - \frac{G_c}{l_c} d = 0 \quad (2.48)$$

It can be shown, that a monotonically increasing evolution of d requires the term $(\psi_R^{mech} - \frac{G_c}{2l_c})$ to be strictly positive for the entire deformation history, [13, 169, 171, 185, 237]. Based on that, a monotonically increasing history field \mathcal{H} is introduced as,

$$\mathcal{H}(t) = \max_{s \in [0, t]} \left| \psi_R^{mech}(s) - \frac{G_c(s)}{2l_c} \right| \quad (2.49)$$

So that the evolution equation has the final form as,

$$2(1 - d)\mathcal{H} - \frac{G_c}{l_c} d + G_c l_c \Delta d = 0 \quad (2.50)$$

2.2.7.0.4 Reaction dependent shear modulus, fracture energy and limiting chain extensibility parameters:- According to the description in section 2.2.3.3, we assume that, shear modulus is directly proportional to the active chain ratio and can be written as,

$$G_{shear}(c_{rc}) = c_{rc} G_0 = c_{rc} c(t_0) k_B \vartheta \quad (2.51)$$

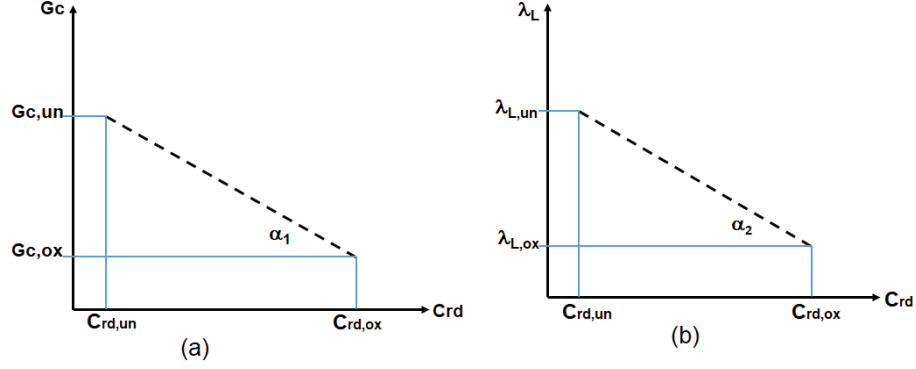


Figure 2.3: Linear trend of fracture energy and limiting chain stretchability paramater as a function of dissociated chain ratio

where G_0 is the virgin shear modulus of the material which is a function of active chain concentration at virgin state $c(t_0)$.

Fracture energy (G_c) and the limiting chain stretchability parameter (λ_L) have been considered as degrading linearly with the dissociated chain ratio (as shown schematically in Fig 2.3), characterizing the increase in brittleness due to oxidative scissions in the network. Thus, we define the reaction dependent fracture energy via a linear relation as,

$$G_c(c_{rd}) = \alpha_1 c_{rd} + C_1 \quad (2.52)$$

with $\alpha_1 = \frac{G_{c,ox} - G_{c,un}}{c_{rd,ox} - c_{rd,un}}$ and $C_1 = [G_{c,ox} + G_{c,un} - \alpha_1(c_{rd,ox} - c_{rd,un})]/2$; where $G_{c,ox}$ and $G_{c,un}$ are the fracture energy at completely oxidized and virgin states respectively, and $c_{rd,ox}$ and $c_{rd,un}$ are the corresponding dissociated chain ratios.

Similarly, we define the limiting chain extensibility parameter as,

$$\lambda_L(c_{rd}) = \alpha_2 c_{rd} + C_2 \quad (2.53)$$

where, $\alpha_2 = \frac{\lambda_{L,ox} - \lambda_{L,un}}{c_{rd,ox} - c_{rd,un}}$ and $C_2 = [\lambda_{L,ox} + \lambda_{L,un} - \alpha_2(c_{rd,ox} - c_{rd,un})]/2$; with $\lambda_{L,ox}$ and $\lambda_{L,un}$ are the stretchability at completely oxidized and virgin states respectively.

2.2.8 Governing differential equations and the boundary conditions

There are three governing partial differential equations required to be solved in this coupled physics problem:

$$\left\{ \begin{array}{l} \text{Div} \mathbf{T}_R + \mathbf{b}_R = \mathbf{0} \\ \dot{c}_R^{O_2} = -\text{Div} \mathbf{j}_R^{O_2} - \dot{\xi}_2 + \dot{\xi}_6 \\ 2(1-d)\mathcal{H} - \frac{G_c}{l_c}d + G_cl_c\Delta d = 0 \end{array} \right. \quad (2.54)$$

We require the initial and boundary conditions to complete the solutions of these differential equations, as detailed in our earlier work for the mechanical and the diffusion [143]. The boundary conditions for the evolution of d are also standard as provided in [170, 171]. Hence the system of equations, Eq. 3.29, combined with the appropriate initial-boundary conditions, are required to be solved for the displacement $\chi(\mathbf{X}, t)$, oxygen concentration $c_R^{O_2}(\mathbf{X}, t)$ and the phase field damage parameter d simultaneously.

Additionally, we require to solve the sets of ordinary differential equations for the active chain concentrations, (Eq. 2.13), chain distribution tensor (Eq. 2.21), and the extent of reactions given in Eq. C.16. In this work, the system of equations are solved numerically by writing a user element subroutine (UEL) in ABAQUS/Standard (2017) [1].

2.3 Material Parameter Estimation

To numerically implement the present theory, a number of material parameters are required for modeling the coupled behavior of multiple chemical reactions-diffusion, large deformation and phase field fracture in polymer. Estimation of the kinetic parameters for the diffusion and chemical reactions has been explained in detail in our previous work [143]. Hence, we ignore that part here for the sake of brevity. The kinetic parameters used in the present work are listed in 1.1.

As described in Section 2.2.3.2, chemical reactions in the oxidation process cause chain-scissions (associated with the rate coefficient k_d) and oxidative crosslinking (associated with the rate coefficient k_a); which in turn, leads to the evolution of the active chain concentration and chain distribution. In order to determine these rate-like reaction dependent coefficients, we have used experimental data as reported in [87]. A simple curve-fitting procedure is adopted assuming an exponential relation

between the concentration data for chain-scissions and crosslinks as a function of oxidation time, as shown in Fig. 2.4. As evident from the data in [87], the chain-scission phenomenon essentially dominates over the oxidative crosslinking in this typical thermoplastic polymer. On the other hand, crosslinking events could be more prominent in the case of some typical thermosets during oxidation, as reported in [80, 81, 82].

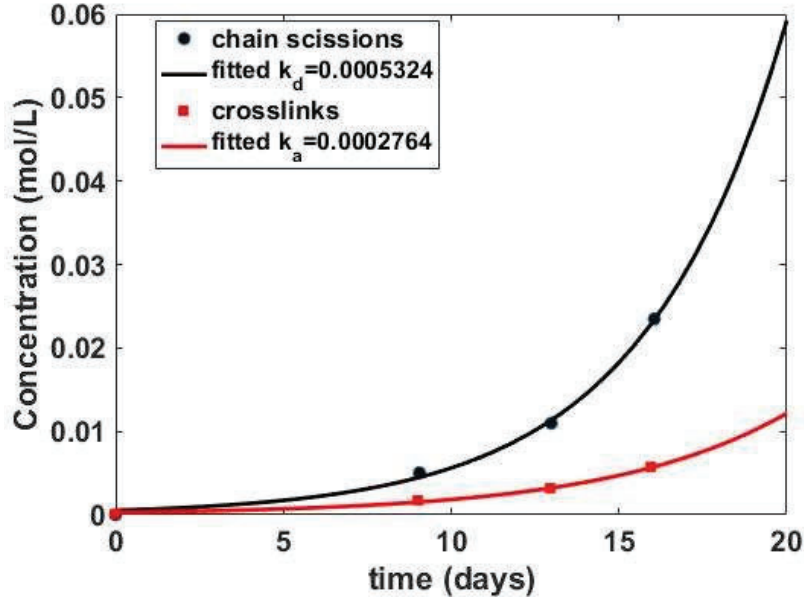


Figure 2.4: Estimation for the k_a and k_d , the rate-like coefficients for polyethylene; the "markers" correspond to the experimental data from [87].

Thermo-oxidative aging significantly affects the critical strain energy release rate or the fracture toughness (G_c) of the material, reducing it by two or three orders of magnitude, as reported in [86, 87]. As identified, the chain-scission mechanism destroys the polymer network structure to a point where plastic deformation process do not initiate and hence the embrittlement occurs [87]. In this work we choose a

Griffith-like fracture energy release rate as 1.44 kN/m for virgin polymer and 100 N/m for a completely oxidized polymer, consistent with the values as reported in the literature [86], for a typical polymer.

The other parameter to describe the mechanical free energy of the polymer network is the limiting chain extensibility (λ_L). Oxidative embrittlement process notably reduces the ultimate failure strain of the material, as the stretchability drops from a value of 800% to 10% as observed in the case of oxidative aging of polypropylene, [86]. For the present simulation, we use $\lambda_L = 9.0$ for the unoxidized polymer and $\lambda_L = 1.9$ for the completely oxidized polymer. The G_c and λ_L values used in the simulations are tabulated in the appendix (Table 3.1).

2.3.0.0.1 Choice of l_c From the material’s microstructure perspective, l_c should represent the length of the lowest micro-structural change that one could use as a representative unit to identify the initiation of macro-scale damage. For an amorphous polymer, it can be as small as in the range of micrometers. However, in the case of the phase field model, in order to maintain computational tractability of the numerical simulation and simultaneously to get a reasonably low l_c value, we first tentatively compute the critical stress at which damage initiates in a linear elastic brittle material having the similar mechanical properties as the polymer under consideration in uniaxial tensile loading. Using Eq. 2.48, we can write the homogeneous

solution for the phase-field variable ignoring the gradient term, d as,

$$d = \frac{\psi_R^{mech} l_c}{G_c + \psi_R^{mech} l_c} \quad (2.55)$$

For a linear elastic material the stored mechanical energy can be approximated as, $\psi_R^{mech} = \frac{1}{2} E \epsilon^2$, where E is the Young's modulus of the polymer and ϵ is the corresponding axial strain. Hence, our degraded mechanical energy is given by, $\frac{1}{2} (1 - d)^2 E \epsilon^2$. For the damage to initiate, this stored energy must be equal to the energy required to create a new surface (Eq. 2.43) over the smallest length scale such as l_c , that is,

$$\frac{1}{2} (1 - d)^2 E \epsilon^2 = G_c \left(\frac{1}{2 l_c} d^2 \right) \quad (2.56)$$

Here once again, the gradient term is ignored. The solution of Eq. 2.56 gives us the critical strain value corresponding to the damage initiation as,

$$\epsilon_c = \sqrt{\frac{G_c}{E l_c}} \quad (2.57)$$

Substituting Eq. 2.57 into the stress equation as, $\sigma_c = (1 - d)^2 E \epsilon_c$, yields the length scale parameter value, l_c in terms of the mechanical properties of the polymer as follows,

$$l_c \approx \frac{G_c E}{16 \sigma_c^2} \quad (2.58)$$

where σ_c is the critical stress, at which damage initiates under uniaxial tensile loading. Considering the values for $G_c = 1.44$ kN/m, $\sigma_c = 35$ MPa and $E = 1.6$ GPa for polypropylene, we get, $l_c \approx 0.12$ mm. Hence, any value ≤ 0.12 mm would be a reasonable choice for l_c in our simulations. Based on the choice of l_c , the smallest element in our FE mesh has been chosen as $h \approx l_c/4$ throughout the simulations.

2.4 Representative numerical simulations

2.4.1 Case study-1: Oxidative aging of a dogbone specimen followed by tensile loading

In this example, we numerically simulate the oxidative aging of a representative polymer dogbone specimen followed by a tensile testing to imitate a typical oxidation experiment performed in a laboratory setting. In the simulation, we consider the initial shear modulus as $G_0 = 0.58$ GPa and a final oxidized modulus as $G_{shear,ox} = 0.7$ GPa. The other important mechanical and kinetic parameters are as listed in Table 3.1 and 1.1 respectively. The geometry of the dogbone sample has been shown in Fig. 2.5(a). Due to the symmetry, we analyze only one-quarter of the sample using 2D plane strain elements and apply symmetric boundary conditions along the mid-planes in the x and y-directions. The length scale parameter to describe the diffuse damage

zone has been chosen as, $l_c = 0.12$ mm. In a traditional lab environment, a sample is first oxidized within an oven at a temperature close or higher than the glass transition temperature of the material for several hours. Subsequently, it is taken out to perform mechanical testing to determine the effect of oxidation on the material's response. In what follows, we perform a two-step simulation where at first, we let the sample oxidize at 80°C for several hours in an accelerated aging environment. In the second step, we pull the sample at a displacement rate of 1×10^{-5} mm/s until the final failure happens. The corresponding chemical and mechanical boundary conditions are shown in Fig. 2.5(b). In the first step, we consider that the sample surface is surrounded by a constant flow of O_2 with partial pressure of 2 atm, which translates to a constant O_2 concentration of 2.8×10^{-2} mol/L. In order to avoid the convergence issues, we have applied the chemical boundary condition in a ramp-like manner over a small time period of 2 hours. In the following step, we have applied the displacement boundary condition on the top surface of the specimen linearly as a function of time (Fig. 2.5(b)). Our aim is to study the effect of oxidative aging in terms of mechanical property degradation upon oxidizing the sample for 30, 50 and 200 hours, respectively. We consider two specific cases to understand the kinetics of the chains- i) when chain scission rate is dominant over the reattachment rate ($k_a < k_d$) and ii) when the chain reattachment is higher ($k_a > k_d$) compared to the scission rate. Since oxidation is a time-dependent process, longer exposure to oxidative environment inevitably leads to higher values of the extent of reactions, which, in turn, yields harsher property

degradation, as demonstrated in the simulations results, as discussed in the following paragraph.

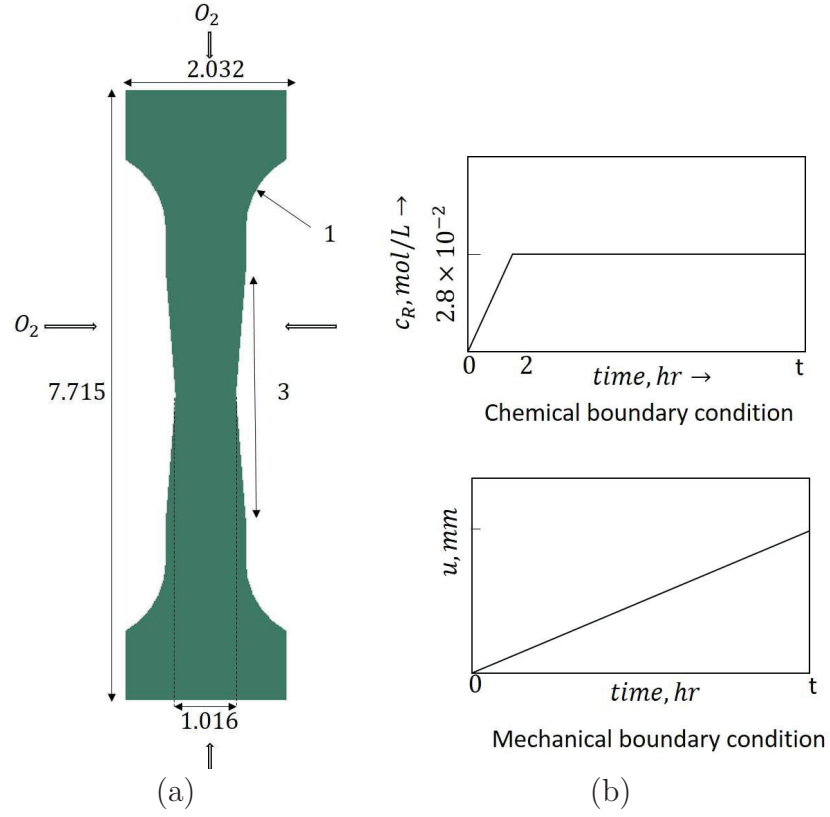


Figure 2.5: (a) Geometry of a dogbone specimen (all dimensions are in mm); (b) boundary condition for the oxygen concentration applied at the edges of the dogbone sample (top) and the displacement boundary condition applied at the top surface of specimen in Step-2 (bottom).

Fig. 2.6(a) and (b) show the contour plots of extent of reaction (III) (ξ_3) and extent of reaction (VI) (ξ_6) at the end of 30 hours (left), 50 hours (middle) and 200 hours (right), respectively. The corresponding changes in G_{shear} and λ_L are shown in Fig. 2.7 and Fig. 2.8, respectively. The extent of reactions monotonically increase in a continuous oxidation process. As time progresses, the evolution of ξ_3 leads to resin depletion

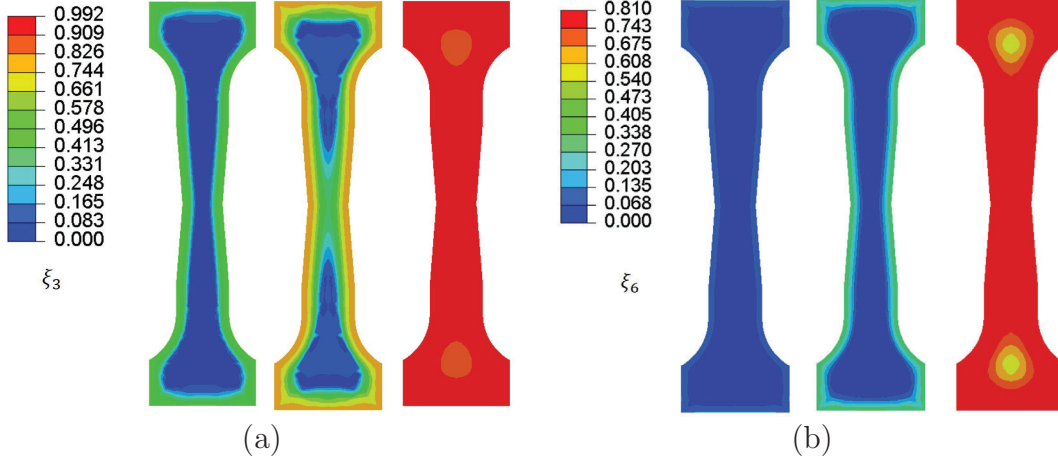


Figure 2.6: Contour plots for (a) extent of reaction ξ_3 after 30 hours (left), 50 hours (middle) and 200 hours (right); (b) extent of reaction ξ_6 after 30 hours (left), 50 hours (middle) and 200 hours (right).

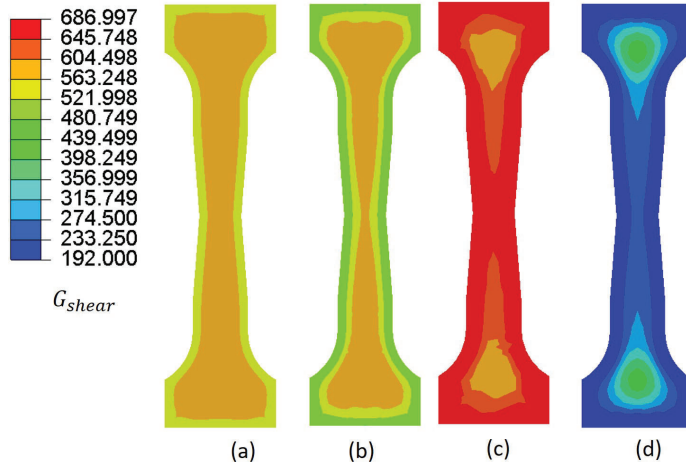


Figure 2.7: Contour plots of shear modulus (in MPa) after (a) 30 hours, (b) after 50 hours (with $k_a < k_d$), (c) 50 hours (with $k_a > k_d$) and (d) 200 hours.

by breaking the PH-chains and formation of some new hydro-peroxides (POOH). On the other hand, the termination reaction (VI) forms new PO-OP bonds and these new bonds accumulate within the material as the reactions progress. As explained in the theory, the chain distribution changes as a function of oxidation reactions and

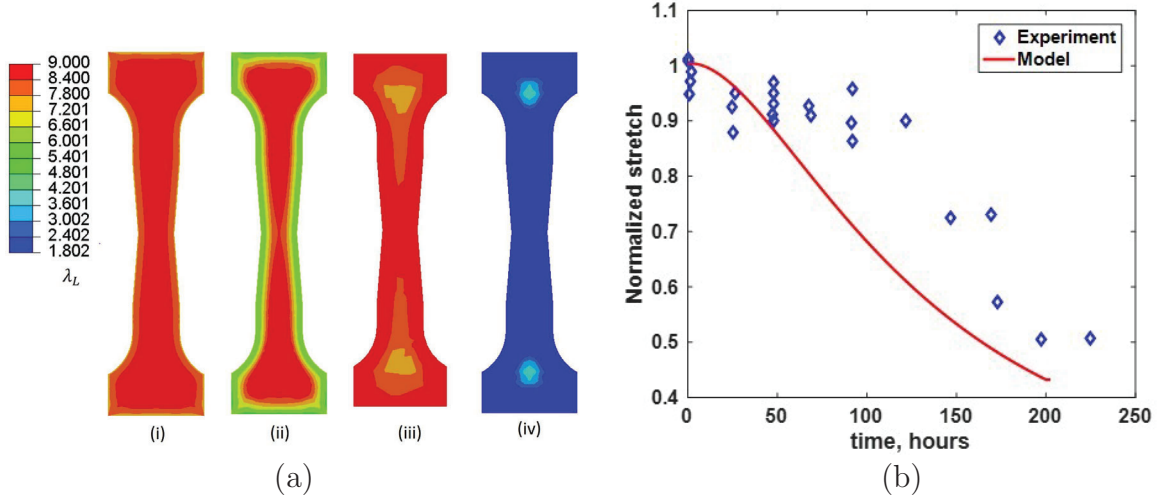


Figure 2.8: (a) Contour plots of λ_L after (i) 30 hours, (ii) after 50 hours (with $k_a < k_d$), (iii) 50 hours (with $k_a > k_d$) and (iv) 200 hours; (b) Comparison of (normalized) limiting stretchability with experiment from [86].

alters the active chain concentrations $c(t)$. For numerical simplicity, we consider only reaction (III) and (VI) as the chain scission and crosslinking reactions, respectively. Hence, following Eq. 2.9, the chain detachment happens as a function of ξ_3 , as $f_d = k_d \xi_3$. Similarly, the chain reattachment happens as a function of ξ_6 as, $f_a = k_a \xi_6$. For $k_d > k_a$ condition, the number of active chains decreases leading to a decrease in the shear modulus (G_{shear}) as seen in Fig. 2.7(a), (b) and (d). On the other hand, when $k_a > k_d$, we observe an increase in G_{shear} with respect to the virgin state, as demonstrated in Fig. 2.7(c). The contour plots of the limiting stretchability parameter, λ_L at various stages of oxidation are also shown in Fig. 2.8(a). It is important to note that λ_L is essentially a function of the dissociated chain ratio, c_{rd} . As the oxidation progresses, the number of dissociated chains goes up, leading to an increase in c_{rd} for the $k_a < k_d$ condition; which in turn causes a reduction in the

stretchability, as shown in Fig. 2.8(i), (ii) and (iv). Fig. 2.8(b) shows a qualitative comparison of the drop in the limiting stretchability (normalized at its virgin value) obtained from our model prediction to the experimental data as reported in [86], for polypropylene. The model prediction shows reasonable agreement with experimental data. In the numerical results, a continuous drop in λ_L is observed between 50 to 150 hours, while the experiments indicate a sharp drop around 150 hours in the data. The reason might be due to the choice of a linear function used in the modeling (Eq. 2.53) for stretchability evolution. A more accurate experimentally informed evolution function could be chosen to improve the numerical prediction in future.

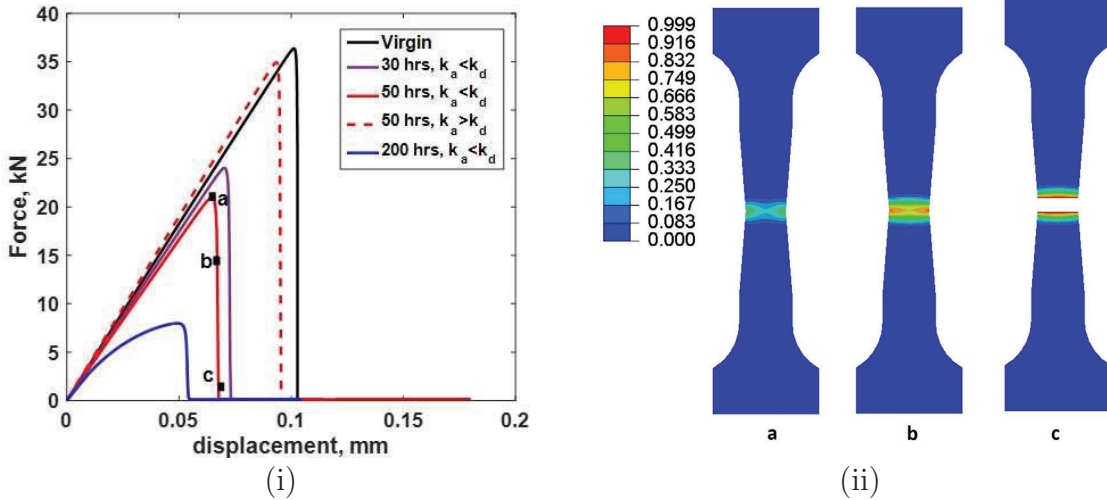


Figure 2.9: (i) Force vs displacement plots for the dogbone sample subjected to tensile loading upon oxidation for various hours; (ii) Contour plots of the phase field damage variable at significant points in the force-displacement plot as marked 'a', 'b' and 'c'.

The changes in the material properties further lead to a change in the constitutive response of the polymer. Fig. 2.9(i) shows the force versus displacement plots for the dogbone samples oxidized for several hours. In general, a significant drop in the

limiting stretchability and tensile strength has been observed for the cases $k_a < k_d$ due to oxidation. Approximately 50% drop in the limiting stretchability has been noticed after 200 hours of oxidation. The maximum tensile strength of the material also decreases significantly. We also observe a slight change in the stiffness of the material during the initial period of oxidation (between 30 to 50 hours), which significantly decreases upon further oxidation (at 200 hours). Fig. 2.9(ii) shows the damage contours of the dogbone sample corresponding to the significant points in the load-deformation curve as denoted in Fig. 2.9(i) for 50 hours of oxidation (corresponding to $k_a < k_d$ condition). The force reaches a maximum value at point a, with a displacement of 0.06 mm. Beyond this point, the force starts dropping, and the sample is unable to stretch any further. The continued loading of the sample ultimately causes rupture of the material, as shown by c in Fig. 2.9(i) with corresponding damage contours in Fig. 2.9(ii)c.

2.4.1.0.1 Case $k_a > k_d$:- For some amorphous thermosets, crosslinking process can be dominating over the chain-scission process, as reported in [80, 81, 82]. However, specific numerical values for the crosslinking and chain-scission density for such cases have not been reported in the literature. For numerical demonstration purpose, we assume $k_a \approx 100 k_d$, and compare the results with the $k_a < k_d$ case, upon 50hrs of oxidation. We observe a significant increase in the shear modulus after 50 hours (Fig. 2.7(c)), almost a rise of $\approx 20\%$ with respect to the virgin material on the oxidized

surface. The limiting stretchability remains almost unchanged as the virgin polymer (Fig. 2.8(iii)). This reflects in the constitutive response of the material, as both the maximum tensile strength and stretchability are observed higher compared to the $k_a < k_d$ case after 50 hours of oxidation, as shown in Fig. 2.9(i).

2.4.2 Case study-2: Oxidation followed by Mode-I loading in a single-edge-notched plate

In this example, we attempt to predict the response of a polymer specimen containing a pre-existing crack undergoing oxidation. In reality, the presence of cracks promotes oxygen diffusion providing favorable paths. Hence pre-existing flaws make the material more prone to oxidation near and around the crack-zones. To simulate one such scenario, we choose to study the effect of oxidation on a single-edge-notched polymer plate, as shown in Fig. 2.10(a). The notch has a width of 2×10^{-3} mm. As earlier, the kinetic and material parameters are chosen from Table 3.1 and 1.1, respectively. The chemical boundary condition is considered as the same as in case study 1. In this simulation, we assume that oxygen diffuses from the left side of the plate and through the entire free surface of the pre-existing crack, with all the other edges being impermeable. We let the sample to oxidize at $80^\circ C$ for 100 hours. Following which, the oxidized sample is pulled at a rate of 1×10^{-5} mm/s along the top-edge, till the final fracture occurs.

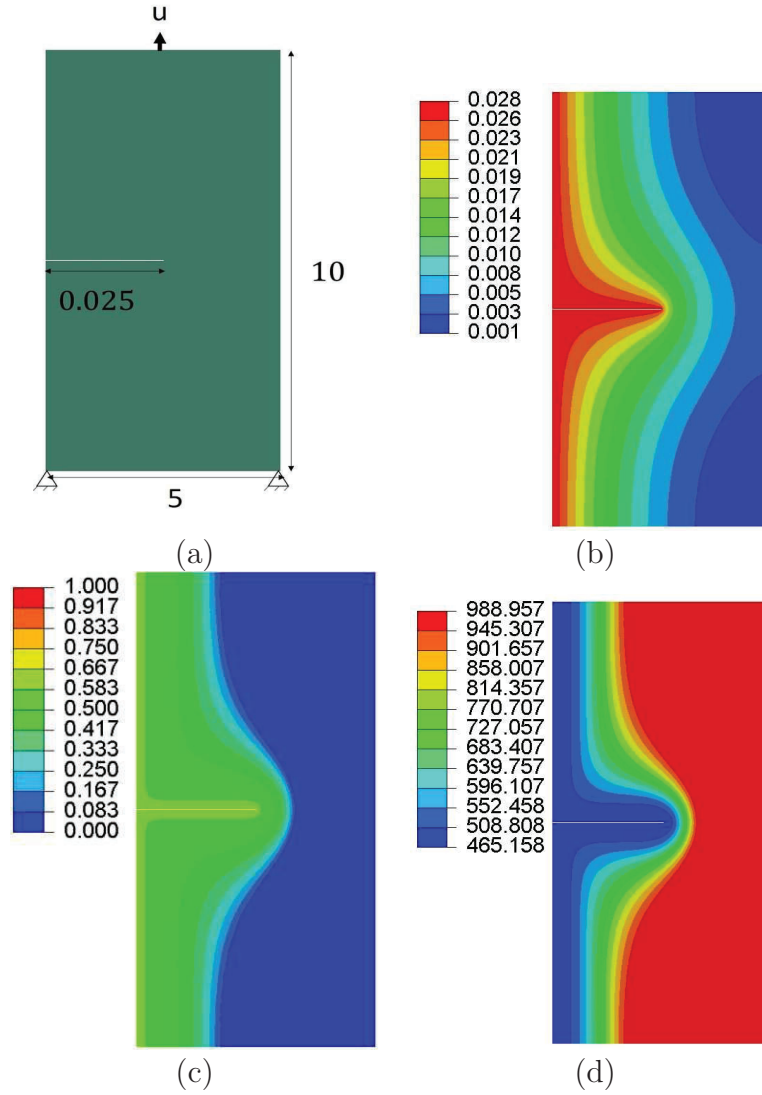


Figure 2.10: (a) Geometry of the single-edge-notched tension sample (all dimensions are in mm); Contour plots for the (b) oxygen concentration (mol/L); (c) extent of reaction (III), ξ_3 ; and (d) chain dissociation ratio c_{rd} , after 100 hours of oxidation.

Fig. 2.10(b) shows the contour plot of oxygen concentration within the plate after 100 hours of oxidation. As observed, oxygen concentration is the maximum at the left side of the boundary and around the pre-existing crack, as a continuous flow is occurring through these surfaces. The concentration gradually plummets through the sample

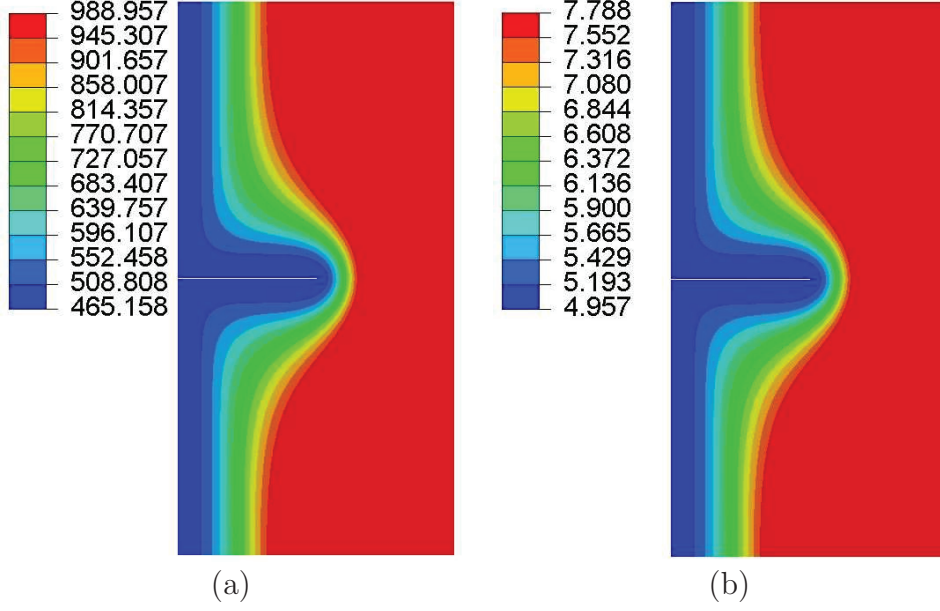


Figure 2.11: Contour plots of (a) G_c in (N/m) ; (b) λ_L after 100 hours of oxidation.

thickness toward the impermeable right side, as a function of the continuous diffusion. It is to be noted that, as the new free surfaces form in a propagating crack, the diffusion and oxidation reactions would become faster due to more access to atmospheric oxygen through the new surfaces. This would eventually degrade local properties and cause further crack propagation. The interaction between the newly formed free surfaces and the diffusion-reaction process promoting further damage propagation has been ignored in the present case study.

Fig. 2.10(c) and (d) show the contour plots of extent of reaction, ξ_3 and the chain dissociation ratio, c_{rd} , respectively after 100 hours of oxidation. As seen in Fig. 2.10(c), ξ_3 , reaches to a value of ≈ 0.6 at the outermost surface along the left boundary as well as around the crack tip, indicating chain-scission would take place predominantly within

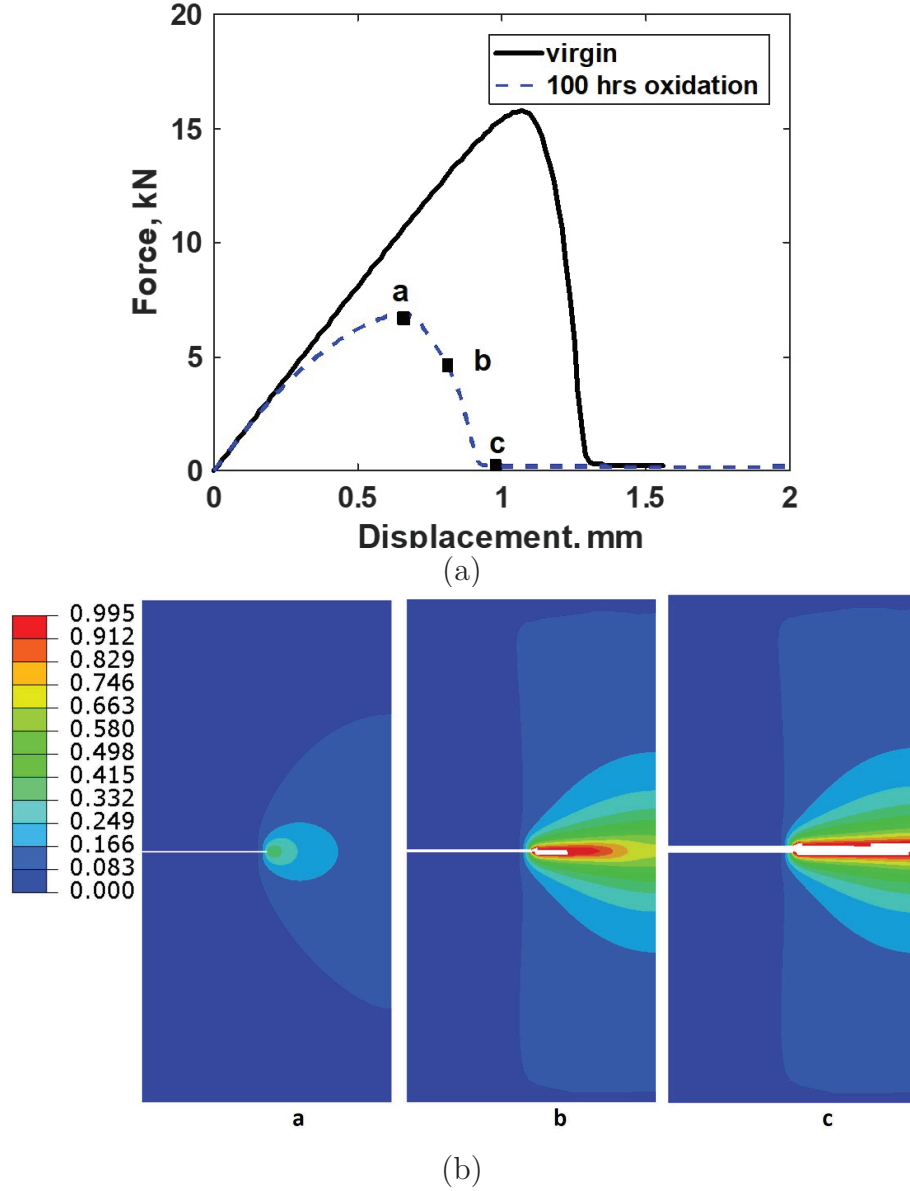


Figure 2.12: (a) Force vs. displacement plot of the single-edge-notch sample ; (b) Contour plots of the phase field variable d at significant points in the force-displacement plot marked as a, b, and c for the oxidized polymer.

this zone. As a result, the chain dissociation ratio continues to increase and reaches a value of $\approx 50\%$ on the left surface and around the crack tip after 100 hrs, as shown in Fig. 2.10(d). This phenomenon further leads to a reduction in the limiting chain extensibility and fracture energy in the oxidized zones, as shown in Fig. 2.11. The

fracture energy drops significantly in the oxidized zone, from 1.44 kN/m to 450 N/m after 100 hrs of oxidation, as seen from Fig. 2.11(a). The limiting chain extensibility also drops down to ≈ 5.0 on the left surface compared to the unoxidized value of 9.0 for the virgin polymer as shown in Fig. 2.11(b). Consequently, these events affect the load-displacement response of the material as demonstrated in Fig. 2.12(a). After 100 hrs of oxidation, we see a significant drop in the maximum load, compared to the virgin material (as $\approx 67\%$). Similarly, the stretchability of the oxidized material has been dropped compared to the virgin material, as seen from the ultimate displacement values corresponding to the final fracture. Fig. 2.12(b) shows the phase field contour plots of the oxidized polymer sample corresponding to the locations marked by a, b and c in the force-displacement curve. The sample reaches the maximum load at the point a. Beyond this point, the load continues to drop with a continuous increase in the phase field parameter value. Finally the sample completely breaks at point c, with the phase field value reaching almost equal to 1, as shown in Fig. 2.12(b)-c.

2.4.3 Case study-3: Effect of oxidative aging in an asymmetrically notched specimen

As mentioned in case study-2, the presence of cracks promotes oxidation by providing new paths for oxygen diffusion and creates secondary oxide zones at the crack-tip.

Therefore, it is expected that the presence of multiple cracks would create heterogeneous oxide layers near and around the crack, eventually governing the local material behavior and damage propagation at the macro-scale. In this simulation, we apply a tensile loading in an asymmetrically notched specimen subjected to various oxidation boundary conditions. Fig. 2.13 refers to the geometry of the asymmetrically notched specimen as considered. The sample dimension is $10\text{ mm} \times 15\text{ mm}$. Similar to the earlier case studies, a two-step simulation is followed, with the sample being oxidized at 80°C for 50 hours (in the 1st step) followed by a vertical displacement applied at the top surface with the bottom held fixed. The notch at the right edge is located closer to the top surface and is larger compared to the one located at the left side of the specimen, as shown in Fig. 2.13. Both cracks possess a width of 0.01 mm. For a pure mechanical loading without any oxidation, it is expected that the larger notch would propagate at a faster rate than the smaller one (as observed in Fig 2.15b-1). However, under the presence of oxidation, the damage propagation is entirely governed by the heterogeneous nature of the property distribution caused by the chemical reactions. To isolate and identify that the heterogeneous oxidation indeed changes the course of damage propagation, we study and compare two different types of oxidation boundary conditions, as-i.) oxygen is allowed to diffuse from both the left and right sides of the specimen and ii) oxygen is allowed to flow only through the left side.

The contour plots for the extent of reaction (III) (ξ_3) after 50 hours of oxidation is

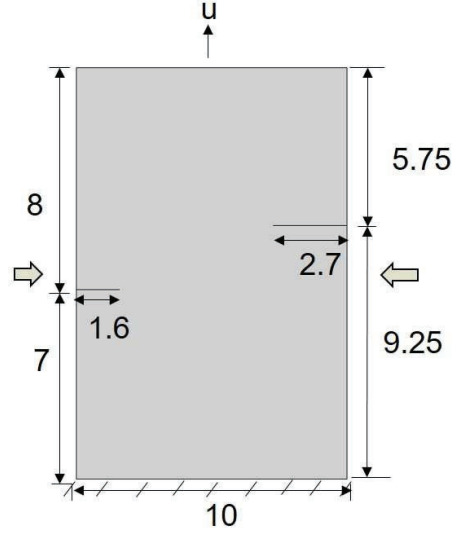


Figure 2.13: Geometry and dimension for the asymmetrically notched specimen.

shown in Fig. 2.14 (a). The top and the bottom row represent the contour for the left-side oxidation and the both-side oxidation conditions, respectively. As can be seen from these contours, the extent of reaction reaches at a higher value toward the core for the specimen allowed to oxidize from both sides compared to the only left-sided one. Consequently, this situation results in completely different property distribution within the sample, for the two cases, as shown in Fig. 2.14(b), and (c), respectively for G_c and λ_L . As expected, these non-uniform property distributions would eventually lead to a very different constitutive response and damage propagation in the specimen, as explained below.

Fig. 2.15(a) shows the force vs. displacement plots for the two different oxidation conditions as compared to the virgin (unoxidized) sample. The unoxidized specimen

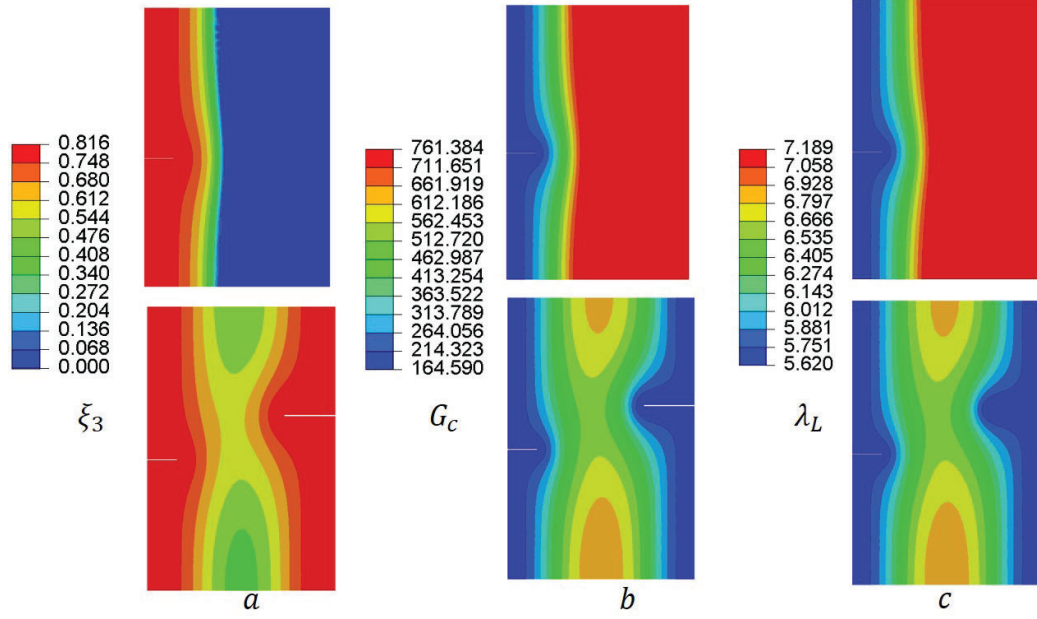


Figure 2.14: a) Contour plots of extent of reaction (III) after 50 hours of oxidation: b) corresponding contour plots of Fracture energy, $G_c(N/m)$ and c) contour plots for limiting stretchability, λ_L ; top row- only left side oxidized; bottom row- both sides oxidized.

can carry the maximum load of about 400N, while the left-side oxidized specimen only carries a maximum load of about 280N, with the both-side oxidized sample has the lowest load carrying capacity of about 250N. Fig. 2.15(b) shows the corresponding damage contours for the three cases, respectively. It is already mentioned, in the case of the unoxidized sample, the larger crack propagates at a much faster rate, dominating the final failure of the specimen. In the case of both side oxidation, still the larger crack propagates dominantly, with the smaller one closely following. On the other hand, for the case where only left side is oxidized, the smaller crack propagates faster compared to the larger one. This is due to the fact that the property degradation near the left edge due to oxidation is dominant compared to the right

edge, and an increase in local brittleness influences the crack propagation path near the left edge. Hence, it is observed that oxidative aging introduces local heterogeneity in the mechanical properties, which in turn governs the localized damage initiation, propagation, and the final response of the oxidized polymer.

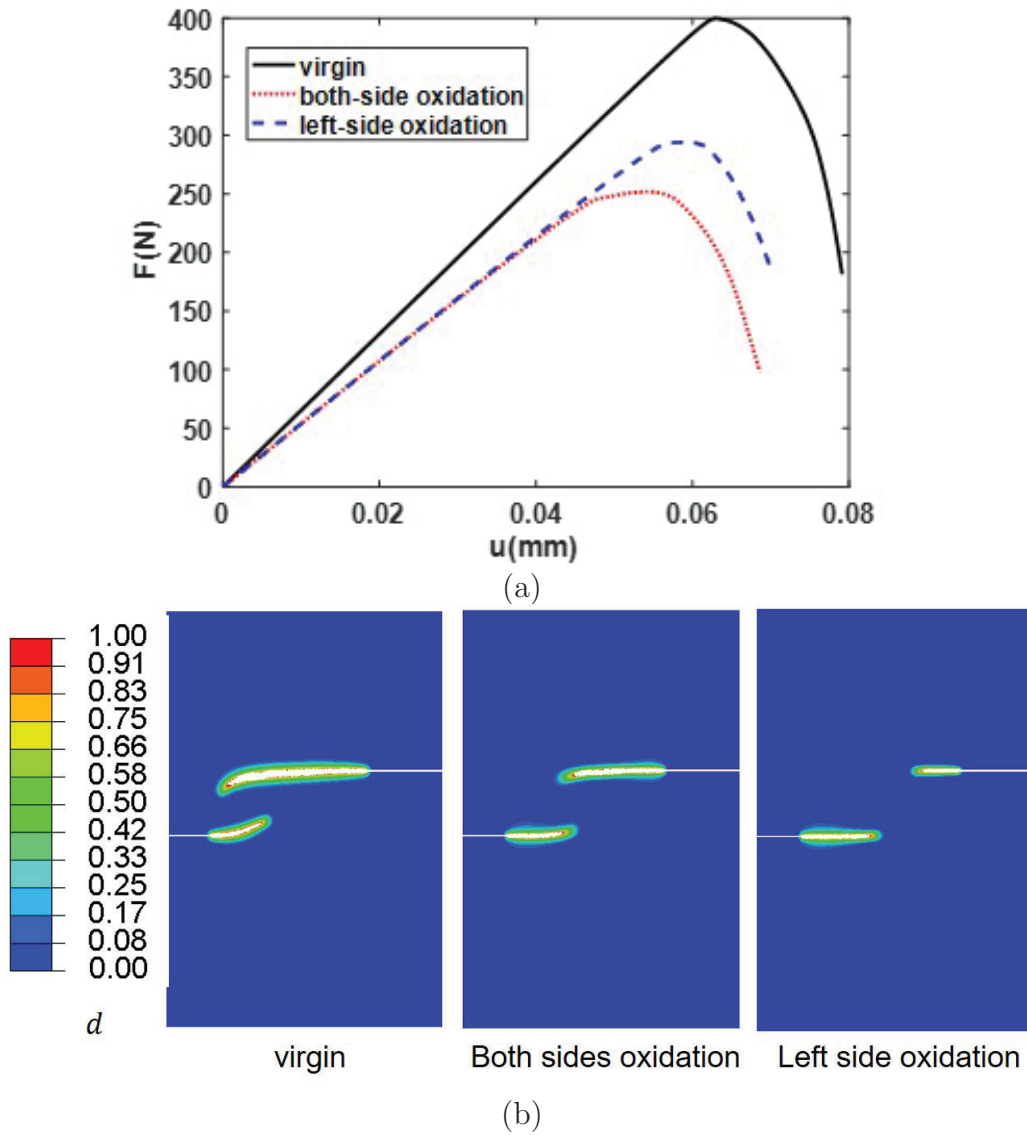


Figure 2.15: (a) Force vs. displacement plot for the asymmetric notched specimen under different oxidation conditions; (b) the corresponding damage contours near the final failure point.

2.5 Concluding remark

In this work, we have developed a reaction-driven evolving polymer network theory coupled with phase-field fracture to model the high-temperature oxidative degradation and fracture in amorphous polymers. The proposed theory considers the closed-loop chain reaction kinetics occurring at the polymer chain level and incorporates them into the statistical mechanics based network theory to account for the network alternation and mechanical property degradation. The proposed theory is capable of quantifying and reflecting the network level changes in the polymer via the active and dissociated chain ratios; both of which evolve as a function of oxidative crosslinking and chain scission. Upon establishing a seamless connection between the micro and macro-scale kinematics, the continuum level constitutive response of the material is further derived. In addition, we have used a continuum level phase-field fracture theory to model the macroscopic damage originating due to the heterogeneous stress distribution in the material under prolonged oxidation. We further tested the capability of the proposed model by numerically implementing it in a commercial FE-setting and performing several important case studies.

Chapter 3

A homogenized large deformation constitutive model for thermo-oxidation in fiber-reinforced polymers

3.1 Introduction

Long-term durability and the use of polymer matrix composites at elevated temperatures are limited by their susceptibility to thermo-oxidative degradation. Thermo-oxidation in PMCs is a type of aging process, where the polymer matrix reacts with

atmospheric oxygen, at a temperature close to or above the glass transition temperature (T_g) [57, 63, 64], causing significant degradation in mechanical performance and long term durability. The chemical reactions at high temperature in the presence of oxygen cause mass and density variations and irreversible shrinkage strains responsible for residual stress in the PMCs. Other effects of thermo-oxidation consist of a substantial change in local mechanical properties, fiber-matrix debonding, matrix microcracking etc.

The basic oxidation mechanism in polymer matrix has been widely investigated in the recent literature both from an experimental and modeling point of view, as [22, 59, 62, 63, 102, 104, 143, 175, 200, 240, 241]. However, the presence of fibers in the composites results in complicated interaction between the composite's microstructures and the multiphysics character of the matrix's thermo-oxidation process involving diffusion, chemical reactions and thermomechanics. When carbon/glass fiber PMC is concerned, since the fibers are reasonably inert to oxidation, the degradation effects concern the polymer matrix only [58, 63, 201, 241]. Incorporation of the fibers results in directional dependencies (anisotropy) in the oxygen diffusion, chemical reactions and further the shrinkage strains in the composites. Recent studies have focused on carbon-epoxy systems, to address the effect of the fiber reinforcement on the oxidative degradation of the composites across different length scales [68, 174] and for various composite's microstructure [273]. The visible effect of oxidation in the composites in the form of a growing oxide layer (few microns in size) on the outer surface of a

specimen has been characterized by microscopic measurements [172, 200, 256]. The formation of the degraded oxide layer is further accompanied by a local gradient in the mechanical properties within this layer. To characterize and quantify the extent of oxidation, measurements of local elastic indentation modulus, shrinkage strain etc. have been extensively used for polymers and PMCs, cf. [55, 102, 103, 104, 193, 256].

The oxidation-induced anisotropic degradation in PMC was first reported by [188], where a dominant degradation was observed in graphite/polyimides composite at the surface perpendicular to the fiber. The presence of a much thicker oxide layer along the fiber direction was also experimentally observed by [224]. Though the fibers are mostly inert to chemical reactions, their presence introduces additional factors such as, orientation of the fibers [200, 202, 224, 241], fiber volume fraction [102, 103], sizing of the fiber [251], stacking sequence [202] etc., to influence the diffusion-reaction process in thermo-oxidation. The anisotropic effect in oxidation as driven by the preferential diffusion of oxygen along the fiber direction— reported to be 8 to 10 times higher compared to the perpendicular direction [40, 184, 200, 202, 241]. This preferential diffusion promotes heterogeneous rates in the chemical reactions, and thus the resulting shrinkage strain is also much higher along the fiber path [224, 241]. By using experimental technique such as, interferometric microscopy, experiments have been performed to measure these shrinkage strains and damage development. In [256], it was shown for a unidirectional IM7/977 – 2 carbon-epoxy composite systems, matrix shrinkage between fibers increases with aging time and the value is significantly

higher in the resin rich zones. Since the fibers do not deform with aging, they constrain the development of matrix resin shrinkage-which is more visible in the resin-rich zones. Similar experiments are also done by [102] on a HTS/TACTIX carbon-epoxy composite to measure the surface shrinkage strain (microscopic) and compare the values with virgin samples and at different values of oxygen partial pressure. Their study showed a significant effect of fibers arrangement and volume fraction on matrix shrinkage development. In [148, 202], a comprehensive experimental effort has been detailed on characterizing thermo-oxidation in laminated and woven carbon-fiber polyimide composites, to understand the influence of ply layup, laminate architecture and thickness.

In addition to the experimental efforts, various modeling frameworks to describe thermo-oxidation in PMCs have also been reported in the literature. Incorporating the anisotropy in oxygen diffusion in the fiber and fiber-matrix interphases, modeling route has been provided by [200, 202] to simulate oxidation in PMCs. The stiffness changes due to oxidation as well as shrinkage strains are also modeled explicitly in their study. Based on the thermodynamics of irreversible process, in [104], a theory and numerical implementation has been presented to model thermo-oxidation induced shrinkage strains, stresses in polymer composites and compared with experiments in good agreement. The existing modeling efforts are limited in terms of incorporating the interaction between the composite microstructures (fiber direction, volume fraction) and the coupled nature of the oxidation process involving reaction, diffusion

and thermo-mechanics.

In this work, we present a novel continuum-scale homogenized constitutive theory to model the anisotropic diffusion, chemical reactions and a preferential oxide layer growth in a fiber reinforced polymer matrix composite. Based on an existing multiphysics model for the bulk polymer oxidation [143], the present homogenization incorporates the effect of fiber in the composites for predicting the thermo-oxidation behavior in fiber-reinforced PMCs. In the proposed framework, the composite RVE is modeled as a mixture of fibers and isotropic matrix, where the fibers are characterized by their orientations and respective volume fractions. The oxygen diffusion, and the resulting shrinkage strain developed due to the chemical reactions are considered as anisotropic, being dominant along the fiber direction. In addition, a heterogeneous RVE consisting of the fibers and matrix separately is also considered to simulate the anisotropic diffusion and reactions. The models are numerically implemented by writing user-element subroutines (UEL) in Abaqus/Standard [1] and various numerical simulations are performed in 2-D and 3-D to elucidate the effect of fibers in the composite's thermo-oxidation process. It is important to note that the oxidative aging can occur along the fiber/matrix interfaces, causing delamination. However the present homogenized approach does not consider any explicit account for the interfaces. The heterogeneous model could be extended to incorporate the interfaces and a cohesive-zone type model can be used to simulate the delamination type failures combining with the present framework. It is also important to note, that the homogenized model

would be helpful to predict the effect of oxidation at the composite's component level such as lamina or panel etc. On the other hand, the heterogeneous model would demonstrate the oxidation behavior (such as local failure, matrix cracking, degradation etc.) at the composites' microscale, where the details of the microstructural features are particularly important.

3.2 Homogenized constitutive theory of oxidation in a fiber-reinforced polymer matrix composite

In this section, we present the homogenized theory of oxidation in composites that incorporates the anisotropic effect due to the presence of fibers on the oxidative constitutive response. Based on an earlier developed model for bulk polymers [143], the present formulation also considers the coupled effect between the oxygen diffusion, chemical reactions and large deformation behavior of the fiber-reinforced composite system. Since the fibers are mostly inert to chemical reactions, the oxidation reactions affect only the polymer matrix. However the kinematics of the homogenized RVE depends on the fiber arrangements and thus influences the overall response of the composite during oxidative aging.

3.2.1 Oxidation reaction kinetics and the associated state variable

Based on the kinetics of the oxidation reaction for polymers [58, 59, 60, 63], we have adopted a closed-loop chain reaction scheme in our earlier work [143]. For the sake of completeness, we present a highlight of that scheme in the following. For details the reader is referred to our previous work [143] and the references therein.

In the thermo-oxidation of polymers, the oxidative reactions consist of hydroperoxide generation and various reactants and substrate consumption phenomena. The mechanistic scheme as identified in [57, 58, 59, 60, 61, 62, 63, 64], describes different chemical species such as-POOH, PH, volatiles, O₂, P*, PO₂* and three species of inactive products being involved in the set of six reactions. The closed-loop chain reaction scheme as adopted in the present work has been provided in ??, for reference. To calculate the progression of the chemical reactions as a function of aging time, a set of thermodynamic state variables (internal variables) named as ***extent of reaction*** have been introduced in our earlier work [143]. In the present setting, we use the same set of six state variables, as extent of reactions, denoted by $\xi_n(\mathbf{x}_R, t)$; with $0 \leq \xi_n(\mathbf{x}_R, t) \leq 1$, where n is the reaction number. Hence, $\xi_n = 0$ indicates reaction n has not occurred and $\xi_n = 1$ indicates the reaction has been completed at the material point \mathbf{x}_R . Subsequently, we would be able to track the rate of change of

concentration for a reacting species or product β as, $r^\beta = \sum_n \left[\mathcal{R}_{n\beta} \dot{\xi}_n \right]$, where $\mathcal{R}_{n\beta}$ is the stoichiometric coefficient in reaction n . It is to note that r^β is measured in mol/m^3 .

Further it is also important to note that the extent of reaction can be used as an indicator of the oxidation progression in the material domain. In particular, we have used $\xi_2 \approx 1$ as an indication of complete oxidation, since the reaction kinetics suggest reaction II being a characteristic reaction for the oxidation process. Hence, by measuring the domain on which the value of ξ_2 has reached one, we have tracked the evolution of oxide layer thickness as a function of time in the bulk material, as described later. In the present study the evolution of oxide layer has not been treated as a (separate) free surface formation and thus any kind of stress or diffusion induced surface instabilities arising due to the stiffness mismatch between the bulk unoxidized material and the oxide surface has been avoided[70].

3.2.2 Kinematics-incorporating the anisotropic effect due to the fibers

Let us consider the domain of a composite representative volume element (RVE) as \mathcal{B}_R , constitutes of α different fiber families embedded into a polymer matrix. Each fiber family is represented by their volume fraction f_R^α and direction \mathbf{a}_R^α . The presence

of fiber generates anisotropy in the kinematics of the composite's deformation. We assume the fibers are chemically inert to the diffusion-reaction process and perfectly bonded with the matrix. Following the constitutive theory of highly anisotropic material [232], deformation in the fibers in a fiber-reinforced composite can be described by introducing an additional pseudo-invariant (as done previously in [24, 36, 124, 189]). Assuming the fiber family α is oriented along the direction of the unit vector \mathbf{a}_R^α , the pseudo-invariant can be defined as,

$$\mathcal{I}_4^\alpha = \mathbf{a}_R^\alpha \cdot \mathbf{C} \mathbf{a}_R^\alpha = (\lambda^\alpha)^2 \quad (3.1)$$

where, $\mathbf{C} = \mathbf{F}^T \mathbf{F}$ is the right Green-Cauchy tensor, with the deformation gradient as $\mathbf{F} = \nabla \chi$, for a continuous deformation map as, $\mathbf{x} = \chi(\mathbf{x}_R, t)$, within the domain \mathcal{B}_R ; and λ^α is the stretch of fiber α along the direction \mathbf{a}_R^α .

As mentioned in the introduction, the volatile products generated during the chemical reactions in oxidation of polymers escape the material volume creating mass loss for the material. At the same time the oxide formation results in an increase in the local density-the combined effect of which causes irreversible volumetric shrinkage in the material. As per the literature data supporting the preferential direction of oxidation along the fiber path [202, 241] in unidirectional composites, we also assume anisotropic diffusion leading to higher reaction rates along the fiber direction compared to the transverse direction. Since the oxidation reactions occur preferentially along the fiber

direction as well as the presence of fibers provide constrain to the matrix in the transverse direction, it is conceivable that the resulting shrinkage is also anisotropic in nature. Treating oxidation induced shrinkage as thermodynamically irreversible, we apply a multiplicative decomposition of the total deformation gradient, based on the large deformation theory of polymers [12] as,

$$\mathbf{F} = \mathbf{F}^e \mathbf{F}^s \quad (3.2)$$

where \mathbf{F}^e is the elastic component of the deformation gradient, and \mathbf{F}^s is the irreversible shrinkage component, which incorporates the deformation due to permanent volumetric shrinkage occurring due to the chemical reactions. We also conclude that the jacobians $J^e = \det \mathbf{F}^e$ and $J^s = \det \mathbf{F}^s$ are both greater than 0, such that \mathbf{F}^e and \mathbf{F}^s are both invertible.

Further, introducing the velocity gradient as, $\mathbf{L} = \dot{\mathbf{F}}\mathbf{F}^{-1} = \mathbf{L}^e + \mathbf{L}^s$, where \mathbf{L}^e and \mathbf{L}^s are the elastic and irreversible part of the velocity gradient, \mathbf{L}^s can be further decomposed into (\mathbf{D}^s) and the spin tensor (\mathbf{W}^s) . Assuming $\mathbf{W}^s = 0$, we can re-write $\mathbf{L}^s \equiv \mathbf{D}^s$. Considering the anisotropic effect in the shrinkage, the rate of shrinkage strain tensor can be defined as

$$\mathbf{D}^s = \dot{\xi}_2 \mathbb{S}^\alpha \quad (3.3)$$

where, an anisotropic tensor, \mathbb{S}^α is introduced as,

$$\mathbb{S}^\alpha = \beta_I^\alpha \mathbf{a}_R^\alpha \otimes \mathbf{a}_R^\alpha + \beta_{II}^\alpha (\mathbf{1} - \mathbf{a}_R^\alpha \otimes \mathbf{a}_R^\alpha) \quad (3.4)$$

where β_I and β_{II} are the scalar quantifying the magnitudes of the shrinkage in the direction of fiber (α) and perpendicular to the fiber, respectively (cf.[26, 153, 187]).

It is to be noted that $\beta_I > \beta_{II}$, as the magnitude of the volume shrinkage would be lesser in the transverse direction compared to the axial due to the constrain provided by the fibers. Further we have assumed that the shrinkage strain evolution \mathbf{D}^s is a function of the extent of reaction (II) (ξ_2). Since reaction (II) is the dominant reaction indicating the propagation of the oxidation front, it is reasonable to assume that the shrinkage strain would evolve as a function of the extent of reaction (II). However, oxidation reaction is a closed-loop chain reaction scheme; hence consideration of any other reaction would also predict similar trend of the shrinkage strain evolution.

We further define a mean shrinkage strain rate along the (fiber) direction α as,

$$\dot{\beta}^\alpha = \frac{1}{3} \text{tr} \mathbf{D}^s = \frac{\dot{\xi}_2}{3} (\beta_I^\alpha + 2\beta_{II}^\alpha) \quad (3.5)$$

Introducing the standard result of continuum mechanics as, $\dot{J}^s = J^s \text{tr} \mathbf{D}^s$, combined with Eq. 3.5, standard integration results in the volumetric shrinkage as,

$$J^s = \exp(3\beta^\alpha) \quad (3.6)$$

3.2.3 Mass balance for the diffusing and reacting species

The local mass balance equation for any species β , participating in the underlying diffusion-reaction process of thermo-oxidation, holds up as,

$$\dot{c}_R^\beta = -\text{Div} \mathbf{j}_R^\beta + \sum_n [\mathcal{R}_{n\beta} \dot{\xi}_n] \quad (3.7)$$

where \mathbf{j}_R is the diffusive flux. At the outset, we consider that oxygen is the only diffusing species and the other constituents present in the system, such as, POOH, PH and POOP only participate in the chemical reactions. Hence, we can write the following mass balance equations for the constituents involved in a standard oxidation scheme as:

$$\left\{ \begin{array}{l} \dot{c}_R^{O_2} = -\text{Div} \mathbf{j}_R^{O_2} - \dot{\xi}_2 + \dot{\xi}_6 \text{ for } O_2 \\ \dot{c}_R^{POOH} = -\dot{\xi}_{1a} + \dot{\xi}_3 \text{ for POOH} \\ \dot{c}_R^{PH} = -\dot{\xi}_3 \text{ for PH} \\ \dot{c}_R^{POOP} = \dot{\xi}_5 + \dot{\xi}_6 \text{ for POOP} \end{array} \right. \quad (3.8)$$

3.2.4 Balance of forces and moments

From standard continuum mechanics, we can write the force and momentum balance equations as:

$$\text{Div} \mathbf{T}_R + \mathbf{b}_R = \mathbf{0} \quad \text{and} \quad \mathbf{T}_R \mathbf{F}^T = \mathbf{F} \mathbf{T}_R^T \quad (3.9)$$

where \mathbf{T}_R and \mathbf{b}_R are the Piola stress and external body force, respectively in a reference body. As is standard, Piola stress is related to the symmetric Cauchy stress in the deformed body by,

$$\mathbf{T} = J^{-1} \mathbf{T}_R \mathbf{F}^T \quad (3.10)$$

3.2.4.1 Thermodynamics and the energy balance

The complete thermodynamically consistent derivation of a coupled chemo-mechanical model for polymer oxidation is presented in one of our earlier work [143] and is avoided here. We describe the thermodynamic restrictions in the present constitutive setting for a FRPMC, starting from the local form of energy balance for a

chemo-mechanically coupled system as given by,

$$\dot{\psi}_R - \mathbf{T}_R : \dot{\mathbf{F}} + \sum_{\beta} \mathbf{j}_R^{\beta} \cdot \nabla \mu^{\beta} + \sum_{\beta} \mu^{\beta} \sum_n [\mathcal{R}_{n\beta} \dot{\xi}_n] - \sum_{\beta} \mu^{\beta} \dot{c}_R^{\beta} \leq 0 \quad (3.11)$$

where ψ_R represents the free energy of the system and μ^{β} represents the chemical potential of the diffusing species. Since the stress measure \mathbf{T}_R is not symmetric, we decompose the stress-power as [also done in [143]],

$$\begin{aligned} \mathbf{T}_R : \dot{\mathbf{F}} &= \mathbf{T}_R : (\dot{\mathbf{F}}^e \mathbf{F}^s + \mathbf{F}^e \dot{\mathbf{F}}^s) \\ &= (J \mathbf{F}^{e-1} \mathbf{T} \mathbf{F}^{e-T}) : (\mathbf{F}^{eT} \dot{\mathbf{F}}^e) + (\mathbf{C}^e J \mathbf{F}^{e-1} \mathbf{T} \mathbf{F}^{e-T}) : \mathbf{L}^s \end{aligned} \quad (3.12)$$

Introducing the elastic second Piola stress as, $\mathbf{S}^e = J \mathbf{F}^{e-1} \mathbf{T} \mathbf{F}^{e-T}$, right Cauchy-Green strain tensor as $\mathbf{C}^e = \mathbf{F}^{eT} \mathbf{F}^e$, and the Mandel stress as, $\mathbf{M}^e = \mathbf{C}^e \mathbf{S}^e$, we can write the irreversible part of the stress power as,

$$\begin{aligned} \mathbf{M}^e : \mathbf{L}^s &= \mathbf{M}^e : \mathbf{D}^s \\ &= \mathbf{M}^e : \dot{\xi}_2 \mathbb{S} \\ &= \dot{\xi}_2 [\beta_I \text{tr} \mathbf{M}^e + (\beta_I - \beta_{II})(\mathbf{a}_R \cdot \mathbf{M}^e \mathbf{a}_R)] \end{aligned} \quad (3.13)$$

Then Eq. 3.11 can be finally re-written as,

$$\begin{aligned} \dot{\psi}_R - \mathbf{S}^e : \frac{1}{2} \dot{\mathbf{C}}^e - \dot{\xi}_2 [\beta_I \text{tr} \mathbf{M}^e + (\beta_I - \beta_{II}) (\mathbf{a}_R \cdot \mathbf{M}^e \mathbf{a}_R)] + \sum_{\beta} \mathbf{j}_R^{\beta} \cdot \nabla \mu^{\beta} + \sum_{\beta} \mu^{\beta} \sum_n [\mathcal{R}_{n\beta} \dot{\xi}_n] - \\ \sum_{\beta} \mu^{\beta} \dot{c}_R^{\beta} \leq 0 \quad (3.14) \end{aligned}$$

3.2.5 Basic constitutive equations

Using Eq. 3.14 and invoking the thermodynamic restrictions, we can further obtain the constitutive relations for all the processes (diffusion, mechanical deformation etc.) for a given choice of the free energy function as,

$$\psi_R = \hat{\psi}_R(\mathbf{C}^e, c_R^{\beta}, \xi_n) \quad (3.15)$$

Hence, the constitutive forms for second Piola stress and the chemical potential of species β can be obtained as,

$$\mathbf{S}^e = 2 \frac{\partial \hat{\psi}_R(\mathbf{C}^e, c_R^{\beta}, \xi_n)}{\partial \mathbf{C}^e} \quad (3.16)$$

and the chemical potential as,

$$\mu^{\beta} = \frac{\partial \hat{\psi}_R(\mathbf{C}^e, c_R^{\beta}, \xi_n)}{\partial c_R^{\beta}} \quad (3.17)$$

Additionally, we assume that the fluid flux in the reference config. obeys the following constitutive form:

$$\mathbf{j}_R^{(\beta)} = J^{-1} \hat{\mathbf{M}}^\beta(\mathbf{C}^e, c_R^\beta, \xi_n) \mathbf{F}^{-T} \nabla \mu^\beta \quad (3.18)$$

where $\hat{\mathbf{M}}^\beta$ is a mobility tensor associated with the diffusing species β . Finally, we define a dissipative-type driving force as a conjugate to the extent of reactions:

$$\mathcal{F}_n = \begin{cases} \mathcal{A}_2 + [\beta_I \text{tr} \mathbf{M}^e + (\beta_I - \beta_{II})(\mathbf{a}_R \cdot \mathbf{M}^e \mathbf{a}_R)] - \sum_\beta \mu^\beta \mathcal{R}_2, & n = 2 \\ \mathcal{A}_n - \sum_\beta \mu^\beta \mathcal{R}_n, & n \neq 2 \end{cases} \quad (3.19)$$

where \mathcal{A}_n is the chemical affinity defined as,

$$\mathcal{A}_n = - \frac{\partial \psi_R}{\partial \xi_n} \quad (3.20)$$

Assuming each individual reaction follows an Arrhenius type evolution and its progression depends on the availability of the reactants, we can define the evolution of ξ_n as,

$$\dot{\xi}_n = \hat{\xi}_n(\mathcal{F}_n, \vartheta, \xi_n, c_R^\beta) \geq 0 \text{ for } \mathcal{F}_n > 0 \text{ \& } c_R^\beta > c_R^{\beta, crit} \quad (3.21)$$

where ϑ represents the reference temperature and $c_R^{\beta, crit}$ represents the critical concentration of the species β , below which the reaction won't occur.

3.2.6 Specific constitutive form for the homogenized fiber-reinforced polymer composites

We consider the total free energy of the composite undergoing oxidation can be written as a separable form consisting of mechanical free energy, free energy for the diffusion of oxygen into polymer and free energy of the chemical reactions. Separating the mechanical free energy further into the contribution of matrix and fibers, the total mechanical free energy can be written by following the rule of mixture as,

$$\psi_R^{mech} = (1 - \sum_{\alpha} f_R^{\alpha}) \psi_{R,matrix}^{mech} + \sum_{\alpha} f_R^{\alpha} \psi_{R,fiber}^{mech} \quad (3.22)$$

where $\sum_{\alpha} f_R^{\alpha}$ is the total fiber volume fraction. For the brevity of expression, we write $f_R = \sum_{\alpha} f_R^{\alpha}$. For the free energy of the matrix, we consider the Gent hyperelastic form [99]. For the energy contribution due to fibers, we use a quadratic energy form based on the pseudo-invariant approach, as adopted by [36, 124, 187]. For the diffusion of oxygen, we use Flory-Huggin's form of free energy. Finally, for the chemical energy for the reactions, we use a quadratic free energy as a function of the extent of reaction (ξ_n). Hence, the complete expression of free energy is given as,

$$\begin{aligned}
\psi_R = & (1 - f_R) \underbrace{\left[-\frac{1}{2} G_{shear} I_m \ln \left(1 - \frac{\bar{I}_1 - 3}{I_m} \right) + J^s \frac{1}{2} K_{bulk} (\ln J^e)^2 \right]}_{\text{Mechanical energy for matrix}} + \\
& \underbrace{(1 - f_R) \left[\mu_0^{O_2} c_R^{O_2} + R \vartheta c_R^{O_2} \left[\ln \left(\frac{\Omega c_R^{O_2}}{1 + \Omega c_R^{O_2}} \right) + \chi \left(\frac{1}{1 + \Omega c_R^{O_2}} \right) \right] \right]}_{\text{Energy of diffusion}} + \\
& \underbrace{\sum_n \frac{H_n}{2} (1 - \xi_n)^2}_{\text{Chemical energy}} + \underbrace{\sum_\alpha \frac{1}{2} f_R^\alpha E^\alpha (\mathcal{I}_4^\alpha - 1)^2}_{\text{Mechanical energy for fiber}} \quad (3.23)
\end{aligned}$$

where, G_{shear} and K_{bulk} are the ground state shear and bulk modulus of the polymer matrix; $\bar{I}_1 = \text{tr} \bar{\mathbf{C}}^e$, with $\bar{\mathbf{C}}^e = J^{-2/3} \mathbf{C}^e$, being the deviatoric part of the elastic right Green-Cauchy tensor; I_m is the Gent parameter representing the limiting stretchability as $(\bar{I}_1 - 3)$. It is important to note that Gent model is capable of capturing the finite strain hardening response of the polymer chains through this I_m parameter.

In addition, H_n is the chemistry modulus (unit- J/m^3) defined as, $H_n = -2(\sum_p G^p c_R^p - \sum_r G^r c_R^r)$, where G indicates the Gibbs energy for the product p and reactant r , respectively. $\mu_0^{O_2}$ is the reference chemical potential for oxygen, R is the universal gas constant, ϑ is the temperature, χ is the dimensionless Flory-Huggin's interaction parameter, and Ω is the molar volume of oxygen (unit- L/mol). For further details about the free energies, readers are advised to refer to our earlier work [143]. Lastly, E^α is the elastic modulus of the fiber family α .

3.2.6.0.1 Cauchy stress, chemical potential and affinity:- Following the free energy the Cauchy stress can be found using Eq. 3.23, C.6 and 3.16 as,

$$\begin{aligned}
\mathbf{T} &= J^{-1}[2\mathbf{F}^e \mathbf{S}^e \mathbf{F}^e] \\
&= J^{-1}(1 - f_R) \left[G_{shear} \left(\frac{\bar{I}_1 - 3}{I_m} \right)^{-1} (\mathbf{B}_{dis})_0 + J^s K_{bulk} \ln J^e \mathbf{I} \right] \\
&\quad + J^{-1} \sum_{\alpha} 2f_R^{\alpha} E^{\alpha} (J^s)^{2/3} (\mathcal{I}_4^{\alpha} - 1) \mathbf{F}^e (\mathbf{a}_R \otimes \mathbf{a}_R) \mathbf{F}^{eT}
\end{aligned} \tag{3.24}$$

where $(\mathbf{B}_{dis})_0$ is the deviatoric part of the left Green Cauchy tensor, \mathbf{B}^e .

Chemical potential driving the diffusion of O_2 , μ^{O_2} , can be obtained from Eq. 3.23 and 3.17 as,

$$\mu^{O_2} = (1 - f_R) \left[\mu_0^{O_2} + R\vartheta \left(\ln \left(\frac{\Omega c_R^{O_2}}{1 + \Omega c_R^{O_2}} \right) + \frac{1}{1 + \Omega c_R^{O_2}} + \chi \left(\frac{1}{1 + \Omega c_R^{O_2}} \right)^2 \right) \right] \tag{3.25}$$

It is important to note that we have assumed the diffusion and mechanical deformation as uncoupled in the present setting. This assumption is realistic considering the diffused oxygen molecules are extremely small compared to the long chain polymers. Hence diffusion of oxygen does not influence the polymer's deformation. In addition, the chemical reactions occur at a much faster rate than the diffusion. Hence any diffused molecule instantly gets consumed by the reactions. Thus the diffused oxygen

does not affect the deformation of the matrix, but the chemical reactions does through the shrinkage behavior, as described earlier.

Finally, the affinity of any reaction n can be calculated from Eq. 3.20 and 3.23 as,

$$\mathcal{A}_n = H_n(1 - \xi_n) \quad (3.26)$$

3.2.6.0.2 Evolution of extent of reaction ξ_n :- Based on our earlier work [143], we choose a thermally activated Arrhenius type relation for the evolution of extent of reaction $\dot{\xi}_n$ as,

$$\dot{\xi}_n = \begin{cases} k_n \exp\left(\frac{-Q_{act}^n}{R\vartheta}\right) \mathcal{F}_n, & \text{when } \mathcal{F}_n > 0 \text{ and } \xi_n < 1 \\ 0, & \text{otherwise} \end{cases} \quad (3.27)$$

where, k_n is the pre-exponential rate constant for reaction n and has an unit of $\frac{1}{MPa-s}$,

Q_{act}^n is the activation energy for reaction n .

3.2.6.0.3 Oxidation dependent shear modulus, diffusivity and stretchability:- As evident in the polymer oxidation literature, prolonged oxidation leads to an increase in the modulus and diffusivity of the polymer matrix [102, 103, 104, 240, 241].

In the present work, we assume a linear dependence of shear modulus, diffusivity and stretchability as a function of extent of reaction (II), ξ_2 based on our earlier proposition for polymer oxidation [143]. We define,

$$\begin{aligned}
G(\xi_2) &= (1 - \xi_2)G_{un} + \xi_2 G_{ox} \\
D_m(\xi_2) &= (1 - \xi_2)D_{un} + \xi_2 D_{ox} \\
I_m(\xi_2) &= (1 - \xi_2)I_{un} + \xi_2 I_{ox}
\end{aligned} \tag{3.28}$$

where G_{un} and G_{ox} corresponds to the shear modulus of unoxidized and completely oxidized polymer. Similarly, D_{un} and D_{ox} indicate the diffusivity of oxygen in the unoxidized polymer and in the oxide layer, respectively and D_m is the diffusivity of the polymer matrix. I_{un} and I_{ox} are the stretchability of the virgin and oxidized polymer, respectively.

3.2.7 Governing differential equations for the coupled diffusion-reaction-mechanical system

There are two governing partial differential equations required to be solved in the oxidation phenomenon:

$$\begin{cases} \text{Div} \mathbf{T}_R + \mathbf{b}_R = \mathbf{0} \\ \dot{c}_R^{O_2} = -\text{Div} \mathbf{j}_R^{O_2} - \dot{\xi}_2 + \dot{\xi}_6 \end{cases} \quad (3.29)$$

We require the initial and boundary conditions to complete the solutions of these differential equations. Let, S_1 and S_2 are complementary subsurfaces of the boundary ∂B_R of a reference body B_R such that $S_1 \cup S_2 = \partial B_R$ and $S_1 \cap S_2 = \emptyset$. Similarly, let S_{c_R} and S_{j_R} are complementary subsurfaces of the boundary $\partial B_R = S_{c_R} \cup S_{j_R}$ with $S_{c_R} \cap S_{j_R} = \emptyset$. For a time interval $t \in [0, T]$, two boundary conditions can be described such that displacement is known on S_1 and traction on S_2 . Thus, we can write,

$$\begin{aligned} \chi &= \check{\chi} \text{ on } S_1 \forall t \in [0, T] \\ \mathbf{T}_R \mathbf{n}_R &= \check{\mathbf{t}}_R \text{ on } S_2 \forall t \in [0, T] \end{aligned} \quad (3.30)$$

Similarly, another pair of boundary condition can be considered for a time interval

$t \in [0, T]$ such that oxygen concentration is known on S_{c_R} and oxygen flux on S_{j_R} and thus,

$$\begin{aligned} c_R^{O_2} &= \check{c}_R \text{ on } S_{c_R} \quad \forall t \in [0, T] \\ -D(\nabla c_R^{O_2}) \cdot \mathbf{n}_R &= \check{j}_R \text{ on } S_{j_R} \quad \forall t \in [0, T] \end{aligned} \quad (3.31)$$

The initial conditions are,

$$\chi(\mathbf{X}, 0) = \chi_0(\mathbf{X}), \text{ and } c_R^{(O_2)}(\mathbf{X}, 0) = c_{R_0}(\mathbf{X}) \text{ in } B_R. \quad (3.32)$$

Thus the coupled set of equations, Eq. 3.29 together with 3.30, 3.31 and 3.32 pose an initial boundary value problem to be solved for the displacement $\chi(\mathbf{X}, t)$ and concentration $c_R(\mathbf{X}, t)$ simultaneously. In addition, there would be a set of ordinary differential equations to solve for the mass balance and evolution equations for the state variables. The proposed model has been implemented in general purpose finite element code Abaqus [1] by writing a user element subroutine (UEL) to solve this coupled system of equations.

3.3 Representative numerical simulations

In this section, we present various numerical simulations for fiber-reinforced polymer composites undergoing oxidation using the proposed homogenized model. For a detailed comparison, the results obtained from the homogenized model are juxtaposed with a heterogeneous modeling framework considering the fiber and matrix as separate constituent materials. In this heterogeneous model, the fibers are considered as linear elastic and impermeable. Further the fiber acts as inert with respect to the oxidation reaction, while the polymer matrix is modeled as a large deformation strain hardening material participating in the oxygen diffusion and the chemical reactions (same as the homogenized model). We demonstrate the capability of the proposed model by performing numerical simulations in both two dimensional and three-dimensional settings. We predicted the important characteristics of the thermo-oxidative aging process in FRPMCs such as the formation of heterogeneous oxide layer as a function of fiber orientation, anisotropic distribution of shrinkage strains, effect of fiber volume fractions etc. The material parameters such as elastic modulus, poisson's ratio, etc., are chosen for a HTS/TACTIX carbon-epoxy composite as reported in [102]. The solubility and diffusivity parameters of epoxy are taken from [79]. The mechanical properties of the representative fiber-matrix composites samples are reported in Table 3.1. For other kinetic constants related to the diffusion and chemical reactions, we use the parameters reported in our earlier work as given in Table 1.1, [143]. The

choice of the reaction kinetic parameters for a generic polymer system is considered acceptable to model the carbon fiber-reinforced composite system, as it is expected to only affect the magnitude of the oxidation rates without altering the underlying physics. Based on the experimental data provided by [202, 224], we assume the oxygen diffusivity to be ten times higher along the fiber direction compared to the transverse direction. It is to be noted that, the consistent experimental data was not available in the literature to calibrate the reaction kinetic parameters for a specific polymer matrix composite system. Hence, in the present work, we restrict ourselves with a qualitative comparison between the model predictions and the experimental data. In the following, case studies are done to explore -

† variation in oxide layer growth along the fiber direction compared to the transverse direction in 2-D and 3-D composite RVE.

† effect of fiber volume fraction on the oxidation rate and shrinkage strain evolution in the RVE.

† oxidative aging in a composite bracket containing two different fiber families aligned in mutually perpendicular directions.

3.3.0.0.1 Case study 1-2-D unidirectional fiber-reinforced composite RVE undergoing isothermal oxidation:- In this simulation we consider a 2-D fiber-reinforced polymer matrix composite RVE undergoing isothermal oxidative

Matrix	K_{bulk}	2395 MPa [103]
	G_{un}	850 MPa [103]
	G_{ox}	1000 MPa
	I_m	3
Fiber	E^α	230 GPa
	ν^α	0.3
Shrinkage	β_I	-0.05
	β_{II}	-0.005

Table 3.1

Material parameters for a representative fiber-reinforced composite undergoing oxidation

aging. The block has a dimension of $1 \text{ mm} \times 1 \text{ mm}$, in which cylindrical fibers of 0.2 mm diameter are embedded along the vertical direction (unit vector \mathbf{e}_2), as shown in Fig. 3.1(a). The RVE consists of a fiber volume fraction of 0.4. The corresponding homogenized model is shown in the right of Fig. 3.1(a). For the mechanical boundary condition, we consider symmetry along 1 and 2 direction for the left and bottom edges, respectively. The other two sides are left free. For the chemical boundary condition, we consider as oxygen flowing from the right and top side of the sample, while the other two sides are impermeable. The chemical boundary in terms of the oxygen concentration is applied in a ramp-like manner on the respective surfaces, as shown in Fig. 3.1(c). In what follows, by maintaining the constant atmospheric pressure on the pertinent edges a concentration of $5 \times 10^{-4} \text{ mol/L}$ as absorbed oxygen is obtained on the surface. It is to be noted that to compute oxygen adsorption on the surface, Henry's law of solubility is used [79]. For the present study, we assume $D_2 = 10 D_1$, where $D_1 = D_m$ is the diffusivity of oxygen in bulk epoxy as listed in Table 1.1. We take the initial resin concentration as, $c_0^{PH*} = (1 - f_R) c_0^{PH}$, where c_0^{PH} is the available resin concentration in the RVE without the presence of fibers. The

sample is then oxidized at 150°C for several hours and examined to study the effect of fiber presence in the RVE through the course of oxidation.

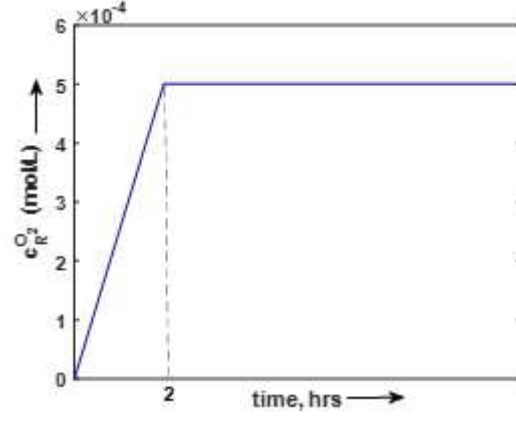
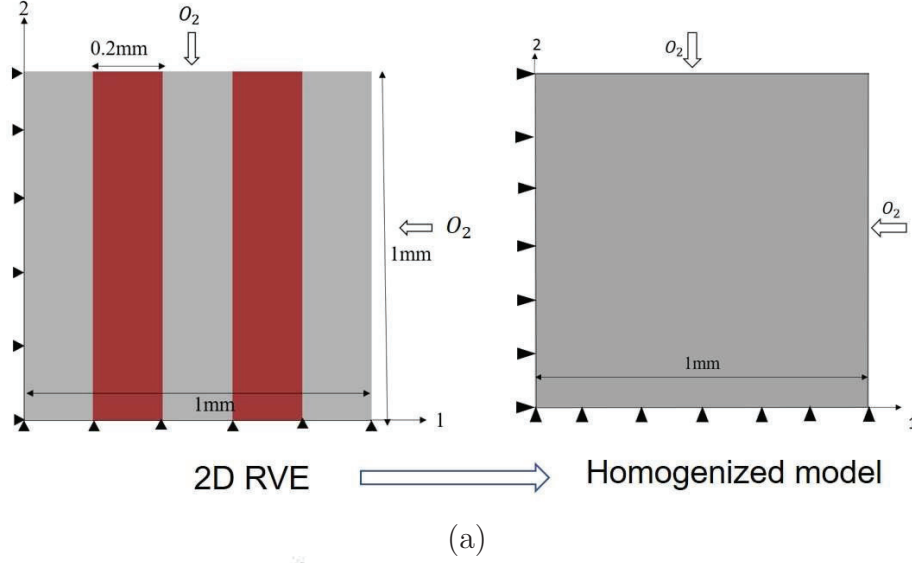


Figure 3.1: Geometry and boundary conditions for 2D unidirectional composite RVE: (a) (left) Heterogeneous RVE showing fibers and polymer matrix; (right) corresponding homogenized 2D version; (b) chemical boundary condition for oxygen concentration.

Fig. 3.2 shows the comparison of contour plots for the extent of reaction (II), volumetric shrinkage (J^s) and von-mises stress (σ_{eq}) after 80 hours of oxidation for heterogeneous (left) and homogenized (right) model predictions. As seen in Fig. 3.2

(a.) both the heterogeneous and homogenized models predict very similar profile for extent of oxidation. After 80 hours of oxidation, ξ_2 reaches to a value of 0.545 on the outermost surfaces. However, the top surface grows a thicker oxide zone compared to the right edge, as the fibers are aligned along the vertical direction. Since the oxygen diffusion along the fiber direction is faster than the transverse direction, the extent of oxidation is also faster along the fiber direction. A very similar behavior is also observed in the case of the volumetric shrinkage and Von Mises stress evolution. Higher extent of oxidation on the top and right surfaces results in higher volumetric shrinkage and equivalent stress on the respective areas, while the RVE core stays almost unaffected. We observe a maximum J^s of 0.968 on the oxidized surfaces, indicating an average volumetric shrinkage of 4.2% (as seen in Fig. 3.2(b)) generating an average stress of 45 MPa on these elements (Fig. 3.2(c)). It is to be noted that the volumetric shrinkage and the resulting stresses generated during oxidation is considered as permanent due to the irreversible nature of the chemical reactions. Hence these stresses would remain in the RVE as residual stresses even after the oxidative aging is completed. It is important to note that, while the magnitudes of the plots from both heterogeneous and homogenized models are same, there is a slight variation in their respective profiles, as evident from Fig. 3.2. This is expected as the fibers and the matrix are modelled as separate constituents in the heterogeneous case considering the fibers as linearly elastic and chemically inert. These variation in the fiber-matrix properties would influence the output quantities along the interfaces,

as observed in the ξ_2 and J^s plots. On the other hand, in case of the homogenized model fiber and matrix are considered in an average (smeared) sense with the fiber volume fraction as a parameter. Accordingly, the results obtained from the homogenized model do not have the precise information about the presence of interfaces. The difference in the contours is more prominent in the Von-Mises stress plots, as shown in Fig. 3.2(c). Since in the case of heterogeneous model, we assumed fibers are much stiffer and perfectly bonded to the matrix, it acts like a constrained boundary at the fiber-matrix junction (interface) causing a local stress gradient. On the other hand, the homogenized model predicts a smeared stress distribution without the influence of the fiber-matrix property difference along the interfaces.

It is important to note that there could be stresses generating within the domain due to the mismatch in thermal co-efficient between the fibers and matrix as proportional to $(\alpha_f - \alpha_m)\Delta\theta$; where α 's represent the thermal expansion coefficient of the constituents and $\Delta\theta$ represents the temperature difference. However, based on the literature data assuming the composite's thermal expansion coefficient being nearly zero, this stresses has been neglected in the present simulation [75]. Further, the present formulation considers an isothermal oxidative aging; hence the temperature fluctuation wouldn't occur during the aging process.

3.3.0.0.2 Comparison between axial and transverse oxide layer growth in unidirectional RVE:- We continue to oxidize the 2D unidirectional fiber reinforced

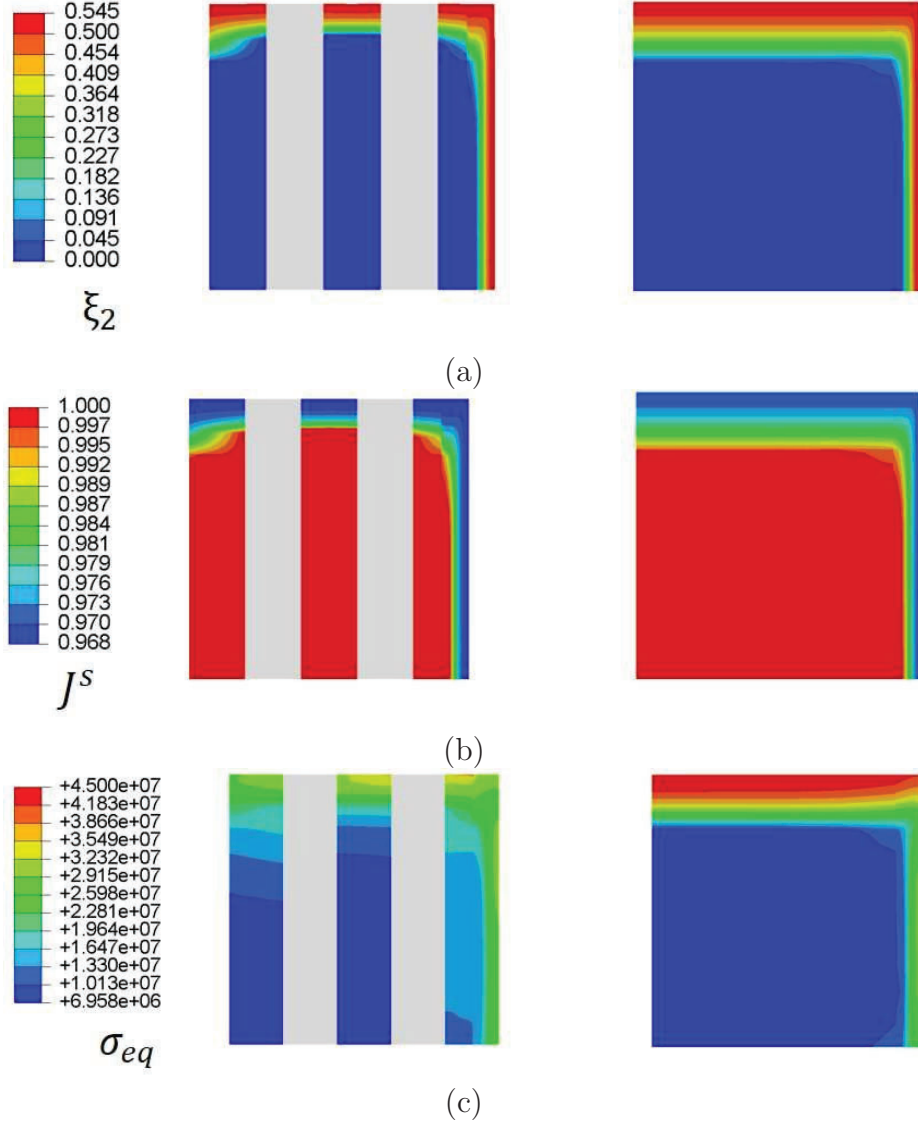


Figure 3.2: Contour plots for the -(a) extent of reaction (II); (b) shrinkage strain and (c) Von-mises stress after 80 hours of oxidation; the left figures correspond to the heterogeneous model while the right figures represent the results from the corresponding homogenized model.

sample as considered earlier for 1000 hours at $150^{\circ}C$ and compare the oxide layer thickness formed along the direction of the fibers (axial) with the same in transverse direction. We assume that a value of $\xi_2 > 0.95$ represents the complete oxidation of that material points. For a qualitative comparison, we present the simulation results

together with the experimental data as reported by [202, 224] on G30-500/PMR-15 Fig. 3.3 shows the oxide layer thickness normalized against the maximum oxide layer formed at the end of 1000 hrs, along the axial (\mathbf{e}_2 in the Fig. 3.1) and the transverse directions. As shown by the solid lines in Fig. 3.3, the oxide layer thickness is much higher along the fiber direction, compared to the transverse direction. This observation is also consistent with the experimental data [202, 224], represented by the dashed lines. As mentioned earlier, in the present study our objective is to compare the qualitative trends between the rate of oxidation along the axial and transverse directions of the fibers. To predict the accurate quantitative growth of oxide layer, the diffusivity, solubility and kinetic parameters pertinent to PMR-15 resin used in the experiment would be required. Due to the non-availability of consistent data for PMR-15, we have used the data for a generic polymer system for which we had the chemistry of reactions known in details as given in Table 1.1. However, it is expected that as the matrix molecular structure changes these reactive and diffusivity parameters would change and hence the model prediction differs quantitatively from the experiments in the present case study.

3.3.0.0.3 Extent of oxidation in composites as a function of fiber volume

fraction:- In this simulation, we vary the fiber volume fraction to study its effect on the oxidative aging in fiber-reinforced PMCs using the homogenized model. The geometry and the boundary conditions for the RVE are considered to be the same

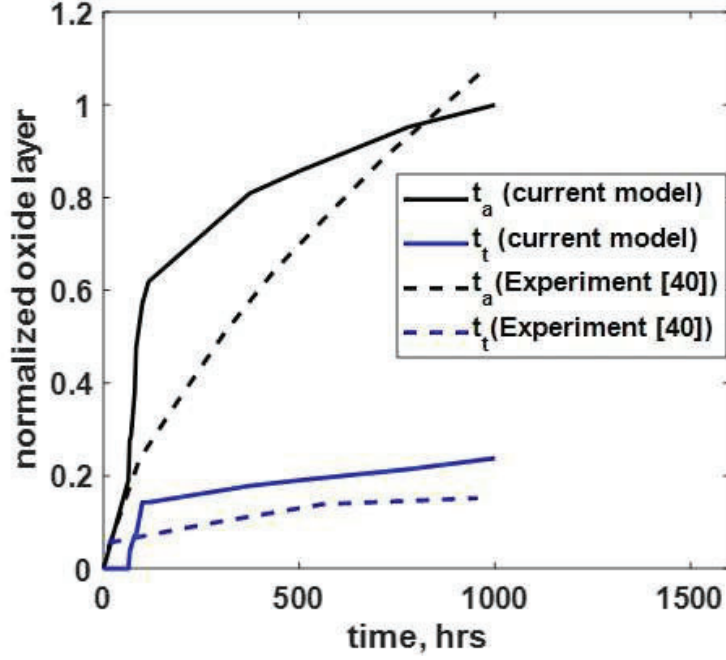


Figure 3.3: Anisotropic growth of the oxide layer in a typical unidirectional fiber-reinforced PMC as a function of time:- t_a corresponds to the normalized oxide layer along the axial direction; t_t denotes the normalized oxide layer in the transverse direction, respectively.

as given in Fig. 3.1. We consider three different volume fractions for the fiber as $f_R = \{0.1, 0.3, 0.5\}$. In what follows, we oxidize the specimen for 100 hours at 150°C at atmospheric air. Fig. 3.4(a) shows the contour plots for the extent of reaction (II) for the three different fiber volume fractions. We observe a decrease in the extent of oxidation as the fiber volume fraction increases. It is seen that ξ_2 has a maximum value of 0.936 for $f_R = 0.1$, whereas it reaches to 0.4 for $f_R = 0.5$, while keeping the aging time and temperature same for both the cases. The corresponding volumetric shrinkage and equivalent stress contours are shown in Fig. 3.4(b) and (c), respectively. The stress and strain plots also corroborate similar findings observed in Fig. 3.4(a), as

the magnitudes drop in both cases as a function of increasing fiber volume fraction. As the fiber volume fraction increases, the available matrix participating in the oxidation reactions reduces, and the effect of oxidative aging goes down as observed in this set of results. It is important to note that in the present formulation the diffusivity

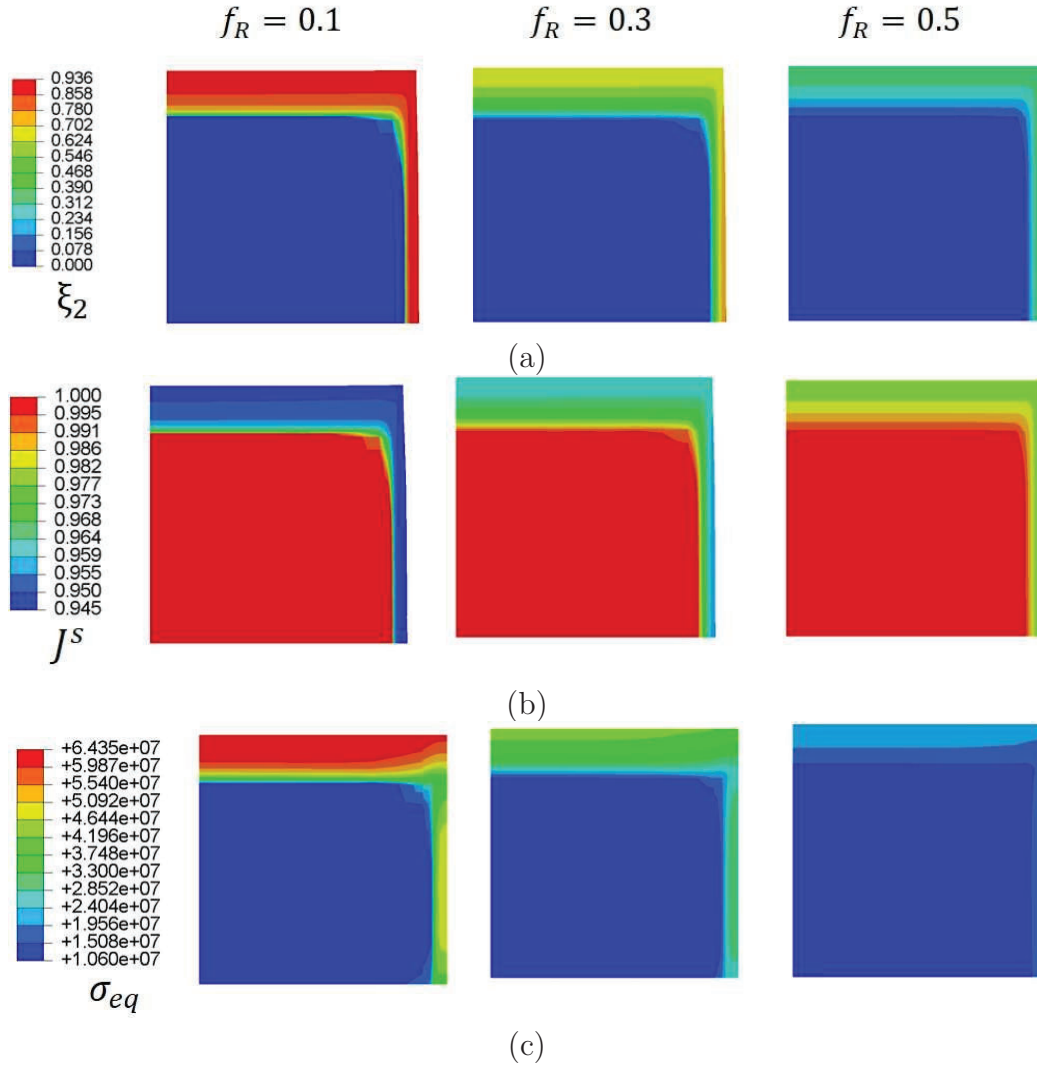


Figure 3.4: Effect of fiber volume fraction on the FRPMC oxidized at $150^{\circ}C$ for 100 hrs- contour plots of (a) extent of reaction (II), ξ_2 ; (b) volume shrinkage, J^s ; and (c) Von-Mises stress.

matrix has been assumed as diagonal. Thus assuming two orthogonal networks of

fibers in the 2D RVE as considered in the present case study, with the fibers being aligned along 1 and 2 directions, respectively, one could anticipate an isotropic nature of diffusion followed by identical growth of oxide layer and the resulting stresses along 1 and 2. However, in reality two orthogonal network of fibers may introduce non-zero off-diagonal coefficients in the diffusivity matrix, resulting into non-isotropic diffusion and heterogeneous oxidation reactions. In such cases these off-diagonal values would be estimated by analyzing the fiber architectures in detail.

3.3.0.0.4 Comparison of shrinkage strain evolution with experiments as a

function of fiber volume fraction:- In the previous case study, we demonstrated that shrinkage strain decreases with increasing fiber volume fraction in a composite RVE. This particular finding can be used to correlate with the local shrinkage development in a FRPMC undergoing thermal oxidation. In this context, we refer to the experimental study on HTS/TACTIX carbon/epoxy composite, where shrinkage strains were measured by the interferometric microscopy reported by [102]. In this study, the fibers were randomly distributed unidirectionally in the specimen, resulting in non-uniform local shrinkage with Zone A having the highest density of fibers, followed by zone B, C and D, respectively. The density of the fibers were characterized by the relative spacing between the fibers in these zones. The authors found out that shrinkage is more prominent in the less fiber dense zones of the composite microstructure. In order to simulate a similar phenomenon, we have considered a

2D homogenized RVE with a given dimension, where the fiber volume fractions are used to control the spacing between the fibers. In what follows, we found $f_R = 0.66$ represents the zone A, 0.33 for zone B, 0.22 for zone C and 0.165 for zone D, respectively. Next, we simulate the RVEs to oxidize at $150^\circ C$ under 2 bar of oxygen pressure for 42 hours and compare the shrinkage developed in these 4 zones. The simulation parameters are taken from Table 3.1 and Table 1.1, as before. The normalized shrinkage values computed as $(\frac{J^s}{J_{max}^s})$; where J_{max}^s is the maximum shrinkage obtained in the simulations corresponding to the zone D, are plotted in Fig. 3.5 and compared with the experimental (normalized in the same way) data as observed by [102]. The results show a good agreement with the experiment at lower f_R values or larger fiber spacing, but deviates at higher f_R . Once again, the prediction could possibly be improved by choosing the kinetic parameters specific to the epoxy resin for the composite used in the experiment. Thus, the present homogenized approach qualitatively predicts the oxidation mechanism in FRP composites.

3.3.0.0.5 Case study 2-oxidation in a unidirectional 3-D composite RVE:-

In order to further explore the capability of the proposed model, we perform numerical simulation considering a 3-D composite RVE. The geometry of the 3-D composite RVE is shown in Fig. 3.6. The left image shows the heterogeneous RVE and the right image represents the corresponding homogenized model. The fibers are indicated with the red circles, consisting a volume fraction of 0.3 and their orientation is along

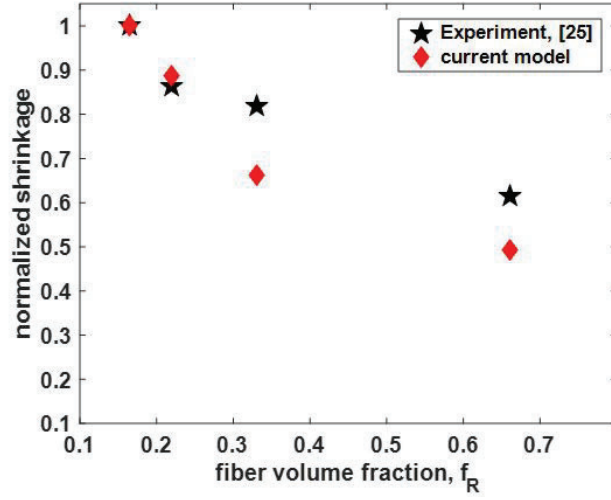


Figure 3.5: Effect of fiber volume fraction (or the fiber spacing) on the residual shrinkage generated in the FRPMC – normalized oxidative shrinkage plotted as a function of fiber volume fraction.

3-3 direction (denoted by the unit vector \mathbf{e}_3). For the diffusion boundary condition, oxygen is allowed to flow from the top and front surface of the specimen with all the other sides assumed as impermeable. For the mechanical boundary conditions the back surface is considered fixed in all degrees of freedom. We let the specimen to oxidize for 80 hours at 150°C in atmospheric air. To incorporate the anisotropic diffusion due to the presence of fibers the diffusivity is considered as a tensor given by,

$$\mathbf{D} = \begin{bmatrix} D_m & 0 & 0 \\ 0 & D_m & 0 \\ 0 & 0 & 10 D_m \end{bmatrix}$$

Simulation results are compared for the heterogeneous and homogenized model. Fig. 3.7(a) represents the contour plots for the extent of reaction (II) after 80 hours of oxidation. Qualitatively, both heterogeneous (left) and homogenized (right) model

predict the similar extent of reaction profile. Along \mathbf{e}_3 *i.e.* the fiber direction, the oxidized zone is more prominent compared to the transverse direction, which in turn, generates a wider shrinkage zone along the direction \mathbf{e}_3 , as shown in Fig. 3.7(b). Hence, the 3-D implementation of the proposed homogenized model also predicts the preferential growth of oxide layer along the fiber direction and compares well with the heterogeneous model results.

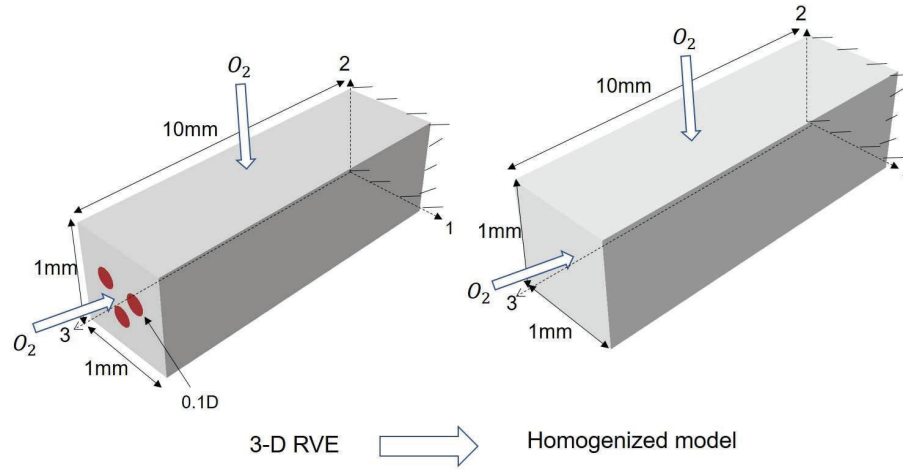


Figure 3.6: Geometry for the 3D unidirectional composite RVE:- (left) the 3-D heterogeneous RVE; (right) the corresponding homogenized model.

3.3.0.0.6 Case study 3-oxidative aging in a composite bracket with two different fiber orientations:- In this example, we simulate an *L*-shaped composite bracket containing fibers aligned in two mutually perpendicular directions using the homogenized model. The geometry and boundary conditions of the RVE are shown in Fig. 3.8. Fibers are aligned along 1-1 direction in the horizontal leg of the bracket

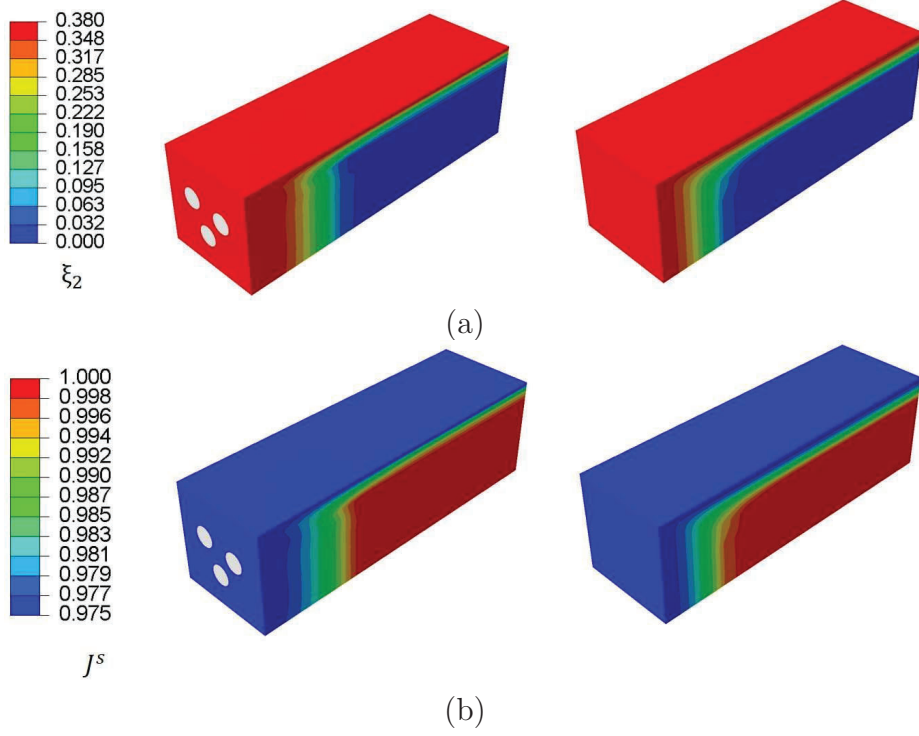


Figure 3.7: Contour plot for the (a) extent of reaction (II) (ξ_2); (b) volumetric shrinkage J^s , after 80 hrs of oxidation.

and along 2-2 for the vertical part as shown in Fig. 3.8. The two legs are assumed to be perfectly bonded at the corner. In both the legs fiber volume fraction is $f_R = 0.1$. Assuming oxygen could flow from all sides of the sample the whole bracket is considered as susceptible to oxidation. Keeping the chemical boundary conditions in terms of the O_2 concentrations as the same as used in the previous studies, we let the bracket oxidize for 100 hours and study the effect of oxidative aging in the presence of fibers. The bracket is mechanically supported at the left and right corner of the horizontal leg to prevent any rigid body motion.

Fig. 3.9(a), (b) and (c) show the contour plots of extent of reaction (II), volumetric

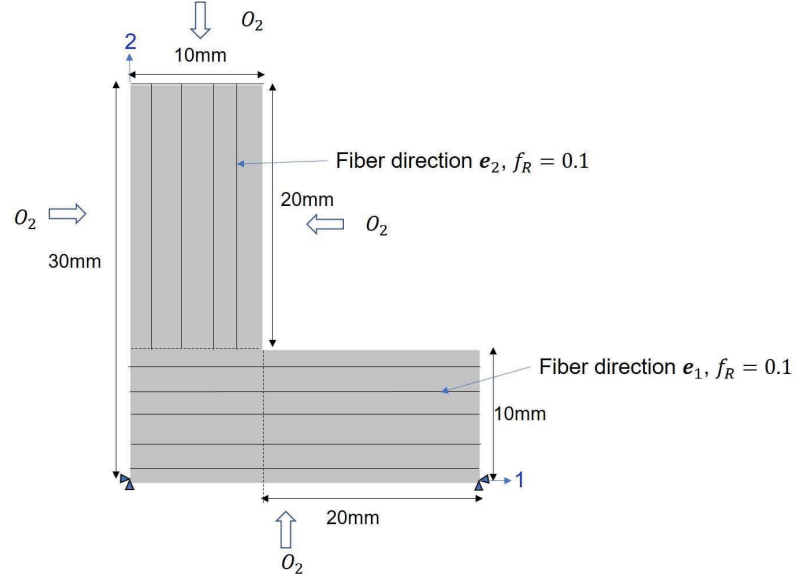


Figure 3.8: Geometry and the boundary conditions of the composite bracket.

shrinkage strain and von-mises stress, respectively. The effect of the fiber orientation in the two legs is apparently clear in these plots, as we see heterogeneous oxide layers around the surfaces and the thickness of these layers being dependent on the fiber orientation. The layer is much thicker at the top of the vertical leg, as well as at the left and right edge of the horizontal leg-further establishing the preferred oxidation direction along the fibers. This heterogeneity in oxidation causes heterogeneous shrinkage and the residual stress distribution, as seen in Fig. 3.9(b) and (c), respectively.

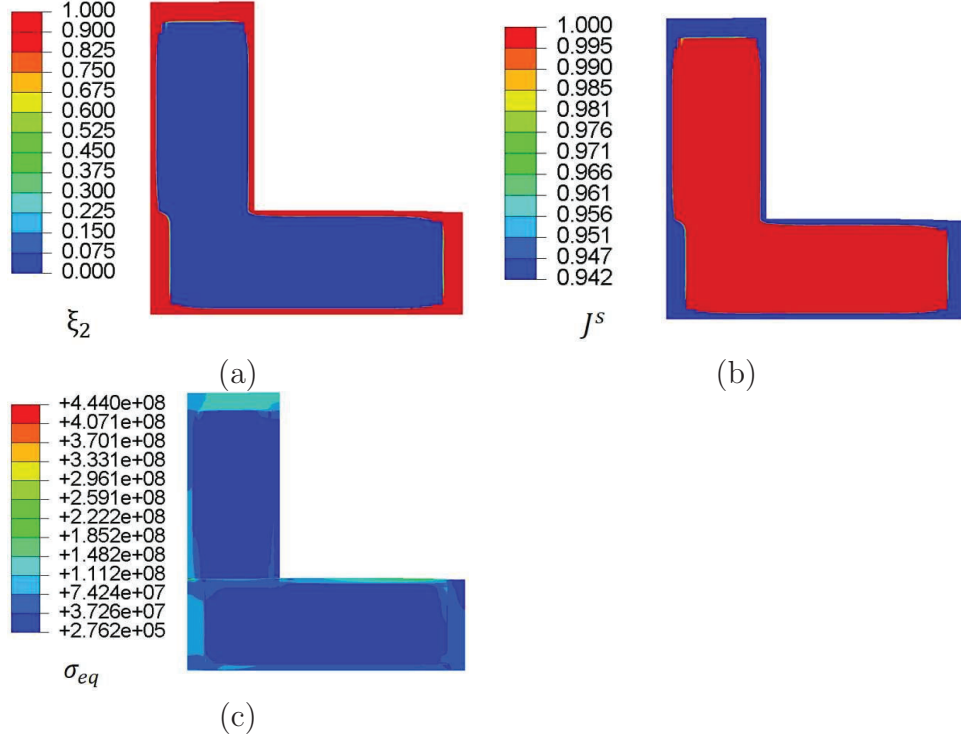


Figure 3.9: Contour plots for the (a) extent of reaction (II); (b) volumetric shrinkage; and (c) Von-mises stress after 100hrs of oxidation

3.4 Concluding remark

In this work, we investigate the effect of the presence of fibers on the oxidation of polymer matrix composite by using a thermodynamically consistent large deformation homogenized constitutive model. Incorporating the effect of anisotropy in the diffusion-reaction process due to the fibers, an existing chemo-mechanically coupled framework of polymer oxidation is modified to represent the high temperature oxidation in FRPMC in a homogenized sense. Numerical implementation of the model has been done in a finite element framework and various simulations are performed

to demonstrate the preferential oxide layer growth and the resulting heterogeneous volumetric shrinkage within the composite's RVE. This heterogeneity in the stress distribution has been identified as a major cause of failure for these materials in a thermo-oxidative environment in the existing literature. The homogenized model qualitatively agrees with the heterogeneous model predictions and captures the trend observed in the experiments. Further, the computational efficiency of the homogenized model is worth noting-as for a standard 3D RVE simulation the CPU time is several order of magnitude faster (≈ 140 times) compared to a heterogeneous simulation. In addition, for the heterogeneous model to predict results for various different volume fractions and fiber alignments, the simulation domain requires remeshing, which can be entirely avoided in the homogenized framework without altering the accuracy. In future, we aim to perform more quantitative validations of the model predictions with experiments.

Chapter 4

A unified phase-field fracture model for fiber-reinforced polymer composites

4.1 Introduction

Fiber reinforced composite materials have emerged as an effective alternative to metals-owing to their high specific strength, stiffness and better resistance against adverse environment. These materials are now being used in several fields of engineering such as aerospace, automotive, marine vessels, wind turbine blades, where the

composites undergo adverse and coupled mechanical and thermal loading causing various forms of damage. In general, fracture in a FRP composite laminate is a collection of damage events-namely matrix cracking, delamination, fiber/matrix debonding and fiber breakage. These multi-form damage events interact with each other depending on the composite's microstructure (anisotropy, fiber architecture), properties of the fiber, matrix and the interfaces, as well as characteristics of the externally applied loading. Due to the interactive nature of the damage modes the task of composite's progressive damage modeling is a complex one. It is challenging to address the significant variability in the microscopic damage mechanisms as well as the macroscale fracture response of FRPC through a predictive modeling framework.

Experimental studies on the quasi-static and damage response of these materials reveal a strong dependence on the fiber volume fraction and orientations [41, 42, 51]. At low fiber content, matrix cracking and interfacial debonding are the main damage mechanisms for FRP, while fiber pullouts and fiber breakage are the main cause of failure with increased fiber content [42]. On the other hand, off-axis fiber orientations cause a drop in the stiffness and strength of the material, showing a drastic reduction as the orientation changes from 0 to 90° [41]. For fiber orientations below 45°, increasing the fiber volume fraction improves the composite's property, while at higher angles the effect is negligible.

Additionally, the high-strain rate loading often shows an increase in the tensile

strength and modulus, and a drop in the ultimate strain in these materials- as detailed in [134] and the references therein [105, 123, 142, 194, 217, 230, 247]. However, it is important to mention that, the strain-rate effect is negligible in angled ply composites, especially at angles 45° or higher, as reported in [41, 151]. Further, the ambient temperature significantly influences the fracture behavior of FRPCs. If the matrix is in glassy stage (below T_g), stiffness and toughness could improve with increasing temperature over a short range; however closer to the glass transition temperature, the stiffness and the fracture toughness always decrease [14, 89, 90, 194, 211, 214, 259]. The high-temperature degradation of FRPCs are often explained as a consequence of polymer-matrix softening, causing the inability of the matrix to transfer load from the fiber reinforcements [89, 90, 194]. As reported in [23, 244], high-strain rates and high-temperature significantly alter the thermo-viscoelastic properties of the matrix, which in turn, influence the FRPC behavior.

The traditional strength-based models consider composites as homogeneous solids and cannot distinguish between the different failure modes [74] in the constituents. In the finite element modeling, failures within the lamina and at the interfaces are often modeled in a decoupled fashion- with the continuum damage model (CDM) or extended finite element types (XFEM) approach for fiber breakage and matrix cracking, combining with a cohesive zone model to predict delamination or debonding [160, 160, 248, 258, 268]. However, these models are computationally expensive, (often) mesh-sensitive and unable to predict complex crack propagation and mixed

failure mechanisms [207]. A more recent modeling strategy involves phase-field fracture modeling of anisotropic materials, that relies on the variational principle of energy minimization proposed by [93] and regularized by [38] for numerical implementation. The anisotropic phase-field theory has been used to model fracture in composite laminates and proven useful to predict fiber-orientation dependent crack-growth in a straight-forward manner [3, 30, 74, 207, 208, 210].

In this work, we use an experimentally informed, unified phase-field fracture theory to model progressive damage and fracture in unidirectional FRPCs based on a homogenized constitutive model incorporating the effect of fiber orientations and finite thermo-viscoelasticity of the polymer matrix. Based on the classical Ambrosio-Tortelli type (AT-2) second order phase-field model, the present theory considers an unified framework to incorporate two competing damage mechanisms namely the matrix cracking and fiber breakage for predicting unidirectional FRPCs' fracture response. We introduce a novel split in the crack-driving force calculation to distinguish between the two competing failure mechanisms finally to incorporate within an anisotropic phase-field evolution. The model is also exploited to derive the fracture behavior of the FRPC system at high ambient temperature to study the effect of thermo-viscoelasticity of the matrix. We numerically implement the proposed model in a commercial finite element package ABAQUS/Standard and establish the reliability of the model predictions by comparing with the in-house experimental data. Finally, we demonstrate the usefulness of the model by simulating few important case

studies.

4.2 Theoretical aspects of the model:-

Basic kinematics

Let us consider a continuum domain of FRPC at a reference time t_0 represented by \mathcal{B}_R with the material point (\mathbf{X}, t_0) . The body undergoes a deformation with a mapping function $\chi(\mathbf{X})$, such that $\mathbf{x} = \chi(\mathbf{X})$, where (\mathbf{x}, t) is the coordinate of the deformed body \mathcal{B} at current time t . The deformation gradient is then given by, $\mathbf{F} = \nabla \chi(\mathbf{X})$, with $J = \det \mathbf{F} > 0$. As standard, we define the left and right Green-Cauchy tensor as, $\mathbf{b} = \mathbf{F}\mathbf{F}^T$ and $\mathbf{C} = \mathbf{F}^T\mathbf{F}$, respectively.

For a weakly compressible polymer, assuming viscoelasticity effects are exclusively restricted to the isochoric part of the deformation, we can decompose the deformation gradient, \mathbf{F} into the volumetric (dilatational) and isochoric (distortional) part as [92, 125, 209, 223],

$$\mathbf{F} = \mathbf{F}_{vol} \bar{\mathbf{F}}, \text{ with } \mathbf{F}_{vol} = J^{1/3} \mathbf{I}, \quad (4.1)$$

where \mathbf{F}_{vol} is the volumetric and $\bar{\mathbf{F}}$ is the isochoric part of the deformation gradient, respectively. We consider the deviatoric part of the deformation gradient as

unimodular, such that,

$$\bar{\mathbf{F}} = J^{-1/3} \mathbf{F} \text{ with } \det \bar{\mathbf{F}} = 1 \quad (4.2)$$

Viscoelasticity in the polymer matrix

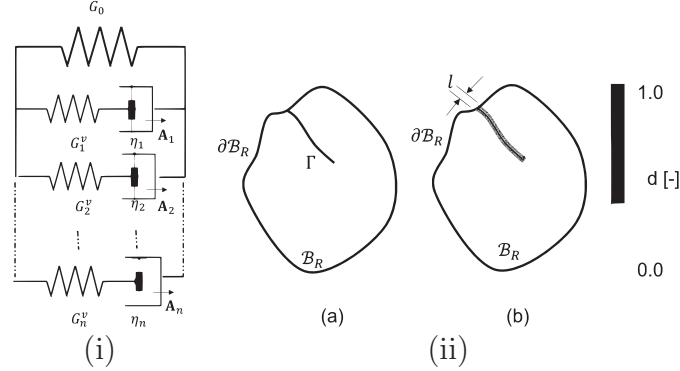


Figure 4.1: (i) Schematic representation of the finite viscoelastic model; (ii) schematic representation of the phase-field approximation of a crack in a 2-D domain: (a) Sharp crack topology and (b) regularized crack approximation over the length l .

To characterize the viscoelastic behavior of the polymer matrix, we follow the micromechanically motivated model as proposed in [152], for the finite deformation setting. Let us consider a simple rheological model as shown in Fig. 4.1(i), containing the time-independent spring with relaxed shear modulus G_0 and $k = 1, 2, \dots, n$, number of time-dependent branches represented by a series of springs and dashpots, characterized by their shear modulus G_k^v and dashpot constant η_k , respectively. The relaxation time for each Maxwell branch is calculated as, $\tau^k = G_k^v / \eta_k$. The macroscopic tensorial stretch in each branch is expressed by a series of internal variables,

$[\mathbf{A}_k, k = 1, 2, \dots, n]$. Each \mathbf{A}_k is symmetric and analogous to the isochoric symmetric strain tensor $\bar{\mathbf{C}}$. It is important to mention that, \mathbf{A}'_k s are the internal variables in the essence of a phenomenological model and are not experimentally measurable quantities. The evolution of these viscoelastic internal variables are given by [152],

$$\dot{\mathbf{A}}_k = \frac{1}{\tau_k}(\bar{\mathbf{C}}_k^{-1} - \mathbf{A}_k) \quad (4.3)$$

Eq. 4.3 can be physically interpreted as the evolution of these tensorial quantities (\mathbf{A}_k) being dependent on the difference between the viscous overstress and inverse of the isochoric right Green-Cauchy tensor. The difference diminishes as the model approaches to a fully relaxed state and the time-dependent behavior vanishes.

Kinematics for the FRPC incorporating fiber-induced anisotropy

The presence of fibers in polymer matrix composite introduces anisotropy in the deformation. In the present study of interest, fibers can deform either due to mechanical loading or due to thermal expansion. Considering that fibers do not impart any viscous response (perfectly elastic), we introduce two pseudo-invariants to account for the deformation of fibers due to mechanical loading and thermal expansion, respectively. At this stage, we consider that the body \mathcal{B}_R contains a fiber family, γ ,

characterized by the fiber volume fraction, f_R^γ and a reference direction \mathbf{a}_R^γ , such that $\mathbf{a}^\gamma = \mathbf{F}\mathbf{a}_R^\gamma$, with \mathbf{a}^γ being the fiber direction in the deformed configuration. Following the theory in [232], in a composite the deformation in fibers can be described by introducing an additional invariant as done in [24, 36, 46, 114, 115, 124, 189]. Herein, we define the first pseudo-invariant accounting for the mechanical stretch as,

$$\mathbb{I}_{4,M}^\gamma = \mathbf{a}_R^\gamma \cdot \mathbf{C}\mathbf{a}_R^\gamma = (\lambda_M^\gamma)^2 \quad (4.4)$$

where, λ_M^γ is the mechanical stretch of the fiber family γ along the direction \mathbf{a}_R^γ .

Next, we define a second pseudo-invariant to account for the deformation due to thermal expansion as,

$$\mathbb{I}_{4,\vartheta}^\gamma = (\lambda_\vartheta^\gamma)^2 \mathbf{a}_R^\gamma \cdot \mathbf{a}_R^\gamma \quad (4.5)$$

where λ_ϑ^γ is the magnitude of stretch in the fiber due to temperature rise as given by,

$$\lambda_\vartheta^\gamma = 1 + \alpha_f(\vartheta - \vartheta_0) \quad (4.6)$$

where α_f is the thermal expansion coefficient of fiber, ϑ_0 is the reference temperature and ϑ is the working temperature. It is important to note that the thermal contraction would introduce a negative stretch in the fibers, which has not been considered here. Since the focus of the present work is to study tension-dominated fracture, we consider positive stretches due to thermal expansion as, $\lambda_\vartheta^\gamma \geq 1$, only.

Phase-field description of fracture

In this section, we first present the standard phase-field fracture theory considering isotropic material. Following which, we present a modification to incorporate anisotropy imparted by the fibers in the FRPCs. In classical phase-field theory, a sharp crack Γ is approximated by the local variation of a continuous or diffusive scalar field variable, termed as phase-field (d) that smoothly varies between 0 and 1, within a zone of interest [5, 6, 169, 171]. At the center of the crack it takes a value of $d = 1$ and at the location away from the crack or undamaged region, $d = 0$, as shown in Fig. 4.1(ii). This transition from cracked to undamaged region occurs over a small zone whose width is controlled by the regularization (localization) length, l . When the length scale parameter, $l \rightarrow 0$, the phase field model converges to the Griffith's formulation of brittle fracture [93]. The theory also considers that d monotonically increases, such that $\dot{d} \geq 0$, implying the damage being irreversible. Following the standard practice in the phase-field literature, we also include ∇d to incorporate the spatial inhomogeneity arising due to damage in the form of a non-local term to overcome the mesh dependency associated with the continuum damage models. The crack surface, Γ is then approximated through a regularized crack surface density functional, γ_d , which successively converts a surface integral to a volume integral,

and one can write [5, 39],

$$\Gamma(d) = \int_{\Gamma} dA \approx \Gamma_l(d) = \int_{\mathcal{B}} \gamma_d(d, \nabla d) dV \quad (4.7)$$

For an isotropic material, a widely used regularized surface density functional is given by the well known Ambrosio-Tortelli type (AT-2) model as, [5, 46, 169, 170, 171],

$$\gamma_d(d, \nabla d) = \frac{1}{2l}(d^2 + l^2|\nabla d|^2) \quad (4.8)$$

In the case of an anisotropic material such as FRPC, the orientation of the fibers also becomes a deciding factor to evaluate the damage initiation, propagation and the direction of the crack growth. Thus, a modification in the surface density functional is required to incorporate the direction dependent crack-growth in such cases. This is often accomplished by introducing an additional structural tensor, cf., [74, 115, 182, 207, 270]. In case of an unidirectional FRPC, the intra-ply fracture mechanism changes based on the mode of loading, the fiber volume fraction and the orientation of the fibers. The damage can occur either due to matrix cracking, fiber pullout/breakage or due to delamination. Predicting delamination is beyond the scope of the present work; herein we are interested to predict the FRPC fracture response as dominated by the other two modes namely, the matrix cracking and fiber breakage, as influenced by the fiber orientations in an unidirectional lamina. This has

been incorporated by considering the fracture criteria for matrix and fiber separately (based on their respective fracture energies) and by introducing two separate length-scale parameters associated with those two damage mechanisms, while considering a single phase-field damage variable (d) to predict the overall fracture response of the composite. In order to do so, firstly we adopt the anisotropic structural tensor introduced by [115] to incorporate the influence of fibers on direction dependent damage propagation in the FRPC. The modified surface density functional then reads,

$$\gamma_d(d, \nabla d; \mathcal{L}) = \frac{1}{2l_M} (d^2 + \nabla d \cdot \mathcal{L} \nabla d) \quad (4.9)$$

where, \mathcal{L} is an anisotropic tensor, whose specific form closely resembles the form proposed in [207], such that it contains both the fiber and the transverse directions to promote the fracture path to be aligned along the fiber direction in a unidirectional FRPC. The specific form of \mathcal{L} is given by,

$$\mathcal{L} = l_M^2 [\omega^\gamma \mathbf{a}_R^\gamma \otimes \mathbf{a}_R^\gamma + (\mathbf{I} - \mathbf{a}_R^\gamma \otimes \mathbf{a}_R^\gamma)] \quad (4.10)$$

Here, the dyad $(\mathbf{a}_R^\gamma \otimes \mathbf{a}_R^\gamma)$ denotes the fiber direction, and $(\mathbf{I} - \mathbf{a}_R^\gamma \otimes \mathbf{a}_R^\gamma)$ represents the transverse direction. Further, ω^γ is an anisotropic parameter, that regulates the transition from weak to strong directional dependence, which lies in the open range of $(-1 < \omega^\gamma < \infty)$, as necessary to satisfy the ellipticity condition of Γ_L , cf. [115],

and l_M is the length regularization parameter associated with the damage in polymer matrix.

Remark: In the absence of fibers, setting $\mathbf{a}_R^\gamma \otimes \mathbf{a}_R^\gamma = [\mathbf{0}]$ and $\omega^\gamma = 1$, the anisotropic term vanishes in Eq. 4.9, and one can recover the crack density functional corresponding to an isotropic case as given by Eq. 4.8.

4.2.1 Balance laws

In this section, we have formulated a thermodynamically consistent phase-field fracture theory for FRPC incorporating the thermo-viscoelastic response of the composites based on a homogenized constitutive description. The theory is derived upon the principle of virtual power which requires development of macro and microforce balances and the free energy imbalance guided by the thermodynamic laws [118, 186]. The macroforce balance is the standard momentum balance equation, and the microforce balance is coming from the phase field kinematic quantities, \dot{d} and $\nabla \dot{d}$. The dissipation inequality rises due to the viscous contribution of the matrix, dissipation due to damage evolution and the non-isothermal temperature rise. These balance equations provide a set of thermodynamic constraints to derive the constitutive equations for the present formulation.

4.2.1.0.1 Macro and micro-force balance— Negelecting inertia, the standard macro-force balance equation is given by,

$$\text{Div} \mathbf{T}_R + \mathbf{b}_R = \mathbf{0} \quad (4.11)$$

where \mathbf{T}_R is the 1st Piola stress and \mathbf{b}_R is a reference body force. The Cauchy stress, \mathbf{T} is related to the Piola stress by the relation,

$$\mathbf{T} = J^{-1} \mathbf{T}_R \mathbf{F}^T \quad (4.12)$$

Similarly, the non-standard micro-force balance in the reference configuration is expressed as [13, 145, 185],

$$\text{Div} \boldsymbol{\zeta} - \varpi = \mathbf{0} \quad (4.13)$$

where $\boldsymbol{\zeta}$ is a vector microstress that spends power over the rate of the gradient $\nabla \dot{d}$, and ϖ is a scalar microstress that spends power over the rate \dot{d} .

4.2.1.0.2 Balance of energy- thermodynamic consideration— considering ϵ_R as the internal energy density, η_R as the entropy, \mathbf{q}_R as the heat flux, ϑ as the absolute temperature and q_R as the external heat supply per unit reference volume,

the balance of energy in the local form is written as,

$$\dot{\epsilon}_R = \mathbf{T}_R : \dot{\mathbf{F}} - \text{Div } \mathbf{q}_R + q_R + \varpi \dot{d} + \boldsymbol{\zeta} \cdot \nabla \dot{d} \quad (4.14)$$

and the local entropy imbalance has the form,

$$\dot{\eta}_R \geq -\text{Div} \left(\frac{\mathbf{q}_R}{\vartheta} \right) + \frac{q_R}{\vartheta} \quad (4.15)$$

It is convenient to introduce a symmetric 2nd P-K stress tensor, \mathbf{S} and following the standard continuum mechanics theory the stress power can be written as,

$$\mathbf{T}_R : \dot{\mathbf{F}} = \frac{1}{2} \mathbf{S} : \dot{\mathbf{C}} \quad (4.16)$$

Substituting Eq. 4.14 and 4.16 into Eq. 4.15 and after few mathematical manipulation we end up with the following local energy imbalance as,

$$(\dot{\epsilon}_R - \vartheta \dot{\eta}_R) - \frac{1}{2} \mathbf{S} : \dot{\mathbf{C}} + \frac{1}{\vartheta} \mathbf{q}_R \cdot \nabla \vartheta - \varpi \dot{d} - \boldsymbol{\zeta} \cdot \nabla \dot{d} \leq 0 \quad (4.17)$$

In this context, we introduce the standard Helmholtz free energy as,

$$\psi_R = \epsilon_R - \vartheta \eta_R \quad (4.18)$$

Substituting Eq. 4.18 into 4.17 yields the local form of energy imbalance as,

$$\dot{\psi}_R + \eta_R \dot{\vartheta} - \frac{1}{2} \mathbf{S} : \dot{\mathbf{C}} + \frac{1}{\vartheta} \mathbf{q}_R \cdot \nabla \vartheta - \varpi \dot{d} - \boldsymbol{\zeta} \cdot \nabla \dot{d} \leq 0 \quad (4.19)$$

Next, we define the set of kinematical and internal variables as, $\boldsymbol{\Lambda} = (\mathbf{C}, \mathbf{A}_k, k = 1, 2, \dots, n, \vartheta, d, \nabla d; \mathbb{I}_{4,M}, \mathbb{I}_{4,\vartheta})$. This leads to the following dependencies as [56, 186, 209],

$$\psi_R = \hat{\psi}_R(\boldsymbol{\Lambda}) ; \mathbf{S} = \hat{\mathbf{S}}(\boldsymbol{\Lambda}) ; \eta_R = \hat{\eta}_R(\boldsymbol{\Lambda}) ; \mathbf{q}_R = \hat{\mathbf{q}}_R(\boldsymbol{\Lambda}) ; \boldsymbol{\zeta} = \hat{\boldsymbol{\zeta}}(\boldsymbol{\Lambda}) ; \mathbf{T}_k^v = \hat{\mathbf{T}}_k^v(\boldsymbol{\Lambda}) \quad (4.20)$$

Using Eq. 4.20 into 4.19, we get the following expression:

$$\left(\mathbf{S} - 2 \frac{\partial \psi_R}{\partial \mathbf{C}} \right) : \frac{1}{2} \dot{\mathbf{C}} - \sum_{k=1}^n \frac{\partial \psi_R}{\partial \mathbf{A}_k} : \dot{\mathbf{A}}_k - \left(\frac{\partial \psi_R}{\partial \vartheta} + \eta_R \right) \dot{\vartheta} - \left(\varpi - \frac{\partial \psi_R}{\partial d} \right) \dot{d} - \left(\boldsymbol{\zeta} - \frac{\partial \psi_R}{\partial \nabla d} \right) \cdot \nabla \dot{d} + \frac{1}{\vartheta} \mathbf{q}_R \cdot \nabla \vartheta \leq 0 \quad (4.21)$$

Applying the thermodynamic restriction, we can write the specific constitutive relations for the Piola stress (\mathbf{S}), entropy (η), vector microstress ($\boldsymbol{\zeta}$) and viscous overstress (\mathbf{T}_k^v) as,

$$\mathbf{S} = 2 \frac{\partial \psi_R}{\partial \mathbf{C}} ; \eta_R = - \frac{\partial \psi_R}{\partial \vartheta} ; \boldsymbol{\zeta} = \frac{\partial \psi_R}{\partial \nabla d} ; \mathbf{T}_k^v = \frac{\partial \psi_R}{\partial \mathbf{A}_k} \quad (4.22)$$

Also, we consider that the scalar microstress can be additively decomposed into the energetic and the dissipative part, as adopted in our earlier work, [145], based on the theory proposed by [13, 185, 186] as,

$$\varpi = \varpi_{en} + \varpi_{dis} \quad (4.23)$$

where ϖ_{en} and ϖ_{dis} are the energetic and the dissipative microstress, respectively. As done in [185, 186], we take

$$\varpi_{en} = \frac{\partial \psi_R}{\partial d} \quad (4.24)$$

Then the following inequality remains to satisfy the 2nd law of thermodynamics,

$$\sum_{k=1}^n \frac{\partial \psi_R}{\partial \mathbf{A}_k} : \dot{\mathbf{A}}_k + \varpi_{dis} \dot{d} - \frac{1}{\vartheta} \mathbf{q}_R \cdot \nabla \vartheta \geq 0 \quad (4.25)$$

which can be satisfied by choosing certain specific forms for \mathbf{A}_k , \mathbf{q}_R and ϖ_{dis} evolution.

The heat flux obeys the Fourier's law of heat conduction, *i.e.*,

$$\mathbf{q}_R = -\mathbf{K}(\boldsymbol{\Lambda})\nabla\vartheta, \quad (4.26)$$

where \mathbf{K} is the conductivity tensor.

4.2.1.0.3 Further consequences of thermodynamics: evolution of temper-

ature— we obtain the 1st Gibbs relation from Eq. 4.20 as,

$$\dot{\psi}_R = \frac{1}{2} \mathbf{S} : \dot{\mathbf{C}} - \eta_R \dot{\vartheta} + \varpi_{en} \dot{d} + \boldsymbol{\zeta} \nabla \dot{d} + \sum_{k=1}^n \mathbf{T}_k^v : \dot{\mathbf{A}}_k \quad (4.27)$$

and we obtain the second Gibbs relation incorporating Eq. 4.18 into 4.27 as,

$$\dot{\epsilon}_R = \vartheta \dot{\eta}_R + \frac{1}{2} \mathbf{S} : \dot{\mathbf{C}} + \varpi_{en} \dot{d} + \boldsymbol{\zeta} \nabla \dot{d} + \sum_{k=1}^n \mathbf{T}_k^v : \dot{\mathbf{A}}_k \quad (4.28)$$

The rate equation for entropy can be obtained from Eq. 4.20 and 4.27 as,

$$\dot{\eta}_R = - \left(\frac{1}{2} \frac{\partial \mathbf{S}}{\partial \vartheta} : \dot{\mathbf{C}} + \frac{\partial \psi_R^2}{\partial \vartheta^2} \dot{\vartheta} + \frac{\partial \varpi_{en}}{\partial \vartheta} \dot{d} + \frac{\partial \boldsymbol{\zeta}}{\partial \vartheta} \cdot \nabla \dot{d} + \sum_{k=1}^n \frac{\partial \mathbf{T}_k^v}{\partial \vartheta} : \dot{\mathbf{A}}_k \right) \quad (4.29)$$

Since, the energetic scalar and vector microstress related to the damage variables are not temperature dependent, we get $\frac{\partial \varpi_{en}}{\partial \vartheta} = 0$; and $\frac{\partial \boldsymbol{\zeta}}{\partial \vartheta} = \mathbf{0}$.

Further, as a standard, we define the specific heat as,

$$c = -\vartheta \frac{\partial^2 \psi_R(\mathbf{\Lambda})}{\partial \vartheta^2} \quad (4.30)$$

Using Eq. 4.14, 4.29, 4.30 and 4.26 into 4.28, we finally obtain the partial differential equation for temperature evolution as,

$$c\dot{\vartheta} = -\text{Div}(\mathbf{K}\nabla\vartheta) + q_R + \vartheta \left(\frac{1}{2} \frac{\partial \mathbf{S}}{\partial \vartheta} : \dot{\mathbf{C}} + \sum_{k=1}^n \frac{\partial \mathbf{T}_k^v}{\partial \vartheta} : \dot{\mathbf{A}}_k \right) \quad (4.31)$$

4.3 Specialization of the theory for the constitutive forms

4.3.0.0.1 Free Energy:- we start with the assumption that the free energy can be expressed as a sum of separable energies contributed by the thermo-mechanical energy of the matrix and the same for the fibers. Thus, in the absence of damage, we write a total energy expression for the FRPC system as,

$$\psi_R = \left(1 - \sum_{\gamma} f_R \right) \psi_R^M + \sum_{\gamma} f_R^{\gamma} \psi_R^F \quad (4.32)$$

where, ψ_R^M and ψ_R^F denote the energy in the matrix and in the fiber family γ , respectively.

To describe the thermo-viscoelastic response of the matrix the energy can be further decomposed into the time independent elastic part, time-dependent viscous part and the contribution due to temperature induced deformation. Thus,

$$\psi_R^M = \psi_{R,elastic}^M(\bar{\mathbf{C}}, J) + \psi_{R,visco}^M(\bar{\mathbf{C}}, (\mathbf{A}_k, k = 0, 1, ..n), \vartheta) + \psi_{R,thermal}(\vartheta, J) \quad (4.33)$$

Herein, we adopt a NeoHookean hyperelastic model for the time-independent elastic energy. As mentioned before, the specific form of the time-dependent viscous part is taken as derived in [152]. The specific form of the thermal energy in the matrix is considered as the standard thermo-elastic energy, cf. [209]. Hence, we write the complete form of the energy in the polymer matrix as,

$$\begin{aligned} \psi_R^M = & \underbrace{\frac{G_0}{2}(\text{tr}\bar{\mathbf{C}})}_{\text{time independent}} + \underbrace{\frac{K_{bulk}}{2}(\ln J)^2}_{\text{volumetric}} + \underbrace{\sum_{k=1}^n \frac{1}{2}G_k^v(\vartheta)[\mathbf{A}_k(\vartheta) : \bar{\mathbf{C}} - 3 - \ln \det \mathbf{A}_k]}_{\text{time dependent}} - \\ & \underbrace{(\vartheta - \vartheta_0)(3K_{bulk}\alpha_m)(\ln J) - c \ln\left(\frac{\vartheta}{\vartheta_0}\right)}_{\text{thermal}} \end{aligned} \quad (4.34)$$

where, K_{bulk} is the bulk modulus and α_m is the thermal expansion coefficient of polymer matrix. Here, both the time-dependent shear modulus and the viscous stretch tensor are considered as a function of temperature. The reason behind is that the viscoelastic constitutive response of the polymeric material depends on the ambient temperature fluctuation. The specific forms of these dependencies for $G_k^v(\vartheta)$ and $\mathbf{A}_k(\vartheta)$ will be discussed later.

Next, we consider that the energy in the fiber can also be decomposed into elastic and the thermal contribution. For the mechanical or elastic part, we consider a quadratic form depending on $\mathbb{I}_{4,M}^\gamma$, consistent with the standard approach, cf. [74, 144, 205]. For the energy associated with the thermal expansion of the fibers, we adopt a similar quadratic form as a function of $\mathbb{I}_{4,\vartheta}^\gamma$. The thermo-mechanical energy in the fibers then is given by the following expression,

$$\psi_R^F = \sum_{\gamma} \left[\underbrace{\frac{E_\gamma^\gamma}{2} (\mathbb{I}_{4,M}^\gamma - 1)^2}_{\text{elastic}} + \underbrace{\frac{E_\gamma^\gamma}{2} (\mathbb{I}_{4,\vartheta}^\gamma - 1)^2}_{\text{thermal}} \right] \quad (4.35)$$

where, E_γ^γ is the modulus of the fiber family γ .

Finally, we need to provide a specific form of the fracture energy for the fiber-reinforced polymer composite. The fracture energy contains a dissipative component associated with the damage or phase-field variable part and an energetic component that depends on the gradient of damage, ∇d and the anisotropic tensor \mathcal{L} , (as

explained in section 4.2). Here, we write the specific form of the fracture energy considering the contributions from the matrix and the fiber separately in a single ply containing a fiber family γ as,

$$\psi_{R,\text{frac}}^\gamma = \frac{G_{c,M}}{2l_M}(d^2 + l_m^2 \nabla d \cdot (\mathbf{I} - \mathbf{a}_R^\gamma \otimes \mathbf{a}_R^\gamma) \nabla d) + \frac{G_{c,F}^\gamma}{2l_F}(d^2 + l_F^2 \nabla d \cdot (\mathbf{a}_R^\gamma \otimes \mathbf{a}_R^\gamma) \nabla d) \quad (4.36)$$

For the notational convenience we assume a single family of fiber in the domain such that, $\psi_{R,\text{frac}} = \sum_\gamma \psi_{R,\text{frac}}^\gamma$. Here, $G_{c,M}$ is the Griffith-type energy release rate of the polymer matrix and l_M is the corresponding regularization parameter. Similarly, $G_{c,F}^\gamma$ is the Griffith-type energy release rate of the fiber family, and l_F is the corresponding regularization parameter. It is important to note that the fracture energy expression in Eq. 4.36 is valid as long as each individual ply of the composite lamina contains only one fiber family, and would require modification for a single composite ply containing more than one fiber families.

4.3.0.0.2 Energy split:- To avoid the damage evolution due to compression, the total elastic energy is further decomposed into the active/positive (due to tensile) ($\psi_{R,el}^+$) and the inactive/negative part (due to compressive) ($\psi_{R,el}^-$). Hence, we reorganize the total energy expression as,

$$\psi_R = [(1 - d)^2 + \kappa] \psi_{R,el}^+ + \psi_{R,el}^- + \psi_{R,\text{thermal}} + \psi_{R,\text{frac}} \quad (4.37)$$

where $g(d) = [(1 - d)^2 + \kappa]$, is a standard degradation function associated with the elastic energy degradation due to damage, and κ is a small parameter to avoid numerical convergence issues when damage or phase-field parameter reaches to 1. The active elastic energy, $\psi_{R,el}^+$, contains the mechanical energy contributed by the fiber and the matrix during tension and shear and a portion of the viscoelastic energy stored due to stretching in the springs attached in the viscous branches, as shown in Fig. 4.1i). At this stage, we consider that the mechanical part of the active elastic energy comes from the deviatoric contribution of the time-independent energy and the positive part of the volumetric deformation of the polymer matrix ($\ln J \geq 1$), and the mechanical energy stored in the fibers due to tensile stretching, i.e., when $\mathbb{I}_{4,M} \geq 1$. To account for the elastic part from the viscoelastic branches of the matrix, we first calculate the amount of energy lost due to viscous dissipation, which can be determined by calculating the viscous over stresses in each branch and the corresponding strain conjugate. Thus, the lost energy due to viscous dissipation can be approximated as,

$$\psi_{visco,loss} = \mathbf{T}_k^v : (\mathbf{A}_k - \mathbf{I}) \quad (4.38)$$

In what follows, we obtain the viscoelastic contribution in the active elastic energy by deducting this dissipated energy from the total time-dependent energy expression as given in Eq. 4.34. Thus, we obtain a complete expression for the available active

energy driving the evolution of damage as,

$$\begin{aligned} \psi_{R,el}^+ = & \left(1 - \sum_{\gamma} f_R\right) \left[\frac{G_0}{2} (\text{tr} \bar{\mathbf{C}}_0) + \frac{K_{bulk}}{2} H_1(J) (\ln J)^2 + \sum_{k=1}^n \left[\frac{1}{2} G_k^v [\mathbf{A}_k : \bar{\mathbf{C}} - 3 - \ln \det \mathbf{A}_k] - \right. \right. \\ & \left. \left. \mathbf{T}_k^v : (\mathbf{A}_k - \mathbf{I}) \right] + \sum_{\gamma} f_R^{\gamma} H_2(\mathbb{I}_{4,M}^{\gamma}) \frac{E^{\gamma}}{4} (\mathbb{I}_{4,M}^{\gamma} - 1)^2 \right] \end{aligned} \quad (4.39)$$

where, $\bar{\mathbf{C}}_0$ is the deviatoric part of $\bar{\mathbf{C}}$ as, $\bar{\mathbf{C}}_0 = \bar{\mathbf{C}} - \frac{1}{3} \text{tr} \bar{\mathbf{C}}$; H_1 and H_2 are the two Heaviside functions as given by,

$$\begin{aligned} H_1(J) &= 1, \text{ if } \ln J \geq 1 \\ &= 0, \text{ otherwise ;} \\ H_2(\mathbb{I}_{4,M}^{\gamma}) &= 1 \text{ if } \mathbb{I}_{4,M}^{\gamma} \geq 1 \\ &= 0, \text{ otherwise ;} \end{aligned} \quad (4.40)$$

4.3.0.0.3 Cauchy Stress:- Cauchy stress is defined as, $\mathbf{T} = J^{-1} 2\mathbf{F} \frac{\partial \psi_R}{\partial \mathbf{C}} \mathbf{F}^T$. Using Eq. 4.20, we arrive at the specific form of the Cauchy stress as given below,

$$\begin{aligned} \mathbf{T} = & (1-d)^2 J^{-1} \left(1 - \sum_{\gamma} f_R^{\gamma} \right) \left[\left(G_0(\bar{\mathbf{b}}_0) + K_{bulk}(\ln J) + \sum_{k=1}^n G_k^v \bar{\mathbf{F}} \mathbf{A}_k \bar{\mathbf{F}} \right) - 3K_{bulk} \alpha_m (\vartheta - \vartheta_0) \mathbf{I} \right] \\ & + J^{-1} \left[\sum_{\gamma} f_R^{\gamma} E_{\gamma}^{\gamma} (\mathbb{I}_{4,M} - 1) \mathbf{F} \mathbf{a}_R \otimes \mathbf{a}_R \mathbf{F}^T + \sum_{\gamma} f_R^{\gamma} E_{\gamma}^{\gamma} (\mathbb{I}_{4,\vartheta} - 1) \mathbf{F} \mathbf{a}_R \otimes \mathbf{a}_R \mathbf{F}^T \right] \quad (4.41) \end{aligned}$$

where, $\bar{\mathbf{b}}_0$ is the deviatoric part of the left Green-Cauchy tensor $\bar{\mathbf{b}}$ and defined as,
 $\bar{\mathbf{b}}_0 = \bar{\mathbf{b}} - \frac{1}{3} \text{tr} \bar{\mathbf{b}}.$

4.3.0.0.4 Effect of temperature on the FRPC material properties:- The viscoelastic properties of the polymer matrix in the FRPC are influenced by the ambient temperature rise. As mentioned in the literature, non-isothermal heating within the matrix softens the materials, while decreasing the matrix's capacity to transfer load coherently within the fiber reinforcements. As a result the loads are primarily carried by the fibers due to the matrix being softer and the response eventually becomes brittle with a drop in composite's fracture energy.

Assuming the polymer matrix as a thermo-rheologically simple material, the effect of the temperature rise on the viscoelastic parameters can be incorporated by using the well-known time-temperature superposition principle. In this work we adopt the widely used Williams-Landel-Ferry (WLF) shift factor to account for the modification in the viscoelastic relaxation parameters due to local temperature rise in the polymer

matrix [260]. This shift factor, denoted by a_T is simply defined as the ratio of internal viscosity at the operating temperature to the internal viscosity at reference temperature (in this case the glass transition temperature). The shift factor is then used to scale all the relaxation times appropriately. The modified relaxation times of the viscoelastic branches at the operating temperature (other than the reference room temperature) are then given by,

$$\tau_k(\vartheta) = a_T \tau_k(\vartheta_0) \quad (4.42)$$

where ϑ and ϑ_0 are the working and the reference temperature, respectively. The shift factor is calculated as,

$$\log a_T = \frac{-c_1(\vartheta - \vartheta_0)}{c_2 + (\vartheta - \vartheta_0)} \quad (4.43)$$

where, c_1 and c_2 are two empirical constants related to WLF equation. Since the relaxation times at high temperature becomes much faster, all the viscoelastic branches instantly get relaxed upon mechanical deformation and the matrix behaves as an hyperelastic soft solid in the composites. It is observed that the critical energy release rate in elastomeric materials drops with increasing temperature near or above the glass transition temperature [98].

4.3.0.0.5 Anisotropic phase-field evolution in FRPC:- In order to incorporate the anisotropic effect in the damage growth or crack propagation, we consider both the fiber and matrix individually satisfies Eq. C.7. Using the facts, $\zeta_i = \frac{\partial \psi_{R,i,\text{frac}}}{\partial \nabla d}$, $\varpi_{en,i} = \frac{\partial \psi_{R,i,el}^+}{\partial d}$ and $\varpi_{dis,i} = \frac{\partial \psi_{R,i,\text{frac}}}{\partial d}$, where i denotes the matrix or fiber, one can write the damage evolution equation for matrix as,

$$l_M^2 \text{Div}((\mathbf{I} - \mathbf{a}_R^\gamma \otimes \mathbf{a}_R^\gamma) \nabla d) - d + 2(1 - d) \frac{\psi_{R,el,M}^+}{G_{c,M}/l_M} = 0 \quad (4.44)$$

Eq. 4.44, has been normalized with the term $G_{c,M}/l_M$. Similarly, we re-write the normalized micro-force balance equation for the fiber as,

$$l_F^2 \text{Div}((\mathbf{a}_R^\gamma \otimes \mathbf{a}_R^\gamma) \nabla d) - d + 2(1 - d) \frac{\psi_{R,el,F}^+}{G_{c,F}/l_F} = 0 \quad (4.45)$$

Combining Eq. 4.44 and 4.45, we get

$$l_M^2 \text{Div} \left[\left(\mathbf{I} - \mathbf{a}_R^\gamma \otimes \mathbf{a}_R^\gamma + \frac{l_F^2}{l_M^2} \mathbf{a}_R^\gamma \otimes \mathbf{a}_R^\gamma \right) \nabla d \right] - 2d + 2(1 - d) \left(\frac{\psi_{R,el,M}^+}{G_{c,M}/l_M} + \frac{\psi_{R,el,F}^+}{G_{c,F}/l_F} \right) = 0 \quad (4.46)$$

Comparing Eq. 4.10 with 4.46 we obtain a specific expression for, $\omega^\gamma = l_F^2/l_M^2$.

Eq. 4.46 does not ensure damage irreversibility condition. In order to hold the criterion as $\dot{d} \geq 0$, one needs to ensure that the term $\left(\frac{\psi_{R,el,M}^+}{G_{c,M}/l_M} + \frac{\psi_{R,el,F}^+}{G_{c,F}/l_F} \right)$ is always increasing (time derivative ≥ 0), so that the self-healing of the cracked surface can be

avoided. We consider this quantity as the crack driving force, \mathcal{D} and can substitute this driving force with a so called history function to ensure $\dot{\mathcal{D}} \geq 0$, as done in phase-field literature [5, 13, 46, 145, 169, 170, 171, 185, 186, 223]. However, in the FRPC, an useful approach is to split the crack driving force, cf. [170, 207, 208], which allows the association of different driving forces corresponding to different fracture mechanisms. For FRPCs, among the several failure mechanisms we consider the matrix cracking and fiber breakage as the two possible modes of failure in unidirectional composite. Hence, we additively decompose the crack driving force arising due to the matrix and fiber contribution as,

$$\mathcal{D} = \mathcal{D}_M + \mathcal{D}_F \quad (4.47)$$

with

$$\mathcal{D}_M = \left\langle \frac{\psi_{R,el,M}^+}{\frac{G_{c,M}}{2l_M}} - 1 \right\rangle; \text{ and } \mathcal{D}_F = \left\langle \frac{\psi_{R,el,F}^+}{\frac{G_{c,F}}{2l_F}} - 1 \right\rangle \quad (4.48)$$

Note that, here the splitting of the crack driving force physically coincides with the theory of phase-field fracture, that upon minimization of the potential energy, crack will grow in the most favorable energetic path. In this context, we introduce two history variables respectively for the driving forces as,

$$\mathcal{H}_M(t) = \max_{s \in [0,t]} \left[\left\langle \frac{\psi_{R,el,M}^+}{\frac{G_{c,M}}{2l_M}} - 1 \right\rangle \right] \quad (4.49)$$

and

$$\mathcal{H}_F(t) = \max_{s \in [o, t]} \left[\left\langle \frac{\psi_{R,el,F}^+}{\frac{G_{c,F}}{2l_F}} - 1 \right\rangle \right] \quad (4.50)$$

Here the Macaulay bracket denotes $\langle \cdot \rangle = \frac{1}{2}(\cdot + |\cdot|)$. Then, the combined history function can be written as,

$$\mathcal{H} = \mathcal{H}_M + \mathcal{H}_F \quad (4.51)$$

Introducing the history function, Eq. 4.46 can be re-written as a rate-independent evolution equation for the damage variable as,

$$\text{Div}(\mathcal{L}\nabla d) - 2d + 2(1 - d)\mathcal{H} = 0 \quad (4.52)$$

4.4 Experiments and material parameter calibration

4.4.1 Materials and methods

The material used for the experiments in this work is a unidirectional glass-fiber reinforced epoxy composite (GFRC) bar-stock (GC-67-UB) supplied by Avient. This particular composite has a fiber volume fraction of 67%. The flexural modulus and the flexural strength of the material are 5.8 Msi and 153 Ksi respectively, as reported

by Avient. To study the constitutive response of the GFRC under tension, we have prepared various tensile samples with different fiber orientations. In addition, to test the time-dependent behavior of the GFRC, we have performed dynamic mechanical analysis (DMA) and stress relaxation test at 0° and 90° fiber orientations. The fracture patterns of the composite specimens during tensile testing at different fiber orientations are observed by visual inspection and in conjunction with digital image correlation (DIC).

For tensile testing, we have prepared two batches of tensile bars: the first set of bars have a dimension of 5" by 0.5" with approximately 3" gauge length and 0.1" thickness. The second set of bars are 4" by 1" with approximately 1" gauge length and 0.06" thickness. The bars are cut at 0° , 45° and 90° angles to study the effect of fiber orientations on the constitutive response and fracture patterns. To reduce the stress concentration at the grip, the specimens are attached with soft tabs at the grip area using multipurpose flame-retardant garolite G-10/FR4 sheets. Finally, single-edge notches are created in each batches of specimens using diamond saw cutter with notch lengths, $a = 0.2w$ and $a = 0.5w$ (where w is the specimen width) to conduct single-edge notched tensile testing. Fig. 4.2(a) shows the test specimens, where fiber direction is shown in black arrow. Fig. 4.2(b) shows one representative tensile bar with the tabs attached near the grip location. We have performed quasi-static monotonic tensile tests on these specimens using a Instron 4206 tensile and compression testing machine with MTS TestSuite tw elite testing software. A constant displacement rate

of 0.05 inches/sec is applied using a Futek 10k-lb load cell. Additionally, we have used digital image correlation (DIC) to observe the anisotropic fracture patterns of the composite specimens for different fiber orientations. The tension tests are performed in both un-notched and single-edge notched specimens. The tests are performed at room temperature (ϑ_{room}) and at elevated temperatures of 140° C and 150° C using an environmental chamber for 0° and 90° fiber orientations to determine the effect of ambient temperature on the constitutive and fracture response.

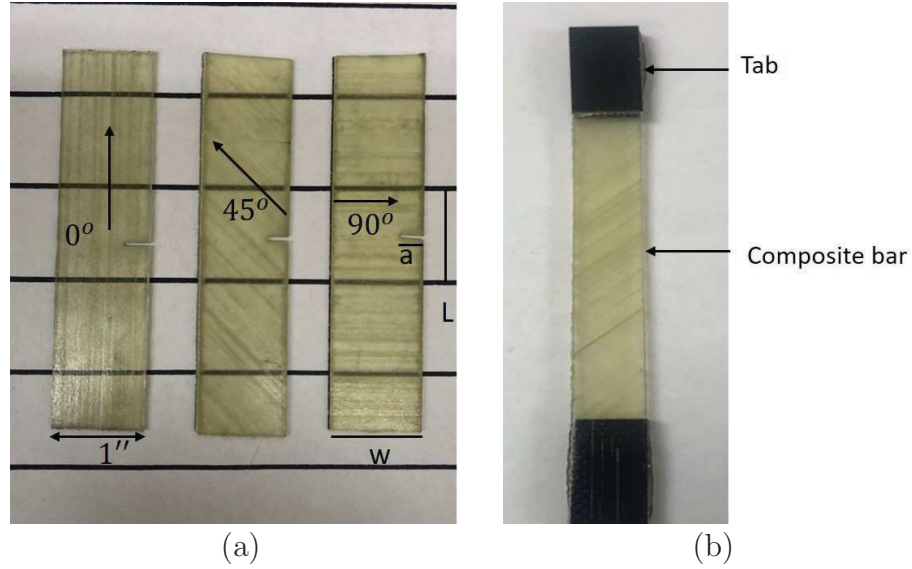


Figure 4.2: (a) Single-edge notched tensile bars at different fiber orientations: fiber orientations are shown with single black arrows, L and w represent the gauge length and the width of the specimen, respectively; here crack length $a = 0.2w$; (b) A composite bar with the tabs attached as grips for the tension test.

For the dynamic mechanical analysis, we used a DMA Q800 V21.3 Build 96 machine. Firstly we have performed stress relaxation tests at 35°C for both 0 and 90° fiber orientations on rectangular bars of dimension $35 \times 9.5 \times 1.85$ mm. The samples are

held at 0.05% constant strain for 10 minutes in a uni-axial load setting. Next, we have performed both temperature and frequency sweeps on the rectangular bars of same dimensions using a 3-point bending clamp having a 90° fiber orientation to obtain the glass transition temperature, storage and loss modulus and the phase-shift ($\tan\delta$). For the temperature sweep, a temperature range of $40 - 160^\circ\text{C}$ at a rate of $3^\circ\text{C}/\text{min}$ at 1 Hz frequency is considered. For the frequency sweep, $1 - 200$ Hz range of frequencies at two temperatures, 35°C and 125°C has been performed. Here it is to note that, 35°C is the lowest temperature setting for DMA machine used in this work, thus it has not been possible to go perform frequency sweep below 35°C .

4.4.2 Experimental results

4.4.2.0.1 Dynamic mechanical analysis The stress relaxation data is plotted in Fig. 4.3(a), which shows that stress does not drop at 0° fiber orientation over the relaxation period, whereas we see a significant stress relaxation at 90° fiber orientation. At 0° fiber orientation, stress response is strongly influenced by the fiber properties, whereas for fibers oriented at 90° , matrix response becomes dominant, and stress drops due to viscoelastic relaxation. Therefore, we choose the 90° fiber orientation to undermine the effect of the fibers and determine the most viscoelastic response due to the matrix for the rest of the DMA studies. In what follows, we

perform temperature and frequency sweeps only for 90° fiber alignment. Fig. 4.3(b-d) show temperature sweep and frequency sweeps of GFRC for 90° fiber orientation. The DMA result with temperature sweep shows a glass transition temperature of 126.4°C for the 90° composite, as plotted in Fig. 4.3(b). The frequency sweep data from DMA showing the storage modulus and the phase-shift ($\tan \delta$) data at 35°C and 125°C (close to T_g) are given in Fig. 4.3(c) and Fig. 4.3(d), respectively. We observe a drastic change between 35°C and 125°C DMA plot. At high temperature $\tan \delta$ values increase significantly, and storage modulus decreases to almost by half in magnitude. The difference becomes even more prominent at high frequency ranges, signifying a detrimental effect is expected in the life-expectancy of the composite material during high frequency fatigue-type applications at high ambient temperature, where matrix softening can cause premature failure in these materials due to thermo-mechanical coupling.

4.4.2.0.2 Quasi-static tensile testing of un-notched bars at different fiber orientations Fig. 4.4(a) shows the load-displacement plots obtained from the monotonic, quasi-static tensile testing at different fiber orientations at room temperature. The influence of fiber-orientation is clearly visible in the constitutive behavior of the composite specimens. Both stiffness and strength of the material is highest at 0° fiber-alignment and both of which drops as the fiber-angle rotates from 0 to 90° . The constitutive response of the composite specimen reveals its poorest behavior at

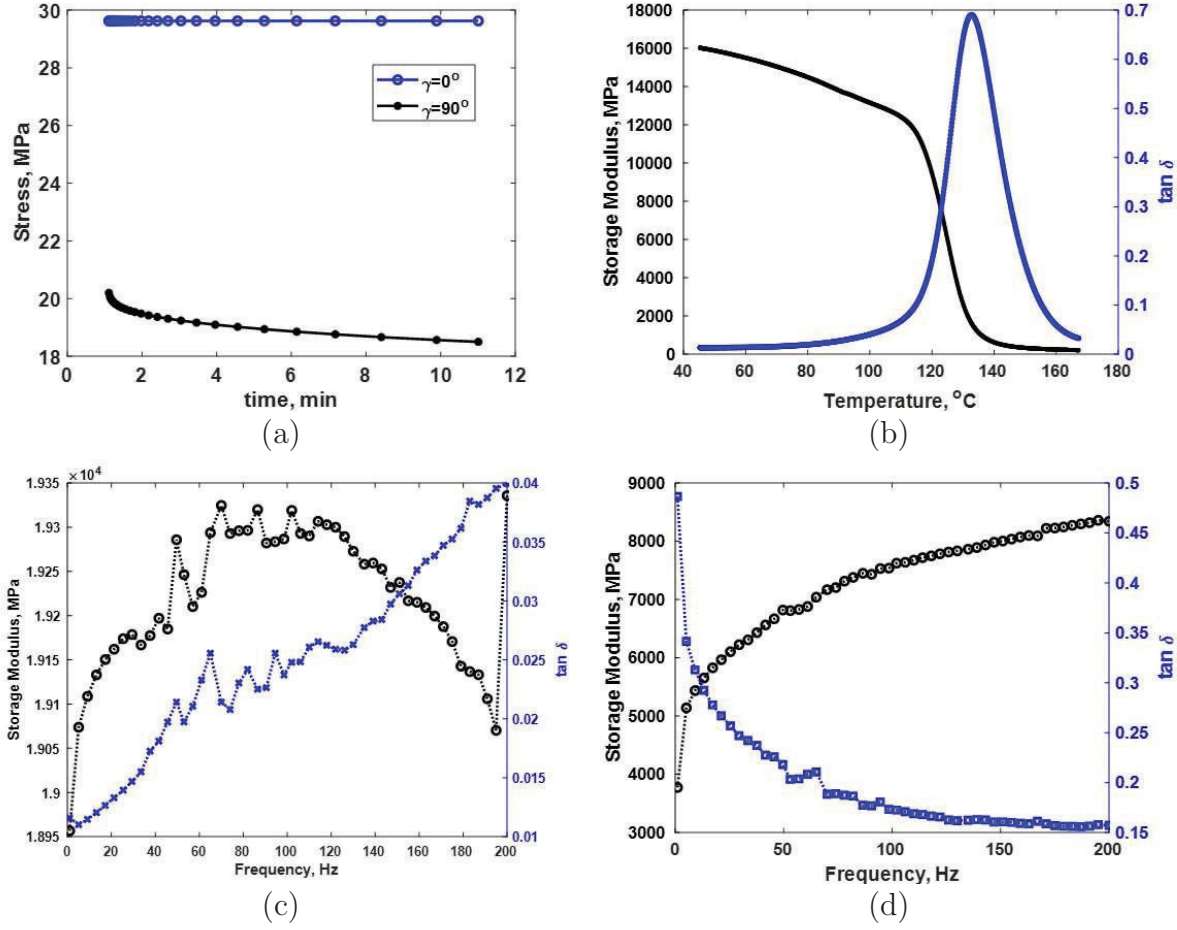


Figure 4.3: DMA results: (a) Stress relaxation data of GFRC at 0° and 90° fiber orientations; (b) Temperature sweep; (c) Frequency sweep at 35°C ; (d) Frequency sweep at 125°C . The plots (b-d) considers 90° fiber orientation.

90° fiber-orientation, where we observe about 40 times drop in the maximum load magnitude compared to the 0° orientation, (as shown in Fig. 4.4). The stretchability of the composite also drops from 0 to 90° alignment.

4.4.2.0.3 Effect of temperature on single-edge notched tension (SENT)

specimens:- Fig. 4.5(a) and (b) show the effect of high-temperatures on the single-edge notched composite specimens ($a/w = 0.2$) at fiber orientations $\gamma = 0^\circ$ and

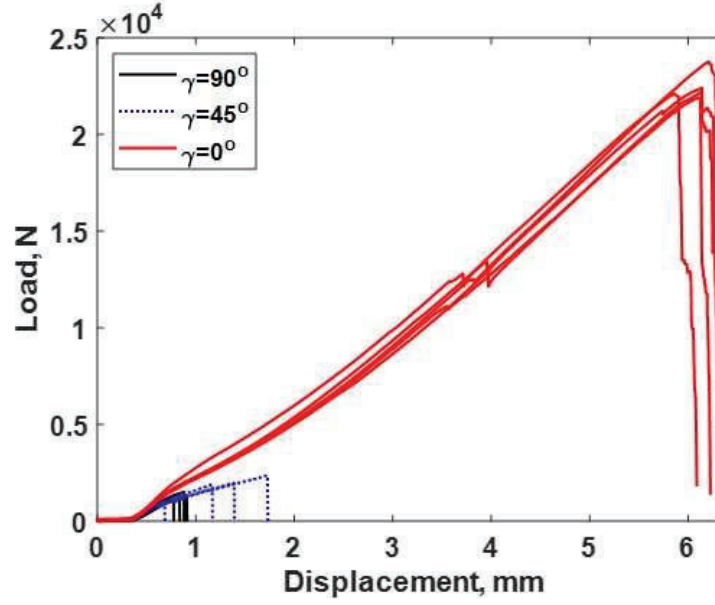


Figure 4.4: Experimental load-displacement plots for un-notched GFRC bars at different fiber orientations.

$\gamma = 90^\circ$, respectively. Here we have performed tensile testing of the SENT specimens at temperatures higher than the glass transition temperature and studied how temperature affected the constitutive and fracture response. As seen in Fig. 4.5, both 140°C and 150°C curves demonstrate softened response of the material, compared to the room temperature, regardless of the fiber orientations. It is observed during experiments that, at 150°C , the matrix becomes extremely soft such that it completely loses the load carrying capacity. The thermo-viscoelastic polymer matrix gets softer with increased temperature, in particular above T_g , which is reflected in the overall composite behavior, through a degradation of stiffness in both orientations. This reduction in the stiffness can be correlated with the storage modulus drop plotted in Fig. 4.3(b). At temperature higher than T_g , the storage modulus drops almost to zero, indicating all the rate-dependent moduli-terms vanishing, and the material

responds proportional to its long-term modulus.

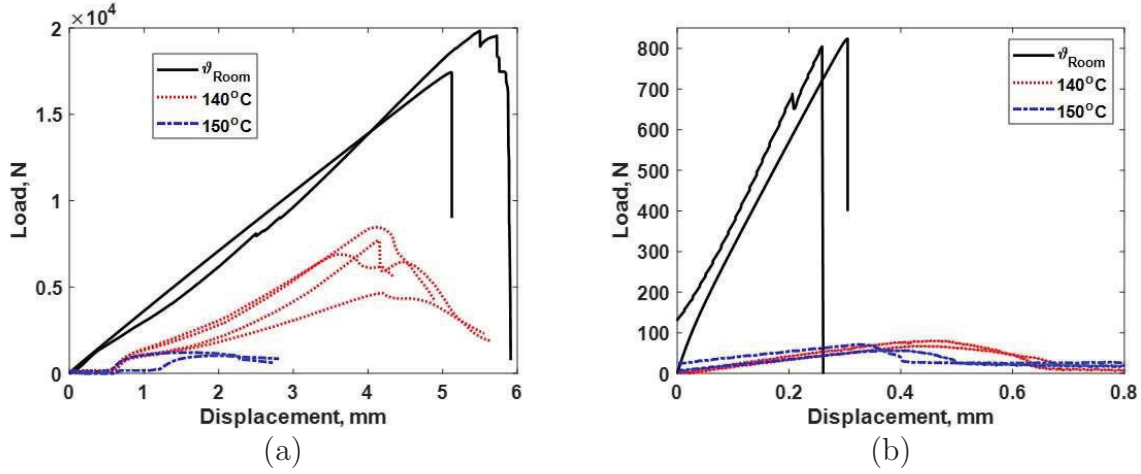


Figure 4.5: Experimental comparison of the load-displacement plots at different temperatures: (a) $\gamma = 0^\circ$; (b) $\gamma = 90^\circ$ (ϑ_{Room} denotes the room temperature).

4.4.2.0.4 DIC analysis of the single-edge notched tensile specimens at

different fiber orientations:- Fig. 4.6 shows the crack patterns as observed by visual examination of the fractured samples of un-notched specimens at different fiber orientations. In all the samples fracture occurred along the fiber direction. Similarly, Fig. 4.7 shows the crack propagation and vertical displacement contour plots obtained through the digital image correlation (DIC) technique on the single-edge notched specimens subjected to tensile loading at different fiber orientations. The images clearly show the influence of fiber anisotropy on the respective crack propagation paths. For an isotropic material, the initial notch would propagate perpendicular to the loading direction in case of Mode-I loading. However, due to the presence of the

embedded fibers in these specimens, cracks propagate parallel to the fiber orientations, as seen in Fig. 4.7(a) for 0° fiber orientation, Fig. 4.7(b) for 45° fiber orientation and Fig. 4.7(c) for 90° fiber orientation, respectively.

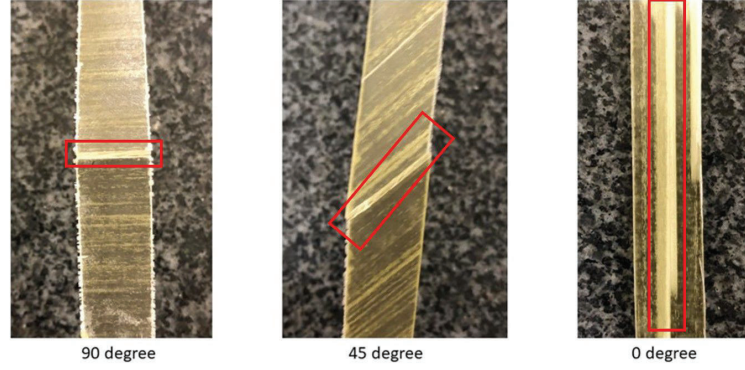


Figure 4.6: Fracture patterns observed at different fiber angles after tensile testing of GFRC specimens. The affected fracture zone is marked with red box.

4.4.3 Calibration of GFRC properties

4.4.3.0.1 Determination of the thermo-viscoelastic parameters of epoxy

matrix and fiber modulus: At first, the storage modulus, loss modulus and $\tan\delta$ obtained as a function of frequencies from the DMA frequency sweep are fitted using a Prony series type model to determine the viscoelastic parameters for the epoxy matrix. Five (5) viscoelastic branches are considered to obtain the shear moduli (G_k) and the relaxation time constants (τ_k) for each of the branches along with the long-term shear modulus of the hyperelastic spring (G_0). The numerically fitted curves are

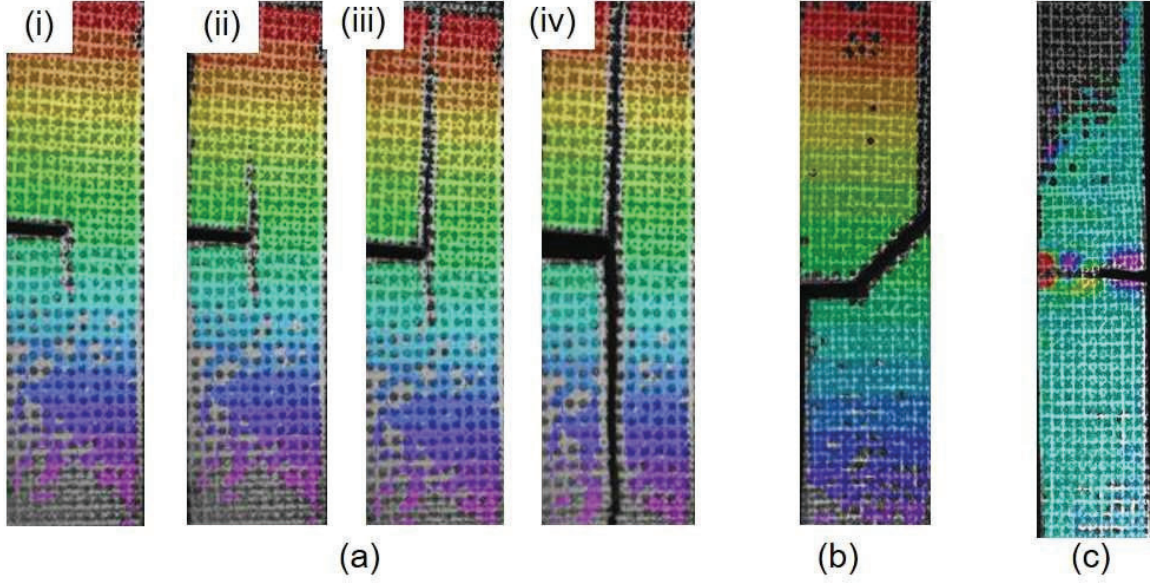


Figure 4.7: DIC images (displacement contour) of single edge-notched tensile specimens at different fiber orientations: (a) Different stages of crack propagation when fibers are embedded at 0° ; (b) Crack propagation path at fracture for 45° fiber orientation; (c) Crack propagation path at fracture for 90° fiber orientation.

shown in Fig. 4.8 at 35°C and Fig. 4.9 at 125°C , respectively. The detailed explanation of the fitting procedure of the viscoelastic parameters is available elsewhere and thus omitted here, cf. [221]. We use the viscoelastic parameters obtained at 35°C to predict the constitutive response of GFRC at room temperature. It is to be noted that, the difference between room temperature and the glass transition temperature (T_g) of the epoxy resin used in this particular composite is more than 100°C . Therefore, it is not possible to use the William-Landel-Ferry (WLF) constants calibrated at T_g to estimate the shear moduli and relaxation time constants at room temperature. Thus, we need a separate set of DMA frequency sweep data to determine these

viscoelastic constants at room temperature. As mentioned in Section 4.4.1, the apparatus for DMA used for these experiments cannot go below 35°C , so we calibrated the viscoelastic parameters at 35°C . However, the other tensile tests are performed at the room temperature or the lab environment temperature (which varied between $25\text{--}32^\circ\text{C}$). Assuming that, at this temperature, which is so far below from T_g , the viscoelastic constants do not vary significantly between $25 - 35^\circ\text{C}$, we use the same viscoelastic constants throughout this temperature range. For temperatures higher than T_g , we use the WLF constants calibrated at T_g to determine the shift factors (in this case, corresponding to 140 and 150°C temperatures, respectively) using Eq. 4.43 to predict the constitutive response of the composite at temperatures higher than T_g , as shown later in the numerical section. In this work, we have taken the WLF constants from [167] at T_g as $c_1 = 21.4$ and $c_2 = 153.7\text{K}$, respectively. The conductivity and other relevant thermal parameters for epoxy are taken from [17]. The fitted parameters for the epoxy matrix are tabulated in Table 4.1.

τ_k (s) (ϑ_{room})	G_k (MPa) (ϑ_{room})	τ_k (s) 125°C	G_k (MPa) 125°C
0.00686	82.9	0.0041	600.9
3892.2	3840.49	0.3895	0.16
414.4	172.9	0.001	673.4
1.16	3375.37	0.3895	1518.8
4.64×10^{-6}	51541.86	0.0256	673.9
G_0 (MPa)		50.78	
ν		0.28	
α_M ($/K$)		70×10^{-6} [17]	
Specific heat ($J/Kg - K$)		1110	
R_{gas} ($Jkg^{-1}K^{-1}$)		8.314	
Conductivity (W/mK)		0.252 [17]	

Table 4.1
Material parameters for epoxy

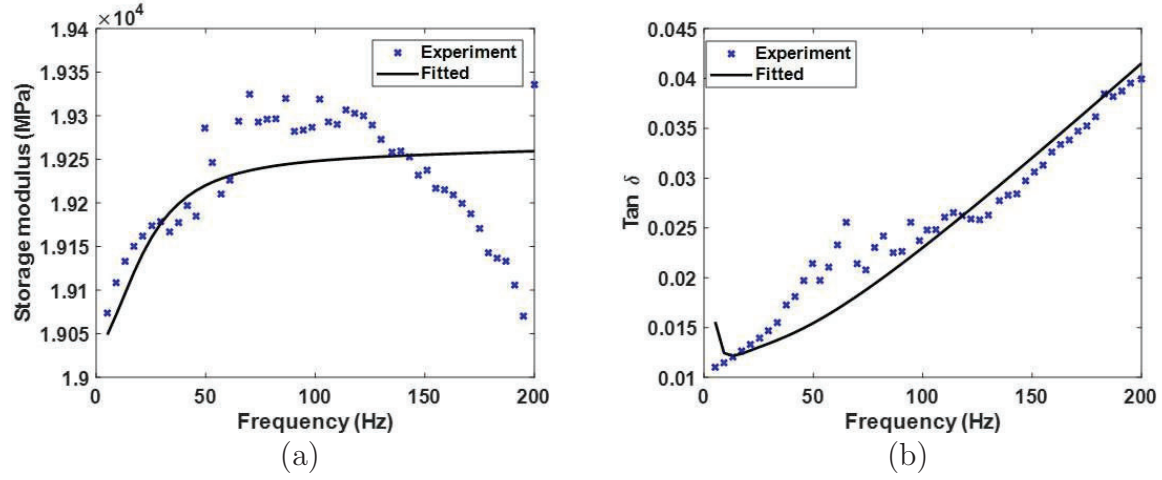


Figure 4.8: Frequency sweep at 35°C fitted against the Prony series model:
(a) Storage modulus; (b) $\tan \delta$ fit

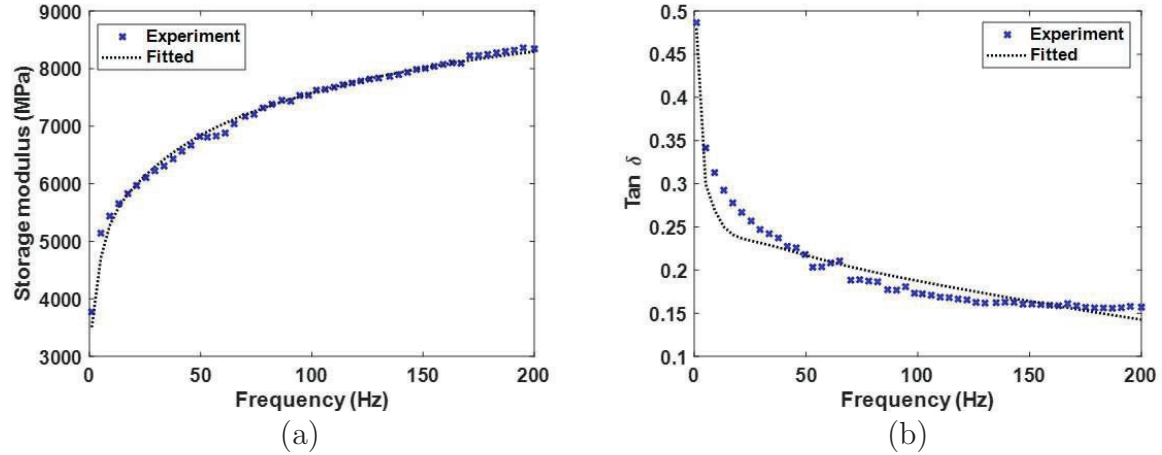


Figure 4.9: Frequency sweep at 125°C fitted against the Prony series model: (a) Storage modulus; (b) $\tan \delta$ fit

Upon calibration of the matrix properties, we use these parameters to simulate the composite response at 90° fiber orientation. For this purpose we choose the unnotched tensile geometry as shown in Fig. 4.2(a). The sample is stretched at a displacement rate of 0.05 inches/sec. The results from numerical simulation is shown in Fig. 4.10 along with the experimental data. As can be seen from this figure, the

numerical results are in very good agreement with the experimental data.

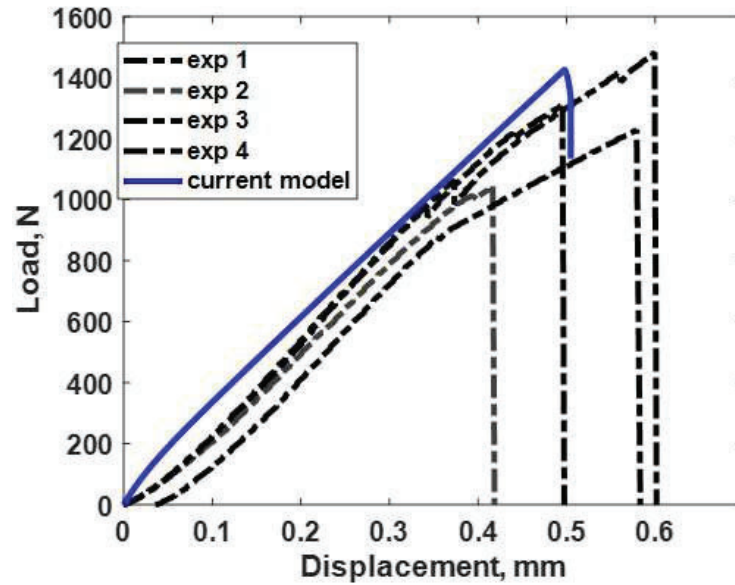


Figure 4.10: Load vs. displacement plot from the quasi-static tensile testing of un-notched composite bars: model vs. experiment for fiber alignment of 90° with respect to the loading axis.

Next, we use the tensile testing data at 0° fiber orientation to calibrate the glass-fiber modulus, E_γ . In order to do that, we numerically simulate the tensile testing of the same composite block mentioned above with 0° fiber orientation. The modulus of the glass fiber is then calibrated with the initial portion of the load-displacement data as shown in Fig. 4.4. This is done due to the fact that the initial stiffness of the samples loaded along the fiber direction is predominantly governed by the fiber modulus. Fig. 4.11 shows the results from the numerical simulation plotted against the experiments, yielding the E_γ value to be 280 MPa.

Subsequently we require to calibrate the fracture properties of the fiber and matrix

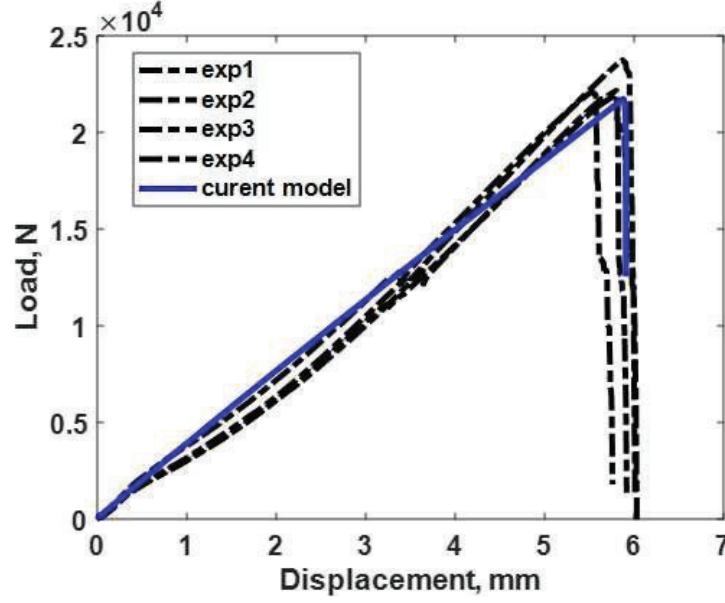


Figure 4.11: Load vs. displacement plot from the quasi-static tensile testing of un-notched composite bars: model vs. experiments for fiber alignment of 0° with respect to the loading axis.

for the 0° and 90° notched specimens in a trial and error basis. In the model, the parameters that are needed to be calibrated are the fracture energies of the matrix and fiber and the associated length-scale parameters, G_c^M, G_c^F, l_c^M , and l_c^F . The detailed explanation of the fracture parameter estimation is provided in the next paragraph.

4.4.3.0.2 Determination of the length-scale parameters and fracture energies for matrix and fiber: In the present phase-field approach, we consider a quadratic crack surface density functional, which is widely known as AT-2 model in the literature [7]. In the AT-2 model, the length-scale parameter influences the ultimate strength of the material, thus it is calibrated as a material parameter rather than a numerical regularization parameter [35, 207]. In particular, along with the

chosen quadratic form of crack density functional, for an elastic material, the homogeneous solution of PF damage gives the following expression for l in terms of the critical stress and fracture energy,

$$l = \frac{27}{256} \frac{GcE}{\sigma_c^2} \quad (4.53)$$

where σ_c is the critical strength of the material. For detailed discussion on how to obtain this relation, readers are referred to [35, 207, 264] and the references therein. For GC-67-UB composite used in this study, the individual fiber and the matrix properties were not accessible. Since we were unable to perform experiments at the individual constituent level, a trial and error is necessary at this stage. We assume that, individually the length-scale parameters are numerical regularization quantities; however, $\frac{G_c^M}{l_M}$ and $\frac{G_c^F}{l_F}$ are material parameters associated with the maximum load or the critical stress in the constitutive response of the composite. In retrospect, we assume that $\frac{G_c^M}{l_M}$ and $\frac{G_c^F}{l_F}$ stay constant for any geometry of interest in the present paper. In what follows, we match the numerical simulation results with the experimentally obtained data to the maximum load point of the single-edge notched bars (with $a/w = 0.2$) to obtain the values for $\frac{G_c^M}{l_M}$ and $\frac{G_c^F}{l_F}$. We have seen that, $\frac{G_c^M}{l_M} = 1.9 \text{ N/mm}^2$ and $\frac{G_c^F}{l_F} = 200 \text{ N/mm}^2$, respectively matches reasonably well with the experimental SENT results for $a/w = 0.2$. In addition, we have considered $l_F = 10l_M$ throughout this work, which, in turn, gives anisotropic parameter, $\omega \approx 100$. It can be noted here that, the length-scale parameter associated with the

fiber can also be orientation dependent, as shown in [150]. However, we have not considered that in the present model. The glass-fiber properties and fracture energies are reported at Table 4.2.

f_R	0.67
E_{γ} (MPa)	280
$\frac{G_c^f}{l_{F_c}} (N/mm^2)$	200
$\frac{G_m^f}{l_M} (N/mm^2)$	1.9
$\alpha_f (/K)$	6.18×10^{-6} [177]

Table 4.2

Material parameters for glass-fiber and fracture properties of GFRC

4.5 Representative numerical examples showing model prediction

4.5.1 Mode-I fracture tests of a single-edge notched specimens at different fiber orientations and crack length

In this example, we study the effect of fiber orientations on the fracture response of a single-edge notched tension specimen. Fig. 4.12 shows the zoomed view of the FE mesh and the boundary conditions for this particular geometry at fiber orientations 0, 45 and 90°, respectively for the crack length of $a/w = 0.5$. As can be seen we have refined the mesh along the prospective crack propagation path using an element

size of $h = 0.1\text{mm}$. The dimension and the loading conditions are consistent with the experiments as discussed in Section 4.4. For these simulations, we have used the length-scale parameters of $l_M = 0.5\text{ mm}$ and $l_F = 5\text{ mm}$, respectively. The other material properties used are listed in Table-4.1 and Table-4.2. The numerical simulations have been conducted for cases $a/w = 0.2$ and $a/w = 0.5$. Fig. 4.13 demonstrates the corresponding load vs. displacement plots at different fiber orientations for both the crack lengths, comparing the results from numerical simulation with the experiments. The numerical results are in good agreement with the experimental results for all the fiber orientations and for the two crack lengths considered. Fig. 4.14 shows the damage contour at the post-peak load regime where the damage propagation always favors along the fiber direction as observed in experiments (in Fig. 4.7). At 0° fiber orientation, fiber debonding becomes the most dominating failure mechanism, resulting crack propagation in-between fibers along the fiber direction. In the simulation we observe that, upon initiation at the notch-tip, the crack indeed propagates parallel to the fiber direction. For 45° fiber orientation, we see crack propagates along the fiber direction as well. However, the dominating failure mechanism is attributed to matrix cracking for this particular orientation, as the elastic energy, $\psi_{R,el}^M \gg \psi_{R,el}^F$ in this case. This is demonstrated in Fig. 4.15, where elastic energy contributions from the matrix and fiber along with the corresponding history function is plotted as a function of time at the notch tip, where the stress concentration is maximum. Lastly, as expected, for 90° fiber orientation, matrix cracking is always the dominating failure

mechanism. The strength and ductility of the composite is also much lower in 45° and 90° compared to 0° , as observed in the load-displacement plot in Fig. 4.13.

Fig. 4.16 shows the contour plots of the local temperature rise during tensile loading of the SENT specimen for $a/w = 0.5$. From this plot, it is evident that the local of temperature of the composite rises along the crack propagation path. The main source of temperature rise is due to the viscous dissipation of the matrix, and the heat generated due to dissipation is maximum along the direction of the crack propagation/ maximum stress. It is important to mention that, for this particular GFRC, the exact thermal conductivity and specific heat parameters for the epoxy matrix are not known. Hence the experimental comparisons were not presented here. The temperature contours demonstrate the model's capability to incorporate a thermo-mechanical coupling framework.

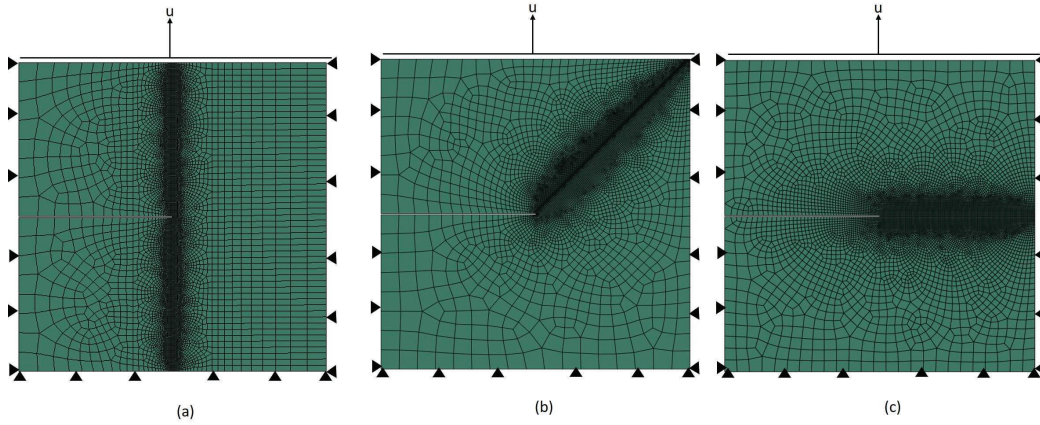


Figure 4.12: Zoomed view of the meshing and the boundary conditions of a single-edge notched $1'' \times 1''$ specimen with $a/w = 0.5$: (a) $\gamma = 0^\circ$; (b) $\gamma = 45^\circ$; and (c) $\gamma = 90^\circ$.

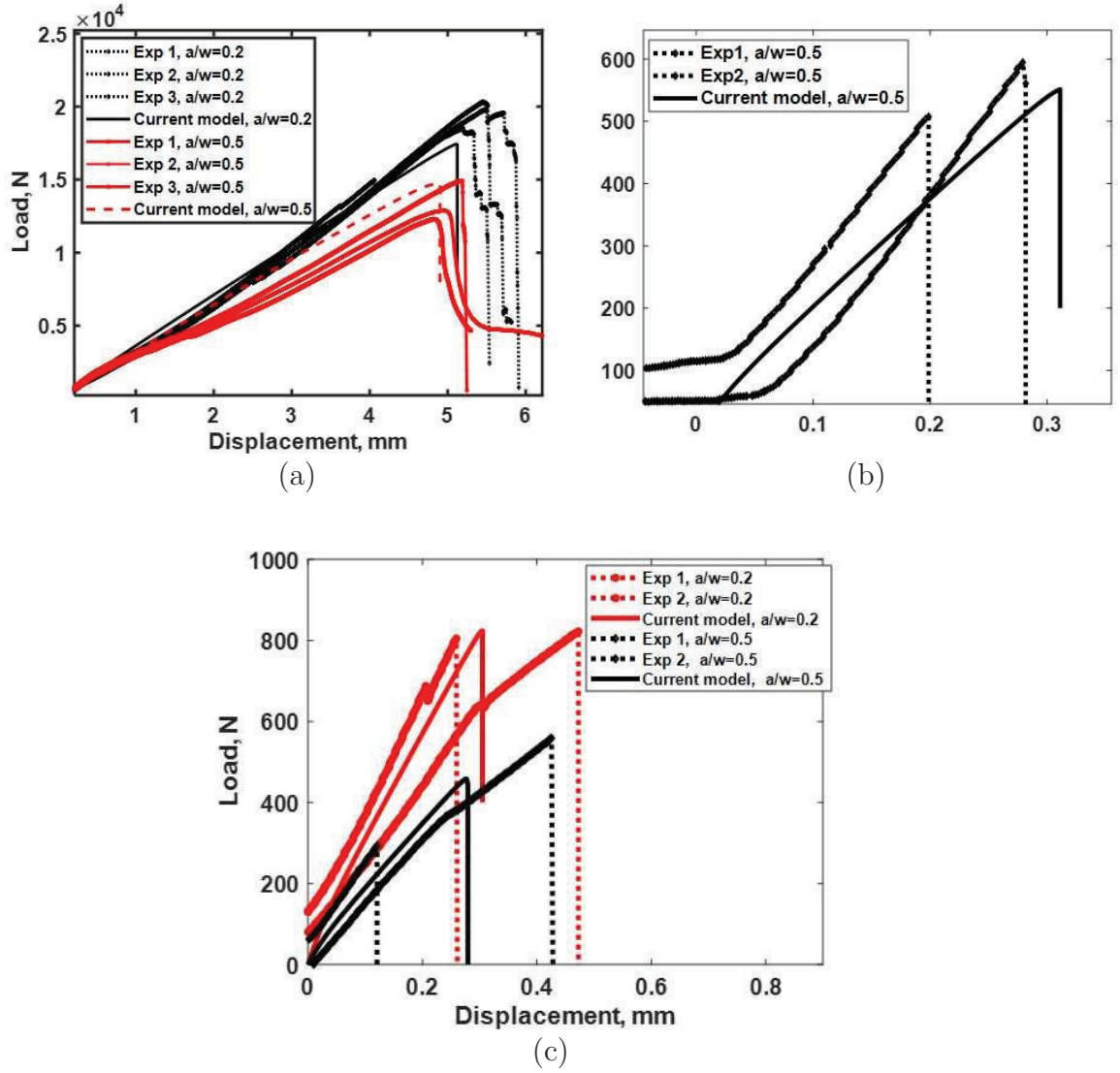


Figure 4.13: Load-displacement plot for SENT specimens: comparison of model prediction with the experiments for (a) 0° with $a/w = 0.2$ and $a/w = 0.5$; (b) 45° with $a/w = 0.5$; (c) 90° with $a/w = 0.2$ and $a/w = 0.5$

4.5.2 Effect of high temperature on the GFRC response

As mentioned in Section 4.1 and shown in our experimental results, at high temperature, specially above the glass transition temperature, the stiffness of the composite

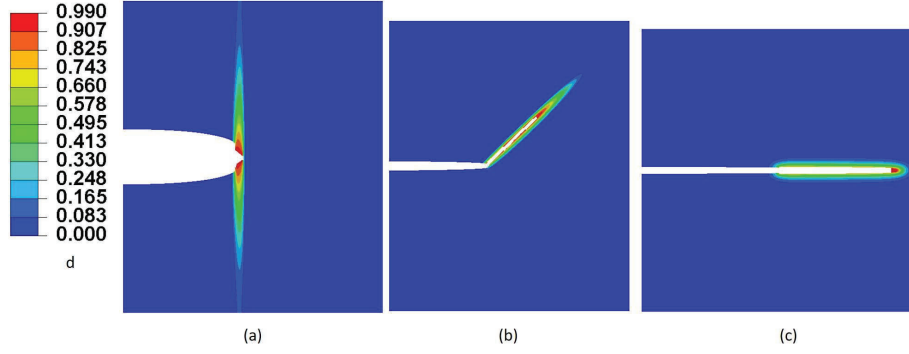


Figure 4.14: Contour plots of d at different fiber orientations for single-edge notched specimen with $a/w = 0.5$ corresponding to Fig. 4.12: (a) $\gamma = 0^\circ$; (b) $\gamma = 45^\circ$; (c) $\gamma = 90^\circ$.

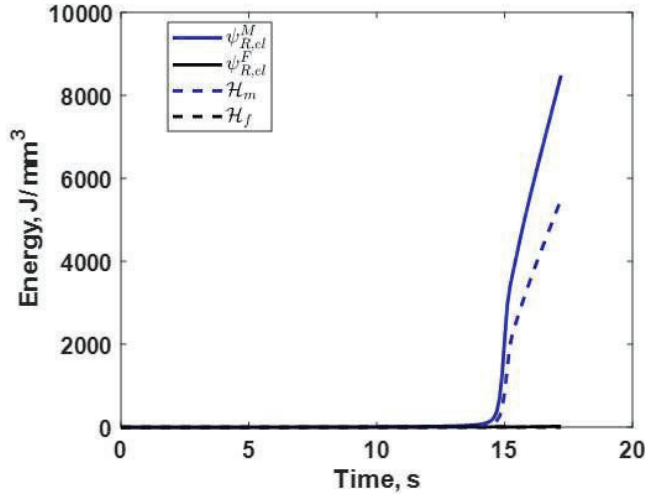


Figure 4.15: Comparison of elastic energy between matrix and fiber and the corresponding history functions at the notch tip of the SENT-specimen with fiber orientation, $\gamma = 45^\circ$.

degrades considerably and results in a softer response. In order to numerically simulate such cases, using time-temperature superposition principle, we calculate a shift factor a_T to modify the relaxation time constants from their known values at T_g . As mentioned in Section 4.4.3, we use a WLF shift factor using Eq. 4.43. The WLF

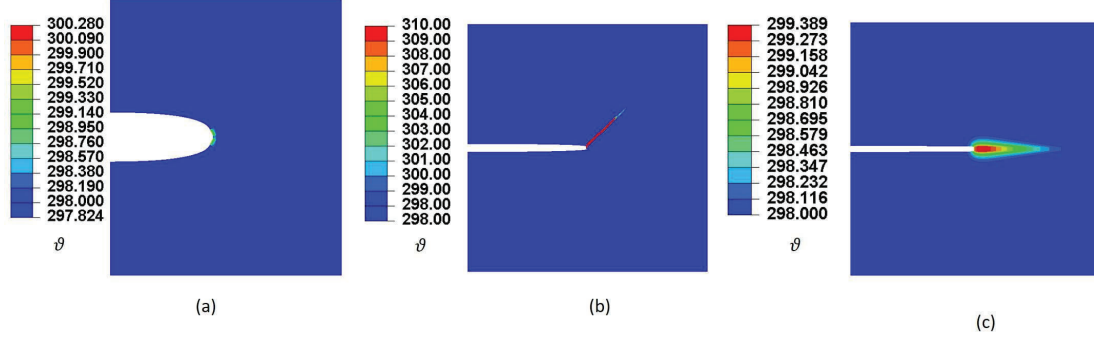


Figure 4.16: Contour plots of temperature, ϑ at different fiber orientations for single-edge notched specimen with $a/w = 0.5$ corresponding to Fig. 4.12: (a) $\gamma = 0^\circ$; (b) $\gamma = 45^\circ$; (c) $\gamma = 90^\circ$.

constants are taken as $c_1 = 21.4$ and $c_2 = 153.7K$ respectively, as mentioned in Section 4.4.1. By using Eq. 4.43, the shift factor for 140°C turns out to be 0.0125. We can therefore estimate the new relaxation time constants at 140°C by multiplying the time constants estimated at T_g with this shift factor by following Eq. 4.42. In what follows, we numerically simulate a the SENT specimen with $a/w = 0.2$, subjected to tensile loading at 140°C . Fig. 4.17(a) and (b) show the comparison between experiments and model predictions at 0° and 90° fiber orientation, respectively. As seen from Fig. 4.17, for both 0° and 90° fiber orientations, experimental plots significantly vary over a range (for 0° orientation a maximum load difference of $\approx 4000\text{ N}$ is observed). A plausible reason being matrix softening at this high temperature causing slippage at the grip loading. Our numerical simulation results (blue solid lines) show a reasonable agreement with the experimental data up until 4 mm displacement for 0° and 0.6 mm displacement for 90° fiber orientation, respectively. However, the model falls short in the the post-peak response for both cases. This is because of the fact

that we use the same $\frac{G_c^M}{l_M}$ and $\frac{G_c^F}{l_F}$ values as used for room temperature simulations, which may not be applicable at 140°C. While it is well known that the critical stress of the composite definitely gets affected by the ambient temperature, it is not clear whether it is needed to lower the fracture energy or alter the length-scale parameter in the present model to accommodate that. However, to match the experimental result observed at 90° fiber orientations, we run one further simulation considering $\frac{G_c^M}{l_M} = 0.095 \text{ N/mm}^2$, as shown by the red line in Fig. 4.17(b). This clearly shows a reasonable load drop and the prediction matches much better with the experimental data. However, more experimental data are needed to reach a specific conclusion at this point to predict how the critical fracture energy of a composite material gets affected at high temperature.

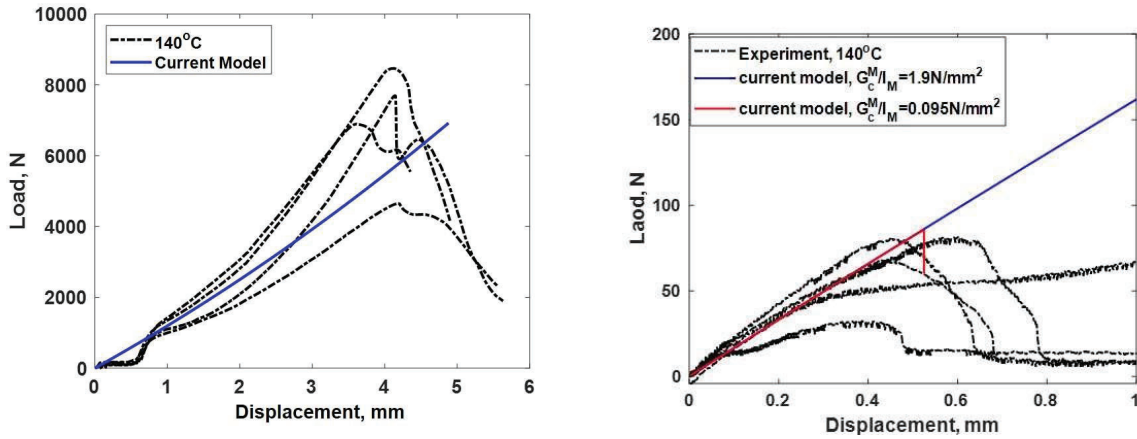


Figure 4.17: Load-displacement plot of GFRC at 140°C: (a) $\gamma = 0^\circ$; (b) $\gamma = 90^\circ$

4.6 Conclusion

In this work, we have developed an experimentally informed, unified phase-field theory to predict anisotropic fracture and damage propagation in a polymer-matrix composite using a single phase-field or damage variable. The theory considers two distinguish failure modes in composite, fiber breakage or pullout and matrix cracking by considering two different energy-based failure criteria. The anisotropic crack propagation is incorporated by using an anisotropic tensorial term in the gradient calculation of the phase-field variable. The constitutive theory for the composite material considers a thermodynamically consistent, large deformation homogenized microstructure of the fiber-reinforced polymer, considering the polymer matrix as thermo-viscoelastic. The model has been numerically implemented in a finite element setting and then validated against a commercially available glass-fiber reinforced epoxy composite's experimental data. It has been shown that the model can successfully predict experimental results. In addition, the model considers a thermo-mechanical coupling in the proposed constitutive framework, which is an essential part of composite fracture modeling, as ambient temperature rise affects the composite's response due to the softening of the matrix. The proposed modeling framework demonstrates a classical phase-field theory based formulation being capable of predicting orientation-dependent crack propagation and the global force response of the fiber-reinforced composite.

Chapter 5

Future recommendations

In light of the current present work and progress, we propose the following futuristic directions:

Polymer Oxidation:

Calibration and validation of the proposed model: Our theory considers a rigorous mathematical model considering all the complex physics and chemistry involved in the thermo-oxidative aging of polymers. However, it still needs a rigorous experimental characterization and validation of based on specific polymers useful for structural, aerospace, and automotive application. For this purpose, we propose the followings: :

- i) Characterize important thermoplastic and glassy polymers using microscopy, FTIR Spectroscopy/ X-ray photoelectron spectroscopy (XPS) at virgin and oxidized state.

These calibrated parameters then can be used to validate the model's reaction kinetics at different oxidized states (longer aging period or at a different temperature).

ii) Perform mechanical testing of the virgin and aged specimens, correlate with experimental observation, and compare with model prediction for complete fracture behavior under oxidative aging.

Modification of present model to improve the accuracy in the lifetime prediction and constitutive response:

i) Our present model requires 18 material parameters to characterize the oxidation process accurately. Some of the reactions during polymer oxidation are instantaneous (especially reactions involving the radicals), and it is impossible to quantify them experimentally in a chain reaction mechanism. To avoid this, we propose using an idealized reaction that considers the contributions from all chain reactions in the evolution kinetics but deals only with the reactant and product species, which are experimentally measurable quantities. Then, the state of oxidation will be expressed using a single 'extent of reaction' (instead of six), and the number of material parameters could be reduced to only 3. This idealization in the reaction kinetics will increase the ease of usability of the present model and appeal to a broader range of end-users.

(ii) The model can be extended to include the effect of change in the degree of crystallinity in thermoplastics.

(iii) The homogenized model proposed in Chapter 3 needs to be further extended to

predict oxidation-induced damage and degradation in polymer-matrix composites.

Polymer-matrix composite fracture:

Inclusion of delamination and debonding using a cohesive-type phase-field (PF-CZM) model:

In the event of a FRP composite's fracture, multiple competing damage mechanisms are involved in the micro/mesoscale such as-matrix cracking, fiber breakage, fiber/matrix debonding, and delamination. Our current work does not consider fiber-matrix debonding and the delamination across the lamina as an important mode of fracture. In that light, we propose modifying the current model by adding a PF-CZM type model for fiber-matrix interface and ply-to-ply interface to simulate a cohesive-type failure response. This will enable to accurately simulate progressive damage and failure in the laminated composite for other loading configuration such as three-point bending and double cantilever beam bending.

Extending the unified phase-field model to incorporate fatigue in phase-field fracture of composites:

The proposed phase-field fracture theory for FRPC can be easily extended to predict fatigue crack propagation in UD composites. Since the fatigue damage is history-dependent, we propose to modify the phase-field fracture theory to take into account the history-dependent degradation of the fracture strength. Here we will introduce a suitable fatigue history variable for each of the damage mechanisms described above

and a function that will modify the dissipated fracture energy depending on the accumulated history variables. All the model modifications will eventually be validated with experimental data to ensure robustness and accuracy of their predictions.

References

- [1] Abaqus/Standard, 2017.
- [2] Albouy, W., Vieille, B., Taleb, L., 2014. Influence of matrix ductility on the high-temperature fatigue behaviour of quasi-isotropic woven-ply thermoplastic and thermoset laminates. *Composites Part A: Applied Science and Manufacturing* 67, 22–36.
- [3] Alessi, R., Freddi, F., 2017. Phase-field modelling of failure in hybrid laminates. *Composite Structures* 181, 9–25.
- [4] Alessi, R., Vidoli, S., De Lorenzis, L., 2018. A phenomenological approach to fatigue with a variational phase-field model: The one-dimensional case. *Engineering fracture mechanics* 190, 53–73.
- [5] Ambati, M., Gerasimov, T., De Lorenzis, L., 2015a. Phase-field modeling of ductile fracture. *Computational Mechanics* 55, 1017–1040.

- [6] Ambati, M., Gerasimov, T., De Lorenzis, L., 2015b. A review on phase-field models of brittle fracture and a new fast hybrid formulation. *Computational Mechanics* 55, 383–405.
- [7] Ambrosio, L., Tortorelli, V.M., 1990. Approximation of functional depending on jumps by elliptic functional via t-convergence. *Communications on Pure and Applied Mathematics* 43, 999–1036.
- [8] Ambu, R., Aymerich, F., Bertolino, F., 2005. Investigation of the effect of damage on the strength of notched composite laminates by digital image correlation. *The Journal of Strain Analysis for Engineering Design* 40, 451–461.
- [9] Ames, N.M., Srivastava, V., Chester, S.A., Anand, L., 2009. A thermo-mechanically coupled theory for large deformations of amorphous polymers. part ii: Applications. *International Journal of Plasticity* 25, 1495–1539.
- [10] Amiri, M., Khonsari, M.M., 2012. On the role of entropy generation in processes involving fatigue. *Entropy* 14, 24–31.
- [11] Anand, L., Ames, N.M., Srivastava, V., Chester, S.A., 2009. A thermo-mechanically coupled theory for large deformations of amorphous polymers. part i: Formulation. *International Journal of Plasticity* 25, 1474–1494.
- [12] Anand, L., Gurtin, M.E., 2003. A theory of amorphous solids undergoing large deformations, with application to polymeric glasses. *International Journal of Solids and Structures* 40, 1465–1487.

- [13] Anand, L., Mao, Y., Talamini, B., 2019. On modeling fracture of ferritic steels due to hydrogen embrittlement. *Journal of the Mechanics and Physics of Solids* 122, 280–314.
- [14] Aoki, T., Ishikawa, T., Kumazawa, H., Morino, Y., 2001. Cryogenic mechanical properties of cf/polymer composites for tanks of reusable rockets. *Advanced composite materials* 10, 349–356.
- [15] Arruda, E.M., Boyce, M.C., 1993a. Evolution of plastic anisotropy in amorphous polymers during finite straining. *International Journal of Plasticity* 9, 697–720.
- [16] Arruda, E.M., Boyce, M.C., 1993b. A three-dimensional constitutive model for the large stretch behavior of rubber elastic materials .
- [17] Assael, M.J., Antoniadis, K.D., Metaxa, I.N., Tzetzis, D., 2009. Measurements on the enhancement of the thermal conductivity of an epoxy resin when reinforced with glass fiber and carbon multiwalled nanotubes. *Journal of Chemical & Engineering Data* 54, 2365–2370.
- [18] Atkins, P.W., De Paula, J., Keeler, J., 2018. *Atkins’ physical chemistry*. Oxford university press.
- [19] Audouin, L., 2000. Kinetic modeling of low-temperature oxidation of hydrocarbon polymers. *Handbook of polymer degradation* , 727–763.

- [20] Audouin, L., Gueguen, V., Tcharkhtchi, A., Verdu, J., 1995. “close loop” mechanistic schemes for hydrocarbon polymer oxidation. *Journal of Polymer Science Part A: Polymer Chemistry* 33, 921–927.
- [21] Audouin, L., Langlois, V., Verdu, J., De Bruijn, J., 1994. Role of oxygen diffusion in polymer ageing: kinetic and mechanical aspects. *Journal of Materials science* 29, 569–583.
- [22] Bahrololoumi, A., Mohammadi, H., Moravati, V., Dargazany, R., 2021. A physically-based model for thermo-oxidative and hydrolytic aging of elastomers. *International Journal of Mechanical Sciences* 194, 106193.
- [23] Bai, Y., Keller, T., Vallée, T., 2008. Modeling of stiffness of frp composites under elevated and high temperatures. *Composites Science and Technology* 68, 3099–3106.
- [24] Balzani, D., Brinkhues, S., Holzapfel, G.A., 2012. Constitutive framework for the modeling of damage in collagenous soft tissues with application to arterial walls. *Computer Methods in Applied Mechanics and Engineering* 213-216, 139 – 151. URL: <http://www.sciencedirect.com/science/article/pii/S0045782511003616>, doi:<https://doi.org/10.1016/j.cma.2011.11.015>.
- [25] Bateman, L., Gee, G., Morris, A., Watson, W., 1951. The velocity coefficients of the chain propagation and termination reactions in olefin oxidations in liquid systems. *Discussions of the Faraday Society* 10, 250–259.

- [26] Battista, D., Curatolo, M., Nardinocchi, P., 2019. Enforcing shaping of thin gel sheets by anisotropic swelling. *Mechanics of Materials* 139, 103199.
- [27] Bergström, J., Boyce, M., 1998. Constitutive modeling of the large strain time-dependent behavior of elastomers. *Journal of the Mechanics and Physics of Solids* 46, 931–954.
- [28] Beurle, D., André, M., Nackenhorst, U., Desmorat, R., 2020. Micromechanically motivated model for oxidation ageing of elastomers, in: *Virtual Design and Validation*. Springer, pp. 271–290.
- [29] Binet, M., Commereuc, S., Verney, V., 2000. Thermo-oxidation of polyterpenes: influence of the physical state. *European polymer journal* 36, 2133–2142.
- [30] Bleyer, J., Alessi, R., 2018. Phase-field modeling of anisotropic brittle fracture including several damage mechanisms. *Computer Methods in Applied Mechanics and Engineering* 336, 213–236.
- [31] Böger, L., Nateghi, A., Miehe, C., 2017. A minimization principle for deformation-diffusion processes in polymeric hydrogels: Constitutive modeling and fe implementation. *International Journal of Solids and Structures* 121, 257–274.
- [32] Bolland, J., 1949. Kinetics of olefin oxidation. *Quarterly Reviews, Chemical Society* 3, 1–21.

- [33] Bolland, J., Gee, G., 1946. Kinetic studies in the chemistry of rubber and related materials. ii. the kinetics of oxidation of unconjugated olefins. Transactions of the Faraday Society 42, 236–243.
- [34] Borden, M.J., Hughes, T.J., Landis, C.M., Anvari, A., Lee, I.J., 2016. A phase-field formulation for fracture in ductile materials: Finite deformation balance law derivation, plastic degradation, and stress triaxiality effects. Computer Methods in Applied Mechanics and Engineering 312, 130–166.
- [35] Borden, M.J., Verhoosel, C.V., Scott, M.A., Hughes, T.J., Landis, C.M., 2012. A phase-field description of dynamic brittle fracture. Computer Methods in Applied Mechanics and Engineering 217, 77–95.
- [36] Bosnjak, N., Wang, S., Han, D., Lee, H., Chester, S.A., 2019. Modeling of fiber-reinforced polymeric gels. Mechanics Research Communications 96, 7–18.
- [37] Bourdin, B., 2007. Numerical implementation of the variational formulation for quasi-static brittle fracture. Interfaces and free boundaries 9, 411–430.
- [38] Bourdin, B., Francfort, G.A., Marigo, J.J., 2000. Numerical experiments in revisited brittle fracture. Journal of the Mechanics and Physics of Solids 48, 797–826.
- [39] Bourdin, B., Francfort, G.A., Marigo, J.J., 2008. The variational approach to fracture. Journal of elasticity 91, 5–148.

- [40] Bowles, K.J., Nowak, G., 1988. Thermo-oxidative stability studies of celion 6000/pmr-15 unidirectional composites, pmr-15, and celion 6000 fiber. *Journal of Composite Materials* 22, 966–985.
- [41] Brunbauer, J., Pinter, G., 2015. Effects of mean stress and fibre volume content on the fatigue-induced damage mechanisms in cfrp. *international Journal of Fatigue* 75, 28–38.
- [42] Brunbauer, J., Stadler, H., Pinter, G., 2015. Mechanical properties, fatigue damage and microstructure of carbon/epoxy laminates depending on fibre volume content. *International Journal of Fatigue* 70, 85–92.
- [43] Bryant, M., Khonsari, M., Ling, F., 2008. On the thermodynamics of degradation. *Proceedings of the royal society A: mathematical, physical and engineering sciences* 464, 2001–2014.
- [44] Buliga, M., 1998. Energy minimizing brittle crack propagation. *Journal of Elasticity* 52, 201.
- [45] Calvert, J.G., Pitts, J.N., 1966. *Photochemistry* .
- [46] Carrara, P., Ambati, M., Alessi, R., De Lorenzis, L., 2020. A framework to model the fatigue behavior of brittle materials based on a variational phase-field approach. *Computer Methods in Applied Mechanics and Engineering* 361, 112731.

- [47] Celina, M., Gillen, K.T., Assink, R., 2005. Accelerated aging and lifetime prediction: review of non-arrhenius behaviour due to two competing processes. *Polymer Degradation and stability* 90, 395–404.
- [48] Celina, M., Wise, J., Ottesen, D., Gillen, K., Clough, R., 2000. Correlation of chemical and mechanical property changes during oxidative degradation of neoprene. *Polymer degradation and Stability* 68, 171–184.
- [49] Celina, M.C., 2013. Review of polymer oxidation and its relationship with materials performance and lifetime prediction. *Polymer Degradation and Stability* 98, 2419–2429.
- [50] Celina, M.C., Dayile, A.R., Quintana, A., 2013. A perspective on the inherent oxidation sensitivity of epoxy materials. *Polymer* 54, 3290–3296.
- [51] Chambers, A., Earl, J., Squires, C., Suhot, M., 2006. The effect of voids on the flexural fatigue performance of unidirectional carbon fibre composites developed for wind turbine applications. *International journal of fatigue* 28, 1389–1398.
- [52] Chester, S.A., Anand, L., 2010. A coupled theory of fluid permeation and large deformations for elastomeric materials. *Journal of the Mechanics and Physics of Solids* 58, 1879–1906.
- [53] Chester, S.A., Anand, L., 2011. A thermo-mechanically coupled theory for fluid permeation in elastomeric materials: application to thermally responsive gels. *Journal of the Mechanics and Physics of Solids* 59, 1978–2006.

- [54] Chester, S.A., Di Leo, C.V., Anand, L., 2015. A finite element implementation of a coupled diffusion-deformation theory for elastomeric gels. *International Journal of Solids and Structures* 52, 1–18.
- [55] Cinquin, J., Colin, X., Fayolle, B., Mille, M., Terekhina, S., Chocinski-Arnault, L., Gigliotti, M., Grandidier, J.C., Lafarie-Frenot, M.C., Minervino, M., et al., 2016. Thermo-oxidation behaviour of organic matrix composite materials at high temperatures. *Advances in aircraft and spacecraft science* 3, 171–195.
- [56] Coleman, B.D., Gurtin, M.E., 1967. Thermodynamics with internal state variables. *The journal of chemical physics* 47, 597–613.
- [57] Colin, X., Audouin, L., Verdu, J., 2004. Determination of thermal oxidation rate constants by an inverse method. application to polyethylene. *Polymer Degradation and Stability* 86, 309–321.
- [58] Colin, X., Audouin, L., Verdu, J., 2007. Kinetic modelling of the thermal oxidation of polyisoprene elastomers. part 1: Unvulcanized unstabilized polyisoprene. *Polymer degradation and stability* 92, 886–897.
- [59] Colin, X., Marais, C., Verdu, J., 2001a. A new method for predicting the thermal oxidation of thermoset matrices: application to an amine crosslinked epoxy. *Polymer Testing* 20, 795–803.
- [60] Colin, X., Marais, C., Verdu, J., 2001b. Thermal oxidation kinetics for a poly (bismaleimide). *Journal of Applied Polymer Science* 82, 3418–3430.

- [61] Colin, X., Marais, C., Verdu, J., 2002. Kinetic modelling and simulation of gravimetric curves: application to the oxidation of bismaleimide and epoxy resins. *Polymer Degradation and Stability* 78, 545–553.
- [62] Colin, X., Verdu, J., 2003. Thermal ageing and lifetime prediction for organic matrix composites. *Plastics, rubber and composites* 32, 349–356.
- [63] Colin, X., Verdu, J., 2005. Strategy for studying thermal oxidation of organic matrix composites. *Composites Science and technology* 65, 411–419.
- [64] Colin, X., Verdu, J., 2012. Mechanisms and kinetics of organic matrix thermal oxidation, in: *Long-term durability of polymeric matrix composites*. Springer, pp. 311–344.
- [65] Coquillat, M., Verdu, J., Colin, X., Audouin, L., Nevière, R., 2007. Thermal oxidation of polybutadiene. part 1: Effect of temperature, oxygen pressure and sample thickness on the thermal oxidation of hydroxyl-terminated polybutadiene. *Polymer degradation and stability* 92, 1326–1333.
- [66] Crupi, V., Guglielmino, E., Risitano, G., Tavilla, F., 2015. Experimental analyses of sfrp material under static and fatigue loading by means of thermographic and dic techniques. *Composites Part B: Engineering* 77, 268–277.
- [67] Curtis, P., 1991. Tensile fatigue mechanisms in unidirectional polymer matrix composite materials. *International journal of fatigue* 13, 377–382.

- [68] Daghia, F., Zhang, F., Cluzel, C., Ladevèze, P., 2015. Thermo-mechano-oxidative behavior at the ply's scale: The effect of oxidation on transverse cracking in carbon–epoxy composites. *Composite Structures* 134, 602–612.
- [69] Dal Maso, G., Toader, R., 2002. A model for the quasi-static growth of brittle fractures: Existence and approximation results. *Archive for Rational Mechanics and Analysis* 162, 101–135.
- [70] Danescu, A., 2001. The asaro–tiller–grinfeld instability revisited. *International journal of solids and structures* 38, 4671–4684.
- [71] De Monte, M., Moosbrugger, E., Quaresimin, M., 2010. Influence of temperature and thickness on the off-axis behaviour of short glass fibre reinforced polyamide 6.6–cyclic loading. *Composites Part A: Applied Science and Manufacturing* 41, 1368–1379.
- [72] Decelle, J., Huet, N., Bellenger, V., 2003. Oxidation induced shrinkage for thermally aged epoxy networks. *Polymer Degradation and Stability* 81, 239–248.
- [73] Dehghany, M., Zhang, H., Naghdabadi, R., Hu, Y., 2018. A thermodynamically-consistent large deformation theory coupling photochemical reaction and electrochemistry for light-responsive gels. *Journal of the Mechanics and Physics of Solids* 116, 239–266.

- [74] Denli, F.A., Gültekin, O., Holzapfel, G.A., Dal, H., 2020. A phase-field model for fracture of unidirectional fiber-reinforced polymer matrix composites. *Computational Mechanics* , 1–18.
- [75] Dong, C., Li, K., Jiang, Y., Arola, D., Zhang, D., 2018. Evaluation of thermal expansion coefficient of carbon fiber reinforced composites using electronic speckle interferometry. *Optics express* 26, 531–543.
- [76] Drozdov, A., 1999. A constitutive model in finite thermoviscoelasticity based on the concept of transient networks. *Acta mechanica* 133, 13–37.
- [77] Duda, F.P., Souza, A.C., Fried, E., 2010. A theory for species migration in a finitely strained solid with application to polymer network swelling. *Journal of the Mechanics and Physics of Solids* 58, 515–529.
- [78] Eleftheroglou, N., Loutas, T., 2016. Fatigue damage diagnostics and prognostics of composites utilizing structural health monitoring data and stochastic processes. *Structural Health Monitoring* 15, 473–488.
- [79] Ernault, E., Dirrenberger, J., Richaud, E., Fayolle, B., 2019. Prediction of stress induced by heterogeneous oxidation: Case of epoxy/amine networks. *Polymer Degradation and Stability* 162, 112–121.
- [80] Ernault, E., Richaud, E., Fayolle, B., 2016. Thermal oxidation of epoxies: influence of diamine hardener. *Polymer Degradation and Stability* 134, 76–86.

- [81] Ernault, E., Richaud, E., Fayolle, B., 2017a. Origin of epoxies embrittlement during oxidative ageing. *Polymer Testing* 63, 448–454.
- [82] Ernault, E., Richaud, E., Fayolle, B., 2017b. Thermal-oxidation of epoxy/amine followed by glass transition temperature changes. *Polymer Degradation and Stability* 138, 82–90.
- [83] Esmaeillou, B., Ferreira, P., Bellenger, V., Tcharkhtchi, A., 2012. Fatigue behavior of polyamide 66/glass fiber under various kinds of applied load. *Polymer Composites* 33, 540–547.
- [84] Esmaeillou, B., Fitoussi, J., Lucas, A., Tcharkhtchi, A., 2011. Multi-scale experimental analysis of the tension-tension fatigue behavior of a short glass fiber reinforced polyamide composite. *Procedia Engineering* 10, 2117–2122.
- [85] Fawaz, Z., Ellyin, F., 1994. Fatigue failure model for fibre-reinforced materials under general loading conditions. *Journal of composite materials* 28, 1432–1451.
- [86] Fayolle, B., Audouin, L., Verdu, J., 2004. A critical molar mass separating the ductile and brittle regimes as revealed by thermal oxidation in polypropylene. *Polymer* 45, 4323–4330.
- [87] Fayolle, B., Colin, X., Audouin, L., Verdu, J., 2007. Mechanism of degradation induced embrittlement in polyethylene. *Polymer Degradation and Stability* 92, 231–238.

- [88] Fayolle, B., Richaud, E., Verdu, J., Farcas, F., 2008. Embrittlement of polypropylene fibre during thermal oxidation. *Journal of materials science* 43, 1026–1032.
- [89] Feih, S., Mouritz, A., 2012. Tensile properties of carbon fibres and carbon fibre–polymer composites in fire. *Composites Part A: Applied Science and Manufacturing* 43, 765–772.
- [90] Feih, S., Mouritz, A., Mathys, Z., Gibson, A., 2007. Tensile strength modeling of glass fiber—polymer composites in fire. *Journal of composite materials* 41, 2387–2410.
- [91] Flory, P., 1953. *Principles of polymer chemistry*; cornell university. Ithaca, New York 579.
- [92] Flory, P., 1961. Thermodynamic relations for high elastic materials. *Transactions of the Faraday Society* 57, 829–838.
- [93] Francfort, G.A., Marigo, J.J., 1998. Revisiting brittle fracture as an energy minimization problem. *Journal of the Mechanics and Physics of Solids* 46, 1319–1342.
- [94] Fried, E., Gurtin, M.E., 1999. Coherent solid-state phase transitions with atomic diffusion: a thermomechanical treatment. *Journal of Statistical Physics* 95, 1361–1427.

- [95] Gaier, C., Fischmeister, S., Maier, J., Pinter, G., 2017. Fatigue analysis of continuously carbon fiber reinforced laminates. *SAE International Journal of Engines* 10, 305–315.
- [96] Gamstedt, E., Talreja, R., 1999. Fatigue damage mechanisms in unidirectional carbon-fibre-reinforced plastics. *Journal of materials science* 34, 2535–2546.
- [97] Gaurav, A., Singh, K.K., 2018. Fatigue behavior of frp composites and cnt-embedded frp composites: A review. *Polymer Composites* 39, 1785–1808.
- [98] Gent, A., Lai, S.M., 1994. Interfacial bonding, energy dissipation, and adhesion. *Journal of Polymer Science Part B: Polymer Physics* 32, 1543–1555.
- [99] Gent, A.N., 1996. A new constitutive relation for rubber. *Rubber chemistry and technology* 69, 59–61.
- [100] Gent, A.N., 2012. *Engineering with rubber: how to design rubber components*. Carl Hanser Verlag GmbH Co KG.
- [101] Gibbs, J.W., 1902. *Elementary principles in statistical mechanics: developed with especial reference to the rational foundation of thermodynamics*. C. Scribner's sons.

- [102] Gigliotti, M., Minervino, M., Lafarie-Frenot, M., 2016a. Thermo-oxidative induced shrinkage in organic matrix composites for high temperature applications: effect of fibre arrangement and oxygen pressure. *Composite Structures* 146, 176–186.
- [103] Gigliotti, M., Minervino, M., Lafarie-Frenot, M., Grandidier, J., 2016b. Effect of thermo-oxidation on the local mechanical behaviour of epoxy polymer materials for high temperature applications. *Mechanics of Materials* 101, 118–135.
- [104] Gigliotti, M., Olivier, L., Vu, D.Q., Grandidier, J.C., Lafarie-Frenot, M.C., 2011. Local shrinkage and stress induced by thermo-oxidation in composite materials at high temperatures. *Journal of the Mechanics and Physics of Solids* 59, 696–712.
- [105] Gilat, A., Goldberg, R.K., Roberts, G.D., 2002. Experimental study of strain-rate-dependent behavior of carbon/epoxy composite. *Composites Science and Technology* 62, 1469–1476. URL: <https://www.sciencedirect.com/science/article/pii/S0266353802001008>, doi:[https://doi.org/10.1016/S0266-3538\(02\)00100-8](https://doi.org/10.1016/S0266-3538(02)00100-8).
- [106] Gillen, K., Celina, M., Bernstein, R., 2004. Review of the ultrasensitive oxygen consumption method for making more reliable extrapolated predictions of polymer lifetimes, in: ANTEC... conference proceedings, Society of Plastics Engineers. pp. 2289–2293.

- [107] Gillen, K.T., Bernstein, R., Celina, M., 2005a. Non-arrhenius behavior for oxidative degradation of chlorosulfonated polyethylene materials. *Polymer degradation and stability* 87, 335–346.
- [108] Gillen, K.T., Bernstein, R., Derzon, D.K., 2005b. Evidence of non-arrhenius behaviour from laboratory aging and 24-year field aging of polychloroprene rubber materials. *Polymer Degradation and Stability* 87, 57–67.
- [109] Gillen, K.T., Celina, M., Keenan, M.R., 2000. Methods for predicting more confident lifetimes of seals in air environments. *Rubber chemistry and technology* 73, 265–283.
- [110] Godara, A., Raabe, D., 2007. Influence of fiber orientation on global mechanical behavior and mesoscale strain localization in a short glass-fiber-reinforced epoxy polymer composite during tensile deformation investigated using digital image correlation. *Composites Science and technology* 67, 2417–2427.
- [111] Goel, A., Chawla, K., Vaidya, U., Chawla, N., Koopman, M., 2009. Characterization of fatigue behavior of long fiber reinforced thermoplastic (lft) composites. *Materials characterization* 60, 537–544.
- [112] Govaert, L., Timmermans, P., Brekelmans, W., 2000. The influence of intrinsic strain softening on strain localization in polycarbonate: modeling and experimental validation. *Journal of Engineering Materials and Technology* 122, 177–185.

- [113] Govindjee, S., Simo, J.C., 1993. Coupled stress-diffusion: Case ii. *Journal of the Mechanics and Physics of Solids* 41, 863–887.
- [114] Gültekin, O., Dal, H., Holzapfel, G.A., 2016. A phase-field approach to model fracture of arterial walls: theory and finite element analysis. *Computer methods in applied mechanics and engineering* 312, 542–566.
- [115] Gültekin, O., Dal, H., Holzapfel, G.A., 2018. Numerical aspects of anisotropic failure in soft biological tissues favor energy-based criteria: A rate-dependent anisotropic crack phase-field model. *Computer methods in applied mechanics and engineering* 331, 23–52.
- [116] Guo, Y., Ruan, K., Shi, X., Yang, X., Gu, J., 2020. Factors affecting thermal conductivities of the polymers and polymer composites: A review. *Composites Science and Technology* 193, 108134.
- [117] Gurtin, M.E., 1996. Generalized ginzburg-landau and cahn-hilliard equations based on a microforce balance. *Physica D: Nonlinear Phenomena* 92, 178–192.
- [118] Gurtin, M.E., Fried, E., Anand, L., 2010. *The mechanics and thermodynamics of continua*. Cambridge University Press.
- [119] Harper, P.W., Hallett, S.R., 2010. A fatigue degradation law for cohesive interface elements—development and application to composite materials. *International Journal of Fatigue* 32, 1774–1787.

- [120] Harris, B., 2003. Fatigue in composites: science and technology of the fatigue response of fibre-reinforced plastics. Woodhead Publishing.
- [121] Hashin, Z., Rotem, A., 1973. A fatigue failure criterion for fiber reinforced materials. *Journal of composite materials* 7, 448–464.
- [122] Haveroth, G., Vale, M., Bittencourt, M., Boldrini, J., 2020. A non-isothermal thermodynamically consistent phase field model for damage, fracture and fatigue evolutions in elasto-plastic materials. *Computer Methods in Applied Mechanics and Engineering* 364, 112962.
- [123] Hoffmann, J., Cui, H., Petrinic, N., 2018. Determination of the strain-energy release rate of a composite laminate under high-rate tensile deformation in fibre direction. *Composites Science and Technology* 164, 110–119.
- [124] Holzapfel, A.G., 2000. *Nonlinear solid mechanics ii* .
- [125] Holzapfel, G.A., 1996. On large strain viscoelasticity: continuum formulation and finite element applications to elastomeric structures. *International Journal for Numerical Methods in Engineering* 39, 3903–3926.
- [126] Holzapfel, G.A., Simo, J., 1996a. Entropy elasticity of isotropic rubber-like solids at finite strains. *Computer Methods in applied mechanics and engineering* 132, 17–44.

- [127] Holzapfel, G.A., Simo, J.C., 1996b. A new viscoelastic constitutive model for continuous media at finite thermomechanical changes. *International Journal of Solids and Structures* 33, 3019–3034.
- [128] Horgan, C.O., Saccomandi, G., 2002. A molecular-statistical basis for the gent constitutive model of rubber elasticity. *Journal of Elasticity* 68, 167–176.
- [129] Hörrmann, S., Adumitroaie, A., Viechtbauer, C., Schagerl, M., 2016. The effect of fiber waviness on the fatigue life of cfrp materials. *International Journal of Fatigue* 90, 139–147.
- [130] Hosoi, A., Kawada, H., 2018. Fatigue life prediction for transverse crack initiation of cfrp cross-ply and quasi-isotropic laminates. *Materials* 11, 1182.
- [131] Huang, J., Pastor, M.L., Garnier, C., Gong, X.J., 2019. A new model for fatigue life prediction based on infrared thermography and degradation process for cfrp composite laminates. *International Journal of Fatigue* 120, 87–95.
- [132] Huang, Z.M., 2002. Fatigue life prediction of a woven fabric composite subjected to biaxial cyclic loads. *Composites Part A: Applied Science and Manufacturing* 33, 253–266.
- [133] Hwang, G.W., Kim, J.W., Cho, J.U., 2018. A study on the fracture behavior of cfrp specimen with bonding interface under mode 1 fatigue load according to laminate angle. *International Journal of Precision Engineering and Manufacturing* 19, 1829–1836.

- [134] Jacob, G.C., Starbuck, J.M., Fellers, J.F., Simunovic, S., Boeman, R.G., 2004. Strain rate effects on the mechanical properties of polymer composite materials. *Journal of Applied Polymer Science* 94, 296–301.
- [135] Jespersen, K.M., Glud, J.A., Zangenberg, J., Hosoi, A., Kawada, H., Mikkelsen, L.P., 2018. Uncovering the fatigue damage initiation and progression in uni-directional non-crimp fabric reinforced polyester composite. *Composites Part A: Applied Science and Manufacturing* 109, 481–497.
- [136] Jespersen, K.M., Zangenberg, J., Lowe, T., Withers, P.J., Mikkelsen, L.P., 2016. Fatigue damage assessment of uni-directional non-crimp fabric reinforced polyester composite using x-ray computed tomography. *Composites Science and Technology* 136, 94–103.
- [137] Katunin, A., 2012. Thermal fatigue of polymeric composites under repeated loading. *Journal of Reinforced Plastics and Composites* 31, 1037–1044.
- [138] Katunin, A., Fidali, M., 2012. Fatigue and thermal failure of polymeric composites subjected to cyclic loading. *Advanced Composites Letters* 21, 096369351202100301.
- [139] Katunin, A., Wronkiewicz, A., 2017. Characterization of failure mechanisms of composite structures subjected to fatigue dominated by the self-heating effect. *Composite Structures* 180, 1–8.

- [140] Kawai, M., Taniguchi, T., 2006. Off-axis fatigue behavior of plain weave carbon/epoxy fabric laminates at room and high temperatures and its mechanical modeling. *Composites Part A: Applied Science and Manufacturing* 37, 243–256.
- [141] Khan, R., Khan, Z., Al-Sulaiman, F., Merah, N., 2002. Fatigue life estimates in woven carbon fabric/epoxy composites at non-ambient temperatures. *Journal of composite materials* 36, 2517–2535.
- [142] Kim, W., Argento, A., Lee, E., Flanigan, C., Houston, D., Harris, A., Mielewski, D.F., 2012. High strain-rate behavior of natural fiber-reinforced polymer composites. *Journal of Composite Materials* 46, 1051–1065.
- [143] Konica, S., Sain, T., 2020. A thermodynamically consistent chemo-mechanically coupled large deformation model for polymer oxidation. *Journal of the Mechanics and Physics of Solids* 137, 103858.
- [144] Konica, S., Sain, T., 2021a. A homogenized large deformation constitutive model for high temperature oxidation in fiber-reinforced polymer composites. *Mechanics of Materials* 160, 103994.
- [145] Konica, S., Sain, T., 2021b. A reaction-driven evolving network theory coupled with phase-field fracture to model polymer oxidative aging. *Journal of the Mechanics and Physics of Solids* 150, 104347.
- [146] Kuhn, W., Grün, F., 1946. Statistical behavior of the single chain molecule and

- its relation to the statistical behavior of assemblies consisting of many chain molecules. *Journal of polymer science* 1, 183–199.
- [147] KUMAR, M., GAUR, K.K., SHAKHER, C., 2015. Measurement of material constants (young’s modulus and poisson’s ratio) of polypropylene using digital speckle pattern interferometry (dspe). *Journal of the Japanese Society for Experimental Mechanics* 15, s87–s91.
- [148] Lafarie-Frenot, M., Grandidier, J.C., Gigliotti, M., Olivier, L., Colin, X., Verdu, J., Cinquin, J., 2010. Thermo-oxidation behaviour of composite materials at high temperatures: A review of research activities carried out within the comedi program. *Polymer Degradation and Stability* 95, 965–974.
- [149] Leibler, L., Sekimoto, K., 1993. On the sorption of gases and liquids in glassy polymers. *Macromolecules* 26, 6937–6939.
- [150] Li, B., Maurini, C., 2019. Crack kinking in a variational phase-field model of brittle fracture with strongly anisotropic surface energy. *Journal of the Mechanics and Physics of Solids* 125, 502–522.
- [151] Lifshitz, J.M., 1976. Impact strength of angle ply fiber reinforced materials. *Journal of Composite Materials* 10, 92–101.
- [152] Linder, C., Tkachuk, M., Miehe, C., 2011. A micromechanically motivated diffusion-based transient network model and its incorporation into finite rubber viscoelasticity. *Journal of the Mechanics and Physics of Solids* 59, 2134–2156.

- [153] Loeffel, K., Anand, L., 2011. A chemo-thermo-mechanically coupled theory for elastic–viscoplastic deformation, diffusion, and volumetric swelling due to a chemical reaction. *International Journal of Plasticity* 27, 1409–1431.
- [154] Logg, A., Mardal, K.A., Wells, G., 2012. Automated solution of differential equations by the finite element method: The FEniCS book. volume 84. Springer Science & Business Media.
- [155] Long, R., Qi, H.J., Dunn, M.L., 2013. Modeling the mechanics of covalently adaptable polymer networks with temperature-dependent bond exchange reactions. *Soft Matter* 9, 4083–4096.
- [156] Lorentz, E., 2017. A nonlocal damage model for plain concrete consistent with cohesive fracture. *International Journal of Fracture* 207, 123–159.
- [157] Lorentz, E., Cuvilliez, S., Kazymyrenko, K., 2011. Convergence of a gradient damage model toward a cohesive zone model. *Comptes Rendus Mécanique* 339, 20–26.
- [158] Loutas, T., Eleftheroglou, N., Zarouchas, D., 2017. A data-driven probabilistic framework towards the in-situ prognostics of fatigue life of composites based on acoustic emission data. *Composite Structures* 161, 522–529.
- [159] Lubarda, V.A., 2004. Constitutive theories based on the multiplicative decomposition of deformation gradient: Thermoelasticity, elastoplasticity, and biomechanics. *Applied Mechanics Reviews* 57, 95–108.

- [160] Maimí, P., Camanho, P.P., Mayugo, J., Dávila, C., 2007. A continuum damage model for composite laminates: Part i—constitutive model. *Mechanics of materials* 39, 897–908.
- [161] Malpot, A., Touchard, F., Bergamo, S., 2017. An investigation of the influence of moisture on fatigue damage mechanisms in a woven glass-fibre-reinforced pa66 composite using acoustic emission and infrared thermography. *Composites Part B: Engineering* 130, 11–20.
- [162] Mangalgiri, P., 2005. Polymer-matrix composites for high-temperature applications. *Defence Science Journal* 55, 175.
- [163] Mao, H., Mahadevan, S., 2002. Fatigue damage modelling of composite materials. *Composite Structures* 58, 405–410.
- [164] Mao, Y., Anand, L., 2018. A theory for fracture of polymeric gels. *Journal of the Mechanics and Physics of Solids* 115, 30–53.
- [165] Mao, Y., Talamini, B., Anand, L., 2017. Rupture of polymers by chain scission. *Extreme Mechanics Letters* 13, 17–24.
- [166] Martínez-Pañeda, E., Golahmar, A., Niordson, C.F., 2018. A phase field formulation for hydrogen assisted cracking. *Computer Methods in Applied Mechanics and Engineering* 342, 742–761.

- [167] Marzocca, A.J., Somoza, A., Goyanes, S.N., Salgueiro, W., König, P., 2002. Characterization of free volume in particulate-filled epoxy resin by means of dynamic mechanical analysis and positron annihilation lifetime spectroscopy. *Polymer international* 51, 1277–1284.
- [168] McManus, H., Foch, B., Cunningham, R., 2000. Mechanism-based modeling of long-term degradation. *Journal of Composites, Technology and Research* 22, 146–152.
- [169] Miehe, C., Hofacker, M., Welschinger, F., 2010a. A phase field model for rate-independent crack propagation: Robust algorithmic implementation based on operator splits. *Computer Methods in Applied Mechanics and Engineering* 199, 2765–2778.
- [170] Miehe, C., Schaenzel, L.M., Ulmer, H., 2015. Phase field modeling of fracture in multi-physics problems. part i. balance of crack surface and failure criteria for brittle crack propagation in thermo-elastic solids. *Computer Methods in Applied Mechanics and Engineering* 294, 449–485.
- [171] Miehe, C., Welschinger, F., Hofacker, M., 2010b. Thermodynamically consistent phase-field models of fracture: Variational principles and multi-field fe implementations. *International Journal for Numerical Methods in Engineering* 83, 1273–1311.

- [172] Minervino, M., Gigliotti, M., Lafarie-Frenot, M., Grandidier, J., 2013. The effect of thermo-oxidation on the mechanical behaviour of polymer epoxy materials. *Polymer Testing* 32, 1020–1028.
- [173] Minervino, M., Gigliotti, M., Lafarie-Frenot, M., Grandidier, J., 2014. A coupled experimental/numerical approach for the modelling of the local mechanical behaviour of epoxy polymer materials. *Journal of the Mechanics and Physics of Solids* 67, 129–151.
- [174] Mlyniec, A., Korta, J., Kudelski, R., Uhl, T., 2014. The influence of the laminate thickness, stacking sequence and thermal aging on the static and dynamic behavior of carbon/epoxy composites. *Composite Structures* 118, 208–216.
- [175] Mohammadi, H., Morovati, V., Poshtan, E., Dargazany, R., 2020. Understanding decay functions and their contribution in modeling of thermal-induced aging of cross-linked polymers. *Polymer Degradation and Stability* , 109108.
- [176] Mohammadi, R., Najafabadi, M.A., Saeedifar, M., Yousefi, J., Minak, G., 2017. Correlation of acoustic emission with finite element predicted damages in open-hole tensile laminated composites. *Composites Part B: Engineering* 108, 427–435.
- [177] Montanini, R., d’Acquisto, L., 2007. Simultaneous measurement of temperature and strain in glass fiber/epoxy composites by embedded fiber optic sensors: I. cure monitoring. *Smart Materials and Structures* 16, 1718.

- [178] Montazeri, A., Pourshamsian, K., Riazian, M., 2012. Viscoelastic properties and determination of free volume fraction of multi-walled carbon nanotube/epoxy composite using dynamic mechanical thermal analysis. *Materials & Design* (1980-2015) 36, 408–414.
- [179] Mulliken, A., Boyce, M., 2006. Mechanics of the rate-dependent elastic–plastic deformation of glassy polymers from low to high strain rates. *International journal of solids and structures* 43, 1331–1356.
- [180] Naderi, M., Khonsari, M., 2012a. A comprehensive fatigue failure criterion based on thermodynamic approach. *Journal of composite materials* 46, 437–447.
- [181] Naderi, M., Khonsari, M., 2012b. Thermodynamic analysis of fatigue failure in a composite laminate. *Mechanics of Materials* 46, 113–122.
- [182] Nagaraja, S., Leichsenring, K., Ambati, M., De Lorenzis, L., Böl, M., 2021. On a phase-field approach to model fracture of small intestine walls. *Acta Biomaterialia* .
- [183] Naghipour, P., Pineda, E., Arnold, S., 2016. Simulation of lightning-induced delamination in un-protected cfrp laminates. *Applied Composite Materials* 23, 523–535.
- [184] Nam, J., Seferis, J., 1992. Anisotropic thermo-oxidative stability of carbon fiber reinforced polymeric composites. *Sampe Quarterly* 24, 10–18.

- [185] Narayan, S., Anand, L., 2019. A gradient-damage theory for fracture of quasi-brittle materials. *Journal of the Mechanics and Physics of Solids* 129, 119–146.
- [186] Narayan, S., Anand, L., 2021. Fracture of amorphous polymers: A gradient-damage theory. *Journal of the Mechanics and Physics of Solids* 146, 104164.
- [187] Nardinocchi, P., Pezzulla, M., Teresi, L., 2015. Anisotropic swelling of thin gel sheets. *Soft Matter* 11, 1492–1499.
- [188] Nelson, J.B., 1983. Thermal aging of graphite/polyimide composites, in: Long-term behavior of composites. ASTM International.
- [189] Nguyen, T., Jones, R., Boyce, B., 2008. A nonlinear anisotropic viscoelastic model for the tensile behavior of the corneal stroma. *Journal of biomechanical engineering* 130.
- [190] Nguyen, T.T., Yvonnet, J., Zhu, Q.Z., Bornert, M., Chateau, C., 2016. A phase-field method for computational modeling of interfacial damage interacting with crack propagation in realistic microstructures obtained by microtomography. *Computer Methods in Applied Mechanics and Engineering* 312, 567–595.
- [191] Nixon-Pearson, O., Hallett, S., Harper, P., Kawashita, L., 2013a. Damage development in open-hole composite specimens in fatigue. part 2: Numerical modelling. *Composite Structures* 106, 890–898.

- [192] Nixon-Pearson, O., Hallett, S., Withers, P., Rouse, J., 2013b. Damage development in open-hole composite specimens in fatigue. part 1: Experimental investigation. *Composite Structures* 106, 882–889.
- [193] Olivier, L., Ho, N., Grandidier, J., Lafarie-Frenot, M., 2008. Characterization by ultra-micro indentation of an oxidized epoxy polymer: correlation with the predictions of a kinetic model of oxidation. *Polymer Degradation and Stability* 93, 489–497.
- [194] Ou, Y., Zhu, D., 2015. Tensile behavior of glass fiber reinforced composite at different strain rates and temperatures. *Construction and Building Materials* 96, 648–656.
- [195] Owen, M., Griffiths, J., 1978. Evaluation of biaxial stress failure surfaces for a glass fabric reinforced polyester resin under static and fatigue loading. *Journal of Materials Science* 13, 1521–1537.
- [196] Pan, Y., Zhong, Z., 2014. A nonlinear constitutive model of unidirectional natural fiber reinforced composites considering moisture absorption. *Journal of the Mechanics and Physics of Solids* 69, 132–142.
- [197] Pecora, M., Pannier, Y., Lafarie-Frenot, M.C., Gigliotti, M., Guigon, C., 2016. Effect of thermo-oxidation on the failure properties of an epoxy resin. *Polymer Testing* 52, 209–217.

- [198] Peng, T., Liu, Y., Saxena, A., Goebel, K., 2015. In-situ fatigue life prognosis for composite laminates based on stiffness degradation. *Composite Structures* 132, 155–165.
- [199] Pham, K., Amor, H., Marigo, J.J., Maurini, C., 2011. Gradient damage models and their use to approximate brittle fracture. *International Journal of Damage Mechanics* 20, 618–652.
- [200] Pochiraju, K., Tandon, G., Schoeppner, G., 2008. Evolution of stress and deformations in high-temperature polymer matrix composites during thermo-oxidative aging. *Mechanics of Time-Dependent Materials* 12, 45–68.
- [201] Pochiraju, K., Tandon, G.P., 2009. Interaction of oxidation and damage in high temperature polymeric matrix composites. *Composites Part A: Applied Science and Manufacturing* 40, 1931–1940.
- [202] Pochiraju, K.V., 2012. Modeling thermo-oxidative aging and degradation of composites, in: *Long-term durability of polymeric matrix composites*. Springer, pp. 383–425.
- [203] Puck, A., Schürmann, H., 2004. Failure analysis of frp laminates by means of physically based phenomenological models, in: *Failure criteria in fibre-reinforced-polymer composites*. Elsevier, pp. 832–876.
- [204] Qi, H.J., Nguyen, T.D., Castro, F., Yakacki, C.M., Shandas, R., 2008. Finite

- deformation thermo-mechanical behavior of thermally induced shape memory polymers. *Journal of the Mechanics and Physics of Solids* 56, 1730–1751.
- [205] Qiu, G., Pence, T., 1997. Remarks on the behavior of simple directionally reinforced incompressible nonlinearly elastic solids. *Journal of Elasticity* 49, 1–30.
- [206] Quintana, A., Celina, M.C., 2018. Overview of dlo modeling and approaches to predict heterogeneous oxidative polymer degradation. *Polymer Degradation and Stability* 149, 173–191.
- [207] Quintanas-Corominas, A., Reinoso, J., Casoni, E., Turon, A., Mayugo, J., 2019. A phase field approach to simulate intralaminar and translaminar fracture in long fiber composite materials. *Composite Structures* 220, 899–911.
- [208] Quintanas-Corominas, A., Turon, A., Reinoso, J., Casoni, E., Paggi, M., Mayugo, J., 2020. A phase field approach enhanced with a cohesive zone model for modeling delamination induced by matrix cracking. *Computer Methods in Applied Mechanics and Engineering* 358, 112618.
- [209] Reese, S., Govindjee, S., 1997. Theoretical and numerical aspects in the thermo-viscoelastic material behaviour of rubber-like polymers. *Mechanics of Time-Dependent Materials* 1, 357–396.
- [210] Reinoso, J., Arteiro, A., Paggi, M., Camanho, P., 2017. Strength prediction of

notched thin ply laminates using finite fracture mechanics and the phase field approach. *Composites Science and Technology* 150, 205–216.

- [211] Reis, J., Coelho, J., Monteiro, A., da Costa Mattos, H., 2012. Tensile behavior of glass/epoxy laminates at varying strain rates and temperatures. *Composites Part B: Engineering* 43, 2041–2046.
- [212] Richaud, E., Farcas, F., Bartolomé, P., Fayolle, B., Audouin, L., Verdu, J., 2006. Effect of oxygen pressure on the oxidation kinetics of unstabilised polypropylene. *Polymer Degradation and Stability* 91, 398–405.
- [213] Rincon-Rubio, L., Fayolle, B., Audouin, L., Verdu, J., 2001. A general solution of the closed-loop kinetic scheme for the thermal oxidation of polypropylene. *Polymer Degradation and Stability* 74, 177–188.
- [214] Robert, M., Benmokrane, B., 2010. Behavior of gfrp reinforcing bars subjected to extreme temperatures. *Journal of Composites for Construction* 14, 353–360.
- [215] Robinson, P., Galvanetto, U., Tumino, D., Bellucci, G., Violeau, D., 2005. Numerical simulation of fatigue-driven delamination using interface elements. *International journal for numerical methods in engineering* 63, 1824–1848.
- [216] Rodriguez, A., Mansoor, B., Ayoub, G., Colin, X., Benzerga, A., 2020. Effect of uv-aging on the mechanical and fracture behavior of low density polyethylene. *Polymer Degradation and Stability* , 109185.

- [217] Rotem, A., Lifshitz, J., 1971. Longitudinal strength of unidirectional fibrous composite under high rate of loading, in: Proceeding of 26th Annual Technology Conference, Society for Plastics Industry, pp. 1–10.
- [218] Rotem, A., Nelson, H., 1989. Failure of a laminated composite under tension-compression fatigue loading. *Composites Science and technology* 36, 45–62.
- [219] Rubinstein, M., Colby, R.H., et al., 2003. *Polymer physics*. volume 23. Oxford university press New York.
- [220] Sain, T., Loeffel, K., Chester, S., 2018. A thermo-chemo-mechanically coupled constitutive model for curing of glassy polymers. *Journal of the Mechanics and Physics of Solids* 116, 267–289.
- [221] Sain, T., Meaud, J., Yeom, B., Waas, A.M., Arruda, E.M., 2015. Rate dependent finite strain constitutive modeling of polyurethane and polyurethane-clay nanocomposites. *International Journal of Solids and Structures* 54, 147–155.
- [222] Salin, I., Seferis, J.C., 1996. Anisotropic degradation of polymeric composites: from neat resin to composite. *Polymer Composites* 17, 430–442.
- [223] Schänzel, L.M., 2015. Phase field modeling of fracture in rubbery and glassy polymers at finite thermo-viscoelastic deformations.
- [224] Schoeppner, G., Tandon, G., Ripberger, E., 2007. Anisotropic oxidation and

- weight loss in pmr-15 composites. *Composites Part A: Applied Science and Manufacturing* 38, 890–904.
- [225] Scholes, C.A., Stevens, G.W., Kentish, S.E., 2010. The effect of hydrogen sulfide, carbon monoxide and water on the performance of a pdms membrane in carbon dioxide/nitrogen separation. *Journal of Membrane Science* 350, 189–199.
- [226] Seiler, M., Linse, T., Hantschke, P., Kästner, M., 2020. An efficient phase-field model for fatigue fracture in ductile materials. *Engineering Fracture Mechanics* 224, 106807.
- [227] Sicsic, P., Marigo, J.J., 2013. From gradient damage laws to griffith’s theory of crack propagation. *Journal of Elasticity* 113, 55–74.
- [228] Sims, D., Brogdon, V., 1977. Fatigue behavior of composites under different loading modes, in: *Fatigue of filamentary composite materials*. ASTM International.
- [229] Sisodia, S., Gamstedt, E.K., Edgren, F., Varna, J., 2015. Effects of voids on quasi-static and tension fatigue behaviour of carbon-fibre composite laminates. *Journal of composite materials* 49, 2137–2148.
- [230] Siviour, C.R., Jordan, J.L., 2016. High strain rate mechanics of polymers: a review. *Journal of Dynamic Behavior of Materials* 2, 15–32.

- [231] Skontorp, A., Wong, M.S., Wang, S.S., 1995. High-temperature anisotropic thermal oxidation of carbon-fiber reinforced polyimide composites: theory and experiment, in: 10th Intern. Conference. on Composite. Material (ICCM-10), pp. 375–382.
- [232] Spencer, A.J.M., 1984. Constitutive Theory for Strongly Anisotropic Solids. Springer Vienna, Vienna. pp. 1–32. URL: https://doi.org/10.1007/978-3-7091-4336-0_1, doi:10.1007/978-3-7091-4336-0_1.
- [233] Srivastava, V., Chester, S.A., Ames, N.M., Anand, L., 2010. A thermo-mechanically-coupled large-deformation theory for amorphous polymers in a temperature range which spans their glass transition. *International Journal of Plasticity* 26, 1138–1182.
- [234] Strobl, G.R., Strobl, G.R., 1997. The physics of polymers. volume 2. Springer.
- [235] Subramanian, S., Reifsnider, K., Stinchcomb, W., 1995. A cumulative damage model to predict the fatigue life of composite laminates including the effect of a fibre-matrix interphase. *International Journal of Fatigue* 17, 343–351.
- [236] Tai, N., Ma, C., Wu, S., 1995. Fatigue behaviour of carbon fibre/peek laminate composites. *Composites* 26, 551–559.
- [237] Talamini, B., Mao, Y., Anand, L., 2018. Progressive damage and rupture in polymers. *Journal of the Mechanics and Physics of Solids* 111, 434–457.

- [238] Talreja, R., 1981. Fatigue of composite materials: damage mechanisms and fatigue-life diagrams. *Proceedings of the Royal Society of London. A. Mathematical and Physical Sciences* 378, 461–475.
- [239] Tanaka, F., Edwards, S., 1992. Viscoelastic properties of physically crosslinked networks. 1. transient network theory. *Macromolecules* 25, 1516–1523.
- [240] Tandon, G., Pochiraju, K., Schoeppner, G., 2006. Modeling of oxidative development in pmr-15 resin. *Polymer Degradation and Stability* 91, 1861–1869.
- [241] Tandon, G., Pochiraju, K., Schoeppner, G., 2008. Thermo-oxidative behavior of high-temperature pmr-15 resin and composites. *Materials Science and Engineering: A* 498, 150–161.
- [242] Tanné, E., Li, T., Bourdin, B., Marigo, J.J., Maurini, C., 2018. Crack nucleation in variational phase-field models of brittle fracture. *Journal of the Mechanics and Physics of Solids* 110, 80–99.
- [243] Tobolsky, A.V., Metz, D.J., Mesrobian, R.B., 1950. Low temperature autoxidation of hydrocarbons: the phenomenon of maximum rates¹, 2. *Journal of the American Chemical Society* 72, 1942–1952.
- [244] Tong, X., Chen, X., Xu, J.s., Zheng, Y., Zhi, S.j., 2018. The heat build-up of a polymer matrix composite under cyclic loading: Experimental assessment and numerical simulation. *International Journal of Fatigue* 116, 323–333.

- [245] Topal, S., Baiocchi, L., Crocombe, A.D., Ogin, S.L., Potluri, P., Withers, P.J., Quaresimin, M., Smith, P.A., Poole, M.C., Bogdanovich, A.E., 2015. Late-stage fatigue damage in a 3d orthogonal non-crimp woven composite: An experimental and numerical study. *Composites Part A: Applied Science and Manufacturing* 79, 155–163.
- [246] Treolar, L., 1975. *The physics of rubber elasticity*. clarendon.
- [247] Tsai, J., Sun, C., 2002. Constitutive model for high strain rate response of polymeric composites. *Composites Science and Technology* 62, 1289–1297.
- [248] Turon, A., Camanho, P.P., Costa, J., Dávila, C., 2006. A damage model for the simulation of delamination in advanced composites under variable-mode loading. *Mechanics of materials* 38, 1072–1089.
- [249] Turon, A., Costa, J., Camanho, P., Dávila, C., 2007. Simulation of delamination in composites under high-cycle fatigue. *Composites Part A: applied science and manufacturing* 38, 2270–2282.
- [250] Ulm, F.J., Coussy, O., Kefei, L., Larive, C., 2000. Thermo-chemo-mechanics of asr expansion in concrete structures. *Journal of engineering mechanics* 126, 233–242.
- [251] Upadhyaya, D., Tsakirooulos, P., 1995. Evaluation of the effect of sizing levels on transverse flexural and shear strengths of carbon/epoxy composites. *Journal of Materials Processing Technology* 54, 17 – 20. URL: <http://www>.

sciencedirect.com/science/article/pii/S092401369501912X, doi:[https://doi.org/10.1016/0924-0136\(95\)01912-X](https://doi.org/10.1016/0924-0136(95)01912-X).

- [252] Veitmann, M., Jumeau, R., Bourson, P., Ferriol, M., Lahure, F., 2014. Understanding and control of high temperature oxidation flaws of low-density poly(ethylene) with raman spectroscopy. *International Journal of Spectroscopy* 2014, 1–9. doi:10.1155/2014/194563.
- [253] Vernerey, F.J., 2018. Transient response of nonlinear polymer networks: A kinetic theory. *Journal of the Mechanics and Physics of Solids* 115, 230–247.
- [254] Vernerey, F.J., Brighenti, R., Long, R., Shen, T., 2018. Statistical damage mechanics of polymer networks. *Macromolecules* 51, 6609–6622.
- [255] Vernerey, F.J., Long, R., Brighenti, R., 2017. A statistically-based continuum theory for polymers with transient networks. *Journal of the Mechanics and Physics of Solids* 107, 1–20.
- [256] Vu, D.Q., Gigliotti, M., Lafarie-Frenot, M.C., 2012. Experimental characterization of thermo-oxidation-induced shrinkage and damage in polymer–matrix composites. *Composites Part A: Applied Science and Manufacturing* 43, 577–586.
- [257] Wang, J., Potter, K., Etches, J., 2013. Experimental investigation and characterisation techniques of compressive fatigue failure of composites with fibre waviness at ply drops. *Composite Structures* 100, 398–403.

- [258] Wang, Y., Waisman, H., 2015. Progressive delamination analysis of composite materials using xfem and a discrete damage zone model. *Computational Mechanics* 55, 1–26.
- [259] Whitley, K.S., Gates, T.S., 2004. Thermal/mechanical response of a polymer matrix composite at cryogenic temperatures. *AIAA journal* 42, 1991–2001.
- [260] Williams, M.L., Landel, R.F., Ferry, J.D., 1955. The temperature dependence of relaxation mechanisms in amorphous polymers and other glass-forming liquids. *Journal of the American Chemical society* 77, 3701–3707.
- [261] Wise, J., Gillen, K., Clough, R., 1995. An ultrasensitive technique for testing the arrhenius extrapolation assumption for thermally aged elastomers. *Polymer Degradation and Stability* 49, 403–418.
- [262] Wise, J., Gillen, K., Clough, R., 1997. Quantitative model for the time development of diffusion-limited oxidation profiles. *Polymer* 38, 1929–1944.
- [263] Wu, J., Zhao, Z., Hamel, C.M., Mu, X., Kuang, X., Guo, Z., Qi, H.J., 2018. Evolution of material properties during free radical photopolymerization. *Journal of the Mechanics and Physics of Solids* 112, 25–49.
- [264] Wu, J.Y., Nguyen, V.P., 2018. A length scale insensitive phase-field damage model for brittle fracture. *Journal of the Mechanics and Physics of Solids* 119, 20–42.

- [265] Wu, P., Van Der Giessen, E., 1993. On improved network models for rubber elasticity and their applications to orientation hardening in glassy polymers. *Journal of the Mechanics and Physics of Solids* 41, 427–456.
- [266] Wu, P., Xu, L., Luo, J., Zhang, X., Bian, W., 2019. Tension-tension fatigue performances of a pultruded carbon fiber reinforced epoxy plate at elevated temperatures. *Composite Structures* 215, 421–431.
- [267] Xuan, C., Jin, L., 2019. Concurrent reaction and diffusion in photo-responsive hydrogels. *Journal of the Mechanics and Physics of Solids* 124, 599–611.
- [268] Yazdani, S., Rust, W.J., Wriggers, P., 2016. An xfem approach for modelling delamination in composite laminates. *Composite Structures* 135, 353–364.
- [269] Yeh, C.J., Dowland, M., Schmidt, R.G., Shull, K.R., 2016. Fracture and thermal aging of resin-filled silicone elastomers. *Journal of Polymer Science Part B: Polymer Physics* 54, 263–273.
- [270] Yin, B., Kaliske, M., 2021. An anisotropic phase-field model at finite strains for composite fracture. *PAMM* 20, e202000096.
- [271] Yu, B., Blanc, R., Soutis, C., Withers, P., 2016. Evolution of damage during the fatigue of 3d woven glass-fibre reinforced composites subjected to tension–tension loading observed by time-lapse x-ray tomography. *Composites Part A: Applied Science and Manufacturing* 82, 279–290.

- [272] Yu, B., Bradley, R., Soutis, C., Hogg, P., Withers, P., 2015. 2d and 3d imaging of fatigue failure mechanisms of 3d woven composites. *Composites Part A: Applied Science and Manufacturing* 77, 37–49.
- [273] Zhang, M., Zuo, C., Sun, B., Gu, B., 2016. Thermal ageing degradation mechanisms on compressive behavior of 3-d braided composites in experimental and numerical study. *Composite Structures* 140, 180–191.

Appendix A

Numerical Implementation of the coupled diffusion-deformation multiphysics problem

The weak forms of the initial boundary value problems described in Eq. 3.29 are obtained by multiplying each of the equations by two weight functions \mathbf{w}_1 and w_2 , respectively; \mathbf{w}_1 vanishes over the boundary S_2 and similarly, w_2 vanishes over S_{j_R} .

In absence of the body forces, the corresponding weak forms are given by

$$\begin{aligned} \int_B \left(\mathbf{T}_R : \frac{\partial \mathbf{w}_1}{\partial \mathbf{x}} \right) dV &= \int_{S_2} (\mathbf{w}_1 \cdot \check{\mathbf{t}}_R) dA \\ \int_B \left(\dot{c}_R^{O_2} + \dot{\xi} - \dot{\xi}_6 + D \frac{\partial w_2}{\partial \mathbf{x}} \frac{\partial c_R}{\partial \mathbf{x}} \right) dV &= - \int_{S_{j_R}} w_2 \frac{\partial c_R}{\partial \mathbf{x}} \check{j}_R dA \end{aligned} \quad (\text{A.1})$$

Next, the body is approximated using finite elements as $B = \cup B_e$. Assuming the nodal solutions are the displacement vector and the oxygen concentration, the trial solutions are interpolated inside each element by,

$$\begin{aligned} \mathbf{u} &= \sum \mathbf{u}^A N^A, \\ c_R^{O_2} &= \sum c_R^A N^A \end{aligned} \quad (\text{A.2})$$

where A denotes the node of the element and N^A is the shape function, \mathbf{u}^A and c_R^A are the nodal displacement and oxygen concentration respectively, and $\mathbf{u} = \mathbf{x} - \mathbf{X}$. The weight functions are interpolated using same the shape function as,

$$\begin{aligned} \mathbf{w}_1 &= \sum \mathbf{w}_1^A N^A, \\ w_2 &= \sum w_2^A N^A \end{aligned} \quad (\text{A.3})$$

Using Eq. A.2 and A.3 into A.1 yields the following system of equations:

$$\begin{aligned} \int_B \left(\mathbf{T}_R : \frac{\partial N^A}{\partial \mathbf{x}} \right) dV &= \int_{S_2} (N^A \check{\mathbf{t}}_R) dA, \\ \int_B \left(N^A (c_R^{(O_2)} + \dot{\xi}_2 - \dot{\xi}_6) + \mathbf{D} \frac{\partial N^A}{\partial \mathbf{x}} \frac{\partial c_R}{\partial \mathbf{x}} \right) dV &= - \int_{S_{j_R}} \left(N^A \check{j}_R \right) dA \end{aligned} \quad (\text{A.4})$$

Following which the system of equations are solved using an iterative Newton solver, with the element level residuals are given in the form as,

$$\mathbf{R}_u^A = - \int_{B^e} \left(\mathbf{T}_R : \frac{\partial N^A}{\partial \mathbf{x}} \right) dV + \int_{S_2} (N^A \check{\mathbf{t}}_R) dA \quad (\text{A.5})$$

for displacement residual and

$$\mathbf{R}_c^A = \int_{B^e} \left(N^A (c_R^{(O_2)} + \dot{\xi}_2 - \dot{\xi}_6) + \mathbf{D} \frac{\partial N^A}{\partial \mathbf{x}} \frac{\partial c_R}{\partial \mathbf{x}} \right) dV - \int_{S_{j_R}} \left(N^A \check{j}_R \right) dA \quad (\text{A.6})$$

for oxygen concentration, respectively.

The tangents for Newton solver are defined as,

$$\begin{aligned} K_{\mathbf{u}\mathbf{u}}^{AB} &= -\frac{\partial \mathbf{R}_{\mathbf{u}}^A}{\partial \mathbf{u}^B}, \quad K_{\mathbf{u}c}^{AB} = -\frac{\partial \mathbf{R}_{\mathbf{u}}^A}{\partial c_R^B} \\ K_{c\mathbf{u}}^{AB} &= -\frac{\partial \mathbf{R}_c^A}{\partial \mathbf{u}^B}, \quad K_{cc}^{AB} = -\frac{\partial \mathbf{R}_c^A}{\partial c_R^B} \end{aligned} \quad (\text{A.7})$$

Considering no traction force working over the boundary S_2 , the index form of $K_{\mathbf{u}\mathbf{u}}^{AB}$ can be written as,

$$K_{u_i u_k}^{AB} = \int_{B^e} \left(\frac{\partial N^A}{\partial x_j} \frac{\partial T_{ij}}{\partial u_k^B} \right) dV \quad (\text{A.8})$$

where u_k^B indicates the nodal displacement in direction k at node B . Using the identity $F_{mn} = \delta_{mn} + \frac{\partial N^A}{\partial \mathbf{X}_n} u_m^A$, such that $\frac{\partial F_{mn}}{\partial u_k^B} = \frac{\partial N^A}{\partial X_n} \delta_{mk}$, it can be obtained as,

$$\frac{\partial T_{ij}}{\partial u_k^B} = \frac{\partial N^B}{\partial X_n} \frac{\partial T_{ij}}{\partial F_{kn}} \quad (\text{A.9})$$

Then Eq. A.8 can be written as,

$$K_{u_i u_k}^{AB} = \int_{B^e} \left(\frac{\partial N^A}{\partial x_j} \frac{\partial N^B}{\partial X_n} \frac{\partial T_{ij}}{\partial F_{kn}} \right) dV \quad (\text{A.10})$$

Next, the tangent related to change in concentration c_R is calculated as,

$$K_{cc}^{AB} = - \int_{B^e} \left(\frac{N^A N^B}{\Delta t} + N^A N^B \left(\frac{\partial \dot{\xi}_2}{\partial c_R} - \frac{\partial \dot{\xi}_6}{\partial c_R} \right) + \mathbf{D} \frac{\partial N^A}{\partial x_i} \frac{\partial N^B}{\partial x_i} + \frac{\partial \mathbf{D}}{\partial c_R} N^B \frac{\partial N^A}{\partial x_i} \frac{\partial c_R}{\partial x_i} \right) dV \quad (\text{A.11})$$

where Δt denotes the difference between two consecutive time steps. Similarly, the

last two tangents are calculated as,

$$K_{uc}^{AB} = \int_{B^e} \left(\frac{\partial N^A}{\partial x_i} N^B \frac{\partial T_{ij}}{\partial \xi} \frac{\partial \xi}{\partial c_R} \right) dV \quad (\text{A.12})$$

and

$$K_{cu_k}^{AB} = - \int_{B^e} \left(\frac{\partial N^A}{\partial x_i} \left(\mathbf{D} \frac{\partial c_R}{\partial x_k} \delta_{il} \right) \frac{\partial N^B}{\partial x_l} \right) dV \quad (\text{A.13})$$

The system of equations are solved numerically for each element by writing a user element subroutine in ABAQUS/Standard (2018) [?].

Appendix B

Evolution of the chain distribution tensor

† while no oxidation (or chemical reaction is taking place), pure deformation Eq. 2.21 can be concisely written as,

$$\dot{\boldsymbol{\mu}} = \mathbf{L}\boldsymbol{\mu} + \boldsymbol{\mu}\mathbf{L}^T \quad (\text{B.1})$$

with all other reaction-dependent terms being zero and assuming the un-reacted network as incompressible. In such case, the solution for $\boldsymbol{\mu}$ turns out to be $\boldsymbol{\mu} = \mathbf{F}\mathbf{F}^T$, which is equivalent to the left Cauchy-Green strain tensor as, $\mathbf{B} = \mathbf{F}\mathbf{F}^T$. [255].

† when the mechanical deformation is held constant ($\mathbf{F} = \mathbf{I}$) and oxidation (only chemical reactions) is allowed to happen

Introducing,

$$\alpha = (\xi_4 + \xi_5 + \xi_6) \frac{C_T - c(t)}{c(t)} \quad (\text{B.2})$$

and $\beta = \xi_{1a} + \xi_3$ in Eq. 2.21, we get,

$$\dot{\boldsymbol{\mu}} = k_a \alpha \mathbf{I} - \left[k_d \beta + \frac{\dot{c}(t)}{c(t)} \right] \boldsymbol{\mu} + (\boldsymbol{\mu} + \boldsymbol{\mu}^T) \quad (\text{B.3})$$

Following which, the solution of $\boldsymbol{\mu}$ turns out as,

$$\boldsymbol{\mu} = \mathbf{F} e^{-(k_d \beta + c_m)t} \mathbf{F}^T + \frac{k_a \alpha}{k_d \beta + c_m} \mathbf{F} \mathbf{F}^T \quad (\text{B.4})$$

where $c_m = \frac{\dot{c}(t)}{c(t)}$, is used.

Appendix C

Principle of virtual power

We can write the external and internal power of the system as,

$$\mathcal{W}_{ext} = \int_{\partial P} \mathbf{t}_R(\mathbf{n}_R) \cdot \dot{\boldsymbol{\chi}} \, da_R + \int_P \mathbf{b}_R \cdot \dot{\boldsymbol{\chi}} \, dv_R + \int_{\partial P} \zeta(\mathbf{n}_R) \, \dot{d} \, da_R \quad (\text{C.1})$$

$$\mathcal{W}_{int} = \int_P \left(\mathbf{T}_R : \dot{\mathbf{F}} + \varpi \dot{d} + \boldsymbol{\zeta} \cdot \nabla \dot{d} \right) dv_R \quad (\text{C.2})$$

where \mathbf{b}_R is the non-inertial body force per unit volume of the reference body. Introducing the virtual rate fields as $(\tilde{\boldsymbol{\chi}}, \tilde{\mathbf{F}}, \tilde{d}, \nabla \tilde{d})$, we can further write the external and

internal expenditures of virtual power as,

$$\mathcal{W}_{ext,\mathcal{V}} = \int_{\partial P} \mathbf{t}_R(\mathbf{n}_R) \cdot \tilde{\boldsymbol{\chi}} \, da_R + \int_P \mathbf{b}_R \cdot \tilde{\boldsymbol{\chi}} \, dv_R + \int_{\partial P} \zeta(\mathbf{n}_R) \, \tilde{d} \, da_R \quad (\text{C.3})$$

$$\mathcal{W}_{int,\mathcal{V}} = \int_P \left(\mathbf{T}_R : \tilde{\mathbf{F}} + \varpi \tilde{d} + \boldsymbol{\zeta} \cdot \nabla \tilde{d} \right) dv_R \quad (\text{C.4})$$

Now the principle of virtual power requires that $\mathcal{W}_{ext,\mathcal{V}} = \mathcal{W}_{int,\mathcal{V}}$, and $\mathcal{W}_{int,\mathcal{V}} = 0$ for rigid virtual velocity \mathcal{V} , for any part P . The consequence of these requirements provides us the macroforce balance consistent with the Piola stress as,

$$\text{Div} \mathbf{T}_R + \mathbf{b}_R = \mathbf{0} \quad \text{and} \quad \mathbf{T}_R \mathbf{F}^T = \mathbf{F} \mathbf{T}_R^T \quad (\text{C.5})$$

Eq. C.5 represent the local macroforce and moment balance for the reference body.

As is standard, Piola stress is related to the symmetric Cauchy stress in the deformed body by,

$$\mathbf{T} = J^{-1} \mathbf{T}_R \mathbf{F}^T \quad (\text{C.6})$$

And the microstresses ζ and ϖ are consistent with the microforce balance equation together with the microtraction condition as:

$$\text{Div}\zeta - \varpi = 0 \quad \text{and} \quad \zeta(\mathbf{n}_R) = \zeta \cdot \mathbf{n}_R \quad (\text{C.7})$$

C.1 Energy imbalance

With reference to [143], for an isothermal polymer oxidation process, the local form of energy balance can be written as in Eq. 2.29, with additional terms appearing for the phase field damage process. Then, following the specific free energy form as Eq. 3.15, we get

$$\dot{\psi}_R = \left(\frac{\partial \hat{\psi}_R}{\partial \boldsymbol{\lambda}} \otimes \boldsymbol{\lambda} \right) : \mathbf{L} + \frac{\partial \hat{\psi}_R}{\partial d} \dot{d} + \frac{\partial \hat{\psi}_R}{\partial \nabla d} \cdot \nabla \dot{d} + \sum_{\beta} \frac{\partial \hat{\psi}_R}{\partial c_{R^{\beta}}} \dot{c}_R^{\beta} + \sum_n \frac{\partial \hat{\psi}_R}{\partial \xi_n} \dot{\xi}_n \quad (\text{C.8})$$

In view of Eq. C.8, the free energy imbalance Eq. 2.29 is equivalent to the requirement that the following inequality must be satisfied for all the constitutive processes:

$$\begin{aligned} & \left(\frac{1}{\bar{\lambda}} \frac{\partial \hat{\psi}_R}{\partial \bar{\lambda}} \boldsymbol{\lambda} \otimes \boldsymbol{\lambda} - J \hat{\mathbf{T}} \right) : \mathbf{L} + \left(\frac{\partial \hat{\psi}_R}{\partial d} - \varpi \right) \dot{d} + \left(\frac{\partial \hat{\psi}_R}{\partial \nabla d} - \zeta \right) \cdot \nabla \dot{d} \\ & + \sum_{\beta} \left(\frac{\partial \hat{\psi}_R}{\partial c_{R^{\beta}}} - \hat{\mu}^{\beta} \right) \dot{c}_R^{\beta} - \left[\left(- \sum_{\beta} \mu^{\beta} \sum_n \mathcal{R}_{n\beta} - \sum_n \frac{\partial \hat{\psi}_R}{\partial \xi_n} \right) \dot{\xi}_n \right] \\ & + \sum_{\beta} \hat{\mathbf{j}}_R^{\beta} \cdot \nabla \mu^{\beta} \leq 0 \quad (\text{C.9}) \end{aligned}$$

In the above equation, the stress-power ($\mathbf{T}_R : \dot{\mathbf{F}}$) has been related to the spatial configuration as,

$$\mathbf{T}_R : \dot{\mathbf{F}} = J \mathbf{T} : \mathbf{L} \quad (\text{C.10})$$

To hold the above inequality true for any arbitrary \mathbf{L} , \dot{c}_R^β and $\nabla \dot{d}$, their coefficients must vanish- the criteria which provides the constraint for the specific constitutive forms for the Cauchy stress, \mathbf{T} , the microstress, ϖ_{en} and ζ (as shown in the main text). In addition, the chemical potential, μ^β is given as [143],

$$\mu^\beta = \frac{\partial \psi_R(\mathbf{L}^m)}{\partial c_R^\beta} \quad (\text{C.11})$$

From the dissipation inequality, further the species flux needs to satisfy the species-transport inequality as,

$$\mathbf{j}_R^\beta(\mathbf{L}^m) \cdot \nabla \mu^\beta \leq 0 \quad (\text{C.12})$$

As in [143], we assume the oxygen flux obeys Fick's law, as,

$$\mathbf{j}_R^\beta = -\mathbf{M}^\beta \nabla \mu^\beta \quad (\text{C.13})$$

with \mathbf{M}^β being the mobility tensor. Substituting Eq. C.13 into C.12, we get the species-transport inequality always satisfied, for a positive definite mobility tensor as,

$$\nabla \mu^\beta \cdot \mathbf{M}^\beta(\mathbf{L}^m) \nabla \mu^\beta \geq 0 \quad (\text{C.14})$$

In addition, based on Eq. 2.37 the driving force for each individual reaction can be defined as,

$$\mathcal{F}_n = -\frac{\partial \psi_R}{\partial \xi_n} - \sum_{\beta} \mu^{\beta} \mathcal{R}_{n\beta}, \quad (\text{C.15})$$

and we choose a thermally activated relation for the evolution of extent of reaction $\dot{\xi}_n$ as,

$$\dot{\xi}_n = k_n \exp\left(\frac{-Q_{act}^n}{R\vartheta}\right) \mathcal{F}_n \quad (\text{C.16})$$

where, k_n is the pre-exponential rate constant for reaction n and has an unit of $\frac{1}{MPa-s}$,

Q_{act}^n is the activation energy for reaction n .